FRETTING-CREVICE CORROSION OF CEMENTED METAL ON METAL TOTAL HIP REPLACEMENTS

By

Michael George Bryant

Submitted in accordance with the requirements for the degree of

Doctor of Philosophy

The University of Leeds

School of Mechanical Engineering

Leeds, UK

August, 2013

The candidate confirms that the work submitted is his/her own, except where work which has formed part of jointly authored publications has been included. The contribution of the candidate and the other authors to this work has been explicitly indicated below. The candidate confirms that appropriate credit has been given within the thesis where reference has been made to the work of others.

In all papers listed below, the primary author completed all experimental studies, evaluation of data and preparation of publications. All authors contributed to proof reading of the articles prior to publication. Mr. John Nolan (Norfolk and Norwich teaching hospital, Norwich, UK) provided up to date clinical data regarding to the retrieved cohort of implants. Transmission Electron Microscope preparation and operation was carried out by Dr. Michael Ward (Institute of Materials Research, University of Leeds, UK).

Papers contributing to this thesis:

- Bryant M, Hu X, Farrar R, Brummitt K, Freeman R, Neville A. **Crevice Corrosion of Biomedical Alloys.** NACE - International Corrosion Conference Series, vol. 5, pp.4105-4120. 2012.
- Bryant M, Hu X, Farrar R, Brummitt K, Freeman R, Neville A. **Crevice Corrosion of Biomedical Alloys: A Novel Method of Assessing the Effects of Bone Cement and its Chemistry**. J Biomed Mater Res Part B (2013). Volume 101B Issue 5 792-803.
- Bryant M, Farrar R, Brummitt K, Freeman R, Neville A. **Fretting Corrosion of Fully Cemented Polished Collarless Tapered Stems: The Influence of PMMA Bone Cement.** Wear 301 (2013) 290-299.

- Bryant M, Ward M, Farrar R, Brummitt K, Freeman R, Nolan J, Neville A. **Failure Analysis Of Cemented Metal-On-Metal Total Hip Replacements From A Single Centre Cohort.** Wear 301 (2013) 226-233.
- Bryant M, Farrar R, Brummitt K, Freeman R, Neville A. **Fretting Corrosion Characteristics Of Cemented Polished Collarless Tapered Stems In A Simulated Biological Environment**. Tribology International 2013. In Press.
- Bryant M, Farrar R, Brummitt K, Freeman R, J. Nolan Neville A. **Characterisation Of The Surface Topography, Tomography And Chemistry Of Fretting Corrosion Product Found On Retrieved Polished Femoral Stems**. Accepted for publication in The Journal of the Mechanical Behaviour of Biomedical Materials
- Bryant M, Farrar R, Brummitt K, Freeman R, Neville A. **Influence Of Galvanic Coupling On The Fretting Corrosion Of Cemented Femoral Stems**. Submitted to Acta Biomaterialia
- Bryant M, Farrar R, Brummitt K, Freeman R, Neville A. **Influence Of Surface Roughness On The Fretting Corrosion Of Cemented Femoral Stems**. Submitted to Tribology International.

ACKNOWLEDGMENTS

Firstly I would like to thank my primary academic supervisor, Professor Anne Neville, for her continued support, enthusiasm, encouragement and advice throughout my studies. Her diligence to reviewing numerous papers, presentations and an extensive thesis is truly appreciated. It has been a pleasure from start to finish and would not have been possible without her.

Secondly I would like to thank my industrial supervisors Dr Richard Farrar, Mr. Robert Freeman, Dr Ken Brummitt and the others at DePuy International who have contributed to the project. Their knowledge, experience and passion for the subject ensured that the project had both a commercial and academic impact. The experience at DePuy International has developed me as not only an engineer but also as an individual with skills and knowledge that will leave me well prepared for the future. Their advice and guidance has been invaluable. I would also like to thank Mr. John Nolan for his clinical advice and continued commitment to fully understand the clinical issues.

I would like to thank Dr Xinming Hu. Although a brief encounter, his knowledge and contribution to electrochemical testing was invaluable. I would also like to thank Dr Michael Ward, Dr Tim Comyn as well as the guys at LEMAS for their help and patience in explaining the ins and outs as well as the pros and cons of crystallography and imaging techniques.

I would like to thank the iETSI and iESD technicians for their help and advice in fixture and sample preparation as well as the use of machinery. In addition I would like to thank the iETSI secretaries who have helped solve many issues over the years.

I would like to also thank the members of the iETSI research group. The opportunity to work with a wide and multi-disciplined range of people has helped widen my knowledge and understanding as an engineer. I would like to thank the guys of office 332a. I couldn't have asked for a better group of guys to work with.

Finally I would like to thank my Parents and Grandparents for their continued support and encouragement. In particular I would like to thank my partner Steff who has borne the brunt of many late nights, early mornings, moans and numerous practices of presentations. Her patience and encouragement has been invaluable.

ABSTRACT

The development and use of 2nd generation Metal-on-Metal (MoM) Total Hip Replacements (THRs) recently became popular due to the advancement of new materials and manufacturing processes promising improved performance compared to traditional metal on metal total hip replacements. The Ultima TPS MoM THR was designed and developed as a 2nd generation MoM THR specifically aimed at younger more active patients due to the anticipated low wear rates and increased longevity of MoM THRs. In 2010, published clinical data highlighted the early failure of the Ultima TPS MoM due to fretting-crevice corrosion at the stem-cement interface. Since 2010 similar observations have been reported by other clinical centres implicating competitor products as well as the Ultima TPS MoM THR.

In this thesis a systematic study has been completed in order to investigate and understand the role of fretting-crevice corrosion, and system variables, on the degradation mechanisms occurring at the stem-cement interface. Static and dynamic experimental approaches were adopted utilising *in-situ* electrochemistry and extensive post-test analysis. A full failure analysis of the retrieved cohort was also conducted in which the surface morphology and surface chemistry were quantified.

The review of the retrieved cohort demonstrated distinct directionality and plastic deformation of the metallic surfaces, characteristic of fretting-crevice corrosion demonstrating that complex fretting, electrochemical and tribo-chemical reactions exist at the stem-cement interfaces. The formation of thick deposited layers was also seen to occur within these interfaces, with films being seen to consist of Cr_2O_3 bound with organic materials.

Experimental investigation indicated that surface roughness, PMMA bone cement chemistry and galvanic coupling influenced the fretting-crevice corrosion rates at the

stem-cement interface. It was found that by increasing the surface roughness the pure and wear enhanced corrosion rates were significantly reduced. This was due to the combination of two influencing factors. An increase in the apparent volume at the stem-cement interface and the formation of a SiO_2 film created due to processing procedures. In an attempt to replicate the entire MoM system, fretting-crevice corrosion tests subjected to galvanic coupling were also conducted. Galvanic coupling was seen to significantly increase the rates of oxidation under static and dynamic conditions. This was due to the large potential differences developed across the system between active and passive areas, increasing the rates of oxidation and metallic ion release. Sulphate containing PMMA bone cements were also seen to decrease a metals' resistance to corrosion.

Cyclic loading was seen to further influence the surface morphology and chemistry of the femoral stem; along with the chemistry of the bulk environment. Distinct directionality of the femoral stem surfaces, characteristic of fretting wear, was seen in the proximal regions whilst localised crevice corrosion was seen in the distal regions. Thick Cr_2O_3 films were observed within the stem-cement interface resulting in a cobalt rich bulk environment. This complimented the retrieval analysis, along with other clinical studies which have associated cobalt rich environments with fretting-corrosion at the stem-cement interface.

From the findings presented in this thesis it has been possible to understand the factors and system variables pertaining to the early failure of the Ultima TPS MoM cohort. Furthermore, the findings and hypothesis developed by the candidate have been used to inform recommendations for current and future product combinations along with new design rules and experimental techniques for the development of future hip prostheses.

TABLE OF CONTENTS

LIST OF FIGURES

LIST OF TABLES

LIST OF EQUATIONS

NONEMCLATURE

(alphabetical order)

		Terms	Unit
A_o	-	Initial scratch area	cm
A_x	-	Area of the cathodic/anodic electrodes	cm
C	-	Material loss due to corrosion in absence of wear	g
C_{dl}	-	Double layer capacitance	
E	-	Measured cell potential	V
e	-	Electron. Subscript denotes the charge of the species	
E_b	-	Breakdown potential	V
E_{corr}	-	Free corrosion potential	V
E_{mixed}	-	Mixed corrosion potential	V
E^o	-	Standard cell potential	V
E_{pp}	-	Passivation potential	V
F	-	Faraday constant	$Cmol^{-1}$
FCC	-	Face Centre Cubic	-
HCP	-	Hexagonal Close Packed	-
I_a	-	Anodic current	A
I_{corr}	-	Corrosion current	A
i_{corr}	-	Corrosion current density	A/cm^2
i_d	-	Ionic dissolution	A/cm^2
i_f	-	Current due to film growth	A/cm^2
I_g	-	Galvanic current	A
I_p	-	Passive current	A
i_p	-	Passive current density	A/cm^2
i_t	-	Total current	A/cm^2
m	-	Mass Loss	g
M	-	Metal species	
M	-	Molecular mass	$gmol^{-1}$
n	-	Valence number of a particular metal species	
OCP	-	Open Circuit Potential	V
Q	-	Total Charge transfer	C
R	-	Ideal gas constant	$J\,K^{-1}\,mol^{-1}$
R_{ct}	-	Resistance to charge transfer	Ωcm^2
R_p	-	Resistance to polarisation	Ωcm^2
R_s	-	Solution resistance	Ωcm^2
S	-	Incremental factor of degradation due to the combined effect of corrosion and wear	g
S_a	-	Mean height of surface topography	µm

S_q	-	A more ‘stable’ expression of surface roughness	µm
S_{sk}	-	Indicates the direction of surface irregularities; zero for randomly rough surfaces, positive where peaks predominate, and negative where pits predominate	µm
S_z	-	Height between tallest peak and deepest valley	µm
T	-	Temperature	K
T_{wc}	-	Total tribocorrosion materials loss	mm^3
V_{chem}	-	Total volume of material removed by chemical attack	mm3
$V_{i\text{-}cement}$	-	Apparent Volume available for interdigitation on the cement surface	$\mu m^3/\mu m^2$
$V_{i\text{-}metal}$	-	Apparent Volume available for interdigitation on the metal surface	$\mu m^3/\mu m^2$
V_{mech}	-	Total volume of material removed by mechanical wear	mm^3
V_{tot}	-	Total volume of material removed	mm^3
W	-	Material loss due to pure wear in absence of corrosion	mm^3
β_x	-	Tafel slope of the corresponding half cell reaction	V/Dec
δ	-	Oxide thickness,	nm
ΔC_w	-	Change in corrosion rate due to wear	g
ΔG	-	Gibbs free energy	
ΔW_c	-	Change in wear rate due to corrosion.	g
η	-	Over-potential	V
Θ	-	Area fraction covered by oxide	
ρ	-	Oxide film density	g/L

CHAPTER 1 - INTRODUCTION

1.1. Motivation for Research

The method of using artificial devices to replace joints has been a method practised since the late nineteenth century by Gluck [1]. However it has only become a long term solution to arthritic and congenital diseased joints since the 1950's due to the advances in both fixation technique and implant design made by Sir John Charnley. The orthopaedics industries have made many advances since and Total Hip Arthroplasty (THA) is now widely accepted as being a successful surgical procedure with results from the National Joint Registry supporting this [2]. THAs are commonly used to treat arthritis or severe joint damage. Osteoarthritis of the hip joint is a painful and debilitating condition, estimated to effect 8 million people in the United Kingdom and 27 million in the United States [2, 3]. Different treatments exist to treat the condition but to date the most effective method of alleviating pain and restoring motion is THA. THAs are also used to mitigate other forms of hip disease such as rheumatoid arthritis, traumatic arthritis, hip fractures and tumours.

Figure 1-1 - Evolution of the Charnley Low Friction Arthroplasty[1]

The United Kingdom's National Joint Registry [3] indicates that in 2011, 71,672 primary hip procedures were conducted. Of the 71,672 primary hip procedures undertaken in 2011, 36% were cemented total hip replacements representing a significant proportion of implants on the NHS. Although the method of cementing the femoral component is a well-established technique, yielding superior short term results, an increasing trend away from the cemented technique to cementless fixation has been seen along with increasing reports of corrosion of the cemented portions of the femoral components.

In 2008, Donell et al [4] reported the dramatic corrosion of generally solidly fixed femoral stems when combined with Metal on Metal (MoM) articulations. It was thought that the necrosis of the surrounding tissue was associated with the release of potentially toxic metal ions such as cobalt and chromium from the stem-cement interface due to corrosion of the alloy. A subsequent publication by Boland et al [5] in 2011 further demonstrated high levels of corrosion on the cemented portions of MoM THRs further highlighting that the degradation mechanisms at the stem-cement interface can have serious implications. Unfortunately, the early failure of THAs has attracted substantial press attention, with the suitability of MoM implants and the metal ion release associated with such implants being questioned by many experts and the tabloid press [6, 7]. Although fretting-crevice corrosion of cemented THR has been identified in retrieval studies to be a source of ionic debris [4, 5, 8, 9], studies into the exact mechanisms of ion release and the factors affecting the rate in which metal ions are released have not yet been carried out.

1.2. Hypothesis, Aims and Objectives

At the time of project conception there was very little clinical and academic evidence regarding the effects of femoral stem corrosion and the system variables influencing the rates and mechanisms of corrosion. Although anecdotal at the time, there was a general believe by the key surgeons that there were some key common factors in each of the cases presented by Donell [4] and Bolland et al [5]. These were thought to be:

1. **Polished CoCrMo surfaces** – Thought to be more susceptible to fretting-corrosion due to the level and nature of slip at the interface. However classic corrosion science literature would suggest that roughened surfaces are more susceptible to corrosion.
2. **Cemented femoral stems** – The mechanical bond at the stem-cement interface was believed to promote crevice corrosion. The addition of antibiotics and radio-pacifiers was also thought to influence dissolution rates.
3. **MoM articulations** – Electrochemical interactions were thought to be established across the interfaces due to an all metal system. It was hypothesized that this would increase oxidation at the stem-cement interface due to galvanic corrosion effects. This will be simulated by means of galvanic coupling to simplified titanium rings in an attempt to represent the passive, static titanium acetabular component typically used *in-vivo*.

Therefore this study was established in an attempt to confirm the hypothesis outlined above. A systematic investigation was undertaken in order to understand the importance of fretting- crevice corrosion at the stem-cement interface. Electrochemical analysis, surface analysis and mass spectrometry techniques were

employed to investigate and quantify the influence of fretting and corrosion on the mechanism and production of debris under *in-vitro* static and dynamic conditions. In order to confirm the above hypothesis the influence of Poly Methyl Methacrylate (PMMA) bone cement chemistry, surface roughness, galvanic coupling and loading profile were investigated in order to gain a full and comprehensive understanding of the degradation mechanisms at the stem-cement interface.

1.3. Structure of Thesis

Chapter 2 presents a comprehensive review of corrosion and clinical literature relating to the use of biomedical materials and their application, identifying any gaps in the current knowledge and understanding. **Chapter 3** presents the experimental methods and techniques developed in order to investigate the degradation at the stem-cement interface. A full retrieval analysis of the cohort reported by Donell et al [4] is presented in **Chapter 4.** This has been included at the start of the thesis in order to set the current clinical position. **Chapter 5** investigates the influence of surface processing on the metallurgy and surface chemistry of LC CoCrMo. The chapters proceeding present the experimental work conducted throughout this project **(Chapters 6-9)**. Each experimental results chapter presents, discusses and concludes the main findings of the chapter. A final discussion highlighting the main findings, along with a comparison of recent clinical, retrieval and experimental studies, is presented in **Chapter 10**. The limitations of this study, future work and overall conclusions are also summarised. Figure 1-2 demonstrates the thesis and research structure.

Figure 1-2 - Thesis and research structure

CHAPTER 2 - LITERATURE REVIEW: THE SCIENCE OF JOINT REPLACEMENT, BIOMATERIALS, CORROSION OF METALS, TRIBOLOGY AND TRIBO-CORROSION

2.1. Introduction

Although the corrosion and tribo-corrosion of biomaterials have been discussed since the 1970s, information relating to the exact mechanism of localised corrosion of biomedical alloys and the potential implications still remains sparse. In light of this, the following literature review covers a large number of topics that are concerned with the science of joint replacement, metallurgy, corrosion and tribo-corrosion of alloys typically used for orthopaedic devices.

2.2. The Natural Hip

The hip approximates to a spherical or ball and socket joint and is connected between the longest bone in the body, the femur, and the pelvis at the lower end of the trunk [10]. The hip is one of the largest and heavily loaded joint in the human body. It has been noted by many people, for example Dowson [10], that the conditions under which a natural and prosthetic hip have to operate in are extremely complex and challenging from a bioengineers point of view. It is therefore important that a comprehensive understanding of the basic mechanics of the natural hip joint is fully understood to appreciate the natural mechanical functions and realistically define conditions for replacement hip design and analysis.

2.2.1. Anatomy of the Hip

The natural hip is a complex, well-structured mechanism that is intended for standing and walking. The hip can be split into three different components; Pelvis, Femur and Acetabular Capsule [11]. The Pelvis is composed of the coxae, the sacrum and coccyx, while the hip is formed by the fusion of the ilium, the pubis and the ischium. The Acetabular is the socket of the hip Joint. Dowson et al [10] describes the Acetabular socket as a deep cavity largely lined with articular cartilage, which faces obliquely forwards, sideways and downwards. Figure 2-1 demonstrates both the male and female pelvis. It is worth noting that the female pelvis is of a different shape to that of the male to allow for childbearing and birth [11].

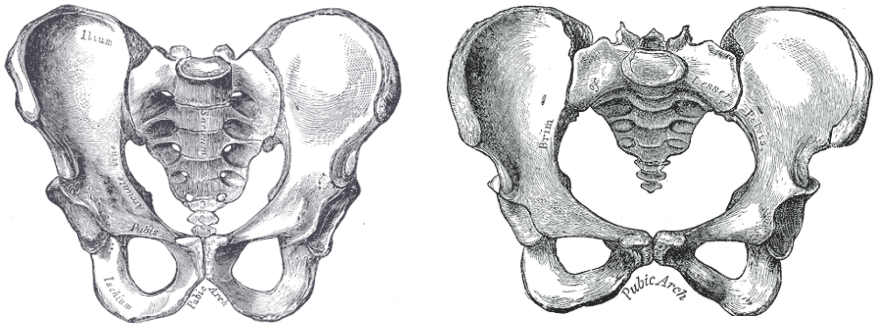

(a) ***(b)***

Figure 2-1 - The a) male and b) female pelvis [11]

The femur is the longest and heaviest bone in the body [11]. The rounded epiphysis or head articulates with the pelvis at the acetabulum. The head of the femur represents about two thirds of a sphere and is entirely covered by cartilage, except for a small depression region round the fovea where the capsule ligament is attached. The neck joins the shaft at an angle of approximately 125°. The greater and lesser trochanters at the proximal end of the femur are long prominences which form the points of attachment of strong muscles. The femur is usually characterized

by having an outer shell of dense cortical bone with cancellous or spongy bone within the cortical shell [10]. Figure 2-2a and b demonstrate the anterior view of the right femur with attachments of ligaments, muscles and membranes labeled and the outer and inner shells of bone.

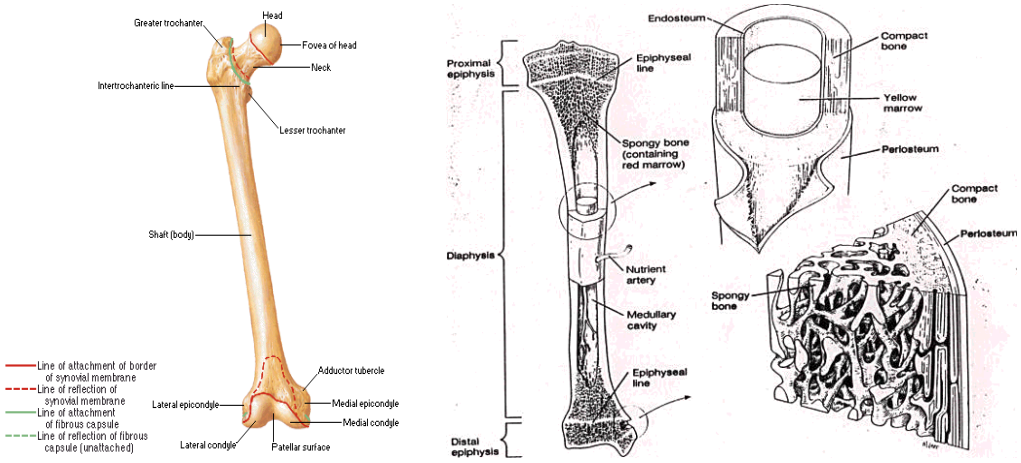

(a) ***(b)***

Figure 2-2 - a) Anterior and b) sectioned view of the adult femur

The hip joint is enclosed by a synovial membrane which is attached to the femoral head. Dowson et al [10] stated that the capsule consists of strong dense structure of ligaments that include three ligaments; ilio – femoral, ischo-femoral and pubo – femoral. In general the ligaments retain the femur lightly in the capsule, prevent extension much beyond the straight position and limit abduction and movements of rotation.

2.3. Kinematics and Dynamics of the Hip Joint

Nearly forty muscles act on the hip joint to effect movement, which is grouped into three major directions. Flexion and extension involves the motion of the thigh forwards and backwards in the sagittal plane, while abduction and adduction consist of movements in the coronal plane forcing the thigh away from the centre line of

body and back towards the body respectively. Finally medial and lateral rotation, also commonly referred to as internal and external rotation, involve rotation of the thigh about its long axis in towards the centre of the body or away respectively.

When evaluating the loading within the joint, one of two main techniques is generally utilised: both calculation and modelling using values from force plates on the ground and derivation of muscle actions across the joint or *in vivo* measurement using instrumented implants. The former technique is more susceptible to variation depending on the exact model developed, but offers the benefit of being easy to perform on a wide range of subjects [12]. The latter can be more accurate in the actual measurements taken, however sample size is limited, and information on the gait during these measurements is not always generated [13].

The values presented in Figure 2-3 demonstrates the data obtained by Bergmann et al [13] from instrumented hip implants where load was measured by means of an instrumented implant, and motion analysed using a laboratory fixed camera system monitoring markers placed on the body. Bergmann found that the major motion occurs in flexion / extension of approximately 34˚, with a twin peak loading profile in the vertical axis with a peak load of 2.3BW. Bergmann also noted that peak load increased from 2.8BW to 4.8BW for a velocity increase of $0.27ms^{-1}$ to $1.35ms^{-.1}$.

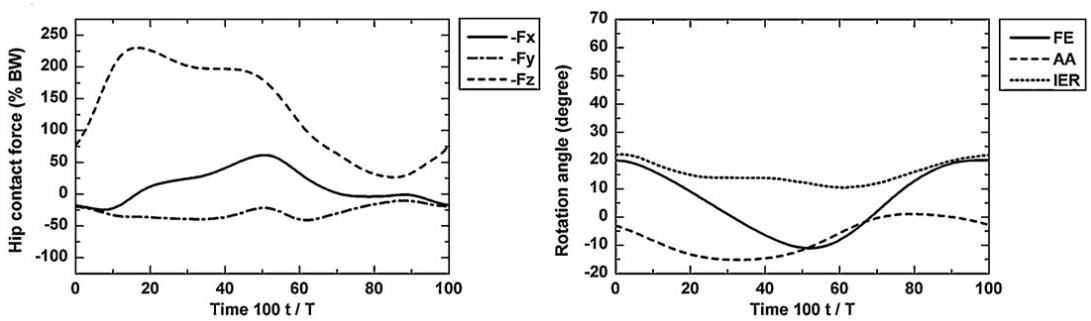

(a) **(b)**

Figure 2-3 – (a) Forces and (b) angular patterns for walking [13]

2.4. Diseases of the Hip

Joint diseases, rheumatoid arthritis, osteoarthritis, osteoporosis, spinal disorders, low back pain, and severe trauma are among 150 musculoskeletal conditions affecting millions of people globally according to the world health organisation [14-15].

2.4.1. Arthritis

Arthritis is a group of conditions in which there is inflammation of the joints, causing pain, stiffness, disability and deformity. The two most common forms of arthritis are rheumatoid arthritis and osteoarthritis. Approximately 20 million people in the United Kingdom will experience a form of arthritis each year, accounting for one-third of those registered severely disabled and effecting 1 in 5 people at some point in their life [15].

The most common form of inflammatory arthritis is rheumatoid arthritis. Rheumatoid arthritis is an auto-immune disease, involving chronic inflammation of the joints, originating within the synovium. Inflammation of the synovium usually results in thickening of the membrane, occupying the space in the joint. The inflammation spreads, resulting in the supporting ligaments becoming stretched, thus reducing stability. Cartilage eventually degrades, exposing the ends of bones, leading to progressive destruction and deformity of the joint. Rheumatoid arthritis occurs mostly in people aged 20 and above with women being 2.5 times prone to hip disease than men [15].

Osteoarthritis is a degenerative condition due mainly to accumulated wear of a joint. It is the degeneration of the articular cartilage and formation of new bone beneath the cartilage, which protrudes at the edges of the joint. Increased joint fluid causes swelling and stiffness, resulting in severe and unbearable pain.

2.4.2. Osteoporosis

Osteoporosis is a progressive loss of bone density which occurs when calcium dissolves from the bones leaving them porous and weak [16]. Osteoporosis is considered to be an age related condition, found to be more common in females. Fagerson [17] explained that bone density reduces by approximately 2% per year from 50 years onwards.

2.4.3. Avascular Necrosis

Avascular necrosis of the femoral head occurs when there is a regional interruption of blood flow to the hip resulting in cellular death [18]. The condition usually occurs in the absence of infection in which severe and prolonged ischemia may cause regionally located osteoblasts and chondrocytes to die. Effort to repair the bone occurs by resoption of bone, ultimately reducing the strength of the bones. It is estimated that avascular necrosis effects 10 to 20 thousand patients a year in the US [18, 19]. It is most common in people 30-70 years of age, with men four times more likely to suffer from the condition. Other causes of avascular necrosis include alcoholism and prolonged use of steroids [19].

2.5. Lubrication of the Hip

The fluid within the natural hip is known as the synovial fluid. The cavity usually contains less than 0.5ml and is described by Gray's Anatomy [11] as a viscid, glairy fluid. Its composition is consistent with the view that it is a dialysate of with the addition of hyaluronic acid, which is secreted by the synovial membrane. It has a small cell count, approximately 60 per ml, mainly consisting of monocytes, histiocytes and lymphocytes with a few synovial cells. Roba et al [20] explained that under physiological conditions, synovial fluid is an aqueous electrolyte solution

rich in proteins, lipids and hyaluronan. When in combination with articular cartilage synovial fluid acts as a lubricant and provides the low friction coefficients found in the hip. Following THA the synovial membrane is reformed and the artificial materials are lubricated by a pseudo-synovial fluid which is believed to be similar in composition to the synovial fluid before surgery.

2.5.1. Proteins and Protein structure

Proteins are complex, high molecular weight organic compounds that consist of amino acids joined by peptide bonds. Albumin is considered the most abundant protein in synovial fluid and has been shown to drastically alter the corrosion regimes of biomaterials. He et al [21] described Human Serum Albumin (HSA) as a three dimensional, three homologous domains that assemble to form a heart shaped molecule (Figure 2-4). HSA consists of 585 amino acids and is comparatively rich in cysteine, which allows HSA to form 17 disulfate bridges. HSA consists of three domains with similar primary structure and is glycosylated at residues Asn-342 and Asp-518 [20-22].

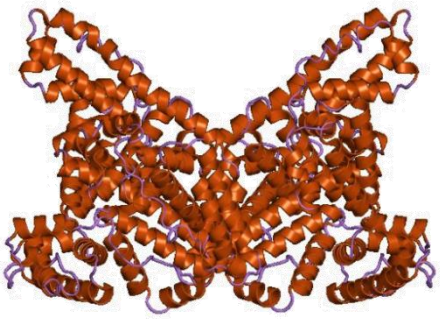

Figure 2-4 - Structure of HSA

2.5.2. Protein Absorption and Interaction with Metals

A protein in its native state is described as being folded. In solutions proteins can be unfolded by a change in chemical environment, pressure or by changes in temperature. Heuberger et al [22] stated that the temperature in articulating joints can reach 45° C below the cartilage surface and 90° C during *in-vitro* simulator tests. Such conditions irreversibly unfold and denature proteins significantly altering lubrication and corrosion properties.

Adsorption is defined as the accumulation of molecules to form a thin film on the surface of a solid. Yu Yan [14] explained that the nature and thickness of a protein adsorption layer depends on a materials surface properties, such as wettability, polar or ionic interaction chemical structures and topography of the surface. Proteins tend to denature or unfold on the surface of some materials due to the change in energy, resulting in an increased amount of adsorption sites. Upon adsorption onto a hydrophobic surface the lubricating fluid is adsorbed and the albumin protein unfolded. This behaviour results in denatured proteins on the surface of a material, resulting in a high shear strength layer with strong hydrophobic interactions between the albumin and the materials surface [20]. The roles proteins play in the tribological aspects of total hip replacements have been well documented. Many authors refer to the layer developed by the adsorption of proteins as a 'tribo-film' [23-25].

2.6. Concept of Joint Replacement

The method of using artificial devices to replace joints has been a method practised since the late nineteenth century. However it has only become a long term solution to arthritic and congenital diseased joints since the 1950's due to the advances made by Sir John Charnley. Orthopaedics has made many advances since, and Total Hip

Arthroplasty (THA) is now widely accepted as being a successful surgical procedure with results from the National Joint Registry supporting this.

The standard process for a THA involves the removal of the femoral head and a large part of the proximal femur through the use of a succession of broaches and reamers that prepare the intramedullary canal [17]. However in the vast majority of cases the disease that necessitates THA only affects the regions of the femoral head and acetabular, resulting in a large removal of healthy bone and tissue. It is therefore important to design a system that helps preserve healthy bone stock whilst transferring loads to the proximal femur evenly. If loading patterns are insufficient, there is a possibility of bone resorption across the large sections of the proximal femur; a phenomenon first quantified by Wolff [26]. The removal of large amounts of healthy bone and tissue also provides a space for debris associated with device degradation to travel into. It is therefore important that during the design process, spaces and inclusions are eliminated by incorporation of suitable design and fixation techniques. Failure to eliminate such factors can result in particle – induced osteolysis, rectified by a revision procedure which tends to be less successful than THA.

In recent years alternative stem designs have been considered in an effort to address these issues. One type is known as the anatomical design which attempts to distribute load as naturally as possible by replicating the geometry of the femur and the natural loading patterns of the body. Other designs have involved the shortening or complete removal of the distal stem to try and preserve as much bone stock as possible [27, 28].

2.7. Implant Design

During the design process of a THR there are many factors that must be taken into consideration.. Anatomic stems have been available on the orthopaedic market for over 20 years [28-30]. Anatomically designed stems usually consist of a proximal medial lateral flare and a distal section. One of the most popular cemented anatomic stems implanted in the UK today is Exeter V40 (Figure 2-5) [30]. Fowler et al [29] explained that the Exeter was the first polished, collarless, double taper geometry stainless steel hip to be introduced in the early 1970s. Although the results for this stem were good for this time, the design was later adjusted in 1976 due to an increased amount of stem fracture. Advances in materials and processing saw the Exeter stem further evolve, with changes in surface finish and material type being adjusted [31].

(a) **(b)**

Figure 2-5 – a) Exeter modular femoral stem b) schematical view of a cemented Exeter femoral stem with large diameter head.

Although initial device design has existed since the ninetieth century, an increased demand for THA in young and active patients has seen the development for a new generation of short or stem less THRs (Figure 2-6). There are numerous benefits from a shortened or no distal stem, some of which include; better load distribution in the medial, lateral anterior and posterior walls of the femur, optimum control of axial and torsion stresses, excellent control of calcar and lateral flare, bone stock preservation and an easier surgical procedure. It has been shown that cementless, anatomically designed femoral components can provide satisfactory, early pain relief and function in a more younger and active patient population [32, 33].

Figure 2-6 - Variety of short stemmed components currently available in the United Kingdom (Image taken from DePuy international promotional material)

2.8. Fixation methods

2.8.1. Cementing Technique

In 2009, 53% of THR procedures carried out in the UK used Poly Methyl Methacrylate bone cement as a method of stabilising the femoral stem component of the hip prosthesis; a practice first pioneered by Sir John Charnley in the 1960's [34]. The performance of cemented THR is strongly supported by both registry figures

and clinical research. This reflects the practice of surgeons in many countries who are comfortable with their cementing technique [35]. Although over the last few years a decline in cemented femoral stems has been seen, the use of PMMA bone cement still remains the preferred method of fixation in patients greater than 70 years of age. There are two types of bone cement commonly used in the fixation of surgical devices. In 2012, antibiotic bone cement was used in 99% of THA operation [30].

Commercial bone cement is packaged as two components: liquid MMA monomer and a powder component containing pre-polymerized beads of PMMA of 20-100 micrometer diameter, along with 1 micrometer diameter radiopacifier particles of barium sulphate or zirconium oxide and benzoyl peroxide reaction initiator (Figure 2-7). The structure of poly (methyl methacrylate) monomer allows polymerisation at room temperature to produce solid PMMA as a result of an exothermic chemical reaction [36, 37].

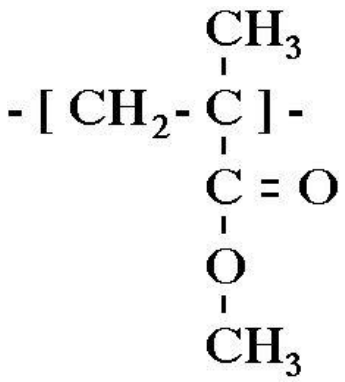

(a) **(b)**

Figure 2-7 – a) Commercially available (Image taken from www. Stryker.com) and b) molecular structure of PMMA bone cement

Although the method of cementing the femoral stem using PMMA bone cement is frequently practiced, there are some problems that are associated with this method. Webb et al [36] explained that the cement can sometimes shrink towards the end of polymerisation which compromises the bone, cement and stem interfaces. They also recognised that there is a conflict between the stiffness of cement and the adjacent bone with cement providing a shock-absorbing layer between elastic bone and a stiff implant. Another recognised pitfall was the cement mantle and its interfaces may be the weak link in the construct, with the bone/cement/stem interface been the key to the survival of a joint replacement. Research has indicated that polished collarless tapered stems generally performed better, compared to cementless femoral stems, when PMMA bone cement is used as the primary method of fixation [38-40]. Webb [36] also recognised that cement particles may cause biological aseptic loosening of the cement and stem, resulting in monomer-mediated bone damage. However this was questioned by some authors as he believed that the failure was due to mechanical reasons as he stated that the cement was inert [36, 40].

Antibiotic cement was first introduced by Buchholz and Engelbrecht in 1970, incorporating Gentamicin in PMMA, with the aim to treat infection in prosthetic joints. The use of antibiotic-loaded acrylic cement in joint replacement provides short- to medium-term protection against prosthetic infection. It aims to overlap with, and then replace, the prophylaxis provided by peri-operative intravenous antibiotics. To achieve this it must be released from cement in high enough concentrations to exceed the minimum inhibitory concentration of potential colonising bacteria [40, 41]. However, adding antibiotics to acrylic bone cement can have adverse effects on the mechanical strength. Lautenschlager et al [40] carried out studies in 1976 indicated that the introduction of Antibiotics into the bone cement can lead to a 40% reduction in compressive strength *in-vitro*. Throughout the

evolution of antibiotic acrylic cement, different types of antibiotics and additives have been introduced, with the aim to fight infection more efficiently.

The most common antibiotic agent used in PMMA bone cement is Gentamicin sulphate. This is reflected in both the British and Swedish national joint registries [42, 43]. Gentamicin is an amino glycoside antibiotic, primarily used to fight gram-negative bacteria. Gentamicin has proven to be effective against many gram-negative bacteria strains, making it an ideal and most common antibiotic to combine with acrylic bone cement [44]. Although the use of antibiotic loaded PMMA bone cement has been seen to significantly reduce the rate of revisions, the evolution of cementing techniques has also had a significant impact. Barrack et al [45] studied the effect of cementing technique with respect to the loosening of femoral component. Barrack compared the revision rate of the first generation cementing technique to the second generation cementing technique. At a 5 year follow up of the first generation cementing techniques, 20% - 24% of implants displayed some sort of aseptic loosening. This increased to 30% - 40% at 10 years. Barrack found that with second generation cementing techniques, no revisions were necessary until around 12 years. Barrack attributed his reduced loosening rate to the introduction of improved cementing techniques and better stem design. It has been reported by Wroblewski et al [46] that stem revision rates due to loosening have reduced from 6% to 0.9%. It is thought that this is due to the introduction of an intramedullary plug and vaccumm mixing and injecting into his cementing technique.

Nowadays less than 1% of all primary THA need to be revised because of primary or secondary infection. However the treatment of an infected THA still remains a major challenge. The introduction of antibiotics into the bone cement has proven to be 85% effective in curing infection. Antibiotic loaded bone cement has had a great

influence in the longevity and survivorship of orthopaedic implants [43, 47]. A study conducted by Parvizi et al [48] demonstrated that the rate of deep infection following THA, at 1.2%, was significantly lower when antibiotic cement was used than when cement without antibiotics was used (2.3%). It was concluded that the introduction of antibiotic-impregnated cement lowered the infection rate by approximately 50% in primary procedures and 40% for revision procedures.

Table 2-1 - Commercial constituents of bone cement

Constituent		Role
Powder Components		
	Polymer	Polymethylmethacrylate
	Co-polymers (eg MA-MMA)	Alter physical properties of the cement
	Barium sulphate or zirconium dioxide	Radio-opacifiers
	Antibiotics	Antimicrobial prophylaxis
	Dye	Distinguish bone cement from bone
Liquid Components		
	Monomer	Methlmethacrylate monomer
	N,N-dimethly-p-toluidine (DMPT)	Initiates cold curing of polymer
	Benzoyl peroxide	Reacts with DMPT to catalyse polymerisation
	Hydroquinone	Stabiliser preventing premature polymerisation
	Dye	Distinguish bone cement from bone

2.8.2. Cementless Stems

The aim of utilising porous coatings on cementless implants is to facilitate boney in growth thus securing a strong interlock between implant and bone to assist in the achievement of long term survivorship [49]. The principal alloys used in proximally porous-coated joint replacement surgery are based on either cobalt chromium or titanium alloys. The physiological response to an inserted proximal porous coated implant resembles the healing cascade cancellous defect, with newly formed bone occupying the porous surface of the metal. Hydroxyapatite (HA) has also been used as a surface attachment. The addition of HA to porous implants was introduced to accelerate the adherence of bone to the surface of the implant and aid the filling of gaps between implant and bone (Figure 2-8) [49].

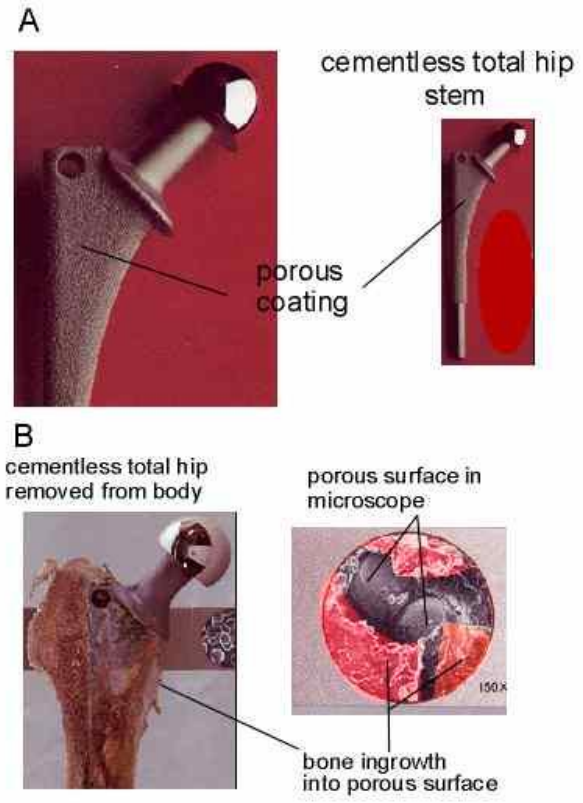

Figure 2-8 - Example of a porous HA coated device [49]

Although porous coatings are an ideal method of fixation of stems, there are still inherent short comings with the method with respect to fixation in the elderly. McAuley et al [50] studied the suitability of porous coated prostheses in patients 65 years and over. McAuley concluded that THA without cement can be successful in older patients. However he did note that fixation of the femoral component without cement in older patients can reduce the stability of implant and failure of the osseous bone in-growth, resulting in stress shielding to occur. McAuley also stated that although osteolysis is still a problem with cementless stems, it was observed that it was less of a problem in patients 65 and over. He concluded that circumferential porous coatings can protect against osteolysis of the distal aspect of the femur.

2.9. Bearing surface materials

Along with different types of materials and fixation methods, there are also numerous bearing materials and combinations that need to be considered during the design of a implant. The common combinations of bearing materials are shown below in Figure 2-9. Although extensive research into the suitability of orthopaedic bearing materials has been conducted, the suitability of MoM bearings still remains controversial. June 2007 saw a MHRA medical device alert issued on the DePuy MoM Bearing followed by another MHRA medical device alert issued for all MoM hip replacements in April 2010. Reports of soft tissue reaction and unexplained hip pain have been associated with MoM THR [51].

(a) **(b)** **(c)**

Figure 2-9 - Typical THR (a) Ceramic-on-Polymer (b) Metal-on-Polymer (c) Metal-on-Metal (Image taken from DePuy international promotional material)

2.9.1. Metal – on – Metal THA

Metal-on-metal was used in the early stage of THR, although not all old designs were successful. The first generation of MoM THR were designed and developed by Philip Wiles in 1938 [52]. However these implants were largely unsuccessful due to the poor quality of material which was primarily stainless steel, poor manufacture and lack of adequate fixation within the body. However with the introduction of methyl methacrylate bone cement in the 1960s by Sir John Charnley and the development of new materials, the 2nd generation of MoM THR were developed. Weber et al [53] was one of the first to realise that in fact the low wear rates of MoM THRs could be related to a reduction in loosening. Chan et al [54] explains that 2nd generation MoM implants are traditionally manufactured from surgical grade CoCrMo alloys because of their corrosion resistance and hardness. Cobalt based alloys are generally well suited as self-bearing materials. They are known for a certain self-healing capacity, the ability to polish out visible surface scratches with continued wear cycles rather than to experience a progressive deterioration of the surface topography leading to accelerated wear [55].

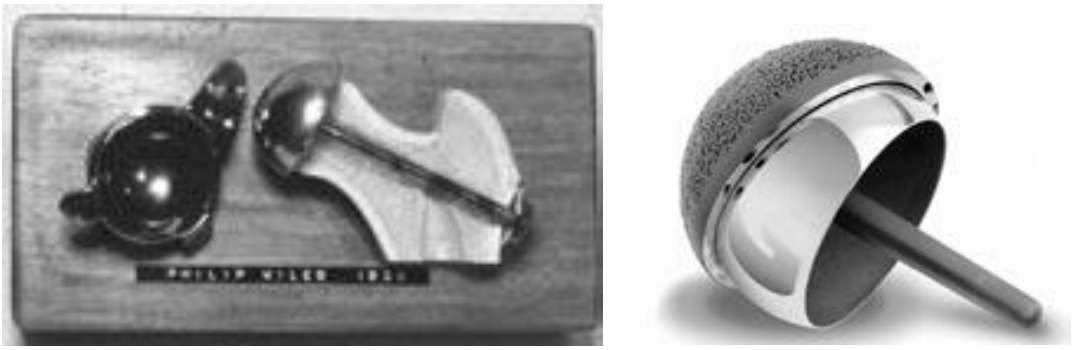

(a) **(b)**

Figure 2-10 – a) Wiles' acetabular cup and resurfacing of the femur. First generation MoM and b) modern MoM hip resurfacing [1]

Although CoCrMo alloys and MoM THRs are ideal from a tribological view, there are still many biological issues that surround these types of implants. Studies of retrieved MoM implants and the accompanying periarticular tissues have indicated that the amount of metal particulate released from well-functioning components is well below the threshold for inducing a substantial osteolytic response. Campbell et al [56] stated that MoM bearings and the corresponding metallic wear debris can release metallic ions in substantially greater concentrations than typically occur in polyethylene or ceramic bearing, forming soluble or precipitated organometallic species. Many authors argue against the use of cobalt alloys in THR as the risk of metal ions within the human biological system is not yet fully understood. Cancers associated with cobalt and chromium implants have been reported in some animal implantation models, but to date, epidemiologic studies of patients with THR have not shown a higher incidence of cancer with MoM prostheses [17]. However most researchers agree that more comprehensive studies of the effects of cobalt and chromium within the human body should be conducted as related musculoskeletal or hematopoietic cancers can take several decades to develop. Campbell et al [56] also

stated that all metals in contact with biologic systems undergo corrosion: corrosion products have been shown to cause dermatitis, urticaria and vasulitis.

MoM THRs have the longest clinical history of any of the bearing combinations, with the majority of the contemporary MoM bearings still functioning well. Retrieval studies indicate that well-functioning MoM THRs produce minimal wear debris and the surrounding tissues appear to have less inflammation compared with typical histiocyte-dominated tissue response to Polyethylene debris. Park et al [57] analysed 165 patients (169 hips) who had undergone primary cementless total hip replacement with a contemporary MoM total hip design between 2000 – 2002. After a minimum follow up time of 24 months, nine patients (10 hips) had osteolytic lesions localised to the greater trochanter. Skin patch tests for metal hypersensitivity were performed, revealing that the patients with early osteolysis had a significantly higher rate of hypersensitivity reaction to cobalt. Park explained that hypersensitivity was caused by the corrosion of the metallic stem. Further explaining that ions released from the corrosion process can activate the immune system by forming metal – protein complexes that are considered to be candidate antigens for eliciting hypersensitivity responses. Although the failure of the first generation metal – on – metal implants has been linked to cobalt, nickel and chromium hypersensitivities, it was unknown if the patients had a pre-existing metal hypersensitivity or if they developed such hypersensitivities as result of implant failure.

Clayton et al [58] outlined the effects of metal ion release into the biological system in a 63 year old woman that underwent MoM THA in June 2005. Clayton reported that after one year postoperative, the patient presented an increased amount of discomfort and swelling in the right hand region of the groin. The patient also

incurred a loss of sensation in the anterior portion of the right thigh and weakness in the right limb. Clinical investigation revealed a firm mass known as a 'Pseudotumor' in the iliac fossa and soft tissue necrosis. The mass contained elevated levels of cobalt and chromium. Clayton concluded that the cause of the implant failure was due to the local and systemic release of large metal ions from the bearing surfaces, initiating chronic inflammatory reactions and extensive soft tissue necrosis. It was reported that cobalt and chromium levels increase eightfold after MoM THR, with levels peaking 6 months after surgery [58].

2.9.2. Other Common Bearing Combinations

There are numerous varieties of bearing combinations, suitable for THA. Although such combinations are considered more suitable than MoM bearings, the wear of different materials is still implicated in the production of particulate debris which, in turn, is associated with osteolysis and loosening of the prosthesis.

In a study conducted by Riskar et al [59], Ceramic-on-Ceramic (CoC) bearings were considered. 143 patients were fitted with a cemented alumina acetabular cup and 112 with a cementless Acetabular cup. For the cemented acetabular patients, 16 patients (11%) underwent some revision, due to failure. 12 cases saw failure due to the acrylic bone cement. In the cases of the patients implanted with the cementless acetabular cup, seven cases had to be revised (7%). Two cases were classed as late infection, one case was technical error and in two, progression of Pigmented villonodular synovitis. Riska et al [59] stated that there had been no wear problems associated with the 255 implanted ceramic endoprostheses.

Prostheses with Ceramic-on-Polyethylene (CoP) and Metal-on-Polyethylene (MoP) articulations are also considered for THA. Zichner et al [60] conducted a study into the suitability of such materials; metal and ceramic femoral heads were studied

against a polyethylene acetabular cup. At a follow up period of 2.5 – 9 years, 95% of CoP bearings had a wear rate of less than 0.2mm/year compared with only 64 – 77% of the MoP articulations. A mean wear value of 0.26mm was found for the ceramic on polyethylene articulation compared to 0.96mm for the MoP bearing. Zichner concluded that the combination of CoP bearing materials gave superior results compared to the metal on polyethylene articulations [60].

2.10. Biomaterials

Biomaterials are defined as materials used in medicine that are intended to come in contact with living tissue [61]. The term biomaterials covers all materials used in medical applications and are mainly manufactured from metals ceramics and polymers. Biomaterial implants improve the quality of life for an increasing number of people each year, not just for an ageing population with greater life expectancy, but for younger people with heart problems, injuries or inherited diseases [61].

The most common metallic materials that are used in prosthetic implants are usually; cobalt based alloys, iron based alloys (stainless steels) and titanium alloys. Sury et al [62] explained that metals are commonly used because of their high resistance to static and dynamic loads and as a result of electrochemical stability. Although pure metals are sometimes used in orthopaedic applications, alloys are commonly used as the mechanical properties are usually enhanced. The disadvantage of metallic materials is that they are susceptible to chemical and electrochemical degradation. However polymers and ceramics can also be subject to corrosion attack [62].

2.10.1. Cobalt-Based Alloys

Cobalt occurs in nature in a fairly widespread but dispersed form, being detectable in trace quantities in many rocks, coals, soils and plant life [63]. The material occurs principally as sulphides, arsenides or oxides. Cobalt was first used by the Egyptians as a colouring agent for pottery and now has a wide range of practical applications, but almost all these involve its use as an alloying constitute or as a chemical compound; the pure metal has few applications but is important as a metal for scientific study, being particularly characterised by its ferromagnetic properties and a high curie temperature (the point at which the metal becomes paramagnetic) [63]. Cobalt alloys are termed austenitic in that the high temperature Face Centred Cubic (FCC) phase is stabilised at room temperature. Although Co based alloys are often termed austenitic, they can be susceptible to shear slip and twinning induced transformation from the FCC to Hexagonal Close Packed (HCP) packing structure. This is due to the relatively low stacking fault energy of the alloy [64]. Numerous studies have demonstrated the role shear plays in the re-orientation of the CoCrMo alloy, hypothesising improved tribological/tribocorrosion properties [65-67]. Cobalt based alloys owe their strength to the precipitation of carbides at the grain boundaries. Other refractory metals are added to give solid solution strengthening, carbide formation and increased corrosion resistance [63].

There are numerous varieties of cobalt based alloys available for surgical implants; however the main cobalt based alloy used in orthopaedic applications is cobalt – chromium–molybdenum (CoCrMo). Cobalt-based alloys, such as Co-Cr-Mo castings, usually consist of a Co-rich matrix, sometimes including tungsten; and modifications including higher nickel contents (MP35N). Cast cobalt alloys have been characterised as one of the least ductile of the alloys, compared with the iron-

and titanium-based composites [68]. However recent manufacturing processes, such as hot isostatically pressed (HIP) and alloy modifications have greatly improved the mechanical properties of the cobalt-based alloys. These alloys have been used in clinical applications since the 1940's, with early studies traced to Strock, Venable and Stuck [68].

2.10.2. Iron-Based Alloys

Stainless steels are iron based alloys that contain a minimum of approximately 11% Cr, the amount needed to stabilize a chromium rich oxide layer (typically Cr_2O_3), with the ability to heal itself in the presence of oxygen. Again, other elements and refractory metals are added to improve certain characteristics [69]. Figure 2-11 demonstrates the influence of different elements on the mechanical and chemical properties of stainless steels

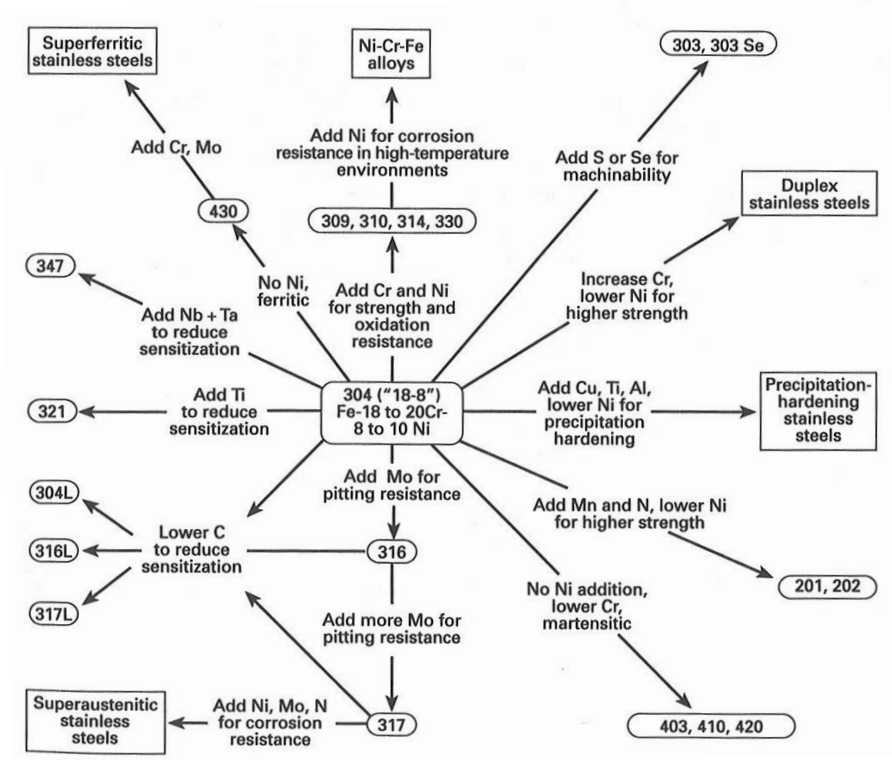

Figure 2-11 - Composition and propensity linkages in the stainless steel family [69]

Austenitic stainless steels constitute the largest stainless family in terms of number of alloys and usage. Austenitic stainless steels are essentially nonmagnetic in the annealed condition and can be hardened by cold working. Stainless steel alloys are termed austenitic in that the high temperature 'FCC' phase is stabilised at room temperature. Although Stainless steel is regarded as corrosion resistant, it is susceptible to localised corrosion such as; crevice, pitting and inter-granular [64, 69, 70].

Austenitic stainless steel was one of the first alloys to be used in orthopaedic applications, with studies conducted in 1912 by Shermon [68]. Today stainless steel is used in a variety of medical applications. 316L Stainless steel is a relatively strong and ductile alloy that can be easily fabricated by standard machining operations. Therefore, the comparative costs of manufacturing are not excessive and large numbers of plates, screws, rods, external fixtures, and other devices have been provided for surgical procedures [69]. Although stainless steel is an ideal material for biomedical application there is one limitation that is often associated with surgical stainless steel. 316L Stainless steel is susceptible to crevice or fretting corrosion, which is associated with the localised loss of the protective complex chromium oxide surface layer. Nitrogen stainless steel (HNSS) is also an alloy commonly used for biomedical applications. Nitrogen was initially added to the alloy to improve fatigue strength. The addition of nitrogen also increases corrosion resistance of stainless steel due to the enrichment of nitrogen on the surface of the passive film, with ammonium ions increasing the local pH value and facilitating repassivation [71-73]. These corrosion and bio-corrosion characteristics have limited the applications of this alloy as an alloy for biologic fixation of prostheses.

2.10.3. Titanium Alloys

Titanium alloy prostheses have been used in patients in the UK since the early 1970's. In 1996, Willert et al [74] described titanium alloys as the material of choice for femoral stems based on their superior mechanical properties and biocompatibilities. Ti–6Al–4V is the most common Ti alloy used in biomedical applications. Compared with stainless steel and cobalt based alloys, the theoretical advantage of titanium alloys is their lower modulus of elasticity, reducing the shielding effect and a high resistance to corrosion, owing to a nano scale (10nm) oxide film (TiO_2) [75]. Although the mechanical properties of Ti alloys are regarded as being superior, titanium alloys are often associated with blackening of the adjacent tissue as a result of abrasive wear. Abrasion from bearing surfaces and mechanical instability of the titanium stems in the cement scuff often lead to implant failure [9, 74, 75].

Table 2-2 – Mechanical properties for metallic biomaterials, according to the American society for testing and materials committee F-4 recommendation

Alloy system	Ultimate tensile strength (MPa)	Yield strength (MPa)	% Elongation (min)	Hardness HRC
Stainless steel				
316L	490 - 1350	190 - 690	12 - 40	25
Nitrogen strengthened	740 - 1100	430 - 1000	10 – 35	-
Cobalt Chromium Molybdenum				
Wrought Alloy 1 (Low carbon)	897 - 1172	517 - 827	12 - 20	25 - 30
Wrought Alloy 2 (High carbon)	897 - 1172	517 - 827	12 - 20	25 - 30
Cast	655	450	8	-
Titanium				
Unalloyed 4	550	483	15	-
Extra-low interstitial	825 - 860	760 - 795	8 - 10	-
Ti – 6Al- 4V	895 - 924	825 - 869	8 - 10	-

Table 2-3 – Elemental composition of biomedical alloys according to the relevant BS ISO standard

Alloy System	Specification	Fe	C	Cr	Ni	Co	Ti	Al	V	Mo	Mn	P	S	Si	N	Cu	Nb	W	O	H
Stainless steel																				
316L	F 138 – 08	Bal.	0.03	17.0	13.0					2.25	2.00	0.02	0.01	0.75	0.1	0.5				
			max	19.0	15.0					3.0	max	max	max	max	max	max				
Nitrogen strengthened	F 1586 – 08	Bal.	0.08	19.5	9.0					2.0	2.00	0.02	0.01	0.75	0.25	0.25	0.25			
			max	22.0	11.0					3.0	4.25	max	max	max	0.50	max	0.80			
Cobalt Chrome Molybdenum																				
Wrought Alloy 1 (Low carbon)	F 1537 – 08	0.75	0.14	26.0	1.0	Bal.				5.0	1.0			1.0	0.25					
		max	max	30.0	max					7.0	max			max	max					
Wrought Alloy 2 (High carbon)	F 1537 – 08	0.75	0.15	26.0	1.0	Bal.				5.0	1.0			1.0	0.25					
		max	0.35	30.0	max					7.0	max			max	max					
Cast	F 75 – 07	0.75	0.35	27.0	0.5	Bal.	0.1	0.1		5.0	1.0	0.02	0.01	1.0	0.25			0.2		
		max	max	30.0	max		max	max		7.0	max	max	max	max	max			max		
Titanium																				
Unalloyed 4	F 67 – 06	0.50	0.08		0.05		Bal.												0.40	0.015
		max	max		max														max	max
Extra-low interstitial	F 136 – 08	0.25	0.08				Bal.	5.50	3.50						0.05				0.13	0.012
		max	max					6.50	4.50						max				max	max
Ti – 6Al- 4V	F 1472 – 08	0.30	0.08				Bal.	5.50	3.50						0.05				0.20	0.015
		max	max					6.75	4.50						max				max	max

2.11. Corrosion of Metallic Materials

Corrosion is defined as the destructive attack of metal by chemical or electrochemical reaction with its environment. Deterioration by physical or mechanical actions is not referred to as corrosion, but described as erosion, galling or wear. In some instances, chemical attack accompanies physical deterioration. Many biomaterials owe their resistance against corrosion to an oxide or passive layer; however materials with a strong passive layer still experience ion transfer and possible dissolution of the passive layer itself [76]. Kamachi et al [77] stated that all implanted biomaterials corrode, leading to the generation of ionic debris, which may in turn aggravate the body environment and elicit both local and systematic biological responses. The use of metals and alloys is very important in orthopaedics, as they play a predominant role in fulfilling almost every situation that arises in implant applications. Revie [78] explained that a loss of metal by corrosion is a waste not only of the metal, but also of the energy, the water and the human effort that was used to produce and fabricate the metal structures in the first place.

The corrosion of alloys commonly used in the biological environment has been studied since the early 1960s. This next section aims to review the current literature with respect to the general and localised corrosion of biomedical alloys and the role that the passive film and the biological environment have on the localised corrosion of biomedical alloys.

2.12. Electrochemistry of Corrosion

The most common form of corrosion related to metallic biomaterials is aqueous corrosion. Corrosion occurs when an electrochemical reaction takes place on a metallic surface in an aqueous electrolyte [79]. This implies that two reactions occur; the anodic oxidation reaction of metal involving oxidation or the removal of electrons from metal atoms and the cathodic reaction, reduction of oxidising agents or consumption of electrons by an oxidizing agent [79]. Equation 2-1 represents the generalised equation for the anodic reaction where M represents Metal.

Equation 2-1 - Anodic half-cell reaction

$$M \rightarrow M^{(n+)} + n(electrons)$$

The cathodic reaction (Equation 2-2 to Equation 2-4), at which electrons are consumed, is demonstrated below. The precise cathodic reaction will depend on the chemistry of the electrolyte. However some of the most common aqueous environments concern the following reaction:

Equation 2-2 - Cathodic half-cell reactions for hydrogen-evolution

$$2H^+ + 2e^- \rightarrow H_2$$

Equation 2-3 - Cathodic half-cell reactions for oxygen-reduction in acidic solutions

$$O_2 + 4H^+ + 4e \rightarrow H_2O$$

Equation 2-4 – Cathodic half-cell reactions for oxygen-reduction in base or alkali solutions

$$O_2 + 2H_2O + 4e \rightarrow 4OH^-$$

A metal can be considered as an array of ions, with the valence electrons of each atom having been transferred to the crystal as a whole. These “free” electrons account for the electrical conductivity of the metal and other electronic properties [80]. The metal in aqueous solution also exists as an ion and thus, the relative tendency for the ion to exist in the metal or in the solution depends, along with other factors such as the concentration, on the relative electrochemical free-energy of the ion in these two phases [80]. When a metal is immersed in a solution, hydration of the metal ions at the interface occurs resulting in a water layer on the metal releasing solvated metal ions into the solutions leaving the metal negatively charged. This results in an actual separation of charge at the electrode interface. By physically separating two planes of electrochemical charge an electrical capacitor and potential difference across metal-solution interface are established. Figure 2-12 demonstrates this schematically.

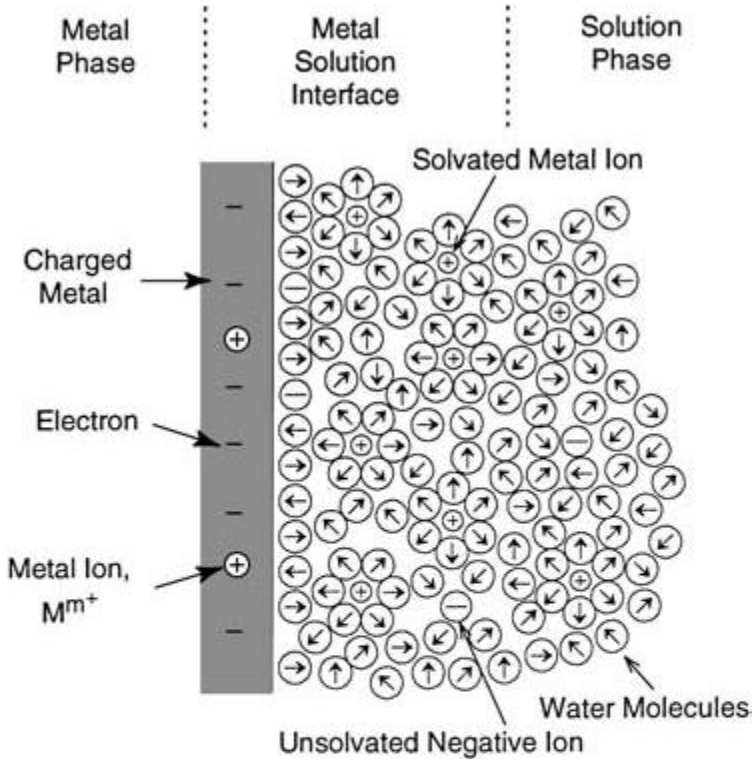

Figure 2-12 - Representation of the environment of metal ions in the metal and aqueous phases at the interface [80]

In order to evaluate a materials susceptibility to corrode the two half-cell reactions may be manipulated to occur at physically distinct surfaces by placing the electrode of interest in a solution relative to another material which is chemically inert. Due to charge separation, a potential difference will exist between the two electrodes. The existence of a measurable electrochemical potential is due to the chemical potential of the given species as well the partial free energy of the species. This can be described by the Nernst equation. Where 'E' is the measured cell potential (V), 'E^o' is the standard cell potential (V) for at a given electrode surface when all activity units equal unity, 'R' is the ideal gas constant ($JK^{-1}mol^{-1}$), 'T' is the temperature (K), 'n' is the valence number of the species in question, 'F' is Faraday's constant ($Cmol^{-1}$) and 'a' is the chemical reactivity of the products or reactants at equilibrium. If the system is not at equilibrium (i.e. two electrode reactions) the final term can be replaced with the reaction quotient (Q_c) which is a measure of the relative amount of products and reactants present during a reaction at a particular point in time. The existence of a cell potential gives rise to the electrochemical series, from which the relative reactivity of metals is established.

Equation 2-5 - Nernst equation for a specific half-cell reduction process at equilibrium

$$E = E^o - \left(\frac{RT}{nF}\right) ln\left\{\frac{(a_{products})}{(a_{reactants})}\right\}$$

Depending on the direction of reaction, metal ion reduction or deposition can occur. In all corrosion processes, the rate of anodic reaction must equal the rate of the cathodic reaction to satisfy charge conservation[79]. Yan et al [14] also stated that the formation of corrosion products, the solubility of corrosion products in the

electrolyte and the formation of passive films all affect the overall rate of the anodic metal dissolution process. For passive materials, passive layers will distinguish themselves from corrosion products, in the sense that these films can provide a higher degree of protection from corrosive attack [79].

2.13. Thermodynamics of Corrosion

Thermodynamics can be used to evaluate the theoretical activity of a given metal or alloy in a known corrosion environment [78]. The ability for any chemical reaction to occur, including the reaction of a metal within its environment is measured by the Gibbs free-energy change (ΔG) which describes the amount of energy available to perform work. By convention, the work supplied by the reactions is negative hence the negative sign convention of Equation 2-6. If the value for ΔG is negative, there is a greater tendency for reaction to occur as the electrode reaction has a greater amount of energy or electromotive force to complete the reaction or 'work'. If the free-energy is positive, the reaction will have no tendency to occur at all. Although the Gibbs free energy change is a good indication of the materials susceptibility to corrosion, it cannot be used to measure the corrosion rate of a material. It has been found that materials with a large negative ΔG are sometimes not accompanied by a large corrosion rate. The tendency for metal to corrode can also be expressed in terms of electromotive force (emf) of the corrosion cell that is an integral part of the corrosion process. The relationship between ΔG (Joules), cell potential (E, Volts) and Faradays constant (F = 96500C/mol) is defined as [78];

Equation 2-6 - Gibbs free energy equation

$$\Delta G = -nFE$$

2.14. Types of Corrosion

Corrosion is usually classified by the forms in which it manifests itself. Fontana [79] presented a comprehensive review of the 8 forms of corrosion which includes: uniform or general attack, galvanic, crevice corrosion, pitting, intergranular, selective leaching, tribo-corrosion and stress cracking corrosion. In this section the most commonly reported types of corrosion in biomedical alloys will be reviewed with an emphasis on crevice corrosion and tribo-corrosion, test methods and factors influencing localised crevice corrosion of alloys.

2.14.1. General Corrosion

General or uniform corrosion is normally characterised by a chemical or electrochemical reaction occurring uniformly over an entire exposed surface. It is thought that uniform corrosion of metals is the most encountered form of corrosion accounting for the greatest destruction of metal on a tonnage basis [79].

2.14.2. Pitting Corrosion

Pitting is a form of extremely localised corrosion that results in areas of localised pitting on the metallic surface. Pitting is considered one of the most destructive and difficult forms of corrosion to predict, often resulting in failure of a system with relatively low material mass loss. Pitting corrosion occurs on metals that owe their engineering usefulness to the formation of a protective oxide film. A corrosion pit is a unique type of anodic process as it is termed ‘autocatalytic’. This is due to existence of metastable phases leading to the gradual formation of an active pit. The formation of an active pit often develops a pit geometry and chemistry capable of sustaining dissolution of the alloy due to the formation of an aggressive environment capable of sustaining dissolution [79].

2.14.3. Galvanic Corrosion

Galvanic corrosion occurs when a potential difference is established between two electrically connected metals immersed in a corrosive or conductive solution according to Ohm's law. This potential difference results in an electron flow between the metals usually resulting in accelerated corrosion of the more susceptible alloy (anode) and protection of the other alloy (cathode). The tendency of a material to corrode can be predicted from the standard emf electrode potential of the metals and the alloy is ranked according to its tendency to corrode. This is known as the galvanic series. This is typically used to predict which materials will preferentially corrode, with the alloy with the lowest electrode potential becoming the anode in the couple. Galvanic corrosion can be affected by numerous factors such as distance from anode to cathode, anode:cathode area ratio and the environment [79].

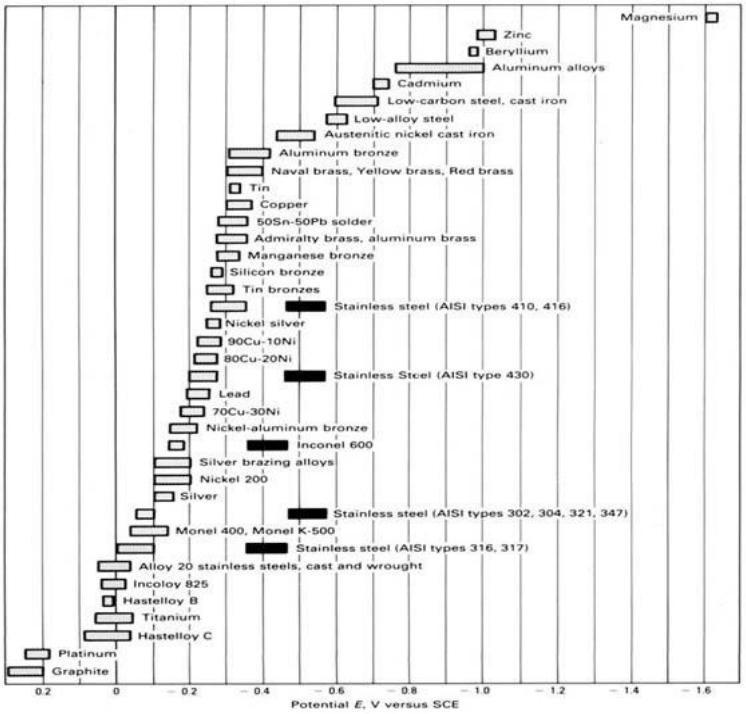

Figure 2-13 - Galvanic series of various metals in salt water according to ASTM G82-98

2.14.4. Intergranular Corrosion

Intergranular corrosion is the preferential corrosion at or adjacent to the grain boundaries of an alloy. The exact mechanism varies between each metal, however the appearance on a microscopic level is not significantly different. In biomedical alloy such as stainless steels and CoCrMo alloys, the most commonly accepted mechanism for intergranular corrosion is the difference in electrode potentials between chromium depleted regions at the grain boundaries and the main bulk alloy. This usually occurs when an alloy has been sensitised allowing chromium carbides ($M_{23}C_6$) to precipitate along the grain boundaries leaving Cr depleted regions [70, 79].

2.14.5. Crevice Corrosion

Crevice corrosion usually occurs in metals that owe their resistance to corrosion to the formation of a passive layer. Fontana [79] recognised that for crevice corrosion to be initiated the following conditions must be satisfied. Firstly, the metallic sample must be electrically connected to the material on the outside of the crevice. Secondly, the concentrated fluid within the crevice must be stagnant to allow migration of ionic species. Thirdly, the material on the outside of the crevice is to remain passive, due to the transportation of ions.

Oldfield et al [81, 82] explained that crevice corrosion occurs when there is a concentration of electrolyte in the crevice which is starved of oxygen, compared to the bulk electrolyte outside the crevice that is plentiful of oxygen. In order to keep the potential energy to a minimum within the crevice and maintain charge conservation, ions are transferred from the bulk electrolyte into the crevice resulting in complex ions, metal dissolution and corrosion product to be formed. Once crevice corrosion is initiated it is an auto catalytic reaction.

2.15. Crevice Corrosion and Pitting Initiation Theories

Currently there are at least four different models detailing the theories behind crevice corrosion initiation and propagation. The theories of crevice corrosion have been developed since the 1960's [81-87]. All mechanisms attempt to provide an explanation for the initiation and propagation of crevice corrosion of passive metals in contact with an electrolyte.

2.15.1.1. Passive Dissolution Model

The first theory to quantify crevice corrosion is known as the 'Passive dissolution model' described by Oldfield and Sutton in 1978 [82, 88]. This model was initially concerned with the crevice corrosion of stainless steels in aerated, neutral chloride solutions. The Oldfield and Sutton model proposed that crevice corrosion was initiated firstly by a gradual decrease in pH resulting in the development of aggressive localised solution. This is due to the slow transportation of metal ions out of the crevice by diffusion or migration, and hydrolysis of these ions leads to a gradual pH decrease [82].

This model consist of 4 stages; the first stating that corrosion occurs as normal both inside and outside of the crevice with the anodic and cathodic reactions according to Equation 2-1 and Equation 2-4 respectively. Stage 2 explains that due to the cathodic reaction taking place within the crevice, most of the available oxygen ions are consumed. To ensure that a minimum potential energy is maintained across the electrolyte and crevice, Cl^- and OH^- diffuse into the crevice. This migration of ions causes metal chloride to be formed. Hydrolysis of metal chloride occurs lowering the pH within the crevice and causing metal hydroxides and hydrochloric acid to be produced (Equation 2-7). In stage 3, Cl^- ions are reduced with metal ions leading to

further hydrolysis and a lower pH within the crevice. The metal dissolution process then accelerates resulting in more metals ions been formed that will result in a lower pH (stage 4) [81, 82, 88].

Equation 2-7 - Hydrolysis of metal chlorides

$$MCl_n + nH_2O \rightarrow M(OH)_n + nHCl$$

This theory was questioned by Alkire et al [83, 89] when they demonstrated that the pH of the electrolyte did not decrease prior to the initiation of crevice corrosion. Alkire's findings were also supported by Nash et al [90] in 1993 who found that the pH within the crevice was not low enough to initiate dissolution of the passive layer in the early stages of the corrosion process. This theory was further strengthened by Sridhar et al [91] who found that the pH did not increase steadily with time; rather it decreased suddenly after the increase in current indicating the onset of stable crevice corrosion.

2.15.2. Thiosulphate Entrapment

Alkire et al [89] were the first people to outline the Thiosulphate entrapment model after their observations of the crevice corrosion chemistry. The model was based on the initiation and dissolution of magnesium sulphate (MnS) inclusions within the crevice, resulting in thiosulphate ions ($S_2O_3^{2-}$) and protons being produced. The model considered dissolution of evenly spaced inclusions together with passive dissolution of the steel within the crevice. They further demonstrated that further dissolution occurs to produce elemental sulphur (Equation 2-8).

Equation 2-8 - Thiosulphate entrapment mode

$$2MnS + 3H_2O \leftrightarrow S^2O_3^{2-} + 2Mn^{2+} + 6H^+ + 8e^-$$

$$2H^+ + MnS \leftrightarrow Mn^{2-} + S + H_2$$

2.15.3. IR Drop

The IR drop mechanism was first introduced by Pickering et al [86]. Extensive research carried out on both iron and stainless steels led to the suggestions that the voltage drop caused by the anodic current from the crevice and the solution resistance within the crevice was enough to essentially force the local electrode potential from the passive region into the active and so initiate corrosion [92, 93] . Chloride is thought to raise the current within the crevice, increasing a materials susceptibility to corrosion. For active metal dissolution to occur the IR drop must be greater that the difference between the free corrosion potential (E_{corr}) and the passivation potential (E_{pp}). In order for metal dissolution according to the IR drop theory the following condition must be met:

Equation 2-9 - IR drop mechanism

$$IR > (E_{corr} - E_{pp})$$

2.16. Factors Affecting Crevice Corrosion of Passive Alloys

There are numerous factors that contribute to the initiation and propagation of crevice corrosion in metals. Environmental factors such as bulk and crevice solution oxygen content, pH, chloride level and temperature have been shown to influence the dissolution rates within a crevice [79]. Kruger et al [94] recognised that alloy composition and alloy structure will affect a materials susceptibility to crevice corrosion. Lee et al [95] further explained that mass transport in and out of the crevice, along with metal dissolution and passive film characteristics, are factors that can affect crevice corrosion. Kennell et al [92] also recognised that geometrical aspects also affect the initiation and propagation of crevice corrosion.

2.16.1. Effects of Temperature and pH

During crevice corrosion, an increase in temperature results in the initiation and acceleration of the corrosion process. Pickering et al [86] explained that an increase in temperature essentially increases the conductivity of electrolytes, therefore increasing the electrochemical reaction and anodic current. However, at higher temperatures, the pitting potential decreases with increasing temperature and chloride concentrations. This is because oxygen solubility is reduced; thereby decreasing the external cathodic reaction rate, which in turn lowers the rate of corrosion [96]. Laycock et al [89] suggested that the critical pitting potential is associated with the stabilising of pit growth at high temperatures and repassivation and low temperatures. Figure 2-14 is a graph obtained by Laycock demonstrating the 'critical crevice corrosion temperature' theory, demonstrating the number of pits as a function of temperature. It can be seen that the number of pits increases when the applied temperature is around 15 – 20°C indicating the CCT for this test.

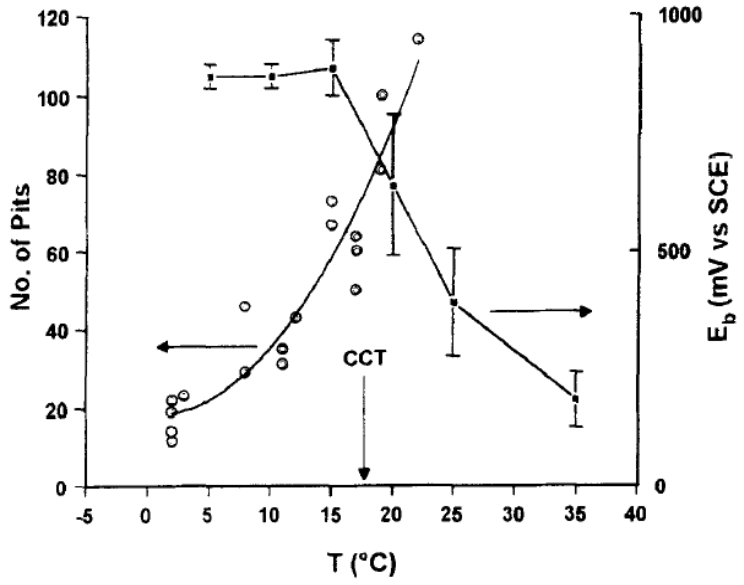

Figure 2-14 - Plot demonstrating the number of pits as a function of temperature and breakdown potential (E_b) [89]

Frankel [96] recognised that crevice corrosion will only occur in the presence of aggressive anionic species with chlorine ions usually being the cause. The severity of crevice corrosion usually tends to vary with the bulk electrolyte concentration. Galvele et al [97] identified that chloride is an anion of a strong acid with many metal cations exhibiting considerable solubility in chloride solutions. Chloride is a small anion with a high diffusion rate, usually interfering with a materials ability to re-passivate. Pickering et al [98] observed a low pH and a sharp decrease in electrode potential due to acidification and chloride build up in the crevice during active stages of crevice corrosion. Wolfe et al [99] reported along with a drop in voltage, there is an increase in resistance across the crevice and bulk electrolyte. Wolfe et al [99] also observed that a decrease in crevice pH will occur until equilibrium in hydrolysis is reached during the initiation period.

2.16.2. Crevice Geometry Effects

Crevice geometry is an important factor to consider. The presence of tight crevices results in the initiation of differential aeration cells. Oldfield et al [82] showed that crevice corrosion initiation time in seawater increased as the crevice gap dimension increased from 0.1 μm to 1 μm.

Mathematical models of crevice corrosion have shown that decreasing the gap dimension (i.e. the tightness) will reduce the initiation time, whilst wider gaps will have the opposite effects. This can be related to the decreased volume of crevice solution that must undergo de-oxygenation, becoming sufficiently acidified to initiate breakdown of the passive layer [82, 93].

Lee et al [95] have used the geometric influence to help explain the variability in crevice corrosion behaviour of stainless steels, stating that crevice tightness can also be related to the physical properties of the crevice former. For example a non-

metallic is more readily deformable, hence more likely to produce more severe crevice conditions.

Shan et al [100] found that the surface roughness of the crevice former also contributed towards the severity of crevice corrosion. They found that by introducing PTFE tape between the crevice former and metal, the asperities of both the metal and counterpart former would be filled thus keeping the size of the crevice opening small. Along with this, three stages of damage evolution were identified from the potentiodynamic polarisation graphs. The initiation and repassivation of metastable phases were observed and characterised by a fluctuation in the current density within the passive region. After initiation multiple initiation and arrest points were observed followed by repassivation characterised by the passive current on the reverse anodic polarisation scan.

2.16.3. Effects of Alloying on Localised Corrosion

The alloy composition and microstructure can have strong effects on the tendency for an alloy to corrode. Metals containing high levels of molybdenum, nickel and chromium are known to increase a materials resistance to depassivation, thus increasing the resistance to localised corrosion. Therefore such alloys usually require a very low pH and high Cl concentration to initiate dissolution of the passive layer [101].

Chromium (Cr) content plays the dominant role in conferring passivity to ferrous metals. It was found that the chromium content dramatically increased the pitting potential as the Cr content increased above 13% [69, 102]. The beneficial effect of chromium ions on passive films is noticed by the shift of the corrosion potential in

the noble direction. However once the corrosion process is initiated, the hydrolysis of chromium ions causes the localised pH within a crevice to decrease.

In stainless steels, increased nickel content stabilises the austenitic grain structure and also improves pitting resistance. Pickering et al [86] found that increasing the nickel content increases corrosion resistance by shifting the potential of the metal in the noble direction. Other alloying elements and refractory metals such as molybdenum (Mo) and nitrogen (N) can greatly reduce materials susceptibility to corrosion, however Mo is only effective in the presence of Cr. Molybdenum is not found in the passive layer of a material, but is enriched in the surface film formed in the active region. It has been suggested by Ogawa et al [103] that Mo, along with N acts by blocking active sites during the dissolution process. Molybdenum-nitrides help retain the molybdenum ion in the passive film by acting as an inhibitor to the dissolution of Mo in the active region. The majority of researchers agree that Mo influences localised corrosion through pit growth and dissolution mechanisms. Small amounts of tungsten (W) and nitrogen (N) also have a strong influence on the materials susceptibility to pitting corrosion. Newman et al [104] suggested that nitrogen strongly affects the anodic dissolution kinetics by making the formation of the passive layer easier.

Corrosive pits occur at some chemical or physical variation at a materials surface such as inclusions, mechanical damage, dislocations and solute segregated grain boundaries [64, 70, 101]. Unfortunately engineering alloys tend to contain such defects, resulting in the formation of pits at these flaws and defects first.

2.16.4. The Role of Proteins on the Corrosion of Passive Alloys

The role of proteins in a corrosive environment is governed by many factors such as chemistry of the metal, protein adsorption characteristics, interaction of protein molecules with other ions present in the electrolyte solution to produce organic complexes and the transport of anionic ad cationic charges around and away from a local environment.

Clark et al [105] explained the role proteins play in the corrosion of metallic corrosion. At the time little work had been conducted into the effects proteins had on corrosion of metallic biomaterials. For highly passivated materials such as aluminium and titanium, corrosion is negligible and the presence of proteins had no effect. Clark found that the corrosion rate of pure metals, such as nickel and chromium were increased two – four fold, while the corrosion rate of copper and cobalt were increased 30-40 times when immersed in protein environments. Chromium and nickel were shown to be the least corroded, with molybdenum inhibiting corrosion. Clark forwarded two models; the first proposed was that for highly passivated materials the rapid corrosion rate is inhibited by the adsorption of proteins on to the surface, preventing the normally very rapid corrosion reactions from occurring. The second model proposed that if the oxidation of a metal is autocatalytic, then the binding of the metal ions will be inhibited by oxidation. It was concluded that corrosion resistance as measured *in-vitro* in salt solutions may not be a true measure of that resistance in the body, and the magnitude of change may be very large [105]. The adsorption of proteins onto a metallic surface was then proven by Munoz et al [106].

Munoz et al [106] explained that the presence of inorganic ions, such as phosphates and organic matter such as proteins can affect the passive film characteristics, subsequently changing the electrochemical behaviour of an orthopaedic implant. Potentiodynamic polarization measurements were taken and demonstrated that albumin shifts the corrosion potential more cathodically, whilst phosphate ions have the opposite effect. Phosphate ions were also seen to decrease the passive current density, compared to albumin which increased the passive current density. EIS analysis was also conducted. This revealed a double-layer structure with an inner oxide layer covered by an adsorption layer containing albumin. For the tests conducted in a solution containing phosphates, anions such as sulphate, chloride, and phosphate are usually found in the outer most part of the passive films formed on both stainless steel and CoCrMo alloys. They concluded that phosphates adsorb onto the outer most surface of the passive film, whilst albumin creates an adsorption film. The following diagram (Figure 2-15) represents the equivalent circuit (EC) for a metal immersed in a protein rich electrolyte. EC analysis allows the electrical properties of the materials surface to be identified [106]. A similar response has been seen by Oured et al [107]. The stability of the passive film depends on the availability of oxygen. The adsorption of proteins to a metals surface could limit the diffusion of oxygen, thus causing breakdown of the passive layer and preferential corrosion at the oxygen deficient sites [14, 105-107].

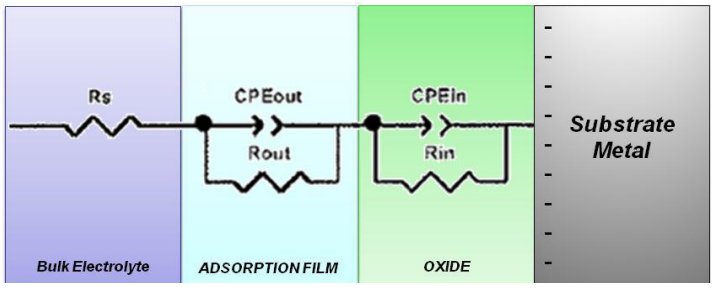

Figure 2-15 - Equivalent circuit for the analysis of impedance spectra of a passive alloy in protein containing solutions. Figure adapted from ref [106]

2.17. Passivity of Commonly used Biomedical Alloys

Metallic materials used for THA normally rely on a stable passive film, which forms spontaneously in air, for their biocompatibility. The passive film can form a barrier which can efficiently separate the metal from the corrosive environment and protect it from further corrosion processes. Yan [25, 108] stated that the passive film inhibits corrosion and keeps current flow and the release of corrosion products at a very low level. Uniform passive dissolution resulting from the slow diffusion of metal ions through the passive film, transpassive dissolution under high oxidizing conditions, or the local breakdown of passivity as a consequence of localised forms of corrosion such as pitting or crevice corrosion, or as a consequence of mechanical events such as fretting and wear corrosion are all possible mechanism for the dissolution of the passive layer [79].

The breakdown of the passive film and initiation of crevice corrosion is currently the least understood aspect of the corrosion process. Under static passive conditions in the absence of any crevices, breakdown of the passive film is a rare occurrence usually occurring on a rapid and very small scale. Although the passive layer is usually shown as an inert layer covering the underlying metal, the reality is much more complicated [109]. Borex et al [110] demonstrated that the passive film consists of two layers: an inner oxide layer and an outer hydroxide layer, occurring in the presence of aqueous solutions. Frankel et al [96, 111] explained that the characteristics of the passive layer depend on the alloy composition, the environment in which they interact with and exposure history. Passive films tend to have a range of thickness (typically 1 – 5nm), structure, composition and protectiveness [112-114]. These films provide a barrier to the oxidation reaction of the metal surface due to their low ionic conductivity; however this layer tends to

become unstable in high chloride concentrations. Theories for passive film dissolution and pit initiation can be categorised into three main mechanisms; passive film penetration, film breaking or absorption.

2.17.1. Passive Film Penetration Theory

Hoar et al [115] was the first to champion the passive film penetration theory (Figure 2-16a). The penetration mechanism involves the transport of aggressive anions through the passive film to the metal/oxide interface where aggressive dissolution of the metal surface is initiated. This mechanism is supported by the existence of an induction time for pitting following the introduction of chloride into the electrolyte. Another model associated with the penetration mechanism is the point defect model developed by Sato et al [116]. This model describes the passive film growth by the movement of electrons via point defects under the influence of an electrostatic field. The major point defects in an oxide layer are considered to be electrons and oxide vacancies.

2.17.2. Passive Film Absorption Mechanism

Another mechanism associated with the breakdown of the passive film is the absorption mechanism developed by Uhlig [117] (Figure 2-16b). This theory is based on the absorption of chloride and oxygen through the several mono-layers thick passive layer. It is believed that this absorption of local species through the thin oxide layers reducing the thickness of the layers, eventually leading to complete breakdown of the passive layer and the formation of pits.

2.17.3. Passive Film Breaking Mechanism

Richardson et al [118] developed the film breaking mechanism (Figure 2-16c). The film breaking mechanism states that the thin film is in a continual state of breakdown and repair. Mechanical stresses and flaws in the material may initiate breakdown of the passive layer, which rapidly heal in a nonaggressive environment. The film breaking mechanism involves initiation based on pit growth stability; breakdown of the passive layer will only lead to pitting when pit growth is sustainable. Galvele [119] suggested that a critical current density is required for breakdown of the passive film and pitting stability to be achieved. Oldfield et al [81, 88, 120] recognised that as the solution becomes more aggressive an 'active peak' appears on the polarisation curve: the solution in which the height of this active peak reaches $10\mu A/cm^2$ is considered aggressive enough to cause breakdown of the passive film, this is known as the critical crevice solution (CCS). In Galvele's model, a critical current density of $10\mu A/cm^2$ was observed for iron based alloys supporting the theory proposed by Oldfield and Sutton.

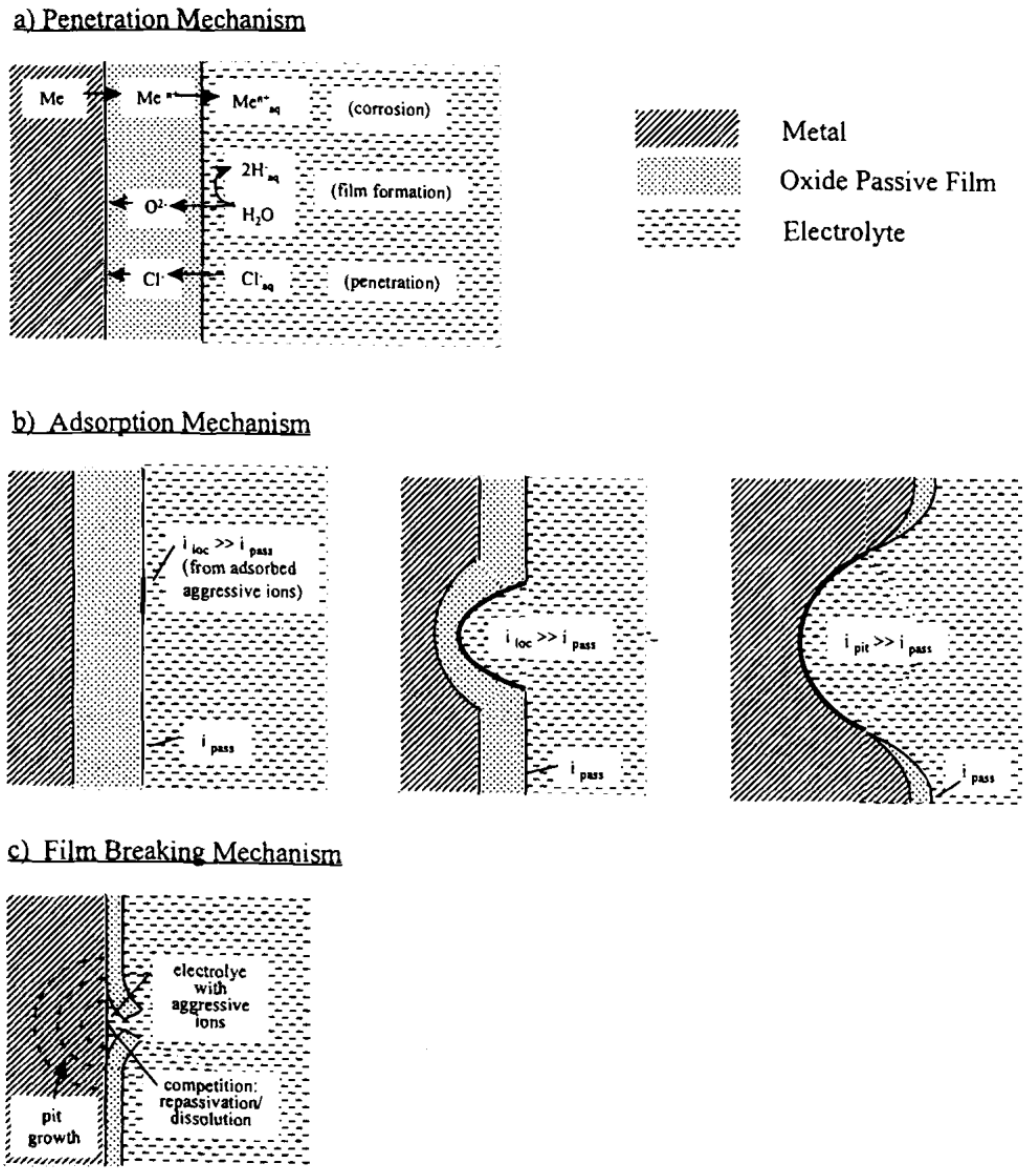

Figure 2-16 - Schematic diagrams representing pit initiation by (a) penetration, (b) adsorption and thinning, and (c) film breaking [96]

2.18. Corrosion Behaviour of Passive Alloys

Passive materials used in the biomedical industry are known to exhibit an active – passive behaviour which is usually measured using electrochemical techniques [79]. Polarisation curves, plotted from the corrosion potential and log current indicated the localised and general corrosion behaviour of these materials [121].

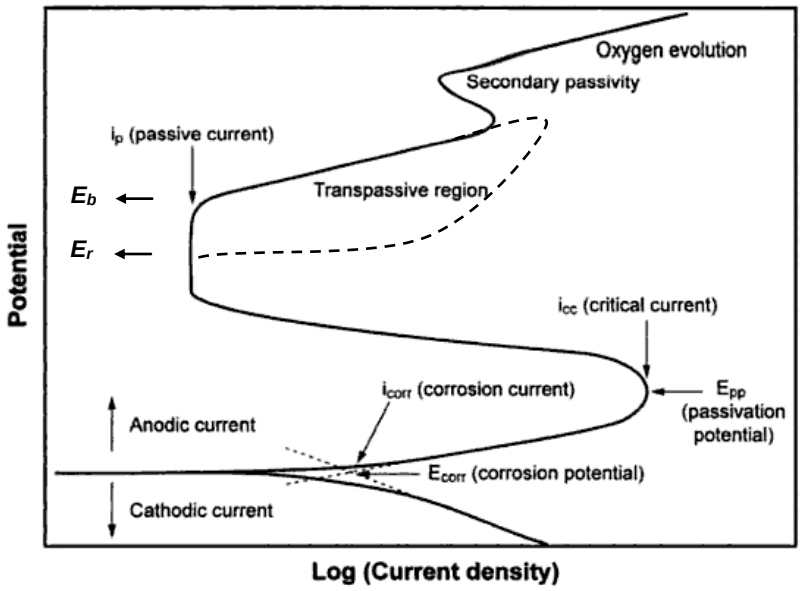

Figure 2-17 - Typical Evans plot for a passive material

A log current versus potential plot is known as a Tafel or Evans plot, obtained from potentiodynamic polarisations tests (Figure 2-17). Developed by U.R. Evans, he recognized the usefulness of these diagrams in predicting corrosion behaviour [78]. From Figure 2-17, at potentials values below the corrosion potential (E_{corr}), the metal is cathodic. As the potential is increased past the corrosion potential (E_{corr}), the metal becomes anodic and remains active in the potential region just above the corrosion potential (E_{corr}) until the passivation potential (E_{pp}). However, when the maximum point of anodic dissolution is met (i_{crit}) the current density drops to a very low value, called the passive current density (i_{pass}). This current drop is characterised by the formation of the protective oxide layer which is typically the self-healing

behaviour of passive metals. It is observed that during passivation, the metal still corrodes but at a significantly lower rate. When the material is in the transpassive region, the material will start to rapidly corrode. The extent to which the material will corrode is dependent on the electrolyte in which the specimen is in.

Polarisation diagrams are useful as Tafel analysis can be performed by extrapolating the linear portions of a log current versus potential plot back to the point at which they intersect (Figure 2-17). The point at which they intersect is known as the free corrosion potential (E_{corr}). It can be found on the polarisation curves where the total rate of the anodic reaction equals the total rates of the cathodic reaction. Values of this intersect at either the anodic or the cathodic current densities are known as the corrosion current (i_{corr}). It is useful to obtain values for i_{corr} as corrosion rates and mass loss estimations due to oxidation can be determined in terms of mm per year by application of electrochemical tests and Faradays Law. Analysis of Figure 2-17 allows the corrosion characteristic to be determined [62, 121];

- The more positive the breakdown potential E_b, the more stable the passive oxide layer.
- The corrosion current i_{corr} is proportional to the corrosion rate in the active state.
- The larger the difference between E_b and E_{corr} (corrosion potential), the higher the stability against pitting and crevice corrosion.
- The smaller the difference between E_b and E_r (re-passivation potential) the higher the resistance to localised corrosion. The extent of localised corrosion will be decreased.

2.19. Faraday's Law

Faraday pioneered the properties of electric current, formulating two basic laws of electrolysis [122]. Faraday's first law states that 'The amount of any substance deposited, evolved, or dissolved at an electrode (m) is directly proportional to the amount of electrical charge passing through the circuit (Q)'; Faraday's second law of electrolysis states that 'The mass of different substances produced by the same quantity of electricity are directly proportional to the molar masses (M) of the substances concerned and inversely proportional to the number of electrons (n) in the relevant half-reaction' therefore the following applies [122]; Equation 2-10 summarises the equivalence between the amounts of chemical change and the amount of electrical energy.

Equation 2-10 - Faraday's equation for mass loss from an electrode

$$m = \left(\frac{Q}{F}\right) \times \left(\frac{M}{n}\right)$$

Where; $W=g$, $Q = C$, $F = Cmol^{-1}$, $M = gmol^{-1}$

2.20. Wear

Wear can be defined as the progressive damage, involving material loss, which occurs on the surface of a component as a result of its motion relative to another body. Lubricants are often utilised in order to minimise wear. However depending on the type of wear and lubrication regime, different wear rates can be observed. The types of wear can be described as the following:

2.20.1. Mechanical Wear

At normalised sliding velocities and distances (typically > 25μm) surface heating is negligible and deformation of the metal surface is principally due to frictional forces resulting in shear stresses been present on the metal surface [123, 124]. Materials that are subjected to mechanical wear often demonstrate transitions from a running in period to steady-state conditions. Running in phases are observed as the conformity, topography and frictional compatibility are optimised. Once running in is complete, a steady state wear rate is usually observed until time become sufficiently long for fatigue dominates [123].

2.20.2. Abrasive Wear

In abrasive wear, damage to a component occurs because of the motion relative to that surface or either harder asperities or particles trapped in the interface. Two-body grooving and three body rolling wear modes are involved in abrasive wear. Such wear mechanisms can lead to micro-cutting, fracture and ploughing of a surface [123, 125].

2.20.3. Erosive Wear

Erosive wear is the defined by the process of material removal by the impingement of particles, usually at high velocity, on a component surface. This impingement of particles has been seen to elastically and plastically deform a material depending on the materials plasticity. Erosion is commonly encountered in pump, valves and pipes [70, 123].

2.20.4. Fretting Wear

Fretting wear typically occurs between two bodies which have a small relative oscillatory motion of small amplitude. Waterhouse [124] stated that fretting occurs at contacts where the relative motion is no greater than a few ten micrometers. A

comprehensive investigation of fretting corrosion characteristics was presented by Feng [126]. Feng proposed a mechanism that followed the fretting process goes through three different stages: the initial stage, the transition period, and the declining stage, before reaching the final steady state. Feng also explained that contact between two surfaces is established only through the surface asperities. With small amplitude relative motion, the wear particles are trapped in the asperities. As wear particles accumulate, these spaces are gradually filled, and the fretting action is thus changed from ordinary wear into abrasion. When these spaces are filled, the individual areas of contact in one company integrate into a united area. The thickness of the layer of wear particles increases as abrasion proceeds [126]. Figure 2-18 schematically demonstrates the mechanisms proposed by Feng.

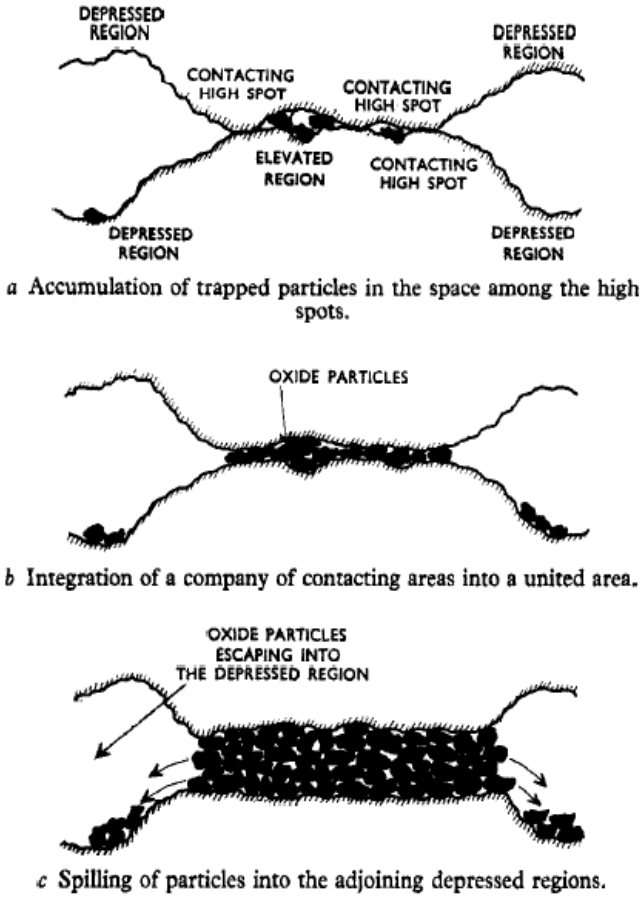

Figure 2-18 - Initiation of Fretting and accumulation of fretting product according to Feng [126]

2.21. Role of Corrosion in Tribological Environments

As mentioned previously, the corrosion rate of a metal is determined by the rate of anodic and cathodic reaction. Biomedical alloys typically owe their corrosion resistance to the formation of an inert protective oxide film resulting very low corrosion rates. In order for a material to form a passive film, the substrate must rapidly react with oxidising agents in the environment [127]. When a passive alloy is utilised in tribological applications, depending on the contact mechanics and lubrication regimes, mechanical removal of the passive film occurs leaving the reactive substrate exposed to the environments. Rapid oxidisation of the substrate usually occurs resulting in metal ions been liberated from the metallic substrate. This process is known as tribocorrosion. Tribocorrosion is found in many engineering applications due the use of lubricating fluid films or the operating environment itself. However the involved mechanisms are not fully understood. Mischler [127] described Tribocorrosion as a material deterioration or transformation resulting from simultaneous action of wear and corrosion. The investigation of tribocorrosion requires the control of the chemical conditions during a wear test.

Because tribocorrosion describes both the mechanical removal of material as well as the chemical degradation of a material, it is important to appreciate and to identify the contribution of corrosion and wear to material loss. Uhlig [127] was amongst the first to recognize the role wear and corrosion play on the degradation in fretting contacts. Uhlig demonstrated that material deterioration results from two distinct mechanisms; mechanical wear and wear-accelerated corrosion to produce a simple mechanistic model as shown in Equation 2-11, where V_{mech} represents the volume

of material removed by mechanical wear, V_{chem} is the material loss due to wear accelerated corrosion.

Equation 2-11 - Uhlig's proposed mechanistic model for fretting-corrosion contacts

$$V_{tot} = V_{mech} + V_{chem}$$

Although Uhlig demonstrated the role corrosion plays in tribological contacts, the model does not take into account of passive corrosion taking place outside the contacts, the fact that the material is in a state of de/re-passivation or any changes in contact mechanics. Today, methods and ASTM standards proposing methods to quantitatively measure the role corrosion plays in tribological contacts. Watson et al [128] was among the first to describe the role of synergy between the different factors affecting the overall mass loss of a contact. According to ASTM G119, the total tribocorrosion materials loss (T) can be represented by Equation 2-12, where W is material loss due to pure wear in absence of corrosion, C is material loss due to corrosion in absence of wear and S is the incremental factor of degradation due to the combined effect of corrosion and wear. The total mass loss can further divided into the wear rate in the absence of corrosion, the corrosion rate in the absence of wear, and the sum of the interactions between the processes where ΔC_w is the change in corrosion rate due to wear and ΔW_c is the change in wear rate due to corrosion [127].

Equation 2-12 - Synergetic approach in calculating mass loss from tribocorrosion contacts

$$T_{wc} = W + C + S$$

$$S = (\Delta C_w + \Delta W_c)$$

2.22. Current Test Setups and Arrangements for Fretting-Corrosion at the Stem-Cement Interface

Because the tribocorrosion reactions are often complex and subject to many variables, controlled and systematic tribocorrosion studies are usually conducted using a variety of tribo-meters with a range of different contact arrangements. In order to facilitate corrosion measurements electrochemical cells are commonly incorporated into the tribometer/simulator tests. Mischler presented a comprehensive review of publications investigating tribocorrosion [127].

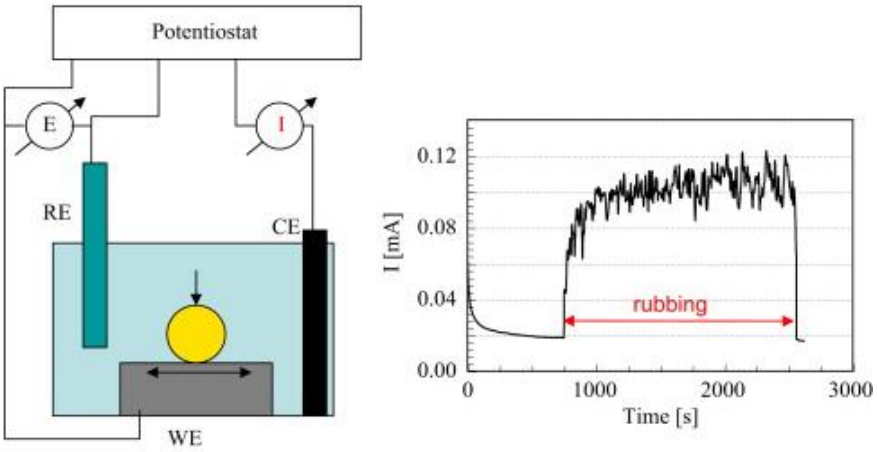

Figure 2-19 - Typical electrochemical cell used in tribo-corrosion contacts [127]

Numerous experimental and computational studies have been conducted in an attempt to understand fretting wear and fretting corrosion at the stem-cement interface. Zhang et al [129-131], through a series of fatigue tests in 0.9% NaCl at room temperature, indentified the importance of the bone cement porosity in the initiation and propagation of fretting wear, whilst Blunt et al [132] further contributed to the knowledge of the contact mechanics existing at the stem cement interface and how the presence of pores within the cement can contribute to the amount of micro-motion found at the interface. Although these studies have highlighted the importance of wear at the stem-cement, in reality the

degradation mechanisms are a complex mixture of wear and corrosion. Recently, controlled fretting tribometer studies by Pellier et al [133] and Geringer et al [134, 135] demonstrated the importance of electrolyte composition and effects of ionic strength on the material loss due to mechanical wear, corrosion and their respective synergies of PMMA bone cement on 316L stainless steel under controlled tribometer tests. Pellier [133] demonstrated the wear induced by corrosion was seen to increase with increasing ionic strength of NaCl. Furthermore a decrease in wear induced corrosion was seen in serum containing lubricants. Although these studies have indicated the importance and the interactions between fretting and corrosion, the exact interface and adhesion between the stem-cement was not considered.

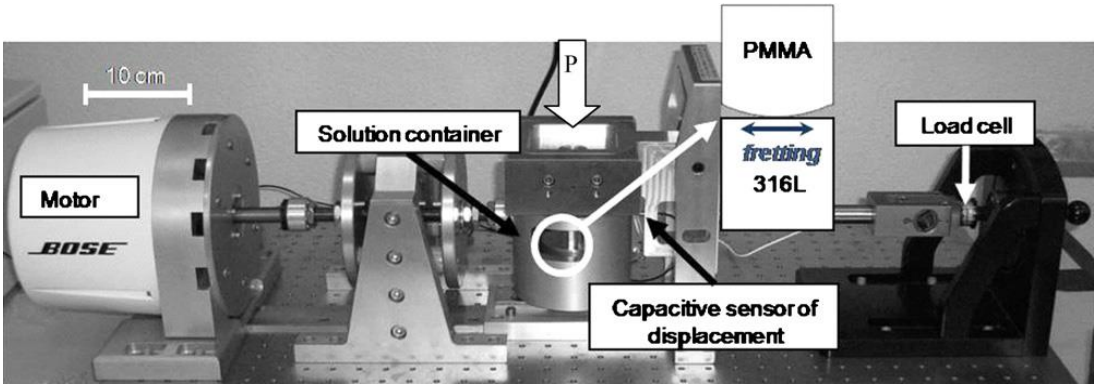

Figure 2-20 - Tribometer used to conduct fretting corrosion tests [133]

2.23. Fretting-Crevice Corrosion of Biomedical Devices

Corrosion of orthopaedic biomaterials is a complex multi-factorial phenomenon that depends on geometry, metallurgy, mechanical and environmental factors. *In-situ*, the degradation of metal alloy implant is undesirable for two reasons; the degradation process may decrease structural integrity of the implant, and the release of degradation products may elicit an adverse biological reaction in the host [136]. Although corrosion of THA isn't often the sole contributor to implant failure, the

subject has been under much discussion attracting national press attention [7, 137]. Degradation of an implant may result from electrochemical dissolution, or a combination of electrochemical dissolution and wear. It is important that the role corrosion plays in the overall degradation of THA is not fully understood, as electrochemical and mechanical processes usually interact causing premature failure of the device and an accelerated release of metal ions and particles [136] .

The clinical importance of the degradation of metal implants is evidenced by corrosion particulate and wear products in tissue surrounding the implant, which may ultimately lead to a cascade of events leading to periprosthetic bone loss. Furthermore, many authors have reported increased concentrations of metals associated with metallic replacements in local and systemic organs. Jacobs et al [136] stated that it is vital to understand that the corrosion of orthopaedic biomaterials is not just an exercise in physics and chemistry. There are real problems related to the corrosion of implants that are in current clinical use.

A current problem relating to THA, is the corrosion at the taper connection of modular joint replacement components [136, 138-140]. Due to the demand of modular THA systems, femoral stems with interchangeable heads are often the desired choice of surgeons. Nowadays, metallic stem design incorporates the use of conical morse taper connections, as a method of securing the femoral head onto the femoral stem, which do have inherent shortcomings. A study conducted by Gilbert et al [140] revealed that approximately 16 to 35% of 138 retrieved THA showed signs of moderate to severe corrosive attack in the taper connection. This was observed in implants with a titanium alloy femoral stem with a cobalt alloy femoral head, as well as a cobalt alloy femoral head and stem. In this case the femoral taper was subject to crevice, galvanic and fretting corrosion and although the corrosion

process alone would not cause failure of the device, when combined with stress and motion the results can be devastating. It has been reported that corrosion products generated at the taper connection have migrated into periprosthetic tissue and the bearing surfaces of the acetabular cup causing further complications [141, 142].

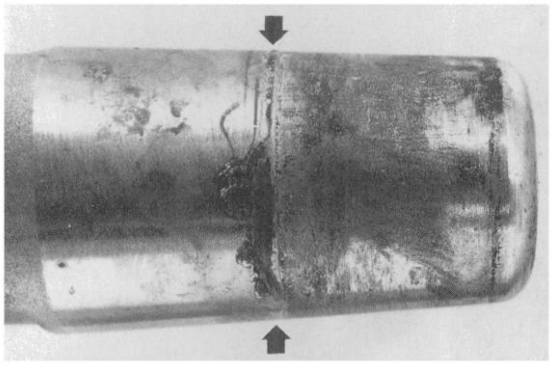

Figure 2-21 - Corrosion of a modular Ti morse taper [136]

Corrosion of biomaterials also occurs on internal fixation plates. Hundreds of internal fixation plates were examined in retrieval studies in the 1960's and 1970's. Many of the stainless steel and cobalt chromium alloy devices were prone to accelerated corrosion because of improper selection of materials, faulty fabrication techniques and the use of mixed metals [136, 142]. Cook et al [143] found some degree of electrochemical crevice corrosion in 89% of the plates and 88% of the screws of 250 multiple-part stainless steel internal fixation devices removed between 1977 – 1985.

Sury et al [62] were the first to recognise the importance of crevice corrosion in cemented THA. They stated that although materials in biomedical applications need to be corrosion resistant, implant materials must be highly resistant to wear and abrasion. The difference in corrosion resistance was measured between wrought CoCrMo, cast CoCrMo and wrought stainless steel. Sury concluded that wrought CoCrMo demonstrated the best resistance to corrosion in *in-vitro* corrosion tests. It

was thought that wrought CoCrMo had optimised mechanical and corrosion properties, as over 100,000 wrought CoCrMo implants had been in operation since 1972, with no indications of any localised crevice corrosion attack.

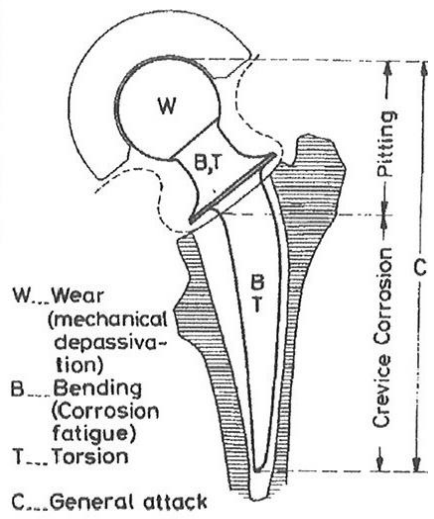

Figure 2-22 - Schematic representation of mechanical and corrosion effects acting on a THA [62]

Willert at al [74] studied a cohort of 28 cemented Müller straight femoral stems that were mainly revised for pain and discomfort. The observed pain pattern differed from aseptic loosening and pain occurred around 14.5 months after implantation. Revisions were performed at an average of 25.5 months after implantation. Upon retrieval it was noted that metallic particles were dominant in the joint capsule, whereas more corrosion product impregnated the cement to bone interface. The distal surfaces of the stem were corroded at a higher rate, whereas the proximal regions more often were subjected to abrasion. They also took pH measurements of the corroded stems and revealed values of high acidity. They stated that recurrence of pain and subperosteal apposition of bone is due to diffusion of acid; subsequent scalloping of osteolysis developed due to particle induced foreign body granulomas. They also concluded that cemented titanium stems should not be recommended for

use, as cementing does not provide a safe enough method of fixation and stated that the mechanisms of crevice corrosion of cemented titanium based alloys are not applicable to cobalt and iron based implant alloys.

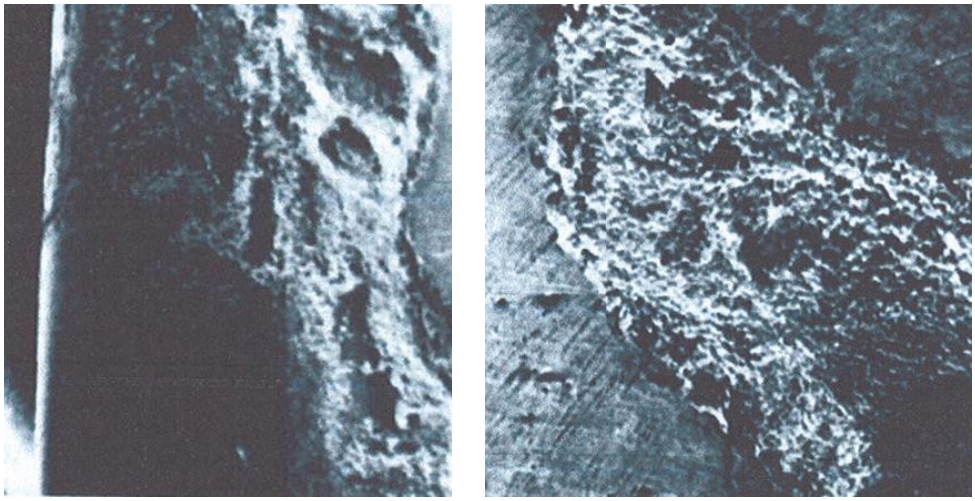

Figure 2-23 - Corrosion product found at the stem cement interface [74]

Collier et al [144] studied the tapered interface between the head and the neck of 139 modular femoral components of hip prostheses which had been removed for a variety of reasons. In 91 the same alloy had been used for the head and the stem; none of them showed evidence of corrosion. In contrast, there was definite corrosion in 25 of the 48 prostheses in which the stem was of titanium alloy and the head of cobalt-chrome. Collier found that the corrosion was time-dependent: no specimens were corroded after less than nine months in the body, but all which had been in place for more than 40 months were damaged. Collier further hypothesized that extensive corrosion at the modular interface was due to galvanically-accelerated crevice corrosion, influenced by the anodic:cathodic area of the porous coated Ti stem and CoCrMo femoral head, which was undetected in laboratory testing of this type of prosthesis [144].

Howell et al [145] further presented a comprehensive study, conducting SEM and 3-D interferometery analysis on both retrieved polished and matte femoral stems,

identifying that polished and matte femoral stems present two very different wear mechanisms. Polished stems were seen to exhibit signs of ductile wear accompanied by pitting of the surface whilst matte stems presented evidence of abrasive or truncation wear. Although the wear mechanism was seen to differ with different surface finishes, the location of wear, typically in the anterolateral and posteromedial aspects of the stem, was unaffected suggesting that the torsional loading is the prominent factor. Even though the surface morphology of a variety of retrieved femoral stems had been observed, the influence corrosion played in the degradation of the implant was discussed, suggesting that wear was the predominant reason for failure [145].

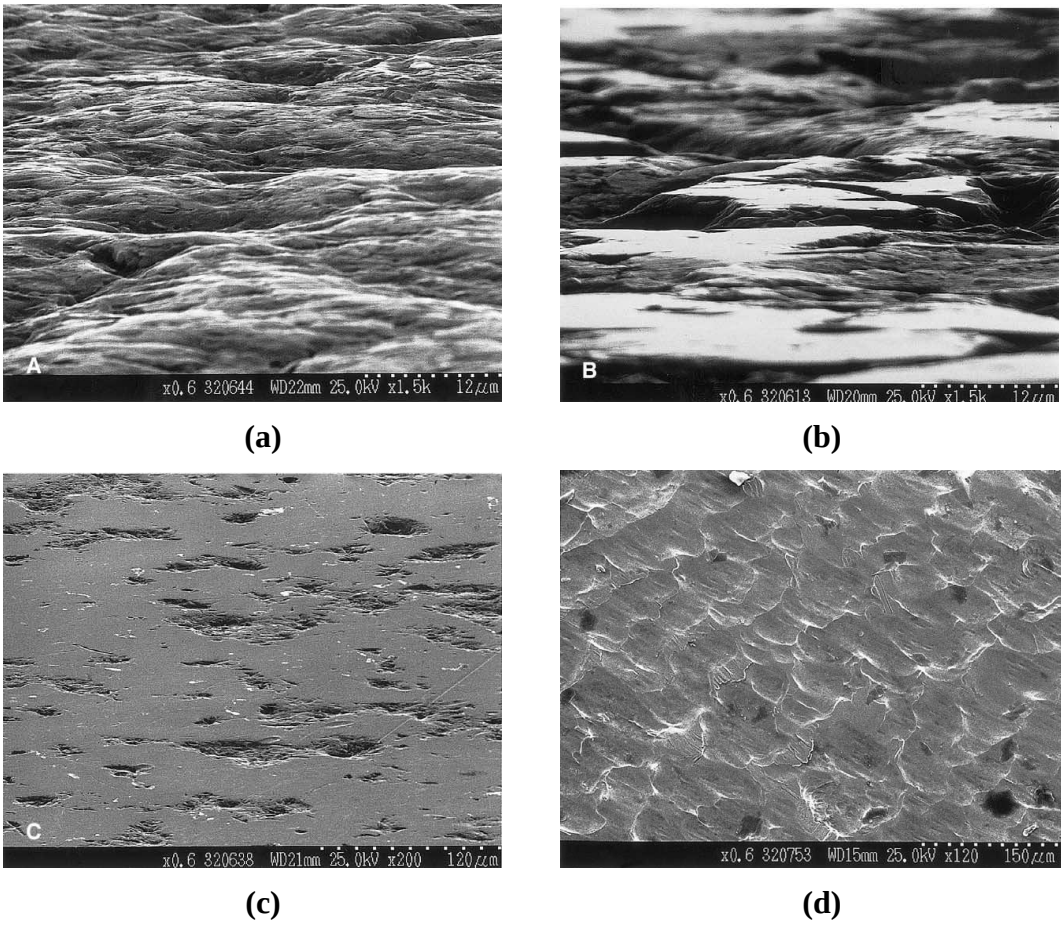

(a) **(b)**

(c) **(d)**

Figure 2-24 - SEM images showing wear of matte-surfaced stems. (a) An unworn area of matte stem. (b) An area of slight polishing wear. (c) An area of marked polishing wear and (d) fretting of a polished Exeter femoral stem [145].

Although Willert stated that the issue of crevice corrosion at the cement mantle was not considered applicable to cobalt and iron based femoral stems, a recent study by Donell et al [4] has demonstrated that this is not the case. In 2008, 90 out of a total series of 652 DePuy Ultima TPS MoMl hip replacements had to undergo early revision. 17 hips required revision for periprosthetic fracture, with early dislocation in 3 and late dislocations in 16. Infection was found in 10 hips. 44 required revision for extensive, symptomatic, peri-articular soft tissue necrosis of which 35 had normal plain radiographs. Dramatic corrosion of generally solidly fixed femoral stems was frequently observed on the retrieved cemented part of the femoral component. It was thought that the necrosis of the surrounding tissue was associated with the release of potentially toxic metal ions such as cobalt and chromium from the stem surface [4].

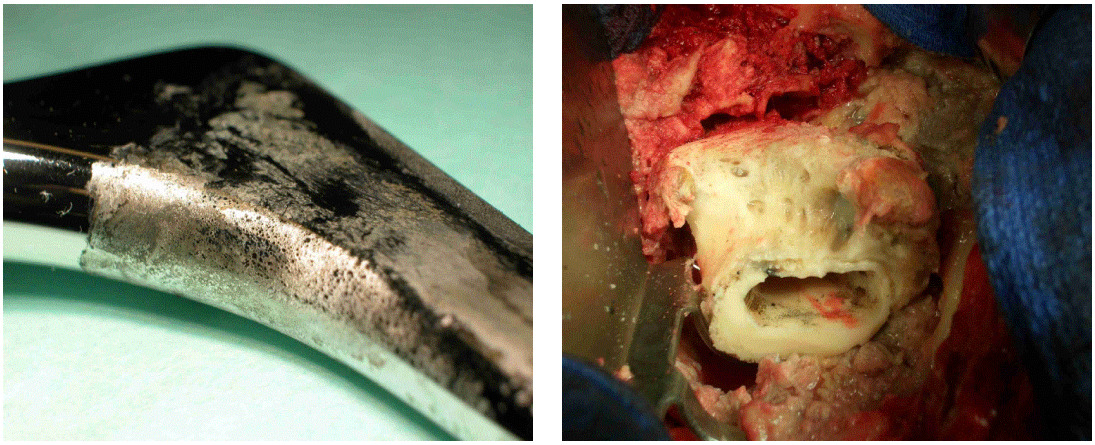

(a) **(b)**

Figure 2-25 - Clinical findings at revision of a) Ultima TPS femoral stem and b) soft tissue reaction [4]

This study was further complimented by Bolland et al [5], who also demonstrated high corrosion of the modular taper interfaces as well as the cemented portions of the cemented femoral stem. Again elevated metal ion levels and extensive soft tissue necrosis were observed at revision.

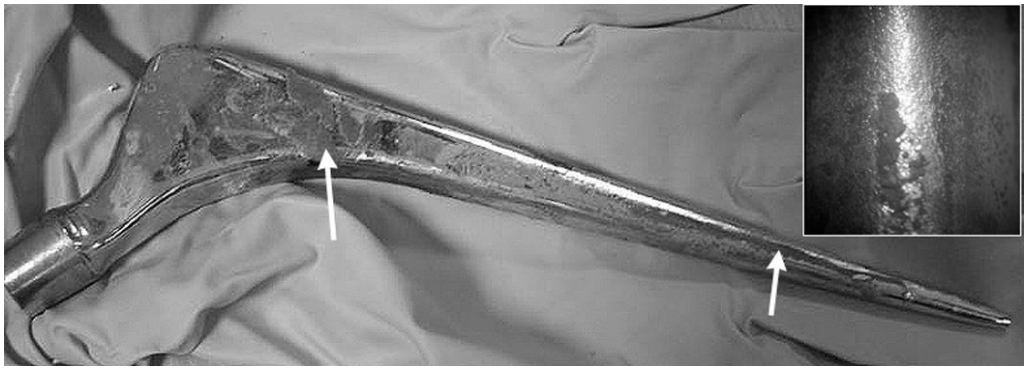

Figure 2-26 - Explanted femoral component, showing evidence of corrosion within the stem-cement interface [4]

Data recently published by Hart et al [146] analysed periprosthetic tissue from two cohorts of patients. Hart found that for patients with the Ultima TPS™ femoral stem; a preferential release of cobalt was seen in the retrieved tissue compared to patients who received hip resurfacing replacements (Figure 2-27). Hart et al hypothesised that this finding was due to the type of degradation mechanisms taking place at the interface due to the acid nature of the interface caused by inflamed tissues [146]. An *in-vivo* and *in-vitro* studies by Heisel et al [147] demonstrated that metallic ions were released in a ratio according to the concentrations in the alloy from the articulation surfaces.

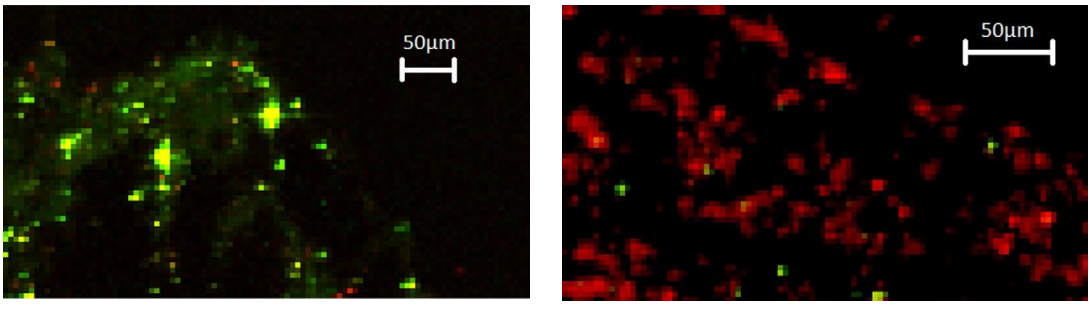

(a) **(b)**

Figure 2-27 - X-Ray fluorescence maps of a) Ultima TPS MoM and b) Resurfacing patients. Green = Co and Red = Cr [146]

Polished tapered femoral stems generally have good survivorship with revision rates of 2.8% at 7 years after operation being seen for commonly cemented stainless steel devices [148]. Similar figures have been presented for CoCrMo polished stems, demonstrating revision rates of 4.1% 10 years postoperative [149]. Shetty et al [150, 151] presented the findings of the Ultima TPS femoral stem when used in conjunction with a MoP articulation. No hips required revision within 5 years due to Adverse Reaction to Metal Debris (ARMD) when used in conjunction with a MoP articulation. The Ultima TPS was seen to have a similar performance as the Exeter femoral stem which has at least 20 years of clinical prevalence.

The biocompatibility of long and short term implants has been a concern for some time with regard to local tissue reaction. As to date, the full extent of potentially toxic metal species released during the corrosion process into the surrounding tissue, it not yet fully understood. Although these ions may stay bound to the neighbouring tissue, there is an increasing recognition that they may also bind to protein moieties that are transported in the bloodstream and lymphatic's, and hence to remote organs [136]. The main concern with the transportation of metal debris is the potential effects of corrosion product transportation, justified by the known potential toxicities of implantable materials and the carcinogenic potential of the metal elements used in MoM THA [57, 58, 152].

A retrospective study conducted by Jacobs et al [142] examined the levels of cobalt, chromium and nickel in the serum and urine of patients that had experienced implant corrosion. They found increased levels cobalt in the serum and chromium in the urine of ten patients who had moderate to severe corrosion at the morse tapered connection of the femoral stem. Even higher increases were seen in patients fitted with a MoM THR.

Michel et al [153] conducted a study into the local and systemic effects of Co-Cr alloy hip joint prosthesis, examining various tissues and organs of 2 deceased implant patients. Previous work had shown massive Co enrichments in serum and whole blood as a consequence of corrosion. Cadaver 1 demonstrated a high Co enrichment in the heart, liver and spleen whilst cadaver B had a higher enrichment of Co, Cr and other elements in the surrounding lymphatic tissue and heart. Traces of Co and Cr were also found in muscles surrounding the implant, this was the case for both cadavers. Michel concluded that analysis of the autopsy tissues and organs demonstrated beyond a doubt a systemic burdening of patients bearing prosthetic implants made out of Co based alloys. The burdening was shown by raised trace element levels both in tissues within the vicinity of the implants, and in organs [153].

Dobbs et al [154] also investigated the effects of ion transportation in two cadavers; Cadaver A had a MoM, CoCrMo stem implant and cadaver B MoP CoCrMo stem implant. Ion concentration measurements were conducted on cadaver A and found concentrations of Co and Cr in the lungs, kidney, liver and spleen were five times 'standard man' values. High values also occurred in the urine and hair. The tissue adjacent to the MoM bearing surfaces also contained a high concentration of metal ions, whereas the tissue adjacent to the MoP bearing was relatively uncontaminated.

It is therefore important that the role corrosion plays in the overall degradation of metallic implants is fully understood. Currently there is little information relating to the pathological effects of increased systemic metal ion levels. Certain diseases are thought to be associated with high doses of metal ions, namely for Co: thyroid hypofunction, polycythaemia and myocardiopathy, and for Cr: liver and kidney disease and carcinoma [152].

2.24. Summary of Reviewed Literature

The anatomy of the hip, THR design, fixation methods, corrosion, wear of materials and the effects associated with metal ion release have been reviewed. However from reviewing various articles and journals, numerous questions have been raised. To date few studies have investigated factors that influence localised and fretting-corrosion at the stem-cement interface and the rate of metal ion production. The influence of PMMA bone cement chemistry, the effects of surface roughness, and galvanic coupling will all be investigated. It is important that these questions are answered in order to gain a full and in-depth understanding of the problems associated with corrosion of implant alloy materials, in particular the effects associated with increased metal ion concentration within the biological system.

CHAPTER 3 – EXPERIMENTAL METHODOLOGY AND SURFACE ANALYSIS TECHNIQUES

3.1. Introduction

This chapter outlines the main experimental procedures undertaken in this project. Preparation of samples, electrochemical measurement and surface analysis methods are all covered in this chapter. Surface chemistry techniques are also discussed.

3.2. Test Conditions

Tests were conducted in 0.9% (w/w) NaCl at a constant temperature of 37±1°C (normal human body temperature). A constant temperature of 37°C was maintained using a combination of hotplates or water baths depending on the nature of the experiment. Isotonic sodium chloride was used as they have similar chloride ion content to that of the human body fluids, allowing the effects of proteins to be isolated. It is important to note that no attempt was made to buffer the solution in order to simply the oxidations mechanisms.

3.3. Experimental Materials

In this study, two commonly used biomedical alloys were studied. For small scale corrosion tests wrought LC CoCrMo (ISO 5832-12:2007) was purchased from Heymark Metals, York, United Kingdom (Table 3-1). In some cases 316L stainless steel was also tested however this material was not the particular focus of this study.

In order to gain a full and comprehensive understanding the role corrosion plays in the overall degradation of cemented femoral stems, LC CoCrMo (Table 3-1) femoral

stems were utilised. Ultima TPS™ (DePuy International, Leeds, United Kingdom) femoral stems were utilised in this study as the WE in long term and dynamic corrosion studies. The Ultima TPS™ was introduced in 1997 as a triple tapered, cemented femoral stem manufactured from cobalt chrome alloy. The surface of the stem is a highly polished with a surface roughness of R_a=0.02-0.04µm to reduce the occurrence of cement debris during subsidence, which have been shown to cause Osteolysis. The triple taper design is intended to accommodate cement creep and self-locking in both the antero–posterior and medio– lateral planes, while the tapered shape is to aid cement interdigitaion and pressurisation during implantation and subsidence. The Ultima TPS™ was primarily used with a MoM bearing typically coupled with a 28mm LC CoCrMo Ultima femoral head, which had a super finished surface of maximum R_a=0.01µm , 28mm High Carbon (HC) CoCrMo Ultima acetabular liner and a Ti–6Al-4Vi cementless acetabular shell that ranged from 48mm – 68mm in size.

Table 3-1 - Chemical composition of alloys tested in this study

	Chemical Composition (% wt)										
	C	**Si**	**Mn**	**P**	**S**	**Cr**	**Fe**	**Mo**	**N**	**Ni**	**Co**
Wrought Bar	0.04	0.21	0.69	<0.005	0.0008	27.65	0.41	5.40	0.17	0.48	Bal.
Ultima TPS	0.05	0.19	0.67	0.005	0.0010	27.65	0.30	5.48	0.18	0.24	Bal.

The key focus of this study is to investigate the localised corrosion behaviour of cemented femoral stems at the stem-cement interfaces. In order to get a comprehensive understanding of how ancillary products influence the corrosion regimes, manufacturer and the individual chemistry of PMMA bone cement were varied. Table 3-2 outlines the commercially available cements used in this study

(Full compositions of commercially-available PMMA bone cements can be found in Appendix A). Cements with various levels and type of antibiotic and radio-oblique agents were also tested to investigate the effects of such additives commonly used by bone cement manufactures (Table 3-3). Bone cements supplied in this study by DePuy CMW, Blackpool were from the same manufacturing batch with manufacturing full traceability. Other manufactures where supplied by RFO Medical, London however not from a single manufacturing batch.

Table 3-2 - Commercially available PMMA bone cements tested in this study

Test Notation	Manufacture	Brand Name
HV	DePuy International	Smartset HV
MV	DePuy International	Smartset MV
GHV	DePuy International	Smartset GHV
BIOMET	Biomet	Refrobacin R20
SHO	Stryker Howmedica Osteonics	Simplex P
SHO A	Stryker Howmedica Osteonics	Simplex P with Eyrthromycin & Colistin sulphomethate sodium

Table 3-3 - Chemistry and composition of self-prepared PMMA bone cements

Base Powder	Additions
40g PMMA	N/A
40g PMMA	1.68g Gentamicin Sulphate
40g PMMA	3.36g Gentamicin Sulphate
40g PMMA	4g Barium Sulphate
40g PMMA	10g Barium Sulphate
40g PMMA	6g Zirconium Dioxide
40g PMMA	12g Zirconium Dioxide

3.4. Sample Preparation

3.4.1. Electrode Preparation

Small scale corrosion specimens were manufactured from wrought bar. Each WE was CNC machined and had a working electrode area of 4.05cm^2 (Figure 3-1). Each sample was then either left in its original machined state or subjected to further mechanical surface finishing depending on the nature of the experiment.

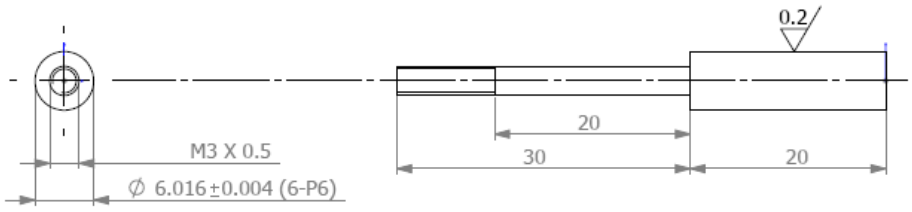

Figure 3-1 - Small scale WE electrodes manufactured for this study

In order to validate the small scale electrochemical tests, experiments were conducted on cemented femoral stems. In this case the metallic femoral stem served as the WE. Each femoral stem was forged from wrought alloy, any excess material removed, stem taper machined and then polished by Symmetry Medical (Sheffield, UK). Each femoral stem was then inspected for any signs of imperfections, cleaned and packaged by DePuy International.

3.4.2. Surface Finish and Pre-treatments

In orthopaedic devices different surface finishes are often adopted in order to optimise surface or mechanical properties. This is often used as a simple way to maximise mechanical properties of a surface, adhesion as well as corrosion properties. One commonly used pre-treatment is polishing. Depending on the design philosophy of the femoral stem, polished or roughened surface may be desired. In

this study, the influence of surface finish has on the localised crevice and fretting corrosion mechanisms has been investigated. In order to replicate the polishing process femoral implants undergo, each sample was polished using a rotating cloth mop and wax until S_a = 8.10±2.98nm, S_{sk} = -0.31±0.23 and S_z = 0.26±0.21µm.

To roughen the stems, an Ultima TPS™ femoral stem was subjected to a process known as vaquasheening, a process used on the Charnley Total Hip Arthroplasty (THA) consisting of a blasting process involving water and glass beads. It is important to note that all stems tested in this study were from the same forging batch and subjected to the same thermal processes. The increased surface roughness was achieved by taking a femoral stem that had already been subjected to the same processes of the Ultima TPS™ femoral stems and then subjected to an aqueous glass bead blast. The blasting process resulting in a S_a = 0.51±0.01µm, S_{sk} = -0.43±0.24 and S_z = 7.11±0.71µm. Because the polishing and blasting processes are manual operations, it is difficult to accurately maintain dimensional tolerances. In order to create consistent crevice conditions tests were conducted with specimens that had consistently machine surfaces (R_a=0.2µm).

3.4.3. Surface Cleaning and Passivation Procedures

Unless using implantable components (stems, heads, liners and shells), which are all supplied in a gamma irradiated sterile packaging to BS ISO 11137-1. All test pieces were degreased and then passivated in 2250 CitriSurf at 25°C for a minimum of 30mins in a series of ultrasonic baths. This treatment provides passivation by surface oxidation and can dissolve certain foreign material that might be present from previous operation. Each sample was then placed in an individual polyurethane bag and sealed to avoid further contamination. Upon testing, samples were handled carefully with latex free gloves to prevent contamination of the metallic surfaces.

3.4.4. Preparation of PMMA Bone Cements

Commercially available PMMA bone cements were prepared and blended according to manufacturer's instructions. All commercially available cements were hand mixed in a vacuum cupboard in glass jars. In addition, cement variation tests to assess the effect of antibiotic concentration and radiopaque agents with respect to localised crevice corrosion mechanisms were conducted. A PMMA base powder was taken and varying levels of gentamicin sulphate, barium sulphate and zirconium dioxide added (Table 3-3). Three concentrations were tested for each addition of gentamicin sulphate, barium sulphate and zirconium dioxide, which was determined with respect to the average content in commercially available cements. Each powder component was passed through a 60 mesh sieve, placed in a polythene liner and then blended for ten minutes. The powder blend and liquid monomer components were mixed at an approximate ratio of 2:1, respectively.

3.4.5. Bone Cement Tapered Collar Preparation

In order to accurately assess the effects PMMA bone cement chemistry has on the localised corrosion rates and mechanism, cement collars with consistent geometry were manufactured (Figure 3-2).

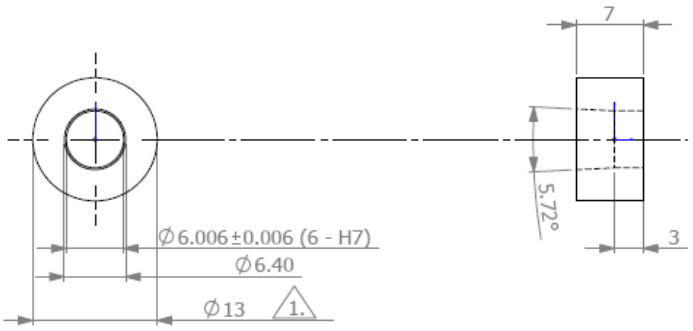

Figure 3-2 - Dimensioned drawing of bone cement washers manufactured to enable consistent crevice geometry conditions

Each cement was hand mixed and placed into a cement injection delivery system and injected in to a Ø15x150mm plastic tube to form a solid PMMA bone cement rod. Each rod was then machined using a CNC lathe to create consistent bone cement tapered collars. Each collar was machined with a 5.72º taper which went down to a reamed 6mm internal diameter with a H7 interference fit. Care was taken to ensure the PMMA cement collars were machined in the absence of cutting fluid to avoid any elution of species out of the cements and also to reduce contamination. Calibrated bore and taper gauges were employed to ensure that each cement collar was consistent in geometry. These particular tests were used as a screening to rank cement and implant alloy combination in order of their resistance to the initiation and propagation of localised corrosion. It is important to note that these particular tests did not take into account any processes that take place at the cement interface during the cementing process allowing the effects of bone cement to be fully understood.

3.5. Experimental Setup

In order to fully evaluate the role corrosion plays in the overall degradation at the stem-cement interface, accelerated and long term static corrosion tests were conducted. A method was also developed in order to quantify the role fretting plays in the dissolution at the interface.

3.5.1. Static Corrosion Measurements

Static corrosion tests were developed as a method to evaluate the role pure electrochemical corrosion, and the associated variables, has on the dissolution at the interface. Static corrosion tests were divided into two types: long term immersion and accelerated corrosion tests.

3.5.1.1. Long Term Corrosion Measurements

Long term corrosion measurements were adopted. In order to achieve this, low carbon CoCrMo femoral stems were cemented using commercially available bone cements. All femoral stems were cemented into specially prepared stainless steel tubes, which were painted and lacquered to avoid any contamination. Extra care was taken to seal any other interfaces, leaving the stem-cement crevice was the only interface open to the bulk electrolyte. Each cemented stem was immersed in 100mL of aerated 0.9% NaCl (pH7.4) at 37 ± 1 °C for 60 days. Approximately 6mL of distilled water was added each day to ensure the volume of solution in each test remained constant. Stems were then allowed to corrode at their free corrosion potential without the application of an external potential, a condition that will be established *in-vitro*. It is important to note that for these tests the initiation and propagation of localised crevice corrosion occurs in real time and is not accelerated, as is the case in many other laboratory evaluations of hip degradation. Figure 3-3 schematically demonstrates the test setup and integration of the electrochemistry.

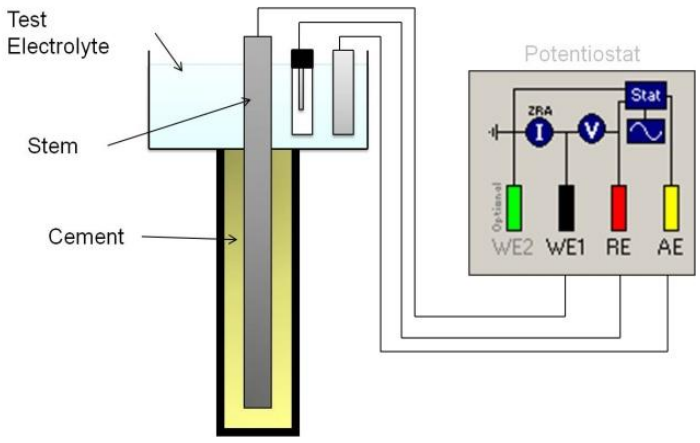

Figure 3-3 - Schematic representation of long term corrosion test arrangement

3.5.1.2. Accelerated Corrosion Measurements

Accelerated electrochemical tests were utilised in order to investigate the influence surface pre-treatment and PMMA bone cement chemistry has on the initiation and propagation mechanisms on localised crevice corrosion. In order to achieve this two different methods were and conducted as outlined below.

3.5.1.2.1. Constant Crevice Geometry Tests

In this study crevice geometry was adapted from ASTM 746-04 to study the crevice corrosion of biomaterials used in THR. A cylindrical metal specimen, with a diameter of 6.00±0.10mm, length of 20.00±0.10mm and an average surface roughness of R_a = 0.20µm were fitted with a PMMA bone cement tapered collar to create a crevice with an opening of approx 0.40±0.10mm and crevice volume of 7.70mm^3. Figure 3-4 schematically demonstrates the test setup.

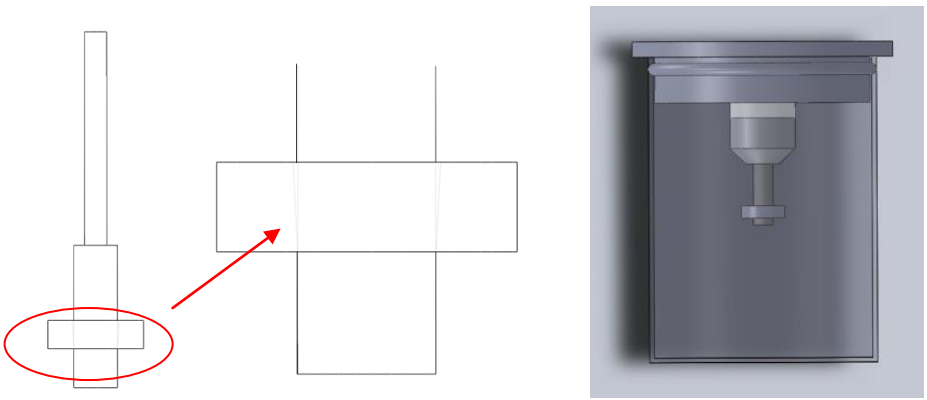

(a) ***(b)***

Figure 3-4 - (a) Tapered washer artificial crevice design (b) CAD representation of corrosion cell

3.5.1.3. Recreating the Stem-Cement Interface

To replicate and study the crevice corrosion mechanisms of cemented biomedical alloys with different surface pre-treatments, an experimental setup was developed as shown schematically in Figure 3-5. The crevice configuration was achieved by mixing the bone cements according to manufacturer's instructions. The cements were then inserted and pressurised into an inert Polyethylene mould during the working phase of the cement. During this phase the cement has a dough like consistency allowing the cement and metallic specimen to be introduced with ease. The WEs were introduced into the bone cement during its working phase and inserted until 5mm remained to create the crevice found at the stem-cement interface. Any excess cement was carefully removed to reveal a clean stem-cement interface. Samples were then allowed to harden for 1 hour before electrochemical testing.

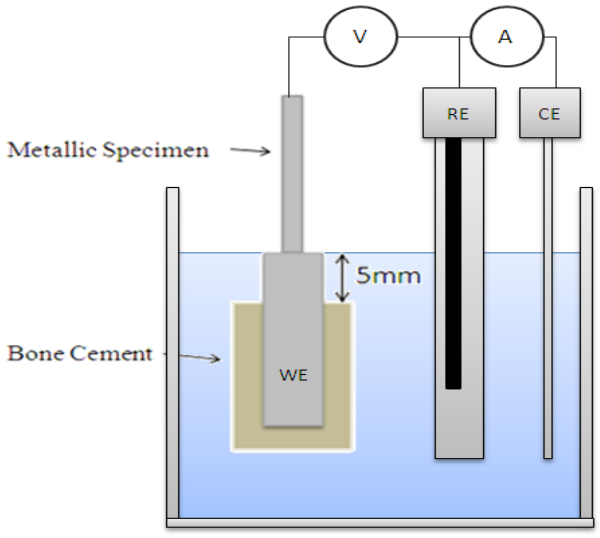

Figure 3-5 - Schematic demonstration of the small scale re-creation of the stem-cement interface

3.5.1.4. Dynamic Corrosion Measurements

A novel test method was developed and conducted in part reference to ISO 7206-4 to evaluate the mechanically enhanced corrosion mechanisms at the stem-cement interfaces of fully cemented femoral components (Figure 3-6a-b). Firstly, a collarless polished LC CoCrMo stemmed component was cemented into a specially designed polymer mould using PMMA bone cement. Once polymerisation of the cement had occurred, the fully cemented stem was removed from the polymer mould, orientated at 10° flexion and 9° abduction to achieve torsional forces experienced *in-vivo* into the test fixtures and set in place using a lab grade PMMA resin (Figure 3-6c). The protruding part of the specimen was then encased in a flexible silicon gaiter and immersed in 600mL of 0.9% NaCl solution at 37±1°C. Initially a static load of 100N was applied to the femoral stem for 24hrs in order to simulate a time of no load bearing after surgery and also to let the system achieve equilibrium before cyclic testing in order to understand the initial passivation mechanics. After 24hrs, a cyclic load of 300N to 2300N at 1Hz for the desired number of cycles was applied to the stem through a Ø28mm LC CoCrMo femoral head and UHMWPE liner. Care was taken to seal the modular taper interfaces so to eliminate any additional effects. The head and liner interfaces were not immersed to ensure they did not contribute to the electrochemical signal. An integrated thrust bearing was also utilised with the intention to mitigate any de-passivation at the loading interface and loads not coincident with the axis of the testing machine. Figure 3-6 demonstrates the test setup utilised in this study.

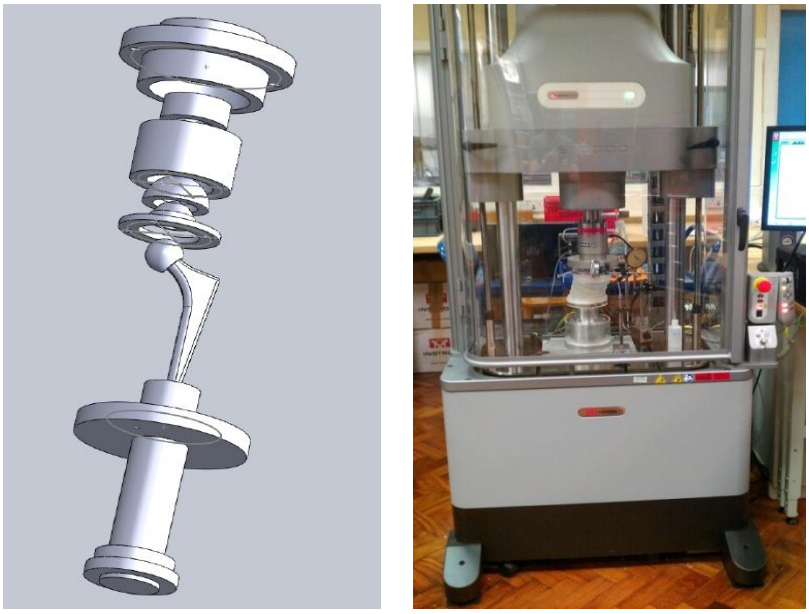

(a) *(b)*

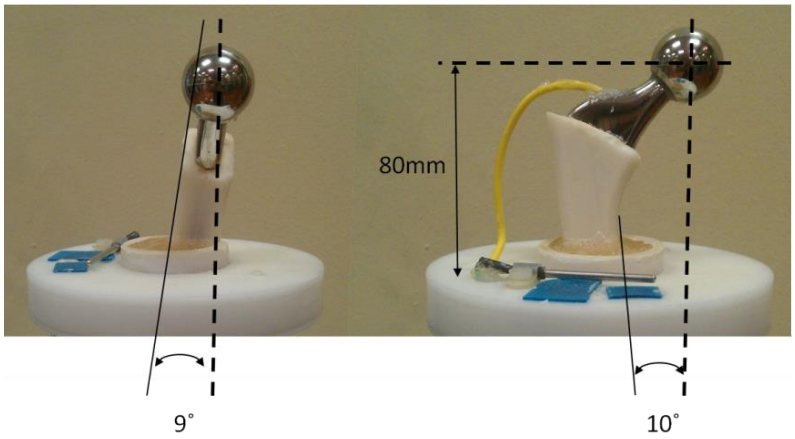

(c)

Figure 3-6 - (a) CAD and (b) Image of test setup and (c) orientation of the femoral stem utilised in order to simulate a gait cycle

In order to replicate the galvanic interaction between the CoCrMo and Ti-6Al-Vi acetabular components, Ti rings with the same surface area of the 68mm Ti acetabular component where manufactured. Because it is difficult to estimate the exact surface area of the Ti acetabular component due to the presence of a porous coating, a CAD package was utilised to calculate the coated and uncoated area of the acetabular component. A total surface area of 139.64cm^2 and a porous coated surface area of 74.69cm^2 was calculate and re-created with the Ti rings. This yields

an approximate area ratio of 3:1 for the Ti and CoCrMo (surface area ≈ 58.09 cm^2) respectively. Once Ti rings had been manufactured and the porous coating applied, each ring was cleaned and passivated by DePuy International. To facilitate electrochemical measurements a plastic coated Cu wire was glued to the surface of the Ti ring and CoCrMo femoral stem using conductive epoxy glue (Figure 3-6). The junction was then carefully sealed with silicone sealant to ensure a water resistant connection.

3.6. Electrochemical Measurements

Throughout this study electrochemical measurements have been utilised to characterise corrosion characteristics of metallic biomaterials, when used in conjunction with PMMA bone cement. In all experiments a 3-electrode electrochemical cell was integrated into the tests to enable electrochemical measurements. Electrochemical measurements were conducted using a potentiostat/galvanostat. The following electrode arrangement was adopted:

- **Working Electrode (WE)**: The working electrode in all experiments was the specimen material, either cylindrical CoCrMo or Femoral stem samples
- **Reference Electrode (RE) :** Ag/AgCl Electrode (+ 0.197V vs SHE)
- **Counter Electrode (CE):** Platinum or Carbon

3.6.1. Open Circuit Potential Measurements (OCP)

At OCP, the anodic and cathodic reactions are equal, therefore no net current flows to or from the electrode. This is usually demonstrated by means of a Tafel plot, and given the notation of E_{corr}. The value E_{corr} is often used to give a semi-qualitative indication of the corrosion regimes of the material, differentiating active and passive

conditions. OCP measurements were utilised in this study to assess the electrochemical behaviour of stems cemented for long periods of time and any changes on a materials surface due to dynamic movements.

OCP consists of recording the corrosion potential, i.e. the potential difference spontaneously established between the WE and a RE placed in the solution close to the working electrode. The measured corrosion potential reflects the galvanic coupling of two distinct surface states of the metal: (1) the passive metal (unworn area) and (2) the bare metal (worn area) exposed to the solution by abrasion of the passive film [127]. This technique can only be used as a semi-quantitative indication of a materials susceptibility to corrosion as the technique doesn't give any information on the reaction kinetics. No electrical potential is applied to the surface of the material.

3.6.2. Zero Resistance Ammeter Measurements (ZRA)

Zero Resistance Ammeter measurements were also utilised in some experiments to measure the influence galvanic coupling has on the localised corrosion at the stem-cement interface. ZRA measurements consist of the WE and another material of interest been connected to a zero-resistance ammeter which will allow a net current to be measured between to the two samples. This technique only considers the excess electrons liberated due to oxidation, neglecting further redox reactions and electron transfer occurring between passive and active areas on the WE. Other techniques need to be utilised to evaluate the self-corrosion current/rate (current resulting from oxidation and reduction reactions) of the WE.

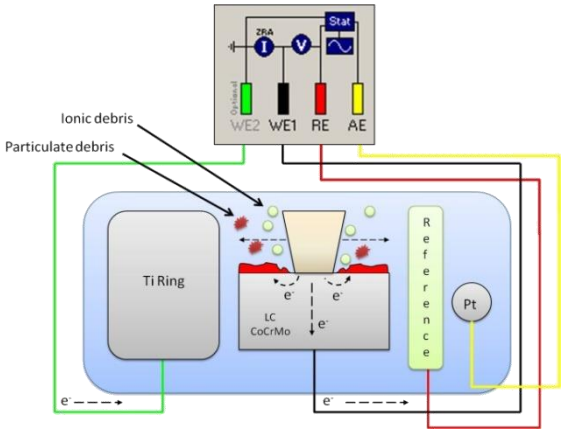

Figure 3-7 - Schematical representation of ZRA arrangement utilised for static and fretting galvanic corrosion tests

3.6.3. Potentiodynamic Polarisation

Potentiodynamic polarisation is a useful technique to investigate the initiation and propagation mechanisms of localised crevice corrosion. This is done by using a standard 3-electrode cell and a computer-controlled potentiostat to shift the potential of the working electrode at a rate of 0.25mV/sec, in our case the CoCrMo samples, from the free corrosion potential in the positive direction. This leads to the sample becoming a net anode and by analysing the rate of charge transfer with respect to the potential, the corrosion behaviour can be evaluated. The over potential is responsible for the breakdown of the passive layer and the magnitude of the breakdown potential *(E_b)*. The break down potential is usually characterised at the point where a rapid increase in the current density occurs, indicating a breakdown of the passive film. For passive materials, such as CoCrMo, the current will stay low in the passive region, usually less than 10µA/cm^2, because of the protective passive film. The break down potential, E_b, was used as an indication of a metals susceptibility to localised crevice corrosion when combined with PMMA bone cement. The scan is then reversed when the current density is approximately 500 µA/cm^2. The reverse scan is stopped when the current has become less than that of forward scan or when

the potential reaches the initial resting potential. The collected data is then plotted with the current density ($\mu A/cm^2$) on the x – axis versus Potential (V) on the y – axis.

The free corrosion potential (E_{corr}), breakdown potential (E_b) repassivation potential (E_r), and the difference between E_b and E_r as an indication of the propagation of localised crevice corrosion (ΔE) were used to characterize a materials resistance to electrochemical corrosion of commonly used biomaterials. A schematic representation and definition of these parameters can be found in Figure 3-8. In each case, E_b was obtained by extrapolating the active and passive regions and taking the point of intersect. E_r was taken at the point at which the reverse scan crossed the forward scan, indicating the potential at which the WE became passive.

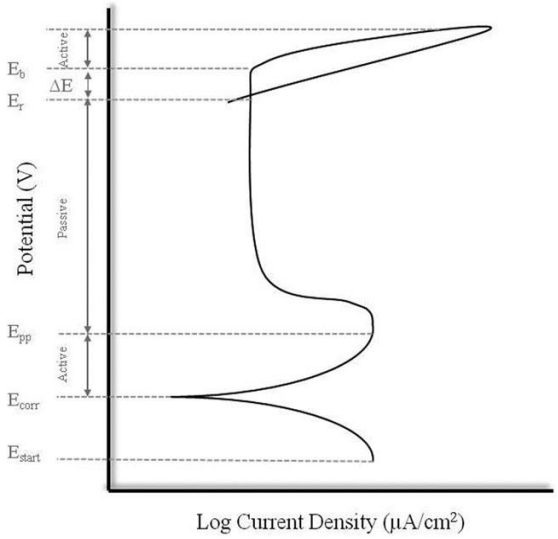

Figure 3-8 - Schematic representation of anodic polarisation curves with studied parameters

3.6.4. Linear Polarisation Resistance (LPR)

Intermittent LPR measurements were utilised in this study in order to quantify the corrosion current and corrosion rates of the working electrode. Typically within 50mV of E_{corr} it is observed that the applied potential is a linear function of the

measured current due to charge separation at the metal solution interface as described in Chapter 2.13. In this study, a potentiostat was used to shift the WE potential ±50mV vs. E_{corr} at a scan rate of 0.25mV/sec. The linear polarisation curve is related to the kinetic parameters of the corroding system, an observation that was observed by Stern and Geary in 1957. Equation 3-1demonstrates the relationship:

Equation 3-1 - Equation used to calculate corrosion current for a system

$$\frac{\Delta E}{\Delta I} = \frac{\beta_a \beta_c}{2.3\ (i_{corr})(\beta_a + \beta_c)}$$

Where β_a and β_c are the Tafel slopes of the anodic and cathodic reactions respectively. The slope of the linear polarisation curve is mainly controlled by I_{corr} and is relatively insensitive to changes in beta values. In this study beta values of 0.12V have been used representing an average of all corrosion systems [79]. These corrosion currents can then be converted to an overall mass loss from an electrode by application of Faraday's law. Figure 3-9 demonstrates a typical LPR plot and extraction of the polarisation resistance. For each LPR dataset, the gradient was fitted to the linear portions of the LPR curve at I=0A and the gradient calculated using CorrView™ software (Scribner Associates, USA).

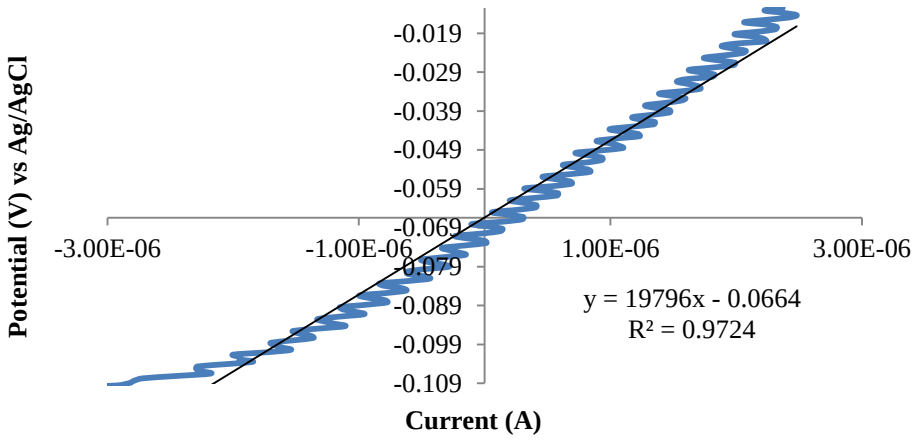

Figure 3-9 - Typical LPR plot obtained in this study

3.6.5. Potentiostatic

In potentiostatic tests a selected potential is imposed on the metal samples by using a three electrode set-up. The three electrodes are connected to a potentiostat, where the current flowing from the WE to the CE is measured at a fixed potential as a function of the time to follow the evolution of the electrochemical kinetics of the involved reactions. Depending on the potential applied (+ anodic, - cathodic vs OCP) the anodic and cathodic currents can be evaluated. In this study potentiostatic measurements were conducted +50mV vs E_{corr}. This technique was synchronised with the loading output on a fatigue test up to evaluate how the current varies per cycle allowing you to pin point the exact source of ion release in fretting/tribo-corrosion systems.

3.6.6. Electrochemical Impedance Spectroscopy (EIS)

Electrochemical Impedance Spectroscopy (EIS) is an electrochemical technique in which a low amplitude alternating potential (or current) wave is applied to the sample and the resultant current measured. The relationship between the voltage and current is used to make a judgment about the corrosion rate and other corrosion characteristics. EIS scans were conducted ±10mV vs E_{corr} from a frequency of 10,000 to 0.01Hz.

EIS data is often analysed using a combinations of analogous circuit elements to represent the metallic surface. EIS allows the electrical properties of the metallic surface, oxide film and any coatings/deposits that may be present on a surface to be estimated. The resistance to charge transfer (R_{ct}) is one parameter often associated with EIS data which can then be converted into a corrosion current/rate. The capacitance of oxides and surface layers can also be evaluated and estimation of the thickness of the films present on an alloys surface.

3.6.7. Calculation of Corrosion and Mass Losses due to Oxidation

The ionic mass loss due to pure oxidation and wear induced corrosion of the metallic surface can be calculated by application of Faraday's Law (Equation 2-10). Where Q is the total electric charge passed through a substance ($Q = \int_0^t I\delta t$, where t is the total time constant, I is the corrosion current obtained through LPR), F = 96,485 C mol^{-1}, M is the molar mass of the substance (58.93g assuming stoichiometric dissolution of the alloy) and n is the valence number of ions in the substance (in this case 2 was assuming oxidation according to $Co \rightarrow Co^{2+} + 2e^{-}$).

3.7. Surface and Chemical Analysis Techniques

Various surface analyses were adopted to gain an understanding the effect corrosion has on the surface of the metallic stem material. Both surface morphology and chemistry were analysed in this study.

3.7.1. Light Microscope Analysis

A Riechert light microscope was used to study the metallic surfaces of the stems. This was to gain an understanding of the structures of the corrosion products and wear behaviour displayed on the interfaces of the samples. A portable 3MP camera on the microscope enabled the observation to be recorded.

3.7.2. Keyence Digital Microscope

The Keyence digital microscope allowed high resolution, high magnification images to be obtained from the surface of samples. Magnification from 25x – 500x was possible, with the option of 2-D or 3-D image stitching. The Keyence machine also allowed features and areas on a surface to be accurately measured and calculated.

3.7.3. White Light Interferometry

Surface profile measurements were taken to characterise the surface of material before and after a test. The TalySurf CCI is an advanced 3-dimensional non-contact optical metrology tool used for advanced surface characterisation, enabling a true topographical representation of a surface with 0.01 nm Z resolution over a full scan range plus a 0.4 nm lateral resolution. A variety of surface parameters such as R_a, R_{sq} and R_{sk} are available using this technique. Analysis of data using Talymap Gold (Taylor-Hobson, Leicester, UK) also allows volumetric analysis of surfaces.

3.7.1. Scanning Electron Microscope (SEM)

Scanning electron microscope analysis was conducted using a Carl Zeiss EVO MA15. Scanning electron microscopes allows the observation and characterization of metallic materials to a nano-meter scale (nm) at a high resolution due to the wavelength of electrons being several orders of magnitude lower than conventional light microscopes. All images were recorded at an accelerating voltage of 20keV corresponding to a volume fraction analysis depth of around 2-3µm.

Scanning electron microscopes produce images by scanning a focused beam of electrons. When an atom is bombarded with electrons, secondry electrons, backscattered electrons and characteristic X-rays of that material are produced. Emission of secondry electrons (SE) occurs when the electron beam interacts with the atoms in the specimen surface. Because the supplied electrons have some kinetic energy the electrons in the sample are knocked out of their orbiting shell. In order to keep the atom in a state of equilibrium, an electron from a higher energy shell will jump to the inner shell. This results in an emission of an X-ray with a characteristic wavelength of the given element. Back-scattered electrons (BSE) are electrons supplied by the beam that are reflected from the sample by elastic scattering.

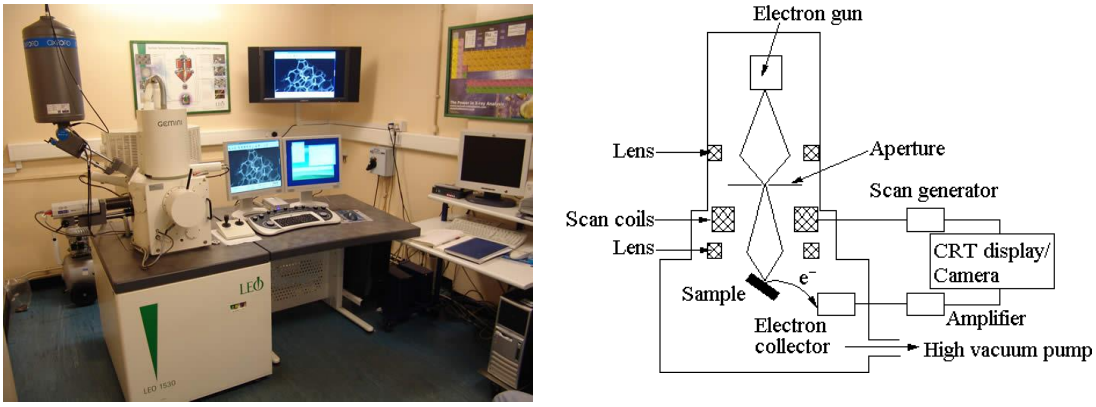

(a) *(b)*

Figure 3-10 - Image of a) SEM used in this study and b) schematical representation

3.7.2. Focused Ion Beam Sample Preparation

Focused Ion Beam (FIB) sample preparation and subsequent Transmission Electron Microscopy (TEM) was also utilised as a technique to quantify the exact composition, thickness and morphology of any deposit or corrosion product at a nano-meter scale. To achieve this, an area of interest was identified on the stem (black deposit and clean area) and a TEM section was prepared for analysis using a FEI Nova200 Nanolab dual beam SEM/FIB. In order to do this, an initial layer of Pt was deposited using an electron beam in order to protect to the surface during preparation (Figure 3-11b). A second layer of Pt, 1.5 µm thick, was then deposited on top of the initial Pt layer using a Ga^+ ion beam (Figure 3-11c). Once this was complete, material either side of the deposited Pt layer was milled away to an approximate depth of 10µm using the ion beam at 30kV (Figure 3-11d). Further thinning of the section was then performed, and the section was partially cut free from the bulk material (Figure 3-11e).

The milled slide was then removed using a Kleindiek micromanipulator mounted inside the chamber of the microscope, attached to a Cu TEM grid and secured via Pt deposition (Figure 3-11f-g). The attached sample was further milled using Ga^+ ions

at approximately 5kV in order to reduce the thickness of the sample to approximately 5-10nm, resulting in a sample that was electron transparent (Figure 3-11h). The sample was then placed in a FEI Tecnai F20 FEGTEM fitted with an Oxford Instruments X-max SDD EDX detector for TEM analysis.

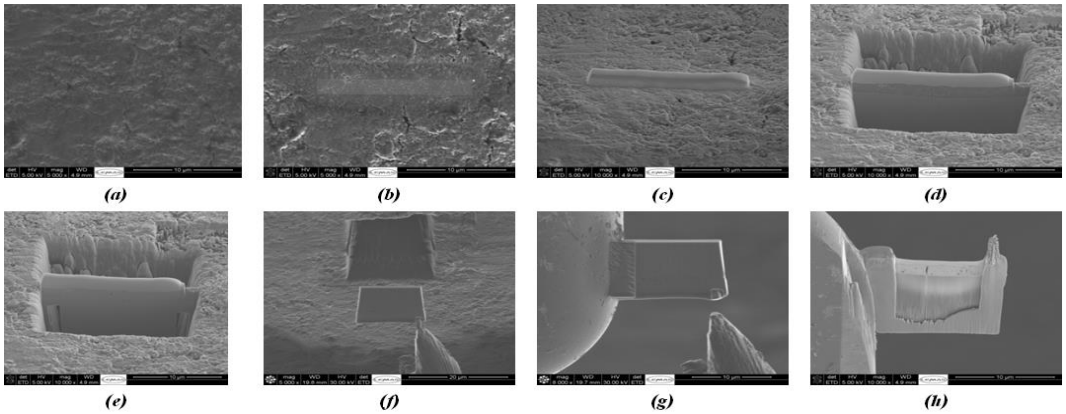

Figure 3-11 - FIB SEM preparation of TEM section (a) surface prior to Pt deposition (b) electron deposited Pt layer (c) ion deposited layer (d) bulk removal of material either side of the section (e) cutting the section free prior to removal (f) removal of the section and (h) mounting on Cu TEM grid

3.7.3. Transmission Electron Microscopy (TEM)

Transmission Electron Microscopy (TEM) is a microscopy technique whereby a beam of electrons is transmitted through an ultra-thin specimen, interacting with the specimen as it passes through. An image is formed from the interaction of the electrons transmitted through the specimen; the image is magnified and focused onto an imaging device. TEMs are capable of imaging at a significantly higher resolution than light microscopes, owing to the small de Broglie wavelength of electrons.

In a TEM, Selective Area Electron Diffraction (SAED) can be conducted in order to assess the orientation of atomic planes within a solid crystal. SAED is where the thin crystalline specimen is subjected to a parallel beam of high-energy electrons

(200kV).Due to the mass and velocity of emitted electrons, electrons are treated as waves. Since the de Broglie wavelength of electrons are very much smaller than the lattice parameters of crystals (>0.3nm) the atoms act as a diffraction grating to the electrons travelling through the samples [155]. Some of the electrons will be scattered to particular angles depending on the orientation of the crystal, while others continue to pass through the sample without deflection [155]. The diffraction of electrons observed in TEM is termed elastic scattering because the scattered electrons lose no energy and therefore suffer no change in wavelength. Whereas X-rays are scattered by the electrons in the lattice, electrons are scattered by the protons in the nuclei [155].

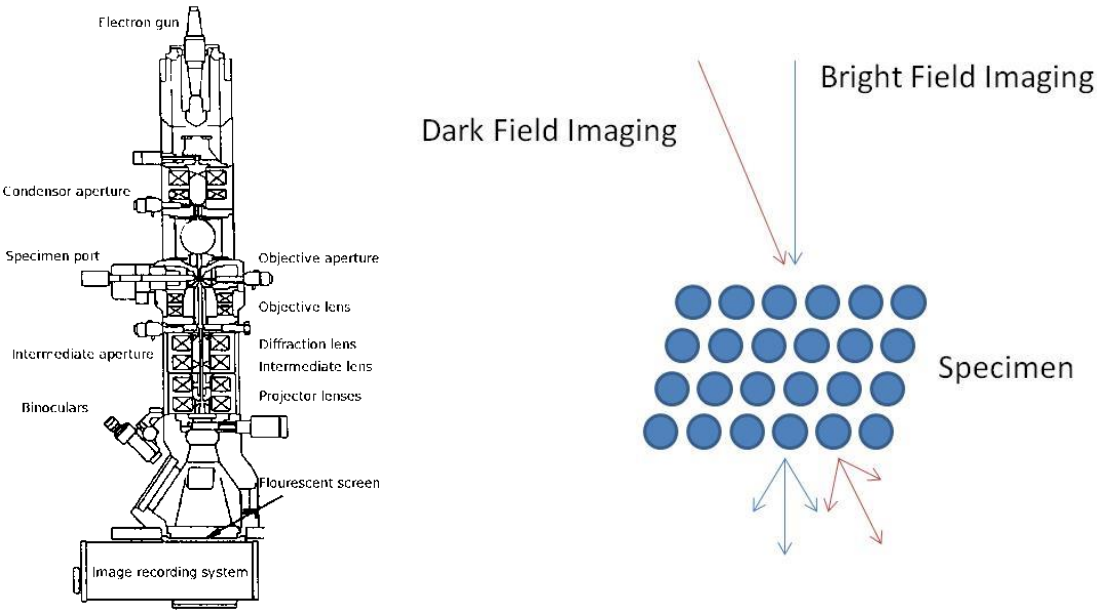

(a) ***(b)***

Figure 3-12 - Schematic diagram of a) TEM and b) scattering of electrons through the sample

3.7.4. Micro and Nano Hardness Measurements

Hardness is defined as resistance to penetration and is associated with many different engineering parameters. A Mitutoyo-MVK-Ha micro-hardness testing machine was used to measure materials micro hardness. A load of 110g was applied and held for 15secs. Tests were carried out a minimum of 10 times on each area of interest.

Nano-indentation was also conducted in order to quantify any change in hardness in the top 600-700nm of the metal due to re-orientation of the crystalline structure of the alloy. The apparatus measures the penetration depth of the calibrated diamond indenter as a function of the applied load during a load-unload cycle. On unloading the elastic component of the displacement starts to recover producing a sloped rather than horizontal unloading curve. It is from this slope that the elastic and plastic properties can be derived. Nano-hardness was determined automatically by the apparatus using the Oliver and Pharr method [64]. For statistical purposes, it is good practice to quote mean values of hardness and reduced modulus from 10-20 indentation curves acquired under the same parameters. Figure 3-13demonstates the test equipment used for Nano-hardness tests

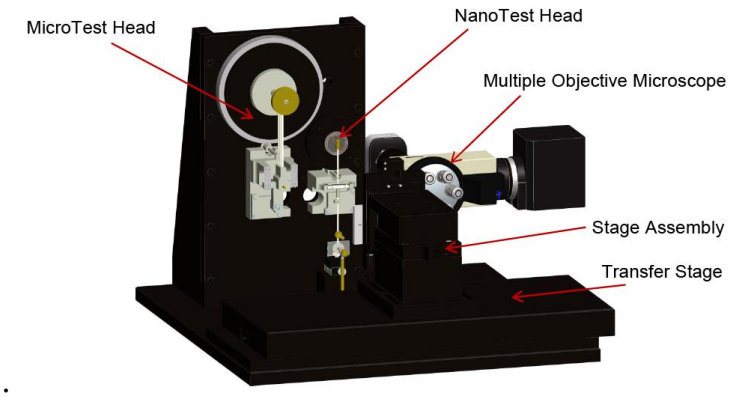

Figure 3-13 - Test equipment used for Nano-hardness tests

3.7.5. Energy Dispersive X-ray Spectroscopy (EDX)

EDX is a technique used for identifying the elemental composition of the specimen, or an area of interest. The EDX analysis system works as an integrated feature of a scanning electron microscope (SEM), and cannot operate on its own without the latter. During EDX Analysis, the specimen is bombarded with an electron beam inside the scanning electron microscope. By measuring the amount of energy present in the X-rays being released from a specimen during electron beam bombardment, the identity of the atom from which the X-ray was emitted can be established. EDX analysis was utilised in this study as a semi-quantitative method of analyzing the surface chemistry of a specimen, allowing the characterization of debris and corrosion products.

3.7.6. X-ray Photoelectron Spectroscopy (XPS)

X-ray photoelectron spectroscopy (XPS) was further utilised to establish the exact chemical composition of any debris or deposit found on the surface. XPS analysis was carried out using a VG Escalab 250 with a high intensity monochromatic Al Kα X-ray source (1486.6eV) with a lateral resolution of 500µm. XPS surveys were initially conducted, followed by high resolution XPS scans on the elements found on the surface. Although X-rays penetrate to a depth of several micrometres, ejected photoelectrons generally come from only the first several nanometres of material making the analysis of the passive film and bulk substrate possible. In order to assess the variation in composition and to mitigate any contamination effects each sample was subjected to an argon-ion etch at 1µA/3mm^2.

Using licensed CasaXPS fitting software, the height, area and position of the peaks was determined alloying the separation of measured XPS spectra. The binding energy scale was calibrated for the C-1s electrons at 284.5eV. All the results in this

paper use the standard format and units (CPS versus BE). Elemental concentrations are given in atomic percentages normalised to 100at% after background removal using Shirley background subtraction. Values of binding energies, FWHM and relative sensitivity factors were taken from literature and applied to the data received [107, 109, 112, 114, 156].

3.7.7. X-Ray Diffraction (XRD) Analysis

XRD analysis was conducted to compliment the diffraction patterns obtained under TEM conditions. Crystals are regular arrays of atoms with a characteristic spacing between each lattice. When a sample is bombarded with radiation, X-rays are typically diffracted from the surface via the electron in the material according to Braggs Diffraction law (Figure 3-14) where d is the spacing between the diffracting planes or lattice, θ is the incident angle, n is any integer and λ is the wavelength of the beam.

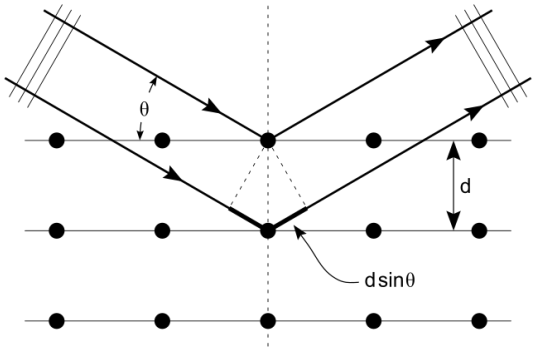

Figure 3-14 - Schematic representation of the XRD technique and Bragg Diffraction

Equation 3-2 - Bragg's Law of Diffraction

$$2d \sin\theta = n\lambda$$

2θ scans between 40° and 50°were carried out using Cu Kα radiation. The scan range selected allows to determine unambiguously the coexistence of the FCC and HCP cobalt phases; within this region the strong $(200)^{fcc}$ and the $(10\bar{1}1)^{HCP}$ are well isolated and do not overlap with any other diffraction peak [157].

3.7.8. Inductively Coupled Plasma-Mass Spectrometry (ICP-MS)

ICP-MS tests were conducted to measure the amount of metal ions released during the corrosion or wear processes. Ion release measurements are directly related to the corrosion of metal and/or metallic debris and are a good method of determining the severity of corrosion present in a given system. ICP-MS is a multi-elemental analysis technique that will separate a sample into ions by ionization which in turn is measured using a mass spectrometer to quantitatively measure the concentration of ions within a solution. Upon completion of each test, electrolyte was drained into a sterile polyethylene bottle and stored in the freezer until analysis to prevent further degradation of the solution. Prior to analysis, samples were defrosted for 24hrs and 2mL of each solution centrifuged at 14,000rpm for 10mins to remove any particulate. 1mL of bulk electrolyte was then extracted using a polymer tipped pipette and stabilised in 10mL 2%HNO_3. Inductively coupled plasma mass spectrometry was utilised to determine concentrations of Co, Cr, Mo and Fe ions released during free corrosion conditions as a result of mass transfer from the interface to the bulk electrolyte. The exact speciation of ions in the solutions is not attainable by ICP-MS. Therefore ion levels reported are a measure of all ions present in the solution, independent of the oxidation state. Isotope Co 59, Cr 52, Mo 96 and Fe 58 were used in order to quantify the amount of metal ions released from the metal-cement interface. Cr 52 was chosen to eliminate any interference from Cl (MW: 34.45) and O (MW: 15.99) present in the electrolyte. Two replicates were

measured for each sample and an average was taken. Background measurements of freshly prepared 0.9% NaCl were conducted in order to mitigate any trace element effect in the stock solutions. Reference samples of Co, Cr and Mo prepared to 50, 100, 200, 500 and 1000ppb where included in each batch of analysis.

3.7.9. Ion Chromatography (IC)

Initial studies utilising ion chromatography where conducted in order to investigate the influence of crevice environment on the egress of sulphate out of PMMA bone cements. Analysis of the sulphate analysis was carried out on a DX500 ion chromatography system a with conductivity detector (Thermo Scientific, USA).

Each sample was passes at a flow rate of 1mL/min onto two guard columns (AG9 4mm HC columns), a slider valve and a 4mm AS9 HC column with carbonate bicarbonate eluent, using a gradient programme and anion self-regenerating electrical suppression. Calibration was carried out with user prepared standards.

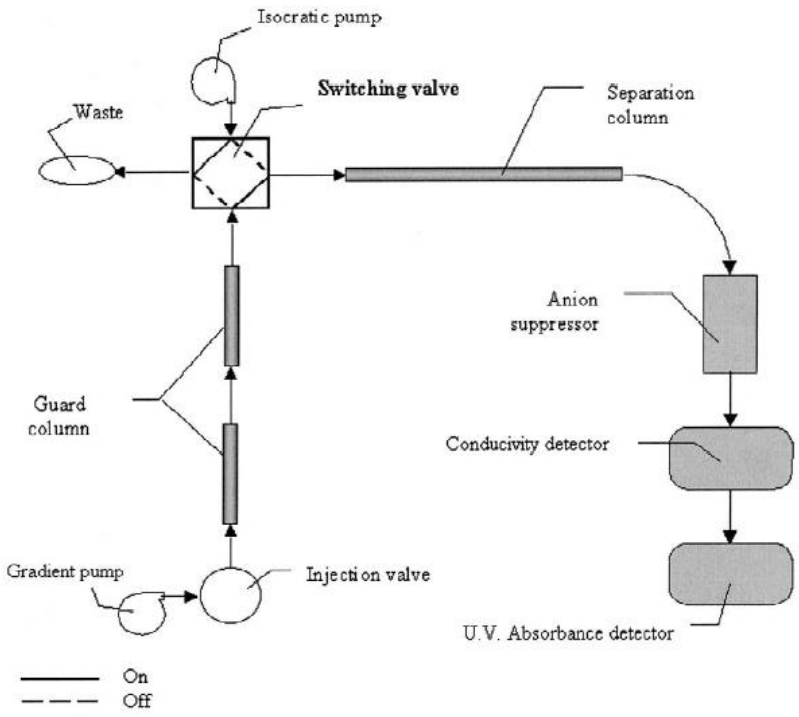

Figure 3-15 - Schematic diagram of chromatographic set-up

3.8. Summary

The experimental techniques and methods of analysis outlined in this chapter make it possible to conduct a comprehensive investigation into the corrosion of cemented femoral stems. Surface analysis makes it possible to observe and characterise what is taking place on the surface of a metal, whilst electrochemical measurements allow the regimes of corrosion to be quantified. Surface chemistry analysis further allows the quantification of anything present on the surface both pre and post testing. Combinations of the techniques listed above were used to complete a full and comprehensive investigation into the corrosion of cemented femoral stems. Figure 3-16 demonstrates the map of experimental work outlined in Chapter 3.

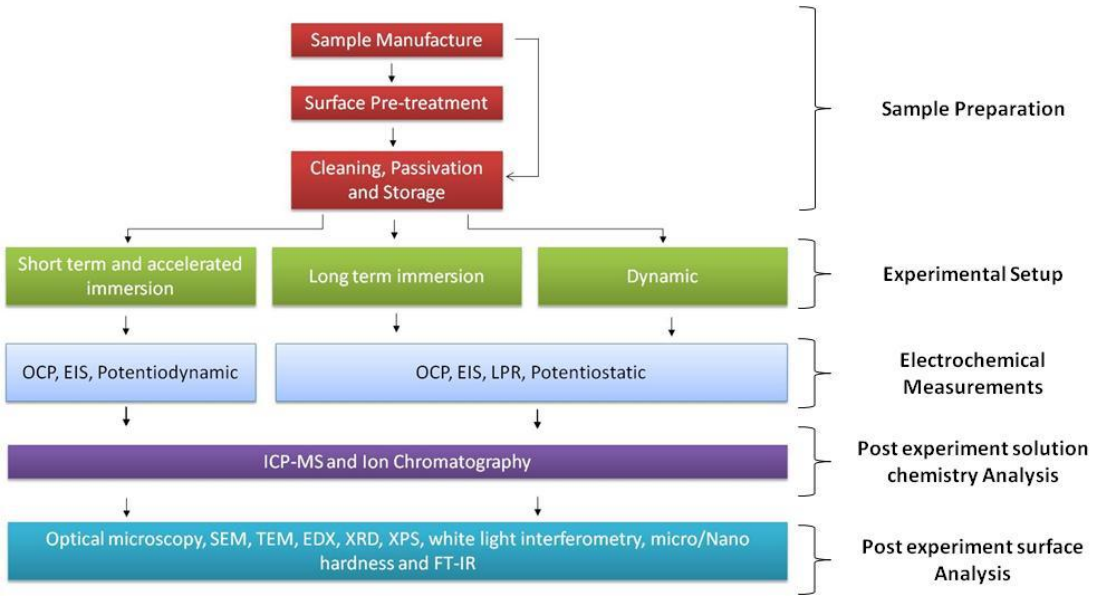

Figure 3-16 - Map of experimental work outlined in Chapter 3

CHAPTER 4 – REVIEW OF CLINICAL CASES

4.1. Introduction

The research work in this thesis was developed around the need to understand a particular failure around Metal-on-Metal Total Hip Replacements. This chapter outlines the particular failure and a review conducted by the candidate of the retrievals. The Ultima TPS™ (DePuy International, Leeds) hip was one of the first second generation Metal–on–Metal hip replacements to be developed and consisted of a collarless, tapered, highly polished wrought low carbon (LC) CoCrMo femoral stem with a 12/14 modular taper. A 28mm MoM articulation was utilised in this cohort consisting of a wrought LC CoCrMo Ultima femoral head and a wrought high carbon (HC) CoCrMo taper lock acetabular insert. A porous coated Ti-6Al-4V Acetabular outer shell with three holes for supplementary fixation was used. Figure 4-1 demonstrates the system that was implanted in the cases presented by Donell *et al* [4].

Figure 4-1 - Ulitma TPS™ MoM total hip replacement used in the Norwich cohort

By 2008, 90 out of a total series of 652 Ultima TPS™ Metal–on–Metal hip replacements had to undergo early revision at the Norfolk and Norwich University Hospital [4]. 17 hips required revision for periprosthetic fracture, with early dislocation in 3 and late dislocations in 16. Infection was found in 10 hips. 44 required revision for extensive, symptomatic, peri-articular soft tissue necrosis of which 35 had normal plain radiographs. The femoral component was cemented with either a plain PMMA bone cement or antibiotic cement containing either the Gentamicin antibiotic or Erythromycin and Colistin. Dramatic corrosion of generally solidly fixed femoral stems was frequently observed on the retrieved cemented part of the femoral component. Blackening of the cemented portions of the stems and staining of the PMMA bone cement, thought to be metallic debris, was also found at revision. It was thought that the necrosis of the surrounding tissue was associated with the release of potentially toxic metal ions such as cobalt and chromium from the stem surface as the bearing surfaces were macroscopically clean of any wear or abrasion. As a result of this a Medical Device Alert MDA/2007/054 dated 14 June 2007 was issued detailing unexplained pain when the Ultima TPS femoral stem was used in conjunction with the 28mm Ulitma MoM articulation.

To date, out of 651 total implantations, 155 have had to be revised representing a 24% revision rate with a 6.3years mean time to revision. Of the hips that were revised, the majority had at least one abnormal MARS MRI scan and two thirds of revisions for symptomatic adverse reaction to metal debris (ARMD) of which three quarters had normal X-rays. 24 hips required revision for peri-prosthetic fractures. A significant indication of complication was a negative Trendelenburg, an indication of poor abductor muscle function. Post revision, observed blood ion levels (Cr and Co) appear to come down with respect to time. Implants are typically revised to MOP, COP or COC.

4.2. Materials and Methods

In this study, 105 Ultima TPS MoM THR were retrieved from the Norfolk and Norwich teaching hospital between 2003-2012. Each stem underwent a sterilisation wash procedure before the analysis was undertaken. Each implant was individually placed in a cardboard surgical tray, sealed in a polythene bag and numbered in numerical order to ensure patient data was kept confidential. Any handling of the implants was performed using latex surgical gloves to avoid contamination. Initially, each stem was macroscopically observed in order to assess the location and extent of fretting-corrosion found on the femoral stem. The location of the fretting corrosion was determined through the use of Gruen zones as outlined by Gruen *et al* (Figure 4-2). Each stem was then graded in terms of surface observation and coverage (Table 4-1). Due to the complex interactions and synergy's associated with wear and corrosion a grading system was developed that allowed the wear and corrosion to be assessed with the same grading criteria. Thorough statistical analysis was also conducted on the retrieved cohort. In order to isolate any population effect (n=105) the observational scores were assessed against impingement, stem offset, head offset, stem size and size of the Ti acetabular component. For a select number of stems (n=71), surgical information such as type of PMMA bone cement used, time in-vivo and patient sex could also be compared. It is important to note here that full cohort details are unknown so results from the statistical analysis must be interpreted with caution as the full population of the cohort is unknown. In all cases the distribution of the observational grading was observed and subjected to statistical testing. A Fishers exact test was utilised for the comparison of contingency tables (frequency distribution of variables). Regression analysis was conducted to

investigate the relationship between dependant and one independent variable. In all cases a 95% confidence interval ($P<0.05$) was chosen for comparison.

Figure 4-2 - Location and orientation of Gruen zones used to map fretting corrosion in this study

Table 4-1 - Observational and grading criteria used in this study

No.	*Scoring*	*Observations/Grading*	*Coverage*
1	Low	Slight marking of the surface.	Less than 10% of the cemented portions affected by corrosion/wear
2	Low-Moderate	Scoring or dulling of the surface.	Between 10% and 25% of the cemented portions show sign of Corrosion/wear.
3	Moderate	Definite abrasion/corrosion of the surface. Indication of black oxide debris.	25% to 50% of the cemented portions affected by corrosion/wear.
4	Moderate-High	Pitting and scarring on the surface. Indication of black oxide debris.	50-75% of the cemented portions affected by Corrosion/wear.
5	High	Severe surface damage and corrosion debris. Indication of black oxide debris.	>75% of the cemented portions affected by severe corrosion/wear.

4.3. Macroscopic observations and grading

Visual analysis indicated that a wide variety of fretting-corrosion damage was seen on surfaces of the retrieved THRs. On visual inspection, fretting-corrosion of various degrees was observed; with assessment and grading of the retrieved cohort demonstrating a spread in the variety of surface morphologies observed (Figure 4-3).

High amounts of fretting-corrosion were typically seen in Gruen zones 1, 2, 6 and 7. Regions of localised corrosion were also seen in the proximal regions of the cemented femoral stems. Areas of black deposit were also commonly seen on the surfaces of the femoral stems in the areas that appeared to demonstrate high amounts of fretting-corrosion. Although some areas of black deposit were observed in samples that scored a low and low-moderate grades an increased occurrence of blackening of the stem surface was seen with increasing amounts of fretting corrosion.

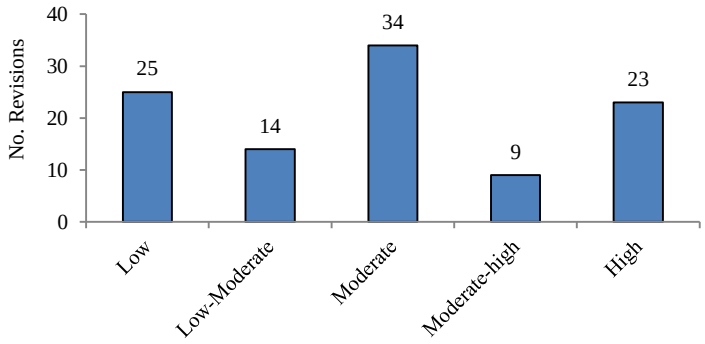

Figure 4-3 - Number of retrieved stems vs. observation/grading stated in Table 9-1

Figure 4-4 demonstrates the difference between femoral stems with a low (Figure 4-4a) and high (Figure 4-4b) visual grading, with white arrows indicating the typical location of black deposits. At a macroscopic level, the black deposit appeared to have a flaky textured appearance, typically being found in regions of high wear and corrosion. Impingement of varying levels was also seen on the retrieved cohort, typically being seen on the proximal portions of the femoral stem neck (Figure 4-4c). Analysis of the cohort data identified that impingent of the femoral neck occurred in 65% of the retrieved cohort almost solely in implants utilising the 10° augmented Ø28mm CoCrMo liner. Instances of fretting-crevice corrosion were also noticed at the modular taper interface (Figure 4-4d). However it was not seen on all retrieved tapers. It is interesting to note that this corrosive attack seemed limited to

the opening of the male taper interface suggesting a purely corrosive attack with no damage being observed on the male taper in the proximal direction.

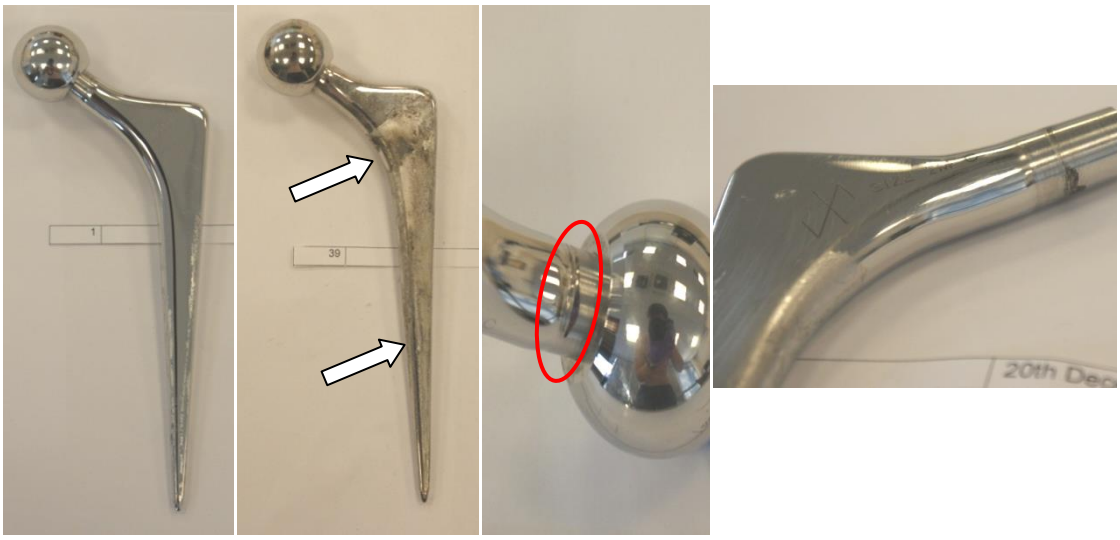

(a) *(b)* *(c)* *(d)*

Figure 4-4 - Typical macroscopic observation of (a) retrieved femoral stem with low and (b) high observation grading (White arrow indicates areas of black deposits) (c) evidence of impingement (d) corrosion at the modular taper interface

4.4. Microscopic results

Figure 4-5 demonstrates the surface morphology obtained from the retrieved Ultima TPS femoral stems. Gross slip and plastic deformation of the surface was observed in the proximal regions as a result of micro-motion at the stem-cement interfaces. Optical microscopy demonstrated clear directionality of the surface in Gruen zones 1 and 7 (Figure 4-5 a-b). A contrast in surface morphology was seen towards the distal portions of the cemented portions of the femoral stem. A more corrosive attack was seen in Gruen zones 3-5 suggesting that micro-motion is not the sole reason for the degradation of cemented femoral stems (Figure 4-5 e-f). Figure 4-5e demonstrates a selective attack of the alloy, appearing to occur at grain boundaries of the alloy. A seemingly intergranular corrosive attack was also seen under and around the areas of black deposit (Figure 4-5f).

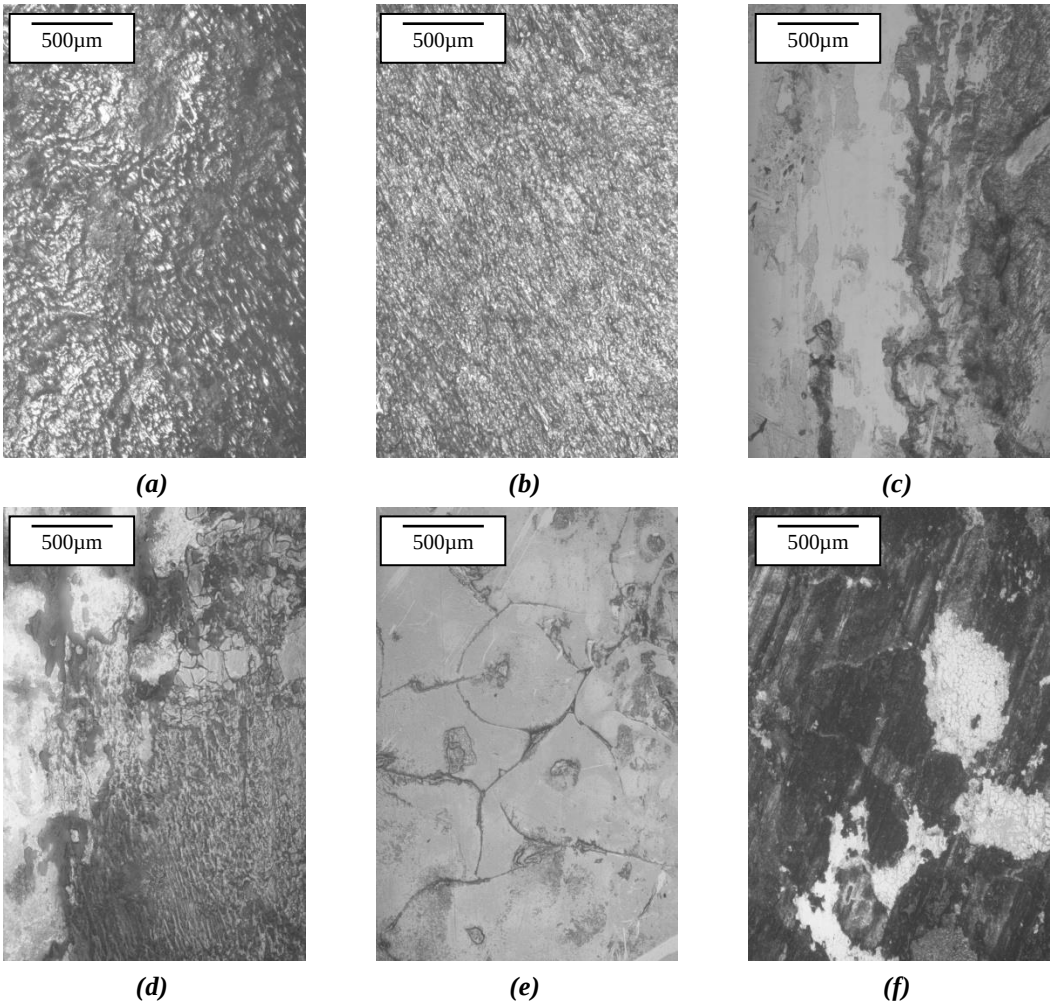

Figure 4-5 - Light microscope images of typical surface morphology in (a-b) the anterolateral and posteromedial regions of Gruen zone 1and 7 (c-d) Gruen zone 2 and 6 (e-f) Gruen zone 4

SEM/EDX analysis was conducted on sectioned femoral stems in order to fully characterise the surface topography and chemistry of retrieved femoral stems (Figure 4-6). At higher magnification, clear ploughing and plastic deformation of the surface could be seen, with retention of debris being seen within the valleys of the troughs (Figure 4-6 a-b). Spot EDX analysis was conducted on the debris seen in Figure 4-6b, suggesting that the debris was Cr, O and C rich. However it is not known if this is fragmented PMMA bone cement with a Cr_2O_3 transfer film or Cr_2O_3 resulting from fretting corrosion at the interface. Again a more corrosive attack, in the absence of any mirco-motion, was seen towards the distal regions of the

retrieved femoral stems, demonstrating localised areas of corrosion resulting in loss of material from the surface.

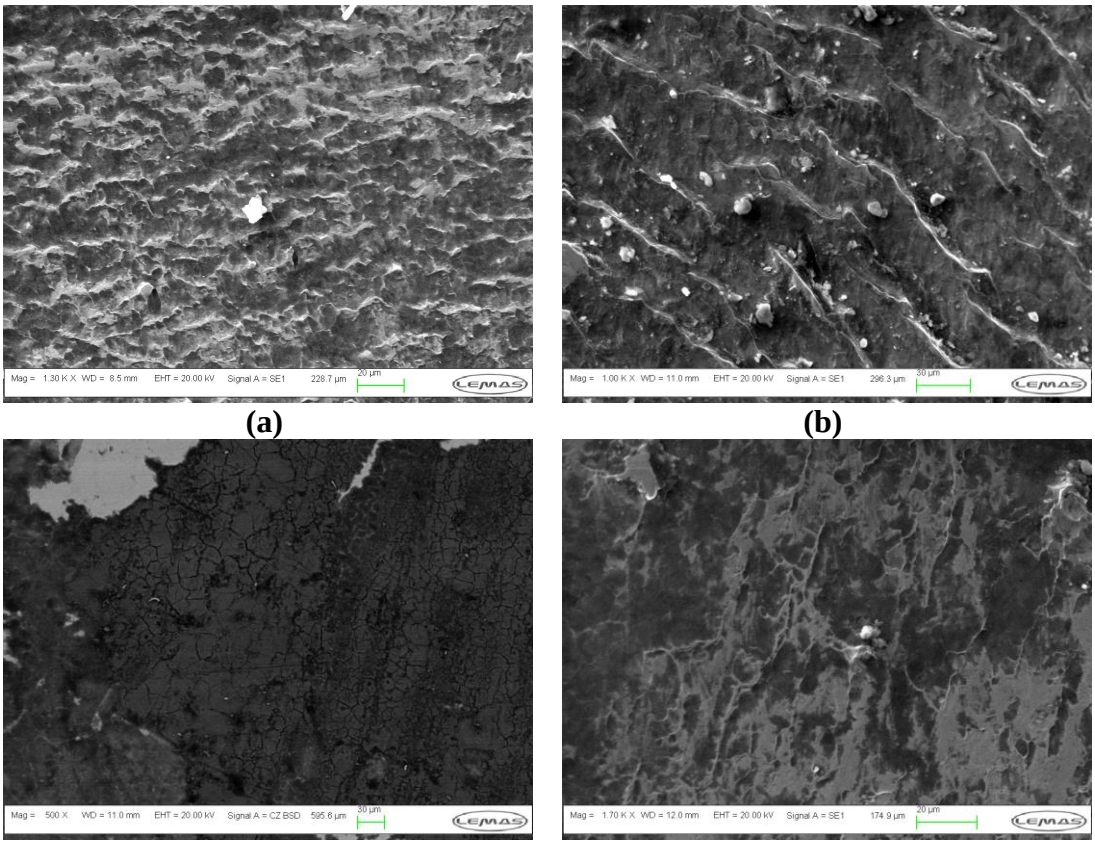

Figure 4-6 – SE and BSE SEM images of (a) plastically deformed surfaces in Gruen Zone 7 (b) surface morphology in Gruen zone 2 demonstrating the retention of debris within the grooves valleys of the plastically deformed surfaces (c) areas of black deposit seen in Gruen zone

Areas of black deposit on the femoral stems were seen to be comprised of smooth plaques with an irregular size and shape as shown in (Figure 4-6c). Under SEM conditions areas with surface deposits demonstrated a semi-conductive nature, suggesting build-up of a non-conducting film. EDX mapping was further utilised, demonstrating that the surface deposit was rich in Cr, O and N (Figure 4-7). Traces of Co and Mo were also seen to be present in the surface deposit, though not in the same quantities observed in the clean bulk material.

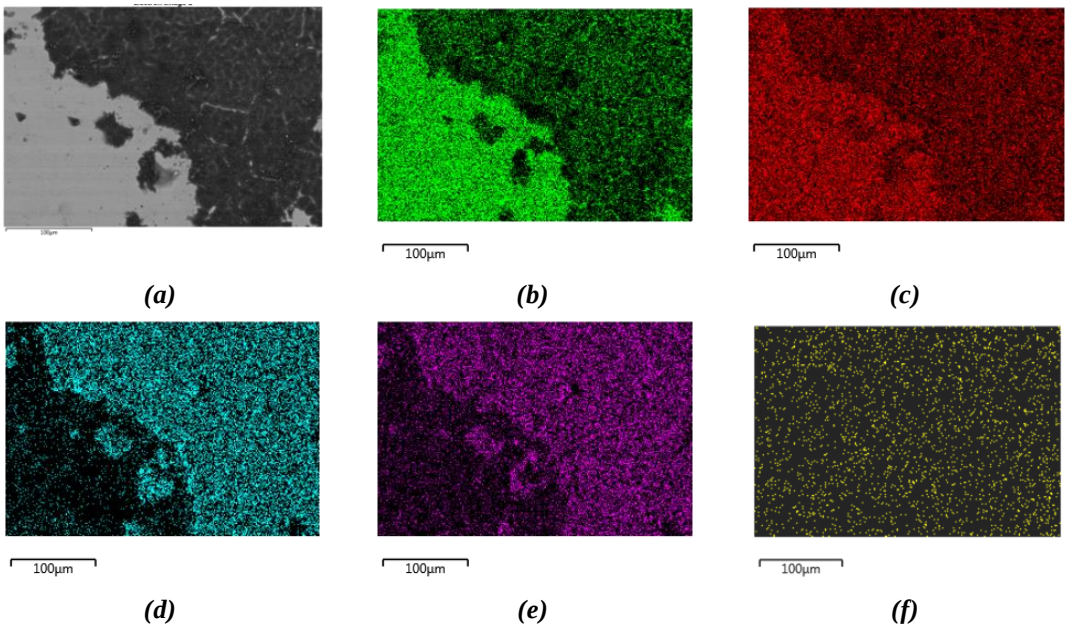

Figure 4-7 - EDX mapping of (a) Electron image (b) Co (c) Cr (d) C (e) O (f) N the deposit commonly seen on femoral stems demonstrating moderate to high fretting-corrosion grading.

SEM analysis was further conducted on a selected number of tapers from the retrieved cohort in order to investigate what effect crevice corrosion at the modular taper interfaces has on the overall degradation of MoM THRs. A clear and distinct difference at the interfaces could be seen between material that had remained passive or un-corroded and material that had become active (Figure 4-8a). A slight directionality of the surface was also seen suggesting that micro motion at the interface may further influence the dissolution rates at these interfaces. Under macroscopic conditions, the proximal regions of the taper appeared to be relatively clean and free from any sign of localised corrosion. However under SEM conditions, a flaky surface appearance was observed (Figure 4-8b). It is difficult to identify what results in the flaky appearance. However the presence of the original machined taper surface, indicated by white arrow and circled area, suggests that the material below the seemingly flaky top surface may result from the initiation and propagation of localised corrosion.

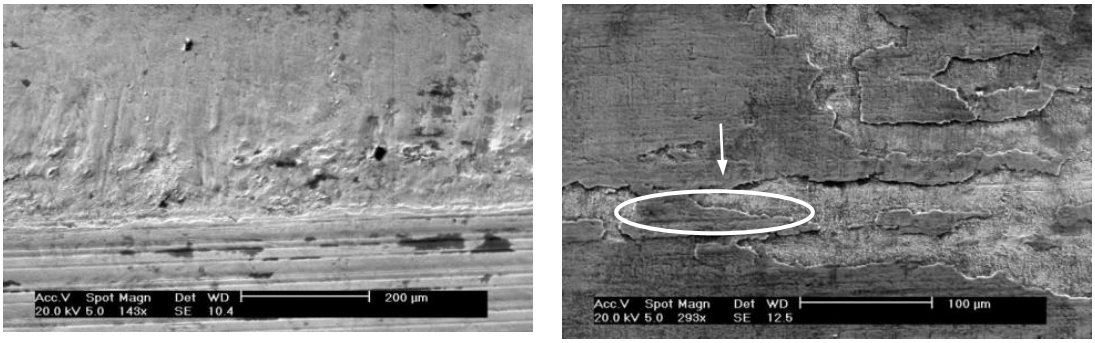

(a) *(b)*

Figure 4-8– SE SEM evidence of fretting-corrosion at the (a) distal regions of the male taper interfaces and (b) proximal regions of male taper interface of the retrieved Ultima TPS femoral stems

FIB/SEM preparation techniques, along with TEM and EDX analysis proved a useful tool when identifying the exact morphology and chemistry of the deposits found on top of the retrieved femoral stems. Figure 4-9a illustrates the thickness and morphology of the film found on the surface of the retrieved femoral stems under TEM conditions. A thick surface film, in the region of 1.04µm, was seen on the surface of the retrieved metallic femoral stems in the regions of high fretting-corrosion. It is interesting to note the heterogeneous nature of the film. Surface films were seen to consist of densely packed nano-sized particles containing large voids. At higher magnifications, TEM analysis indicated that the particles found in surface film commonly consisted of two seemingly ellipsoid shapes joined together (50nm in length and 40nm in width), surrounded by an organic amorphous matrix (Figure 4-9b). Figure 4-9c shows a selected area electron diffraction pattern taken from the surface film. Analysis of the diffraction pattern indicated the presence of Cr_2O_3 particles within the deposited layer. The interface between the metallic stem and deposit found on the femoral component was also analysed in order to assess if any localised chemical or crystalline reorientations had occurred due to chemical dissolution or mechanical wear. At higher magnifications, the metallic surface seems

to show signs of a ‘saw tooth’ like morphology (Figure 4-9d); however it is unknown if this is the original surface topography or a result of fretting-corrosion. Although TEM analysis demonstrated the presence of stacking faults and annealing twins, no localised changes in crystallographic orientation or chemical composition were seen at the interface. This is thought to be due to the nature and magnitude of the slip and stresses present within the interface [64].

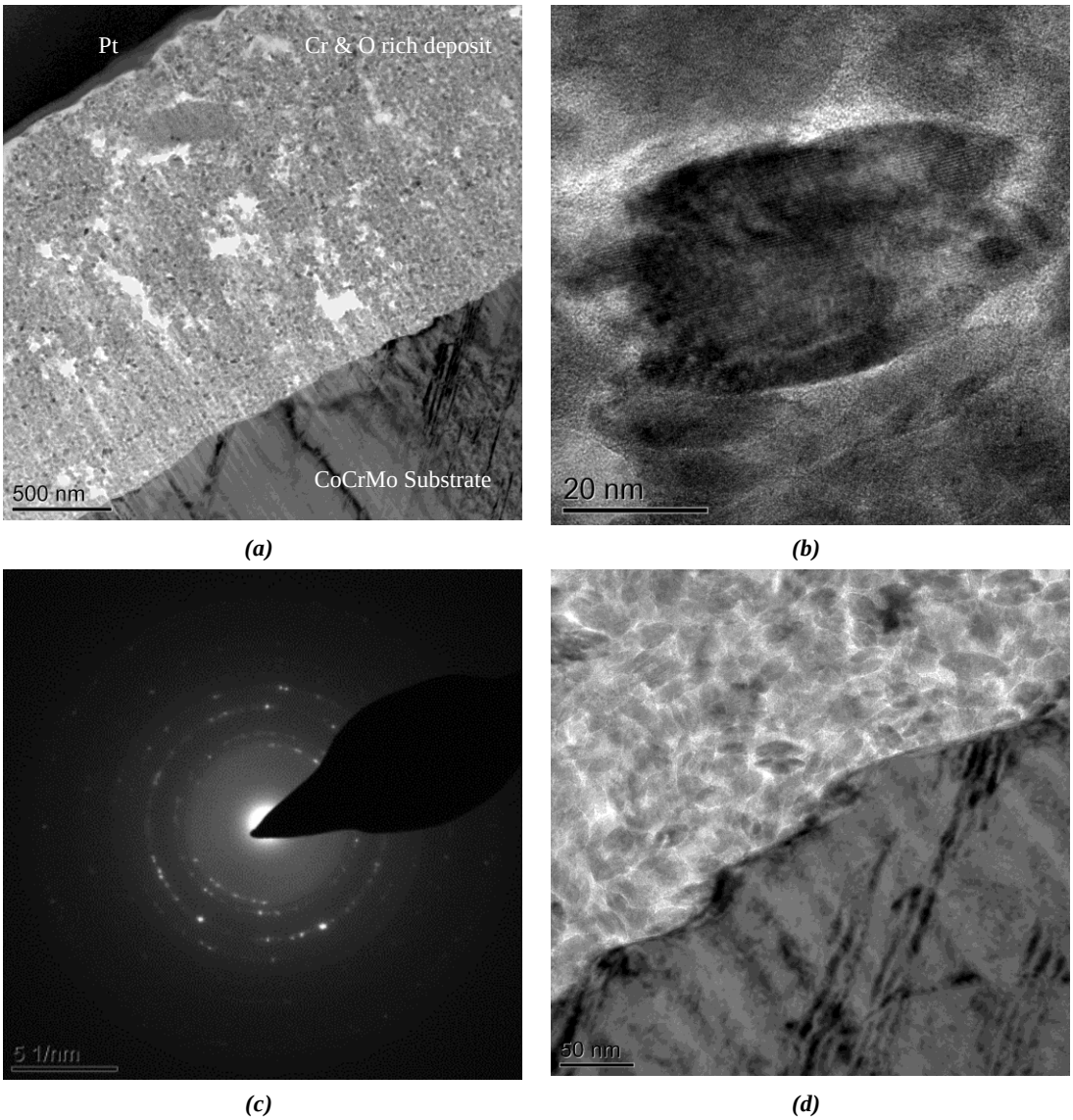

(a) *(b)*

(c) *(d)*

Figure 4-9 – Cross-sectional TEM images of (a) black deposit seen on retrieved femoral stems (b) Cr_2O_3 particles seen within the surface deposit (c) annotated diffraction pattern associated with the Cr2O3 film and (d) the metal-deposit interface

Scanning (S)TEM/EDX mapping of the substrate and surface film was utilised in order to identify the chemical composition of the surface film. Figure 4-10 shows the EDX maps that were obtained for the retrieved sample with the surface film present. It is interesting to note that the film present on the femoral stems mainly consisted of Cr, O and trace amounts of C whilst Mo was seen to be relatively well dispersed within film and the underlying material (although the generally weak signal in the Mo map makes it difficult to accurately assess its dispersion). However a clear and distinct difference in Co content at the interface between the film that had formed and the metallic substrate was seen. Co was not seen to be present in the surface film formed *in-vivo*.

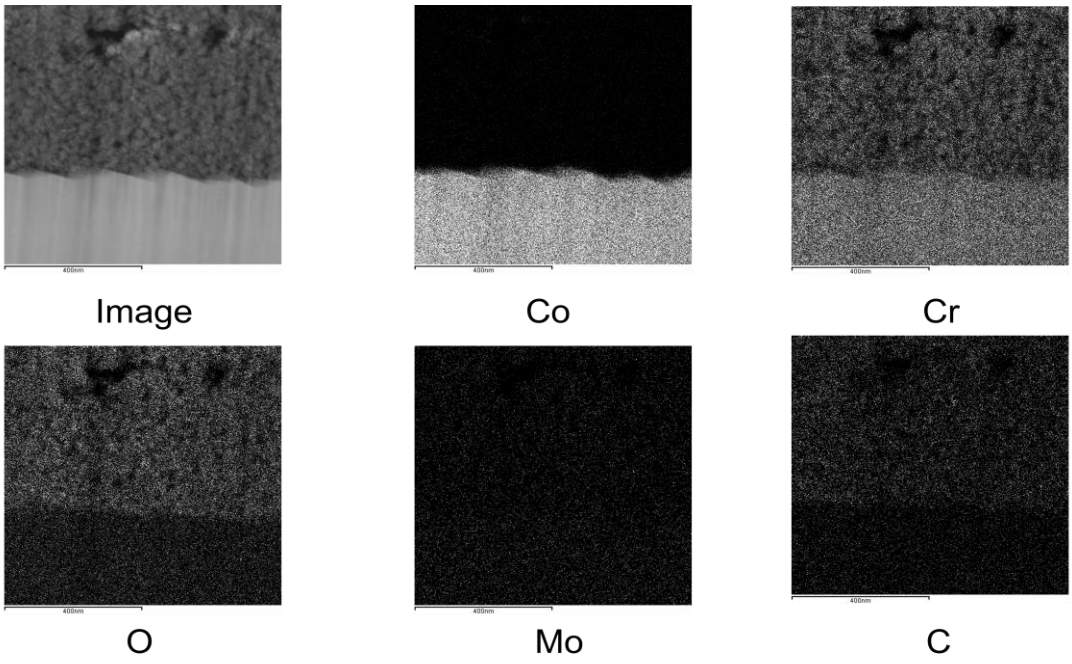

Figure 4-10 - TEM/EDX mapping of the substrate and deposited film. EDX analysis indicated the surface deposit was rich in Cr, O. Traces of C were also seen in the surface deposit

4.5. XPS observations

XPS was further utilised in order to investigate the exact chemical speciation of the surface film. After the initial surface etches had been applied, general surface scans were conducted on areas clean and free from fretting-corrosion in addition to areas demonstrating the deposited layer. Figure 4-11 demonstrates the general survey spectra's that were recorded from a clean and deposited area of a retrieved Ultima TPS femoral stem with the related chemical compositions in Table 4-2. C, O, N and Ca was present at both sites. However an increase in C, O and Ca was seen in the areas of black deposit. N was seen to remain similar in both areas. Decreases in the at% of metallic elements (Fe, Co, Cr, Mo) was seen with the areas of surface deposits. Although a small decrease in Cr was seen in areas of the black deposit, Cr was seen to be the dominant metallic species present in the deposited layer.

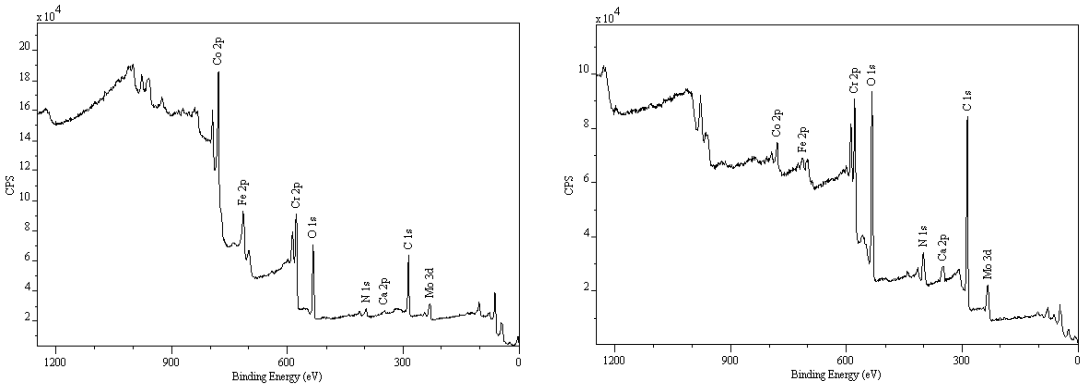

(a) ***(b)***

Figure 4-11-General XPS survey spectra obtained for the (a) clean (b) deposited areas

Table 4-2 - Obtained chemical composition from XPS analysis of (a) clean and (b) deposited areas

Name	Peak Position (eV)	at %
C 1s	284.516	60.79
Ca 2p	347.216	0.96
Co 2p	778.016	5.37
Cr 2p	574.116	6.94
Fe 2p	712.816	2.71
Mo 3d	227.416	1.48
N 1s	398.516	7.41
O 1s	530.516	14.32

(a) Clean area

Name	Peak Position (eV)	at %
C 1s	284.916	66.76
Ca 2p	347.316	1.58
Co 2p	777.916	1.07
Cr 2p	576.216	4.45
Fe 2p	229.316	0.99
Mo 3d	398.816	6.99
N 1s	530.616	18.16
O 1s	284.916	66.76

(b) Deposited areas

The advantage of XPS analysis is the possibility to identify the oxidation state and chemical environment of a particular element. Discrete differences were seen in the high resolution scans demonstrating a difference in the chemical nature of the surfaces. High resolution XPS analysis of the different areas demonstrated subtle differences in chemical state between the deposited and clean areas. Although an increase in at% of elements was seen in the different areas, no changes in chemical states were seen for Co, Ca and O between the clean areas and areas with the deposit present. However, differences in chemical state were seen for Cr, Mo, N and C. Figure 4-12 demonstrates the high resolution Cr, Mo, N and C XPS spectra obtained for both the clean and areas containing the deposit.

Curve fitting of the high resolution Cr 2p spectrum demonstrated that metallic Cr and Cr_2O_3 were seen in both areas with peaks being resolved at 573.98 and 583.188eV and 576.06 and 585.36eV respectively. However the intensity of the peaks was seen to change depending on the area analysed, with deposited areas demonstrating intense Cr_2O_3 peaks when compared to the clean areas which

presented dominant Cr metal peaks. A difference in Mo spectrum was also seen. For the spectra obtained from clean unworn areas, peaks were obtained at 227.35 and 230.49eV and 229.17 and 232.30eV demonstrating the presence of metallic Mo and MoO_2 respectively. For the deposited area, peaks were only observed, at relatively low intensity, at 229.22 and 232.35eV indicating the presence of MoO_2. Traces of N were seen in both areas of the analysis. In each case, peaks were resolved at 395.25 and 399.19eV demonstrating the presence of Nitride and organic N. An increase in organic N was seen in deposited areas demonstrating that the film formed on the surface is a complex mixture of organic and metallic materials. Differences were also seen in the carbon spectra, with peaks being resolved at 284.88 and 286.27eV suggesting elemental C and C-N. An addition peak was seen in the C 1s spectra for surfaces free from deposit indicating the presence of carbides, likely to be Cr_7C_3.

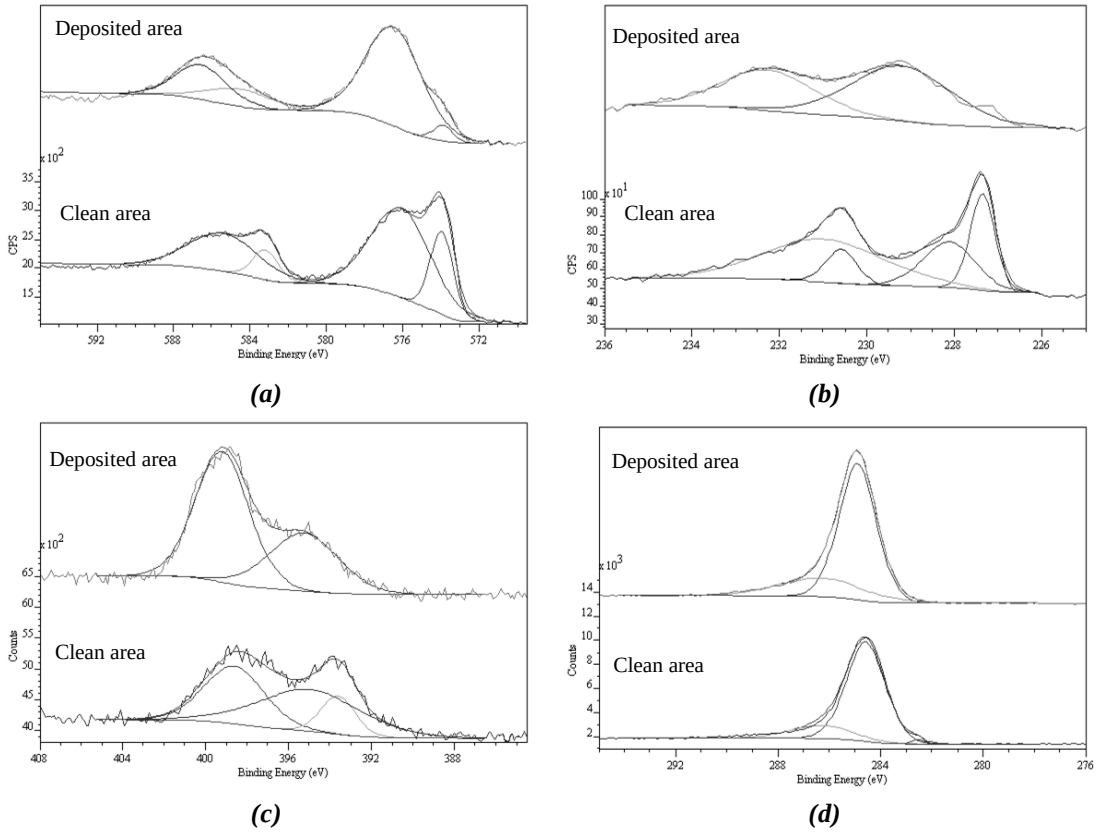

Figure 4-12 - Curve fitted, high resolution XPS spectra obtained for (a) Cr 2p (b) Mo 3d (c) N 1s and (d) C 1s

4.6. Cohort Statistical Analysis

Statistical analysis of the cohort suggested there were there were three significant correlations ($P<0.05$).

1. **Impingement by liner augmentation**. A 10 degree lipped liner had significantly more impingement (P<0.001). This is thought to have no influence on the severity of corrosion as this is purely a mechanical factor resulting from the augmented liner.
2. **Corrosion by gender**: Females had significantly more corrosion (P<0.025). This is a particular interesting correlation as there is no significant correlation between gender and stem. This is not thought to be a population effect as the male to female ratio is 88:90. It is hypothesised that this could be due differences in biology between genders resulting in an increased susceptibility to metallic debris induced reactions or an increased rate of oxidation.
3. **Corrosion by head offset**: +5 offset heads had significantly more 'Moderate' corrosion than the 0 offsets (P< 0.199). This is thought to be due to the increased torsional moment created by the increase in stem neck length. There is no correlation with the maximum head offset (10) versus corrosion damage. This is due to a population constraint as n=1.

There was no significant correlation with time *in-vivo* and corrosion score (P<0.251, R^2=0.018). This is particularly interesting as corrosion is usually thought to be a time dependant response. Collier et al [144] demonstrated a linear relationship between time *in-vivo* and the extent of corrosion for modular taper interfaces. Although on average an increase in the average time in-vivo can be seen with corrosion score this is not thought to be statistically significant (Figure 4-13).

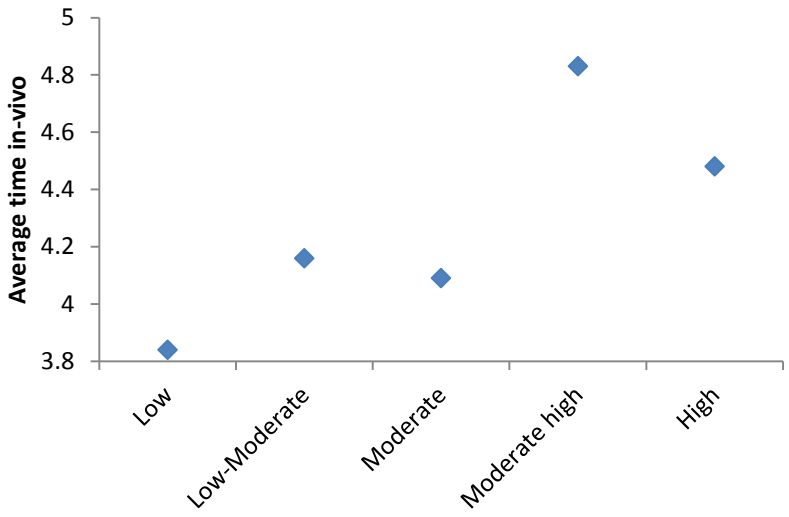

Figure 4-13 - Distribution of corrosion score and time in-vivo

A weak correlation between the corrosion score and the size of the acetabular component was seen (P<0.138). However was not seen to be statistically significant. Observation of the cohort numbers indicated an increased numbers of femoral stems with moderate corrosion with the 48mm acetabular component demonstrating the highest rate of 'moderate' stem corrosion. 50mm acetabular components were seen to account for 29% of the retrieved cohort. However no significant change in the corrosion score distribution was seen with increasing size of acetabular component (Figure 4-14).

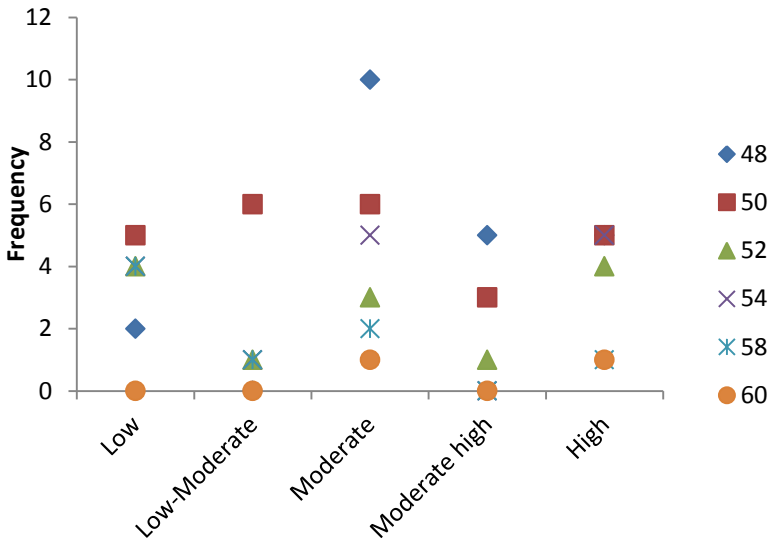

Figure 4-14 - Distribution of Corrosion score vs. Acetabular shell size

No significant correlations where seen for size of femoral stem and corrosion score ($P<0.272$, $R^2=0.015$). This is particularly interesting when compared with the statistically significant result seen for the frequency of corrosion by gender as females tend to be implanted with smaller femoral stems due to their anatomical size. No correlation between the cement type ($P<0.471$) or brand ($P<0.661$) versus corrosion score was seen indicating that cement type or chemistry does not have a significant influence on the extent of fretting-corrosion.

4.7. Discussion and Summary

In this work, a cohort of failed cemented MoM THR has been reviewed and the fretting-corrosion and the tribo-chemical reactions taking place at the stem-cement interface characterised. To date, the occurrence of fretting-corrosion at the stem-cement interface has been extensively reported as a source of wear and PMMA particle debris in clinical studies, being shown to elicit loosening of femoral component and osteolysis. However the exact tribo-chemical and tribological interactions taking place at these interfaces are not well investigated.

This chapter presents the surface morphology of retrieved femoral stems with characteristic signs of fretting-corrosion and evidence of complex tribo-chemical and tribo-corrosion reactions taking place at the stem-cement interfaces. This cohort of implants also demonstrates that the wear debris and the ionic release of species, as a result of mechanically accelerated electrochemical dissolution from this interface, can be a sole contributor to failure of cemented MoM THR. This highlights that the degradation mechanisms at these interfaces are as influential as those at the articulation and taper interfaces [4, 158].

4.7.1. Surface Morphology

All retrieved femoral stems demonstrated signs of fretting-corrosion on the cemented portions of the femoral stem. However closer examination of the retrievals demonstrated that, in fact, there were two complex degradation mechanisms taking place on the surface of the femoral stem. Fretting-corrosion was seen to occur in the proximal regions of the cemented stem where debonding and gross slip between the interfaces occurs. A crevice corrosion phenomena was seen towards the distal regions of the femoral stem due an oxygen gradient been established resulting in extensive localised corrosion of the metallic surface. Fretting-corrosion has been observed in a number of clinical cases on both polished and matte femoral stems [159-162]. Interest into the interaction existing at the stem-cement interfaces has been renewed due to the cases presented by Donell et al and Bolland et al [4, 5]. Recent case studies have demonstrated that the stem-cement interface can drastically influence the longevity of THR, with the stem-cement interface being linked with high levels of metal ion release resulting in extensive soft tissue necrosis. Howell et al [163] presented a comprehensive study, conducting SEM and 3-D interferometry analysis on both

retrieved polished and matte femoral stems, identifying that polished and matte femoral stems present two very different wear mechanisms. Polished stems were seen to exhibit signs of ductile wear accompanied by pitting of the surface, a similar morphology observed in this cohort, whilst matte stems presented evidence of abrasive or truncation wear [163]. From the evidence presented in this chapter it is thought an abrasive wear mechanism exists at the stem-cement interface. This is due to the formation and transfer of a Cr_2O_3 particulate film. Subsequently a hardness differential between the femoral stem (5-10GPa) and Cr_2O_3 film (14-30GPa) will be established, resulting in abrasion of the femoral stem and depassivation of the surface. From these findings, surface roughness is thought to contribute to the type and levels of slip found at the interface as well as the magnitude of load necessary to overcome the initial shear force needed to initiate sliding. Although the wear mechanism was seen to differ with different surface finishes the location of wear, typically in the anterolateral and posteromedial aspects of the stem, was unaffected suggesting that the torsional loading is the prominent factor.

4.7.2. Surface Chemistry

The importance of tribo-chemistry in orthopaedics was first recognised by Wimmer [24], who highlighted the role proteins play at the bearing interfaces. Although the majority of studies to date demonstrate and characterise the complex tribo-chemical reactions taking place at the articulation surface, this study is one of a few to utilise advanced surface microscopy and surface chemistry analytical techniques in order to understand the tribo-corrosion and tribo-chemical interactions at the stem-cement interface.

A study by Walczak et al [164] observed the surface chemistry and surface

morphology of deposits found on Charnley and Müller prosthesis and also retrieved PMMA bone cement. They proposed that a multilayer film existed on the surface with different elemental chemistry. An initial Cr-rich layer was seen on the surface of the sample, accompanied by an Fe-rich plaque and a third chloride/sulphur plaque; however provided no cross-sectional evidence to support this. They also observed that the debris found on the surface of the retrieved PMMA bone cement had a similar chemical composition to the deposits found on the retrieved femoral components.

The formation of fretting-corrosion product and the implication this has on the surrounding environment has also been considered. TEM imagery demonstrated the formation of a thick Cr_2O_3 rich film which could be seen on the CoCrMo femoral stem and counterpart PMMA bone cement. This supports the findings and hypothesis presented by Hart et al [146] who demonstrated that retrieved tissues from the Norwich cohort were Co rich whilst Cr and Mo were not observed. High levels of Co can be explained by the thermodynamic stability of the species. Thermodynamics can be used to evaluate the theoretical activity of a given metal or alloy in a known corrosion environment [78]. It is thought that Cr is favoured as the species to undergo reaction due to the lower activation energy required for oxidation resulting in the formation of thick layers of Cr_2O_3 corrosion product on the metallic femoral stem and counterpart bone cement. This leaves the cobalt, presumably Co^{2+}, known to be extremely soluble at the electrode potential and pH found at the interface, to migrate and leave the interface due to an electrical potential being established due to the separation of anodic and cathodic areas due to fretting-crevice corrosion being established at the interface, explaining the high cobalt levels observed in this study and Hart *et al* [165].

Films formed at the articulation surfaces have been demonstrated to influence tribo-corrosion regimes by reducing the corrosion and wear rates due to the formation of a protective organic layer [25, 166]. Reports investigating films formed on retrieved bearing surfaces have identified subtly different changes in film chemistry with respect to the thickness of the film. Milošev [112] identified that thick deposits were commonly due to denatured proteins, being predominantly C, N and O rich whilst thinner films were often a complex mix of organic material, metal oxides and hydroxides, a similar composition to the deposits observed in this study. A recent study by Liao *et al* [23] further suggested that such films formed at the articulation may be graphitic due to the shear stresses and pressures experienced *in-vivo* contributing to the decrease in friction and wear-enhanced corrosion reported by some authors [14, 23, 24, 25, 66]. This further supports the Harts' hypothesis and demonstrates that the degradation mechanism and electrochemical reactivity of species released at an interface can drastically influence the morphology and chemistry of metallic debris released into the biological environment.

Although this study has demonstrated a surface deposit present on the surface of the samples; TEM/EDX analysis did not demonstrate a multi-layered deposit which has been reported by some authors. A film consisting of Cr_2O_3 crystallites, seemingly compressed and bound together by an amorphous organic material existed on the surface of the CoCrMo femoral stems. Diffraction patterns of the debris on the surface of the CoCrMo femoral stems demonstrated a hexagonal close packed arrangement with a d-spacing associated with Cr_2O_3.

4.8. Summary

Advanced surface microscopy techniques combined with chemical analysis have been used to identify the surface morphology and composition of retrieved femoral components revised due to high levels of fretting-corrosion. Distinct directionality and plastic deformation of the metallic surfaces was seen, characteristic of fretting-crevice corrosion demonstrating that complex fretting, electrochemical and tribochemical reactions exist at the stem-cement interfaces. The formation of thick deposited layers was also seen to occur within these interfaces, with films being seen to consist of Cr_2O_3 bound with organic materials. This study has also highlighted that fretting-corrosion at the stem-cement interface can contribute to high levels of metal ions, resulting in extensive soft tissue necrosis with the associated tribo-corrosion and tribo-chemical mechanism proposed.

CHAPTER 5 – METALLURGY, SURFACE CHEMISTRY AND CORROSION BEHAVIOUR OF COMMONLY USED BIOMEDICAL ALLOYS

5.1. Introduction

The biological environment is a harsh chloride containing environment in which metallic alloys are expected to undergo years of fatigue and also corrosion. In order to increase the longevity of metallic implants, in particularly at the stem-cement interfaces, a variety of surface finishing processes are employed, such as polishing using a mop wheel and wax or an aqueous glass bead blast.

This chapter aims to explore the fundamental metallurgy, crystallography and corrosion behaviour of commonly-used biomedical alloys. In this chapter the microstructure, micro hardness, surface chemistry and crystalline structure of LC CoCrMo was studied. SEM/EDX, XPS and XRD techniques were employed as a method of quantifying surface chemistry and crystalline structure of the alloys. Micro and nano hardness measurements were also conducted in order to access how each surface processing technique affects the hardness of the metallic substrate. Potentiodynamic polarisation was further adopted in order to investigate the corrosion behaviour of the processed alloy.

5.2. Microstructure Analysis

In order to observe the microstructure of the alloys tested in this study samples were sectioned, mounted in epoxy resin and ground with 3µm diamond paste. LC CoCrMo samples were electrochemically etched using 10g ammonium persulphate in 100mL H_2O. Samples were immersed in the etchant at 21°C and held at 5V for

45seconds. The revealed microstructure was then observed under an optical microscope.

Figure 5-1 depicts the microstructure for the wrought LC CoCrMo bar. SE SEM analysis of the microstructure demonstrated a fine, single phase, equiaxed austenitic grain structure in the absence of any annealing twins. A similar microstructure was seen in both the polished and roughened samples. There was no visible indication of the formation of martensitic needles due to any strain induced transformation that may occur as a result of the mechanical pre-treatments. No annealing twinned grains or carbides were observed for the low carbon CoCrMo alloys.

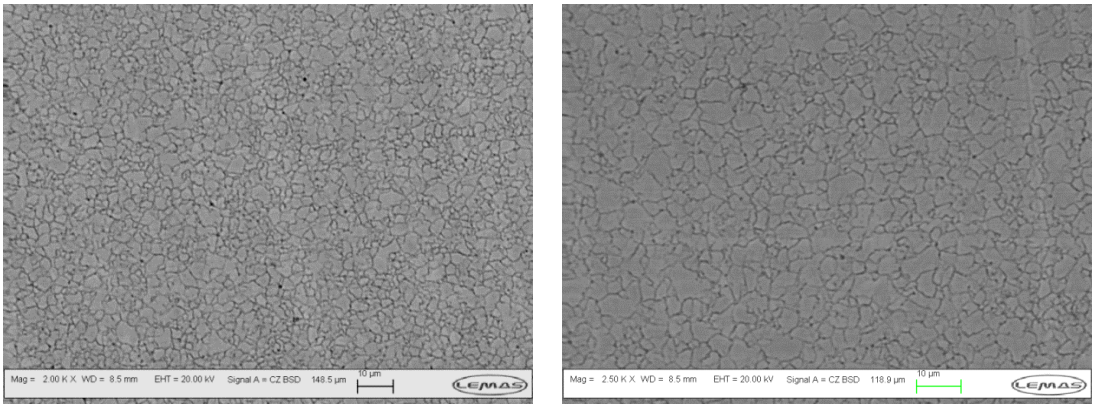

(a) ***(b)***

Figure 5-1 – SE microstructure images of wrought (a) polished (b) roughened LC CoCrMo

A slightly different microstructure was observed for the LC CoCrMo Ultima TPS (Figure 5-2) stems that had undergone the forging process. A slightly larger single phase, austenitic grain structure was observed when compared to the wrought alloy. Optical examination of this microstructure demonstrated that no visible carbides or annealing twins were present after the forging processing.

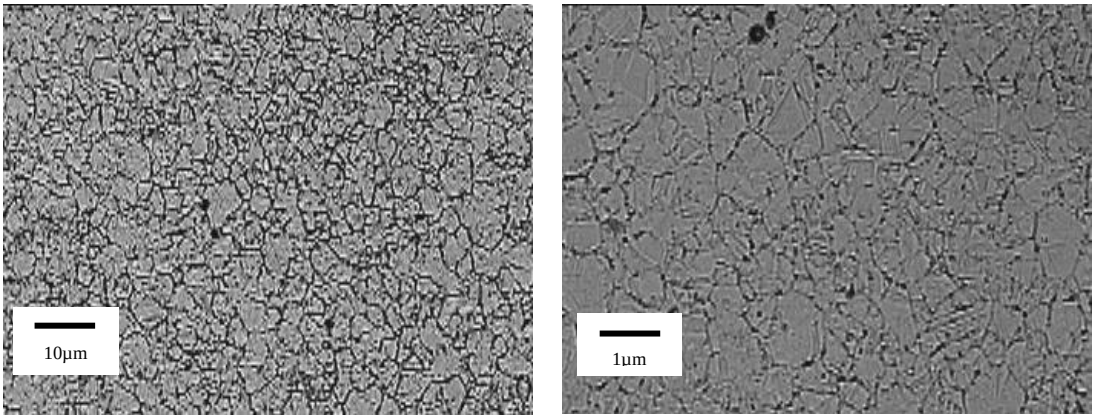

(a) ***(b)***

Figure 5-2 - Microstructure of forged Ultima TPS (a) polished (b) roughened LC CoCrMo

5.2.1. SEM/EDX analysis

Although no visible carbides were seen in the microstructure micrographs, BSE SEM/EDX analysis demonstrated the formation and distribution of carbon rich areas in the polished LC CoCrMo samples. XPS analysis (presented later in this chapter) also demonstrated fairly dominant carbide peaks in the wrought and forged polished samples. BSE SEM imaging (Figure 5-3) revealed dark areas randomly distributed on the surface of the polished LC CoCrMo alloy. These were seen to vary in size from approximately 1-20µm.

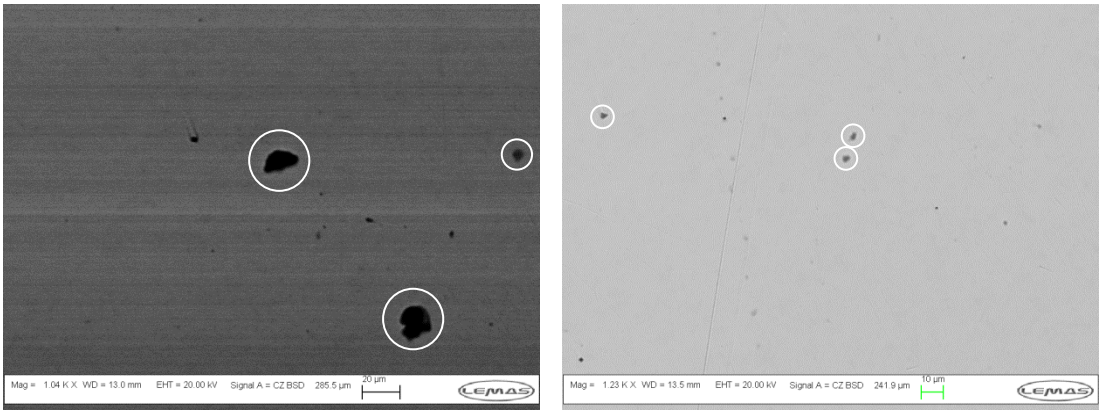

(a) ***(b)***

Figure 5-3 - Backscattered image demonstrating areas of different density on the surface of LC CoCrMo. White circles demonstrate large carbon rich areas

5.3. Hardness of Alloys

As CoCrMo alloys are commonly used in tribological applications, partly due to their hardness, hardness tests were conducted to investigate the role surface pre-treatment has on the micro and nano hardness of forged and wrought LC CoCrMo. Figure 5-4 demonstrates the micro and nano-hardness values obtained for each alloy.

Microhardness results demonstrated differences between the wrought and forged surfaces with an increase in micro hardness being observed with increasing surface roughness. Nano-hardness measurements, within the 600-700nm, indicated an increase in hardness for the forged alloys when compared to micro hardness measurements. This was seen to increase from 5.07-7.74 and 5.70-7.10GPa for the polished and roughened surfaces respectively. This is an important parameter that needs to be considered when subjecting a material to tribological conditions as hardness can drastically influence the wear rates and mechanisms. A hardness difference is thought to exist within the few nanometres of the surface due to a strain induced transformation layer. This is seen to obey the Hall-Petch relationship which describes the inverse relationship between the yield strength of an alloy and the crystal size [64].

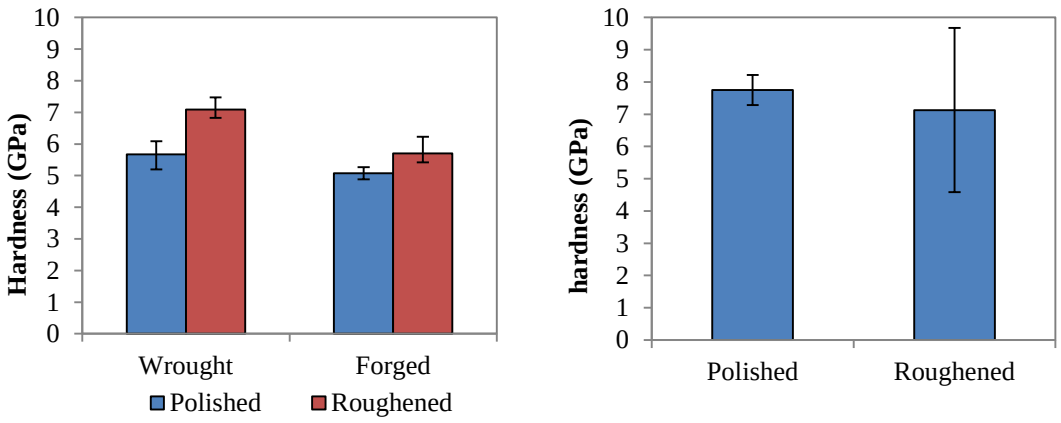

Figure 5-4 – a) Micro hardness of wrought and forged LC CoCrMo and b) Nano-hardness of forged LC CoCrMo when subjected to mechanical pre-treatment (n=10±SD)

5.4. Crystalline Structure of Biomedical Alloys

5.4.1. X-Ray Diffraction Analysis

The crystalline structure of materials was characterised by X-ray diffraction on both wrought and forged samples that had undergone surface pre-treatment. 2θ scans between 40° and 50°were carried out using Cu Kα radiation. The scan range selected enabled the unambiguous determination of the coexistence of the FCC and HCP cobalt phases; within this region the strong $(200)^{FCC}$ and the $(10\bar{1}1)^{HCP}$ are well isolated and do not overlap with any other diffraction peak [157].

Figure 5-5 demonstrates the effects of surface pre-treatment on the X-ray diffraction patterns of LC CoCrMo. It can be seen that a certain amount of HCP exists within the lattice of the metal in its wrought state. However XRD diffraction patterns of the wrought polished LC CoCrMo showed evidence of further transformation from FCC(metastable)→HCP had occurred with mechanical pre-treatment, with the effect been most prominent in samples that had been subjected to an aqueous glass bead blast. A loss of the $(200)^{FCC}$ and gain of a $(10\bar{1}0)^{HCP}$ peak was also seen samples that underwent the aqueous glass bead blast process suggesting increase in micro strain found in the metallic substrate and a preferential orientation of the crystalline structure of the vaquasheened LC CoCrMo.

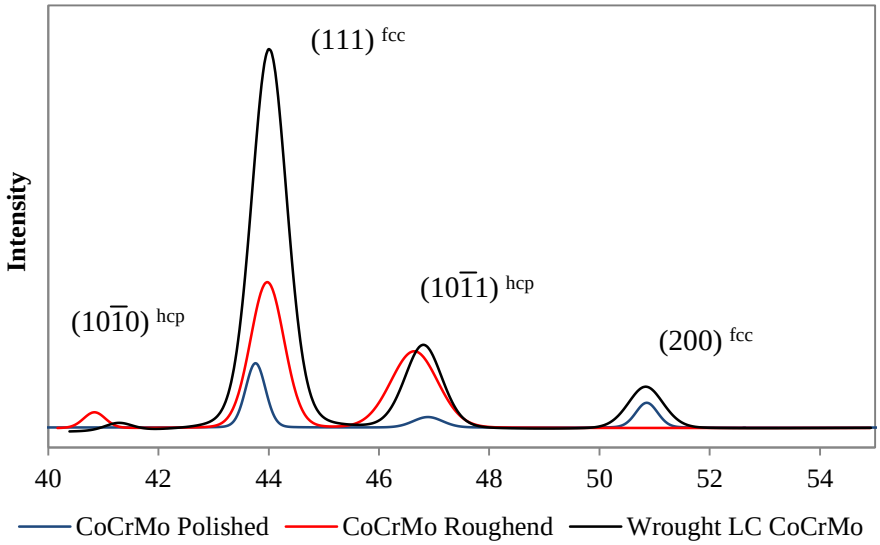

Figure 5-5 - Effect of surface pre-treatment on the X-ray diffraction patterns of wrought LC CoCrMo

XRD diffraction patterns of the forged LC CoCrMo (Figure 5-6) demonstrated evidence of FCC(metastable)→HCP. However a different effect on the crystalline structure was seen compared to the wrought alloys. In both cases, $(111)^{FCC}$ and $(200)^{FCC}$, $(10\bar{1}0)^{HCP}$ and $(10\bar{1}1)^{HCP}$ were observed. However the relative ratios of $(200)^{FCC}$:$(10\bar{1}1)^{HCP}$ were seen to decrease suggesting an increased amount of micro strain been seen in the metallic surface resulting from plastic deformation caused by the aqueous bead blasting process. A broadening of all diffraction peaks was also seen and is thought to be due to the finer crystallite size and inhomogeneous strain of the surface after processing. It is worth noting that all roughened femoral stems tested in this study have been subjected to the same mop polishing process and then aqueous glass bead blasting process.

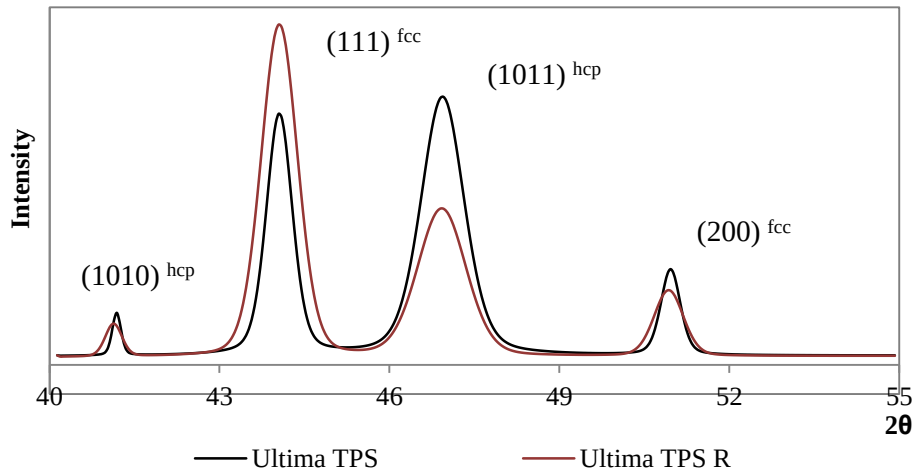

Figure 5-6 - Effect of surface pre-treatment on the X-ray diffraction patterns of forged LC CoCrMo

The penetration depth of the X-rays used in the XRD technique was also estimated using Bragg's law of diffraction (Figure 5-7). The penetration of X-rays is dependent on the incident angle at which they hit the surface. It can be from Figure 5-7 that 99% of X-rays can penetrate the surface up to 7.84μm.

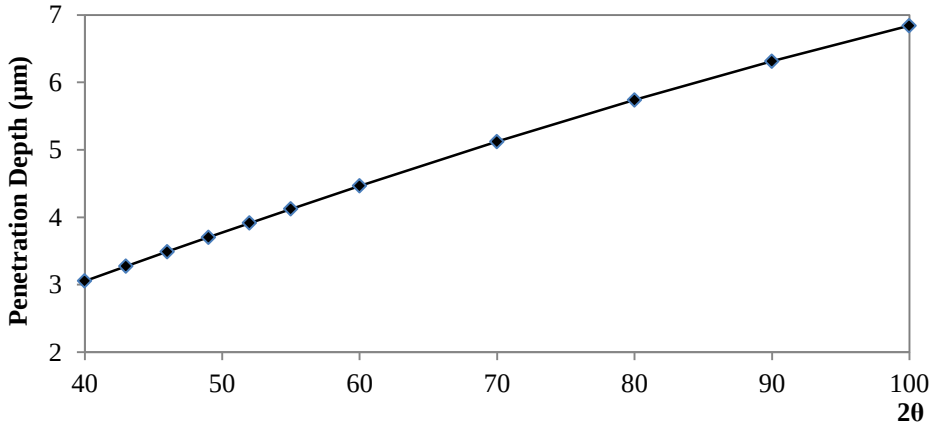

Figure 5-7 - Penetration depth of X-rays used in XRD

5.4.2. Transmission Electron Microscopy (TEM) Analysis

TEM was also used in order assess the influence of surface pre-treatment on the crystalline structure of forged LC CoCrMo. Figure 5-8a demonstrates the light field image of the Pt-CoCrMo interface and bulk alloy with the associated areas in which diffraction analysis was conducted. Some re-crystallisation of the material had occurred within the top 200nm of the alloy, with crystals appearing to be finer. Figure 5-8b demonstrates dark-field image at the Pt-CoCrMo interface. In dark field imaging, only the light scattered by crystals orientated to satisfy Bragg conditions for diffraction are observed. This offers a difference in contrast which will help differentiate nano-crystalline structures. The crystals orientated to give Bragg diffraction in the nano-crystalline layer are usually characterised by finer and brighter spots of light whilst single crystal structures are usually characterised by uniform bright patches.

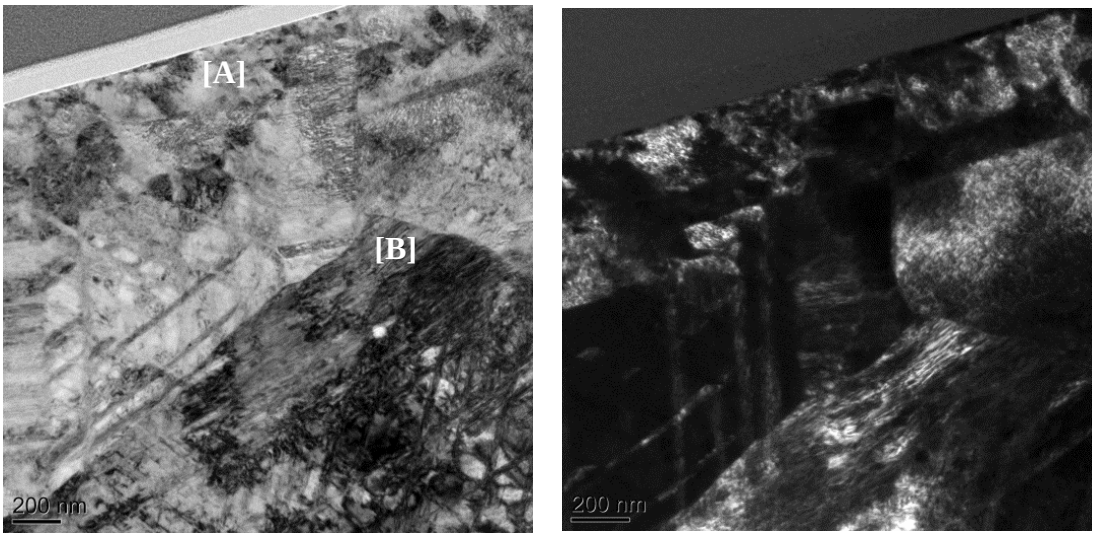

(a) **(b)**

Figure 5-8 - a) Light field and b) dark field TEM imaging of virgin polished CoCrMo surfaces

For added clarity Selected Area Electron Diffraction (SAED) patterns were examined at different subsurface locations (Figure 5-9) The diffraction patterns that where observed in the upper most regions of the surface further supported the images in Figure 5-8, demonstrating a fine nano-crystalline layer typically characterised by the ringed diffraction pattern presented in Figure 5-9a. Indexing of this diffraction pattern demonstrated a d-spacing characteristic of ε-cobalt demonstrating a hexagonal packing structure. The diffraction pattern presented in Figure 5-9b suggests a single crystal with a diameter greater in length than the 300nm microscope aperture. This was indexed against a cubic structure.

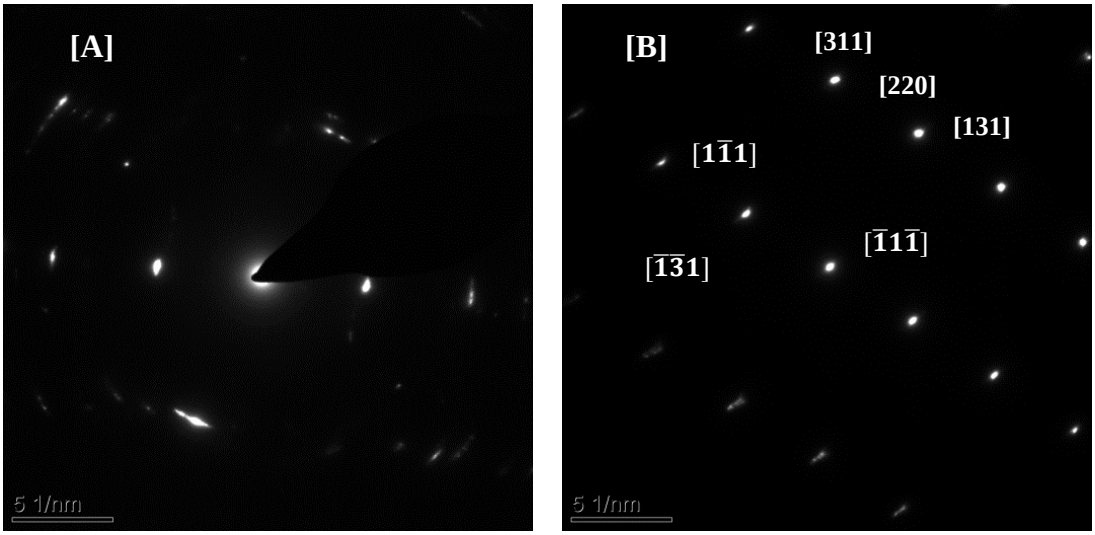

(a) **(b)**

Figure 5-9 - SAED Patterns taken from region a) [A] and b) [B]

Figure 5-10a-b demonstrates the light and dark-field images obtained for the roughened femoral stems. Again, re-crystallisation of the top 200-250nm was seen, with darkfield imaging indicating finer crystallites within the transformed region. SAED patterns further demonstrated an increased amount of crystallites within the transformed layer, with the diffraction pattern again being indexed as ε-Co. A single crystal structure was seen within the bulk alloy. A more complete diffraction ring

(Figure 5-10b) was seen for the vaquasheened surfaces compared to the polished samples. This supports the dark field images, showing that the nano-crystalline layer on the roughened sample contained crystallites of a smaller average diameter.

It is interesting to note the presence of a thick (≈100nm) amorphous film on the surfaces of the roughened samples. To our knowledge this is the first time this has been reported. Point EDX analysis (Figure 5-11) demonstrated this film to rich in Si and O. Traces of Cr, Co and Ca were also observed.

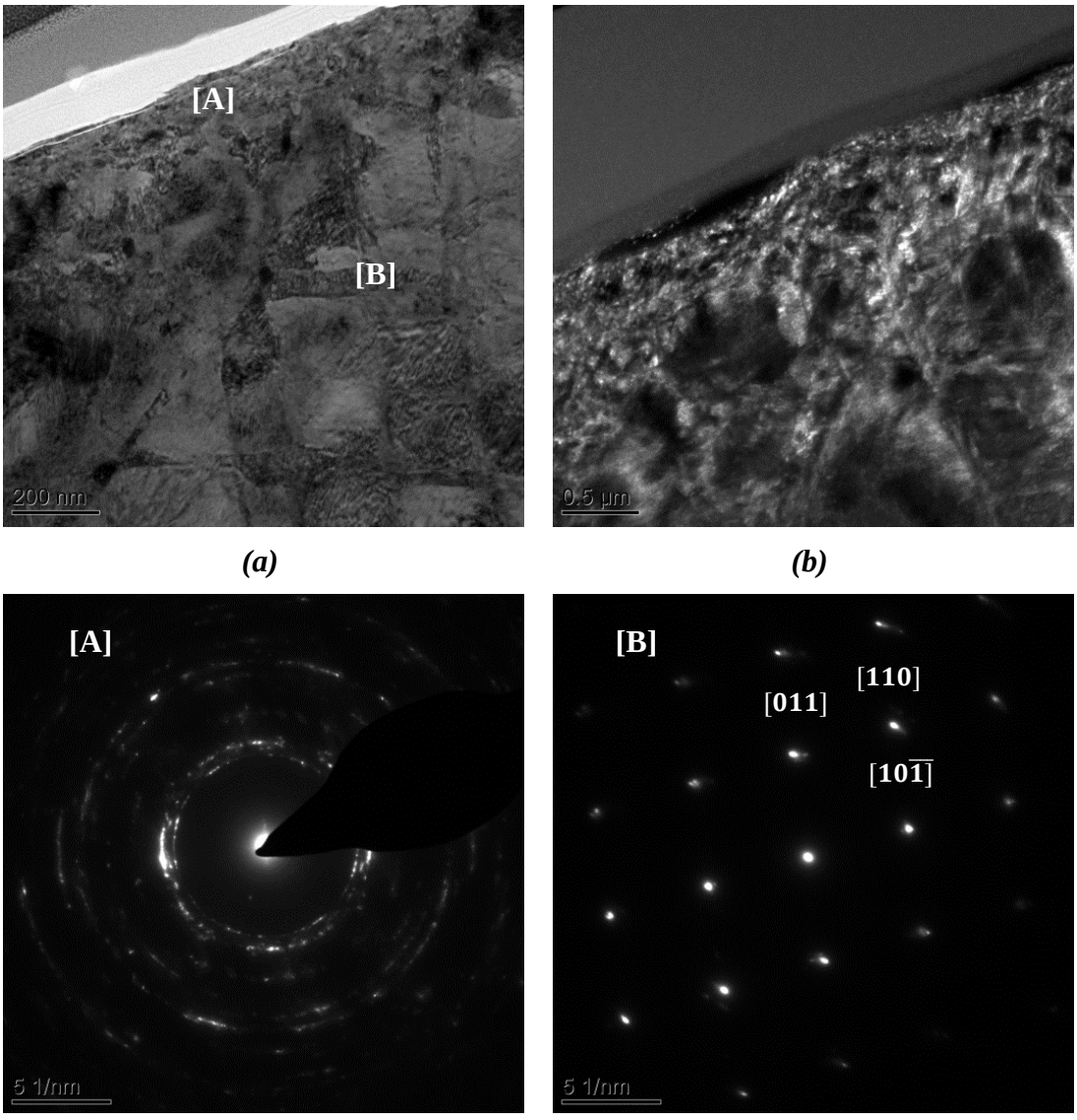

(a) *(b)*

(c) *(d)*

Figure 5-10 - a) Light field and b) dark field imaging of virgin roughened CoCrMo surfaces and (c-d) diffraction pattern analysis of the different crystalline areas

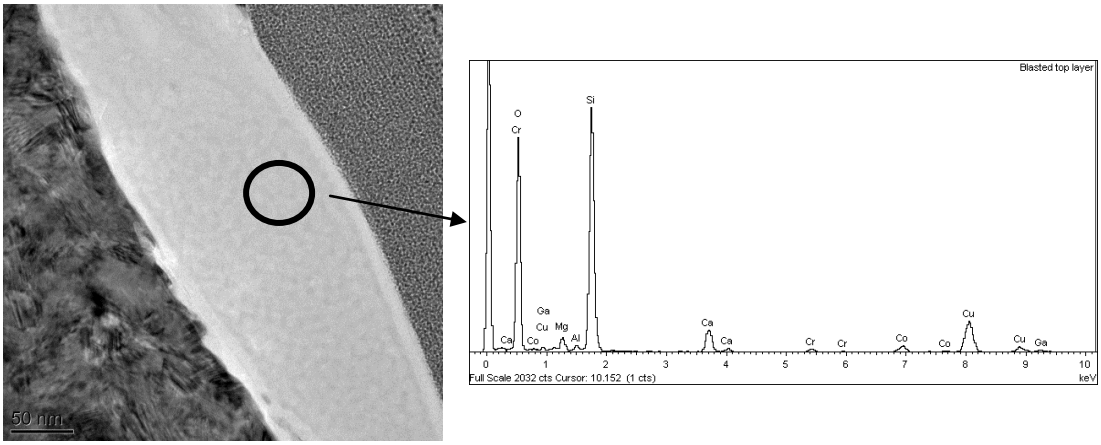

Figure 5-11 - TEM imagery and EDX analysis of the 100nm Si rich film formed on the surface of the vaquasheened femoral stems

5.5. Surface chemistry of biomedical alloys

A variety of surface chemistry techniques were utilised as a method of quantifying the surface chemistry of the alloys tested in this study. The effects of surface pre-treatment were examined on both wrought and forged alloys that had undergone the polishing and aqueous glass bead blast process.

5.5.1. X-ray Photoelectron Spectroscopy (XPS) analysis

XPS was utilised as a method of quantifying the surface chemistry of the alloys tested in this study. Although X-rays penetrate to a depth of several micrometres, ejected photoelectrons generally come from only the first several nanometres of material making the analysis of the passive film and bulk substrate possible. In order to assess the influence surface pre-treatment has on the passivity of CoCrMo alloys each samples was subjected to an argon-ion bombardment in order to displace the first few nanometres of material. A 22 second argon-ion at 1μA/3mm^2 was utilised to achieve an approximate stepped etch depth of 0.5nm. Licensed CasaXPS software was used to fit the curves. All the results in this thesis use the standard format and units (CPS versus BE).

5.5.2. Wrought LC CoCrMo Alloy

Figure 5-12 demonstrates the obtained spectra for the LC CoCrMo samples with associated curves fitted. XPS indicated a similar chemical state for Co in both the polished and roughened samples; however an increased amount of CPS was seen for the polished samples. Peaks at binding energies of 777.98, 779.01, 781.20 and 785.10eV were observed suggesting the presence of metallic Co, $CoO+Co_3O_4/Co_3O_4$ and a Co^{2+} satellite respectively [109, 114, 167]. A similar result was seen for the chromium surveys. Peaks were observed at 574.93, 584.01, 577.01, 586.05eV suggesting the presence of elemental Cr and Cr_2O_3 [109, 167, 168].

Interestingly, different oxygen and carbon spectra were seen for the polished and roughened samples. Elemental oxygen (O 1s) peaks were observed around 529.25 and 532.22eV for both polished and blasted surfaces suggesting the presence of metal oxides and H_2O respectively. An addition peak at 535.37eV was seen on the blasted surfaces suggesting the presence of $C\text{-}O/SiO_2$ [107].

Elemental C was observed in both samples at 284.25 and 284.39eV whilst a prominent carbide (Cr_7C_3) peak at 283.25eV was evident on the polished surfaces. Traces of Si 2s were seen in samples with an increased surface roughness, a result of the aqueous glass bead blast process.

Polished **Roughened**

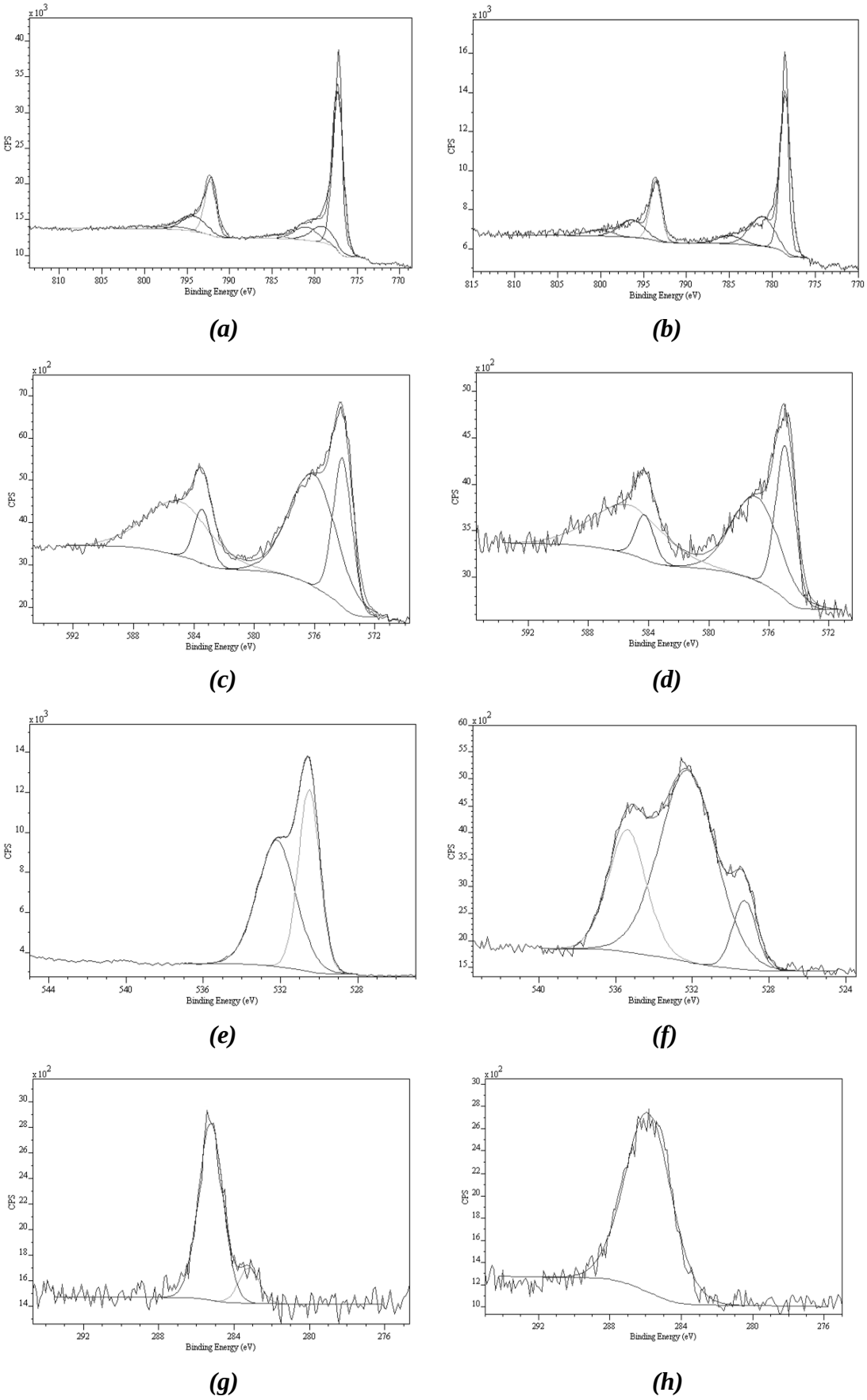

Figure 5-12 - X-ray photon spectroscopy spectra for polished and roughened samples (a-b) Co 2p3/2 (c-d) Cr 2p3/2 (e-f) O 1s (g-h) C 1s. All spectra's were taken at an etch depth of 5nm and the curve fitted

5.5.3. Forged LC CoCrMo Alloys

A similar observation was seen in the forged LC CoCrMo femoral stems (Figure 5-13). A prominent carbide peak was consistently seen on the polished Ultima TPS femoral stems. Carbon was not seen to be as abundant on the roughened surface when compared to the other samples. XPS analysis indicated that the composition of the oxide film was comparable to the wrought LC CoCrMo samples.

Polished ***Roughened***

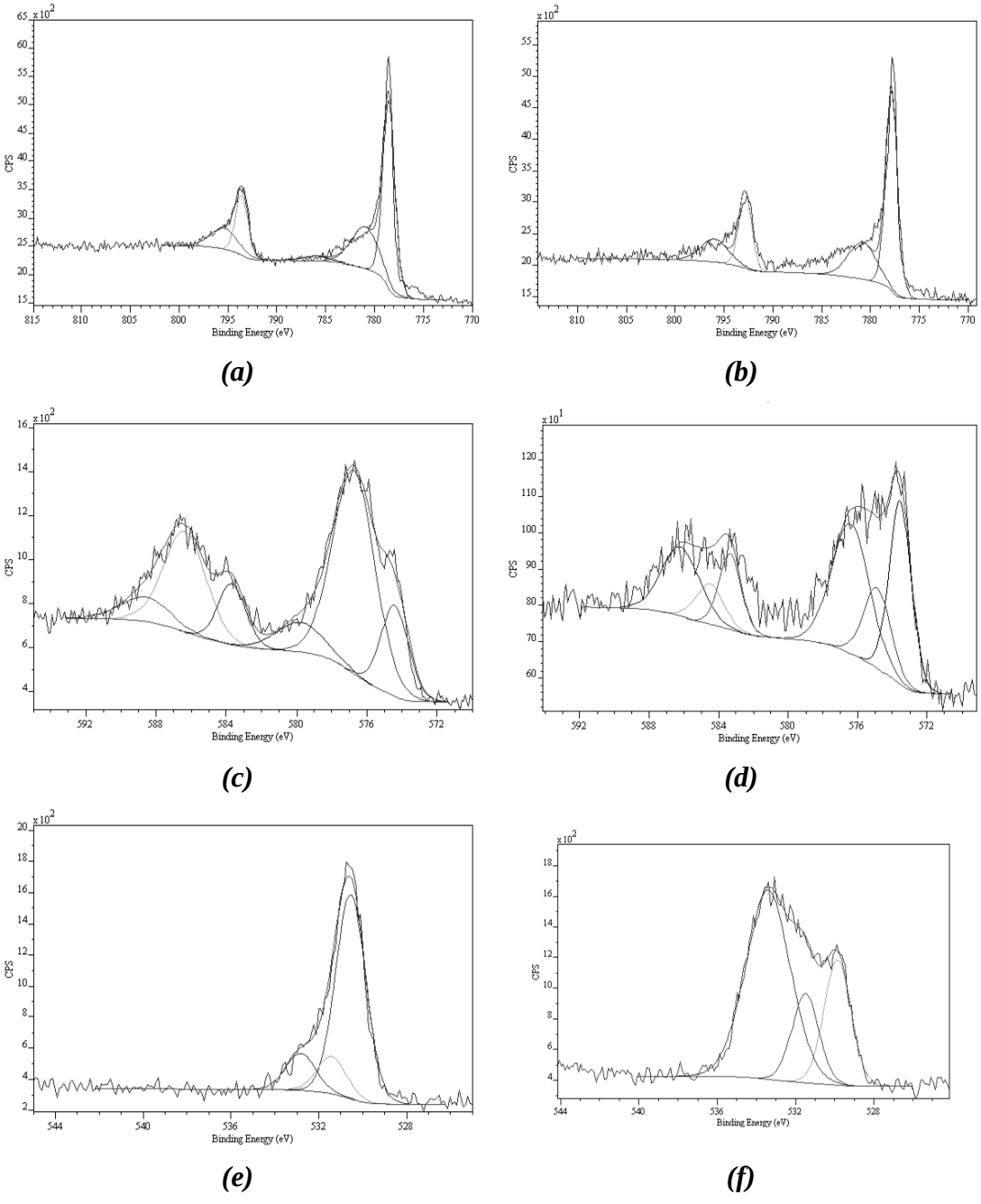

(a) ***(b)***

(c) ***(d)***

(e) ***(f)***

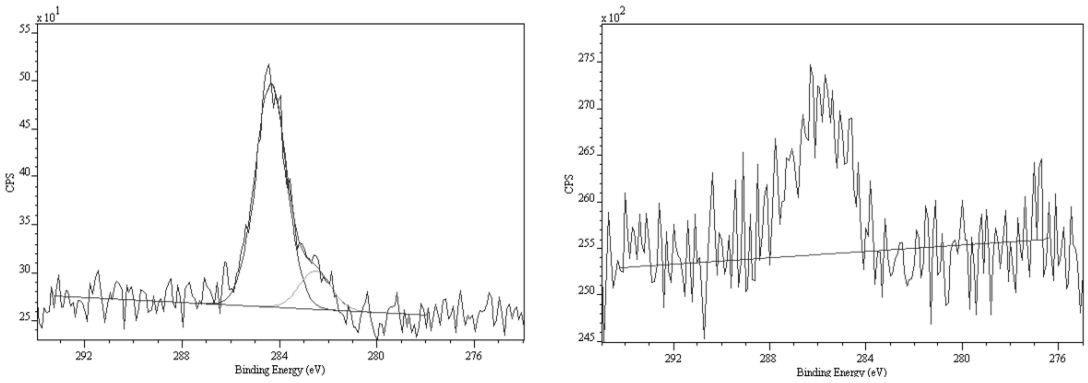

(g) *(h)*

Figure 5-13 - X-ray photon spectroscopy spectra for polished and roughened Ultima TPS femoral stems (a-b) Co 2p3/2 (c-d) Cr 2p3/2 (e-f) O 1s (g-h) C 1s. All spectra's were taken at an etch depth of 5nm and the curve fitted

Si was also seen on all surfaces of the roughened samples further supporting the TEM results (Figure 5-14). Resolution of the Si 2s spectra demonstrated a peaks at 154.01 and 153.50eV for the forged and wrought alloy respectively, suggesting the presence of SiO_2 on the surfaces of the roughened alloy.

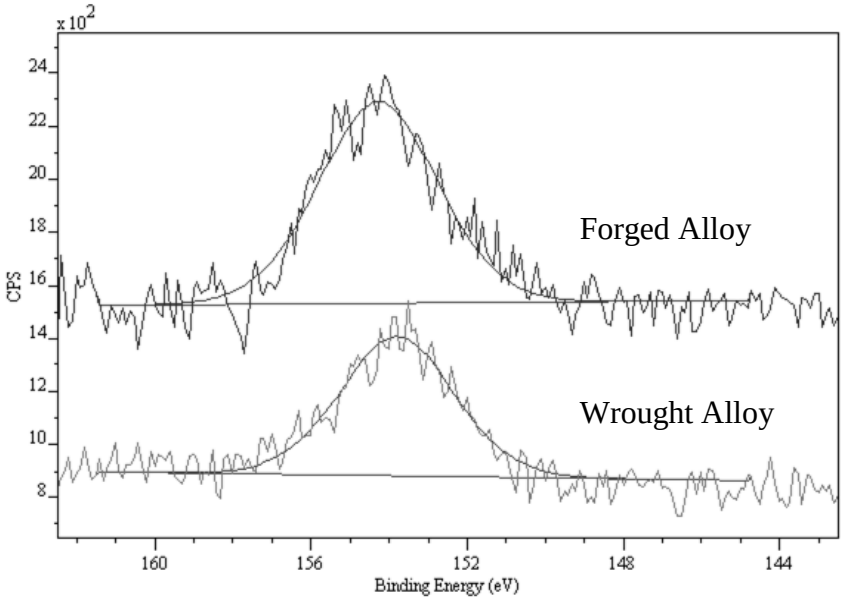

Figure 5-14 - Resolution of the Si 2s curves seen on vaquasheened surfaces

5.6. Corrosion Behaviour of CoCrMo Alloys

Potentiodynamic polarization scans were also conducted on the polished and vaquasheened surfaces. Figure 5-15 demonstrates the typical polarization curves obtained. Upon immersion, the E_{corr} of roughened surfaces was seen to be more noble than the polished samples. After 1hr immersion E_{corr} had settled to $0.06V_{Ag/AgCl}$ and $-0.20V_{Ag/AgCl}$ for roughened and polished samples respectively. Polarization scans were started -100mV vs. E_{corr} to ensure the Tafel region was captured. Roughened samples also demonstrated a lower passive current (I_p = $0.04\mu A/cm^2$) compared to polished surfaces (I_p = $2.86\mu A/cm^2$). According to Pourbaix [169], at an electrode potential of $0.18V_{Ag/AgCl}$ ($0.01V_{SHE}$) and pH of 7.4, the formation of a Cr_2O_3 will occur protecting the metallic surface from further oxidation [79]. Breakdown of the protective oxide film and initiation of localised corrosion was seen to occur at $0.68V_{Ag/AgCl}$ and $0.76V_{Ag/AgCl}$ for polished and roughened surface respectively. This again demonstrates that the surface subjected to vaquasheeing has an increased integrity with respect to the initiation of localised corrosion.

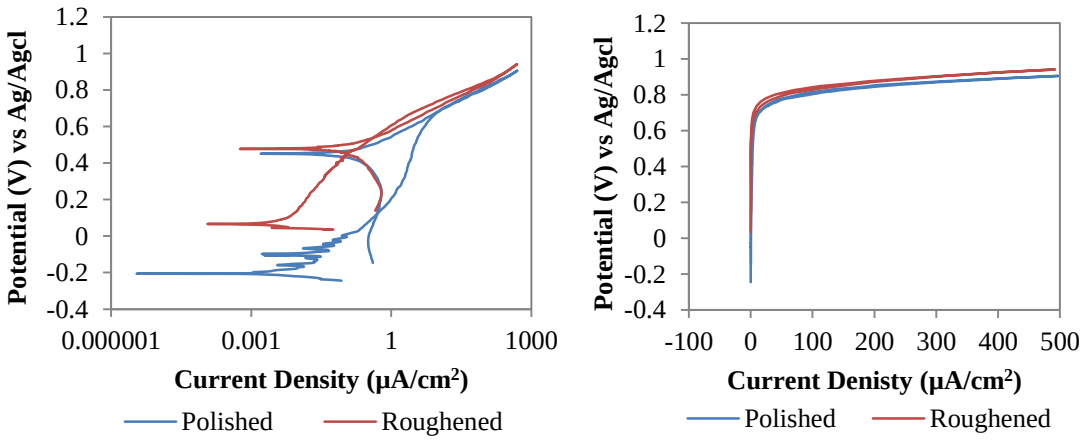

(a) ***(b)***

Figure 5-15 – Typical a) E vs. Log(i) and b) E vs. i Potentiodynamic curves of Polished and Vaquasheened LC CoCrMo Surfaces

Table 5-1 demonstrates the total charge density transferred during potentiodynamic tests. This parameter was observed, along with the repassivation potentials (E_r) in order to understand the materials' ability to repassivate once localised corrosion had been initiated. Polished surfaces were seen to repassivate at E_r =0.67V, whilst vaquasheened surfaces spontaneously repassivate at 0.53V. This demonstrates that although polished surfaces are more susceptible to corrosion, once initiated, the surface possesses the ability to reform the passive oxide film reducing dissolution of the metal/alloy surface.

Table 5-1 – Average total charge transfer during potentiodynamic tests (n=2)

Surface	Charge Transfer (Coul/Cm^2)	Mass Loss (mg)
Polished	0.064	0.131
Roughened	0.068	0.139

5.7. Discussion

It has been demonstrated that surface pre-treatment can have a drastic influence of the interfacial chemistry, crystalline structure and corrosion behaviour of CoCrMo alloys. XPS and SEM/EDX analysis demonstrated that mechanical pre-treatment can affect the chemistry of both the passive film and bulk material of LC CoCrMo. Although increased concentrations of some elemental species was seen for the polished samples, different metallic species and bonds were also observed for the polished and roughened samples. Most interestingly of all is the gain of the Cr_7C_3 carbide peak in the polished samples. The loss of carbides could be beneficial when considering the application of alloys in an environment susceptible to localised corrosion. There are multiple explanations why the chemistry of the alloy may change with surface processes. One explanation with respect to the differences in chemical structure is a result of segregation and diffusion of chemical species during the cooling stages of the mechanical pre-treatment. This may account for the

increase of carbon and carbide being seen in the polished samples due to the locally high temperatures experienced at the interfaces during the polishing process. At high temperatures, austenitic alloys precipitate chromium carbides along grain boundaries via a diffusion process. The chromium used to form the carbide compound is removed from the metal surrounding the grain boundaries, increasing the metal's vulnerability to inter-granular corrosion in its FCC form. Although it is generally thought that low carbon metals do not suffer from carbide precipitation due to the low carbon content, this study has demonstrated the presence of carbides and carbon rich areas in the LC CoCrMo matrix, leaving areas on the metal surface susceptible to inter-granular corrosion attack [170].

The effects of strain induced transformation (SIT), induced during the drawing process of the alloy and plastic deformation is also a factor that needs to be considered when fully understanding how such pre-treatment’s affect the corrosion mechanisms of alloys. *In-vivo* and *in-vitro* studies have indentified and demonstrated different tribological characteristics and depleted areas of some elemental species within the alloy as a result of mechanically induced phase transformation [65, 67, 147]. Although CoCrMo alloys are termed austenitic, a phase change from FCC to HCP due to such mechanical actions is quite credible in these alloys [157, 171]. XRD analysis of the wrought surface demonstrates the presence of both FCC and HCP phases in the absence of any surface processing. This is due to the drawing process resulting in some retention of stress in the lattice due to slip between lattices and twinning [64]. The mechanism for formation of HCP and localised re-crystallisation top 250nm of the surface is due to a shear induced transformation of the lattice, induced by blasting and polishing processing [64]. Shear transformations often result in the formation of a new lattice, resulting in a new crystallographic phase and phase interface. SIT is not thought to be the primary

mechanisms affecting the local chemistry (formation of carbides) of the metal as there is no diffusion processes involved. Micro hardness tests demonstrated differences between the polished and vaquasheened surfaces. An increase in hardness was seen for the roughened samples. Although no difference within standard deviation in hardness was seen between the two surface processing techniques on the nano scale, an increase in nano-hardness (depth of indentation=600-700nm) was seen when compared to micro-hardness measurements. An increase from 5.07 to 7.74GPa and 5.7 to 7.12GPa was seen for polished and roughened surfaces respectively. This is thought to be due to the localised shear transformation of the metallic lattice.

The surface processing procedure was also seen to influence the corrosion behaviour of LC CoCrMo. Vaquasheeing was seen to increase the materials' resistance to the initiation of localised corrosion; however once corrosion was initiated, the vaquasheened surfaces did not have the same ability to spontaneously repassivate. XPS and TEM analysis demonstrated a complex film comprising of SiO_2, Cr_2O_3 along with traces of elemental Co and Cr. It is thought that this film will result in improved corrosion characteristics, by acting as a charge transfer barrier to localised corrosion. Figure 5-16 schematically demonstrates the breakdown and repassivation processes of the protective Cr_2O_3 oxide layer when subjected to different surface processing techniques. It is thought that when breakdown and repassivation of the SiO_2 and Cr_2O_3 films occur, reformation of the SiO_2 will not occur resulting in a partial repassivation of the surface. An increase in localised corrosion is thought to occur on the roughened surface due to the formation of corrosion pits capable of sustaining dissolution within the asperities on the sample surface. Partial breakdown of the SiO_2 film may also lead to geometries capable of sustaining localised corrosion.

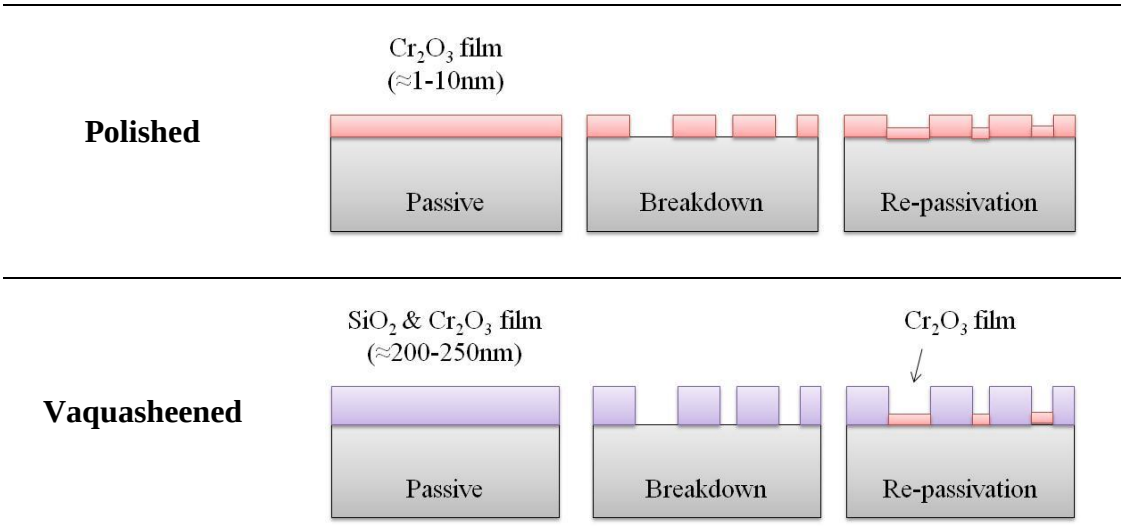

Figure 5-16 - Schematic representation of the breakdown and repassivation of the protective Cr_2O_3 oxide layer when subjected to different surface processing techniques

5.8. Summary and Conclusions

In this chapter, the metallurgy and surface chemistry of wrought and forged LC CoCrMo have been assessed using a variety of different surface analysis techniques. Findings in this section can be summarised into the following:

- A typically equiaxed austenitic grain structure was seen in all alloys.
- Wrought LC CoCrMo alloys demonstrated a finer austenitic grain structure compared to the forged LC CoCrMo alloys.
- Different mechanical pre-treatment's influenced the XRD patterns for LC CoCrMo alloys.
- The aqueous bead blasting process increased the micro strain within the substrate of LC CoCrMo alloy increasing the total fraction of HCP found in the alloy.
- XPS indicated that surface pre-treatment can affect the surface chemistry of LC CoCrMo.

- The polishing process was seen to promote the formation of carbides within the metallic matrix. This was not seen in the blasted samples.
- SEM/EDX analysis demonstrated carbon rich areas present on the surface of the alloy accompanied by the depletion of Co and Cr in the surrounding matrix. Other alloying elements were seen to remain well dispersed within the solid solution of the alloy.
- TEM imagery demonstrated localised re-orientation of the crystalline structure of the metals due to surface processing.
- Vaquasheened surfaces were seen to display SiO_2 films increasing the materials' resistance to the initiation of corrosion.

CHAPTER 6 – CREVICE FORMATION AND EFFECTS OF SURFACE ROUGHNESS ON CREVICE GEOMETRY

6.1. Introduction

In order to fully understand the degradation mechanisms at the stem-cement interface it is important to fully appreciate how mechanical pre-treatment affects the interface and the counterpart bone cement. Many studies investigating the degradation of femoral stems typically employ a 'pin-on-disk' arrangement in order to simulate the fretting-corrosion found at the stem-cement interface; however this is often not representative of the actual interface experienced *in-vivo.*

This chapter aims to establish the exact formation of the crevice at the stem-cement interface and how mechanical surface pre-treatments affect the stem-cement interface and the mechanisms of localised crevice corrosion. A series of experiments was conducted in order to understand how crevice geometry can affect the localised crevice mechanisms of LC CoCrMo. ESEM, white light interferometery and anodic polarisation techniques were employed in order to assess the effects of mechanical pre-treatments.

6.2. Surgical Technique and Crevice Formation

During the surgical procedure the femoral neck is sectioned, femoral canal prepared using gouges and osteotomes, medullary canal reamed and then broached to form a suitable cavity for an optimum cement mantle thickness. A cement restrictor is then placed at the bottom of medullary canal. The cement is then injected in a retrograde fashion into the femur using a cement gun, ensuring that the proximal femur is

sealed during this process. This action will allow for good pressurisation of the cement, and therefore good interdigitation with the rough cancellous bone and metallic stem when inserted. Following injection of the cement, the stem is inserted into the femur to the depth line marked on the femoral stem and any excess cement removed to reveal a clean stem-cement interface. Because the stem is typically introduced into the bone cement in the 'working phase', the proximal regions of the cement are dragged and folded over creating a crevice opening at the stem-cement interface (Figure 6-1).

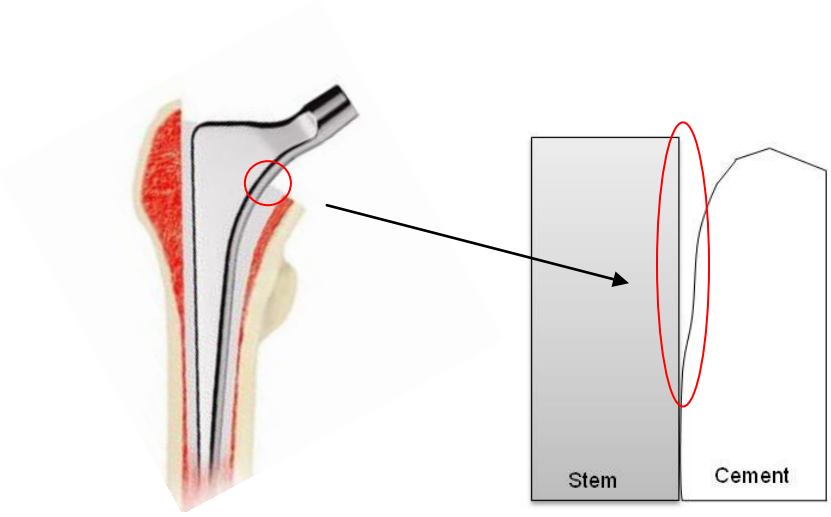

Figure 6-1- Schematic diagram demonstrating the formation of the stem-cement interface resulting from surgery

During the curing process of the PMMA bone cement, contraction of the cement occurs and fixation is achieved via a strong mechanical interlock. However this results in an interface undesirable from a mechanical and electrochemical point of view. Figure 6-2 demonstrates the sections of the interface after the bone cement had cured. Differences were noticed depending on the surface roughness with interdigitation of the bone cement with metallic surface being seen on the samples

that had undergone the aqueous bead blasting process. However, the gap that existed at the stem-cement interface was similar in both cases being seen to vary from 2-4µm.

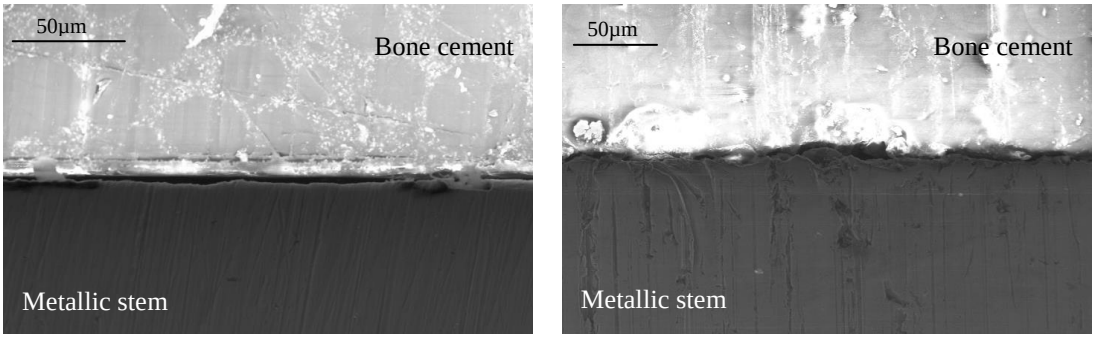

(a) ***(b)***

Figure 6-2 – SE SEM images of the stem-cement interface for a (a) Polished (b) Roughened femoral stem. From cross-sectional analysis of the interfaces the crevice height was seen to be similar in both cases ranging from 2-4µm

Although SEM analysis suggested that the gap at the stem cement interface ranged from 2-4µm, it was difficult to determine if the true interfaces were being observed or if the metallographic polishing processes disrupted the actual interface. It can also be appreciated that in order to characterise the stem-cement interface, a 3D technique must be adopted in order to fully understand how the metallic surface interacts with bone cement.

6.2.1. White Light Interferometery Analysis of Stem-Cement Interface

White light interferometery was employed in order to understand how the cement 'wets' the surface of the metallic stem. Figure 6-3 demonstrates the 3D interferometer profiles obtained for the metallic stem and counterpart cement for both polished and roughened femoral stems. It is clear that the cement 'wets' the surface of the metal sample, producing an almost perfect replica of the metallic

surface. However due to the contraction of the cement during curing a slight difference was seen between the metallic surfaces and counterpart bone cement. Pores were also found in the cement due to the production of gas during curing.

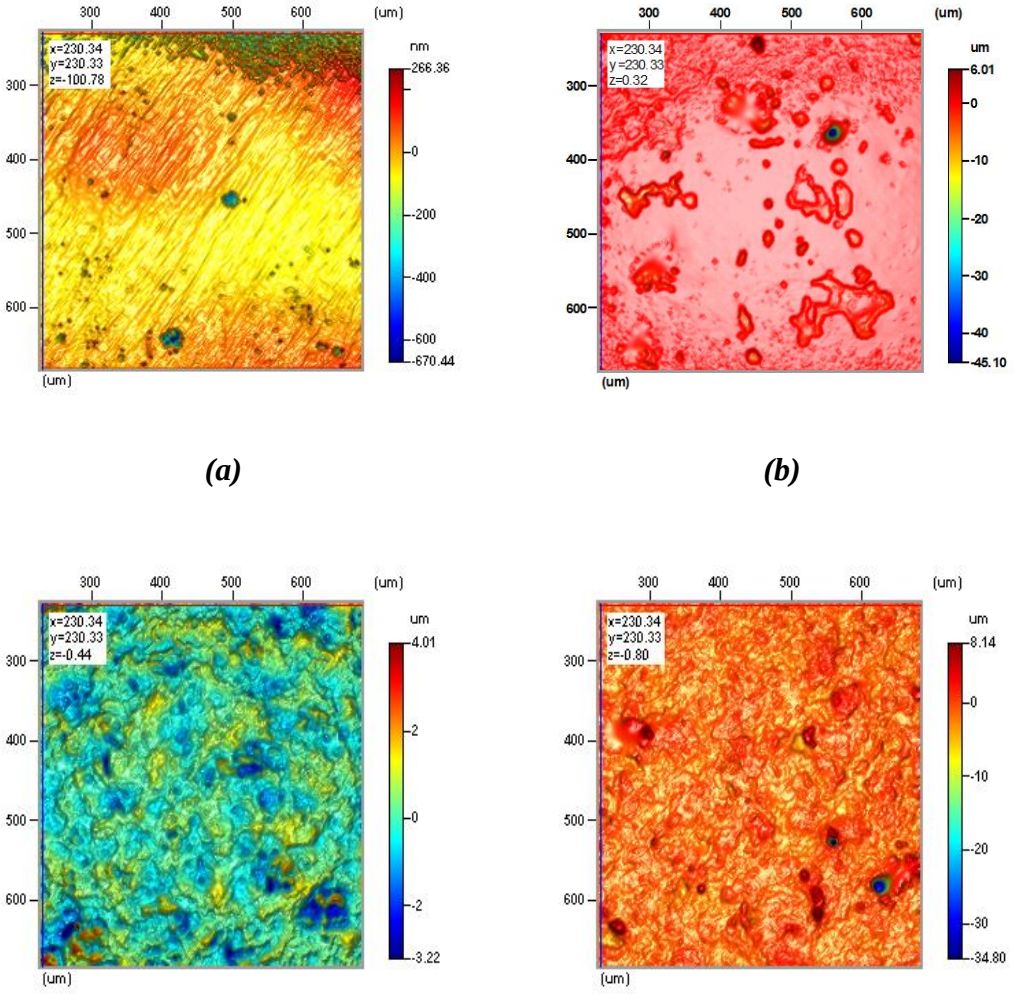

(a) ***(b)***

(c) ***(d)***

Figure 6-3 - Interferometery measurements of the (a-b) polished metallic and counterpart bone cement (c-d) polished metallic and counterpart bone cement (with form removed)

6.2.2. Validation of Interferometery Technique

Interferometery was used as a tool to estimate the apparent volume at the stem-cement interface using the volume of a surface function provided by TalyMap Gold. The apparent volume is the amount of free space between the two faces into which liquid can penertrate. In order to validate this technique with respect to measuring a surface for a volume available for interdigitation, a glass reference object (supplied by Taylor Hobson for calibration purposes) with a known geometry was taken (Figure 6-4). An object with three calibration grooves was selected due to its simple geometry and the volume available for interdigitation on the surface taken as the volume of these groves. The surface roughness of the glass plate was assumed to be negligible. For validation purposes, a 910×910µm scanning region was used.

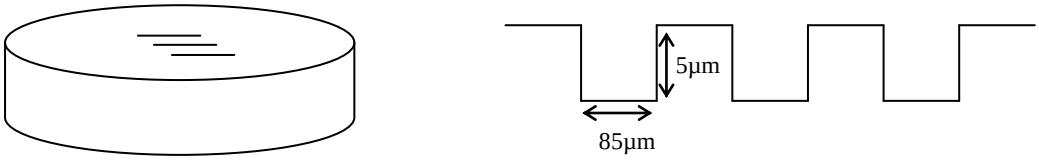

(a) ***(b)***

Figure 6-4 - Simple drawing and schematic cross section of reference object used for validation

Assuming a simple rectangular cuboid geometry, the volume available for one groove was taken as (all measurements are in µm);

$$Height\ of\ groove \times width\ of\ groove \times length\ of\ scan\ region$$

According to this, the calculated volume available for interdigitation of one and three grooves would is 36750 and 1160250µm^3 respectively. Figure 6-5 demonstrates the method and values obtained from TalyMap Gold used in order to calculate the volume available for interdigitation on a surface. It can be seen that

there is a good correlation between the measured and predicted values (Figure 6-6). There was a slight difference when calculating and measuring the $V_{surface}$. This is thought to arise from the in exact dimensions of the glass reference object (Figure 6-7) and any measurement error present in the system.

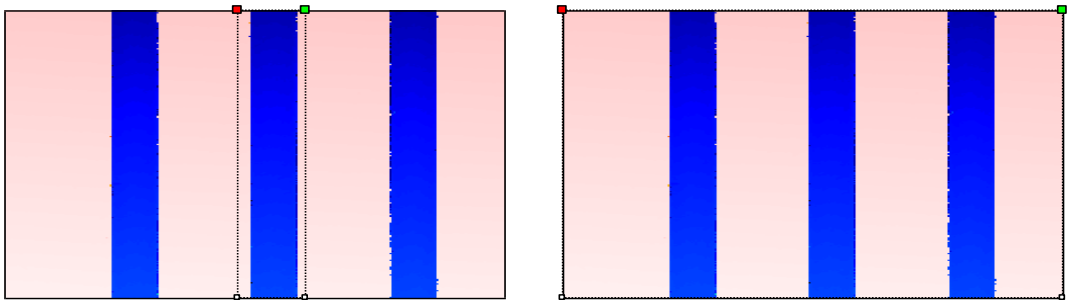

	Hole	Peak
Surface (µm2)	89934	20286
Volume (µm³)	374099	55.8
Max. depth/height (µm)	5.65	0.0367
Mean depth/height (µm)	4.16	0.00275

	Hole	Peak
Surface (mm2)	0.569	0.255
Volume (µm³)	1118974	287
Max. depth/height (µm)	5.65	0.289
Mean depth/height (µm)	1.97	0.00113

(a) ***(b)***

Figure 6-5 - Volume of surface available for interdigitation for (a) one groove (b) three grooves estimated by volume of a surface function in TalyMap Gold. The red and green square represent the field in which the measurements were taken.

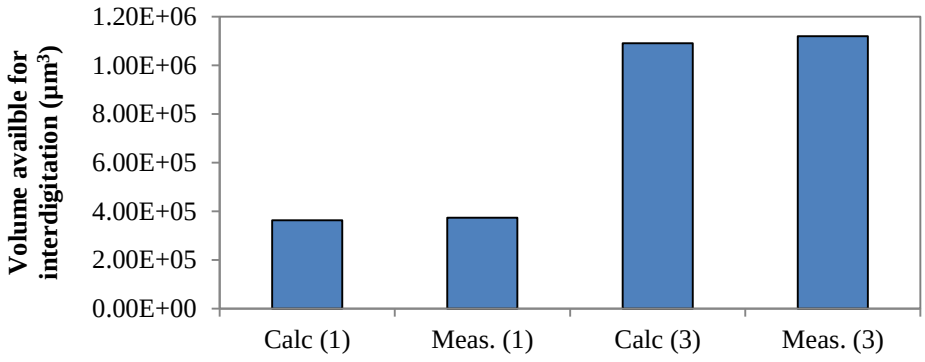

Figure 6-6 - Comparison of calculated and measured volume available for interdigitation

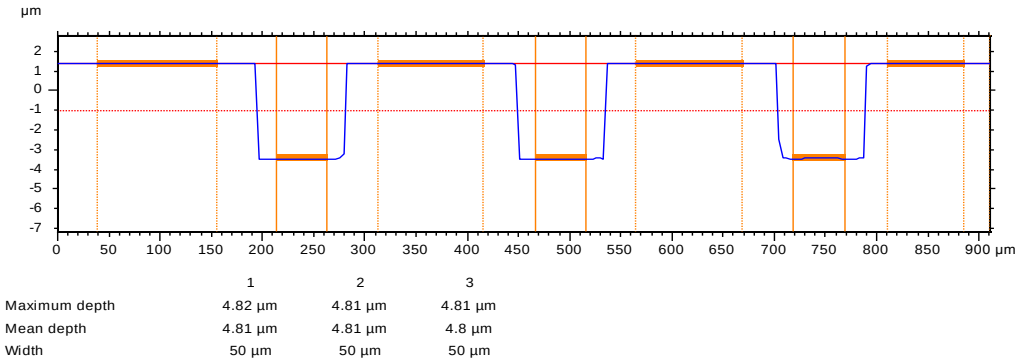

Figure 6-7 - Measured reference object dimension using the TalySurf CCI interferometer.

6.2.3. Calculation of Volumes at the Stem-Cement Interface

The apparent volume of interdigitation was calculated from interferometery measurements for the metal ($V_{i\text{-}metal}$) and bone cement ($V_{i\text{-}cement}$) and then the difference between the two calculated to yield the apparent crevice volume per scan area. Assuming perfect interdigitation of the bone cement with the metal substrate $V_{i\text{-}metal} = V_{i\text{-}cement} = V_{crevice} = 0\mu m^3$. This method was used as an indicator of how the surface roughness affects the crevice geometry.

In order to achieve this metallic samples were subjected to polishing or roughening surface pre-treatments and cemented into a polyethylene holder in a way to replicate the surgical technique. Samples were then carefully sectioned using a precision cut-off machine (Struers Ltd, Rotherham. UK) leaving the cross-sectioned metal specimen and bone cement. Each sample was carefully separated to yield the metallic sample and the counterpart bone cement, on which interferometery was performed. Figure 6-8 demonstrates the volumes predicted within the stem-cement interface ($V_{crevice}$). A larger volume was found between the metal and counterpart cement for samples that had undergone the aqueous glass bead blast process. It is thought that this is a result of the cement initially ‘wetting’ and taking the surface form of the metal and then contracting during polymerisation.

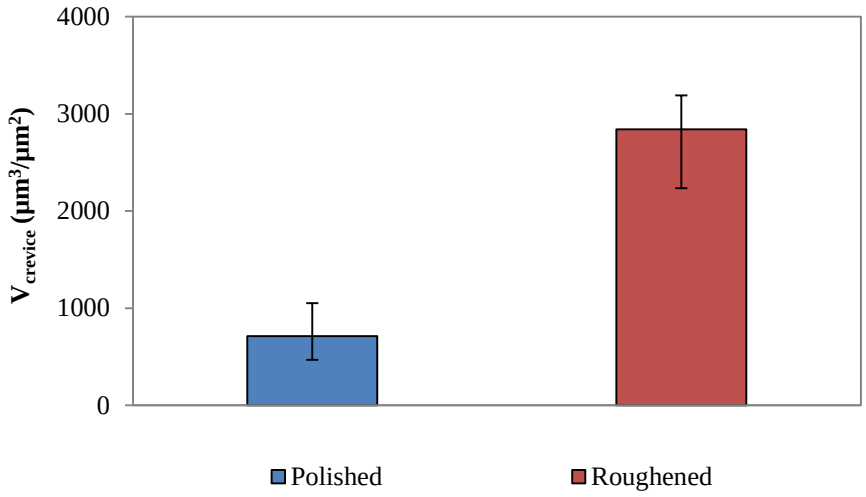

Figure 6-8 - $V_{crevice}$ measurements for CoCrMo corrosion samples (n=3±SD)

6.2.4. Effects of Surface Roughness on the Initiation and Propagation Mechanisms of Localised Corrosion

Potentiodynamic measurements were conducted in order to assess the effect surface roughness had on the initiation and propagation mechanisms of localised crevice corrosion. Potentiodynamic polarisation measurements were measured using an EG&G 663A potentiostat (Princeton Applied Research, USA). Low carbon CoCrMo cylindrical samples were inserted into commercially-available PMMA bone cement to form the stem-cement crevice with these samples as the WEs. The assembly was then immersed in 0.9% NaCl at 37±1°C. The free corrosion potential (E_{corr}), breakdown potential (E_b) and total charge transferred (Q) were used to characterise a materials resistance to electrochemical corrosion of commonly used biomaterials.

6.2.5. Effects of Mechanical Surface Pre-treatment on E_{corr}

Figure 6-9 demonstrates the initial E_{corr} for CoCrMo WEs in 0.9% NaCl when the potential had stabilised to a rate of change less than 3mV/min. E_{corr} measurements were taken as a semi-quantitative indication of the crevice environment prior to polarisation, with a more negative potential associated with a materials' tendency corrode. On average the E_{corr} for the roughened samples was more negative than that of the polished samples.

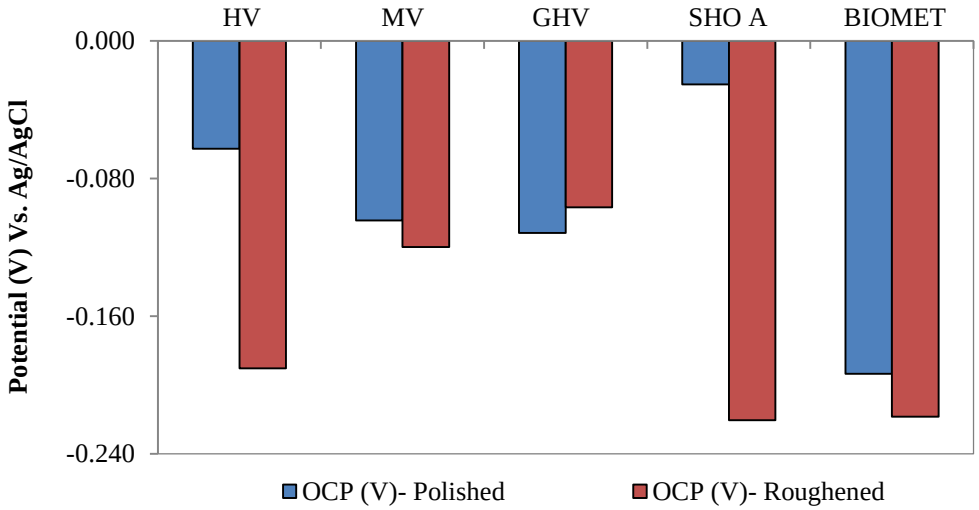

Figure 6-9 - E_{corr} of polished and roughened LC CoCrMo (n=3±SD)

6.2.6. Effects of Mechanical Surface Pre-treatment on E_b

As a method of quantifying the effects of surface treatment on the initiation of localised corrosion E_b was measured. E_b indicates the point at which the passive film is destroyed leaving the substrate to actively corrode. This point is defined as the rapid increase in current with respect to increasing potential. Figure 6-10 demonstrate the E_b for the CoCrMo samples. An increase in E_b was seen for samples with an increased surface roughness. On average E_b values of $0.56V_{Ag/AgCl}$ and $0.52V_{Ag/AgCl}$ were observed for the roughened and polished samples, respectively. It is also interesting to note that cement type had no signifiant effect on the initiation

of localised crevice corrosion. Figure 6-11 demonstrates a typical polarisation curve obtained for the CoCrMo samples. Fluctuations in the current below the E_b were observed demonstrating the occurrence of metastable processes before active pit formation and growth [172]. In the passive region of the material, the current was seen to be around 0.35µA/cm^2.

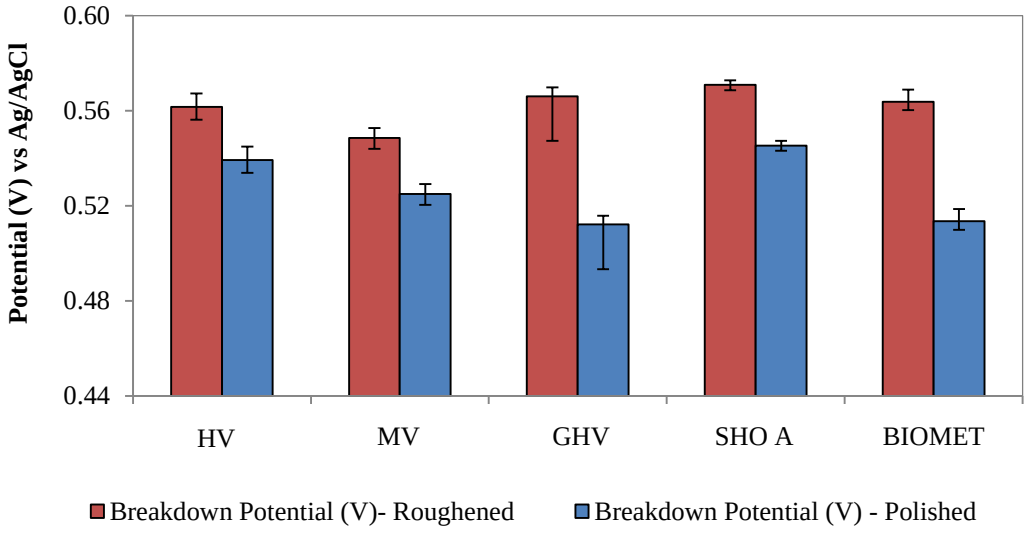

Figure 6-10 - CoCrMo E_b measurements (n=3±SD)

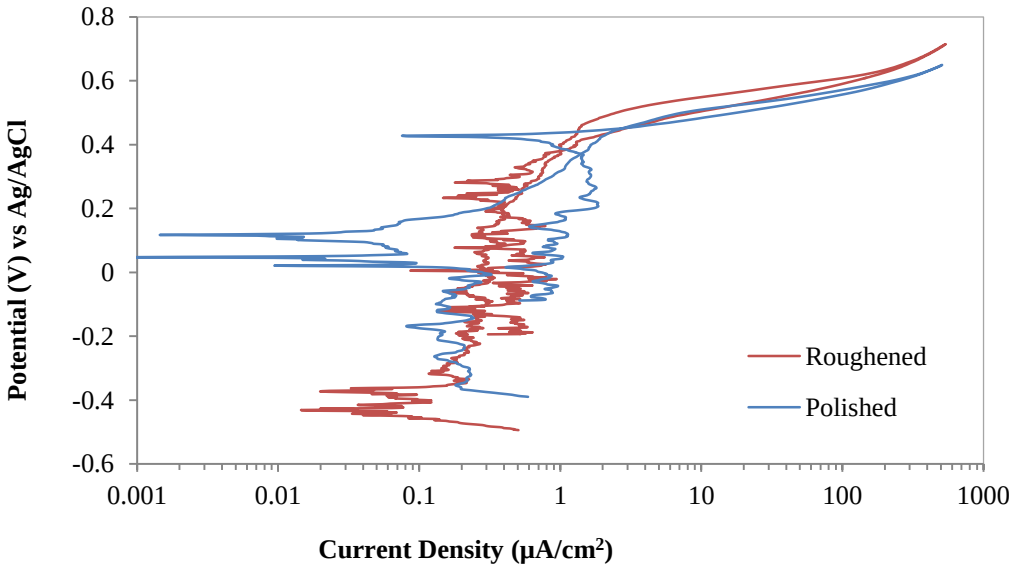

Figure 6-11 - Typical polarisation curves for roughened CoCrMo

6.2.7. Effects of Mechanical Surface Pre-treatment on Total Charge Passed (Q)

In order to fully understand the initiation and propagation mechanisms of crevice corrosion, the total charge passed as a result of localised corrosion was observed. Using Faraday's law of electrolysis, the total charge passed can be calculated. These results have been summarised in the table below (Table 6-1). It is interesting to note that in both cases, the average total charge transferred is higher in the roughened samples compared to the polished samples. Cement type was also seen to have an influence on the total charge transfer.

Table 6-1 – Average total charge transfer as a result of localised crevice corrosion (n=3)

	Charge (Coulomb/cm^2)	
	Polished	**Roughened**
LC CoCrMo	2.70	2.95

6.2.8. Effects of Mechanical Surface Pre-treatments with Respect to Metallic Ion Release from Metallic Implants

60 day immersion tests were also conducted on fully cemented stems. Each stem was cemented in a way to replicate the second generation technique adopted by the Norwich surgeons. Each stem was placed in 100mL of 0.9% NaCl solution at 37°C and allowed to freely corrode without the application of any external potential.

Upon retrieval of the immersed stems, a contrast in localised corrosion could be seen on all of the stem surfaces. Figure 6-12 demonstrates the corrosion profile of a polished femoral stem cemented with non-antibiotic PMMA bone cement. Although surface analysis of polished femoral stems found that localised corrosion

had initiated within the stem-cement crevice after 60 days immersion, the propagation of localised corrosion was not extensive. Light microscope analysis on other areas of the stem demonstrated that localised corrosion had occurred within the stem-cement crevice. Again these areas of localised corrosion were not extensive after 60 days of immersion. Antibiotic bone cement was seen to increase localised corrosion found at the stem-cement interface (Figure 6-13). Surface analysis was also conducted on the vaquasheened immersion tests. After 60 days immersion, femoral stems with an increased surface roughness indicated little to no localised corrosion had taken place within the stem – cement crevice (Figure 6-14).

Figure 6-12 – Stem-cement interface of forged polished LC CoCrMo Ulitma TPS stem after 60 days immersion with antibiotic free bone cement

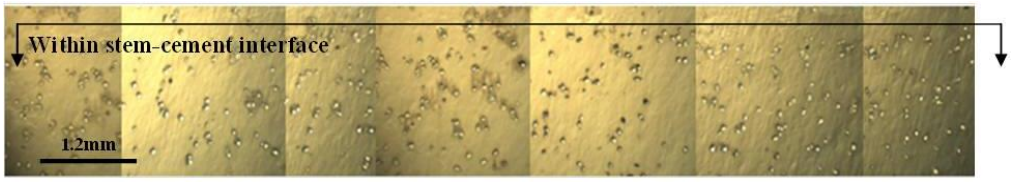

Figure 6-13 – Localised corrosion at the stem-cement interface of forged polished LC CoCrMo Ulitma TPS stem after 60 days immersion with antibiotic bone cement

Figure 6-14 - Stem-cement interface of forged vaquasheened LC CoCrMo Ulitma TPS stem after 60 days immersion with antibiotic bone cement

6.3. Discussion

6.3.1. Effects of Crevice Geometry

The purpose of this chapter was to quantify the effects of surface pre-treatments on the localised crevice corrosion mechanisms of commonly used biomaterials when PMMA bone cement is used as a fixation method. This chapter has demonstrated that the surface pre-treatment can influence the crevice corrosion mechanisms and surface chemistry of commonly used orthopaedic materials using electrochemical and novel surface analysis techniques.

The crevice corrosion mechanisms of passive orthopaedic alloys are thought to follow the passive dissolution model which can be summarised into five stages [79, 82]:

1. Uniform corrosion occurring inside and outside of the crevice.
2. Depletion of oxygen within the crevice solution.
3. Increase in acidity and chloride content of the crevice solution.
4. Permanent breakdown of the passive film and the onset of rapid corrosion.
5. Propagation of crevice corrosion.

Electrochemical measurements suggest that samples with an increased surface roughness have increased resistance to the initiation of localised corrosion (Figure 6-15) although the roughened samples demonstrated an increased total charge transfer once initiation had taken place. This is against common understanding in crevice/pitting corrosion where rough surfaces are less resistant to the initiation of localised corrosion. This is due to the asperities formed on the surface creating areas with a secluded geometry susceptible to localised corrosion. However it is important to appreciate that the process in which the crevice formed is somewhat different to

traditional crevice arrangements presented. Cement type and chemistry is also thought to have an effect on the localised crevice corrosion mechanisms and will be discussed in detail in the following chapter.

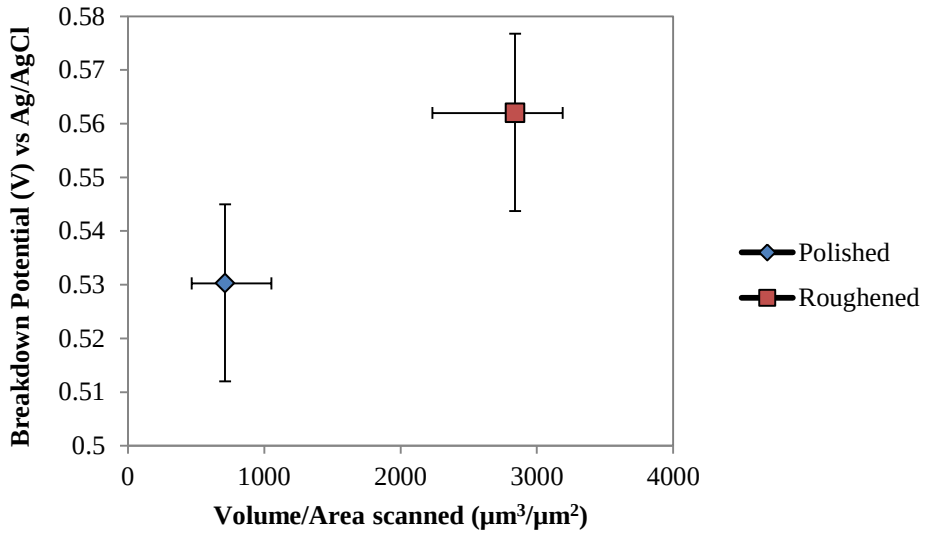

Figure 6-15 - E_b vs $V_{crevice}$ for polished and roughened LC CoCrMo. Data incorporates different types of PMMA bone cement and demonstrates the average E_b vs $V_{crevice}$ with standard deviation (n=3±SD)

The effects of surface pre-treatment and crevice geometry have been a subject that has received much attention in the past with respect to the initiation and propagation mechanisms of localised crevice corrosion [9, 173]. It is common practice in corrosion science for a crevice former, usually in the form of a polymer plate or washer, to be clamped to the surface under a known force to achieve known crevice geometries [85, 174-176]. However during THA the metallic femoral stem is inserted into a deformable PMMA crevice former that undergoes a polymerisation process. During the curing stage, shrinkage of the PMMA occurs resulting in the formation of a crevice with an increased susceptibility to localised corrosion when compared with other geometries tested in this study and other literature [62, 177].

It is widely accepted that fixation of cemented femoral stems is achieved through a strong mechanical interface rather than an adhesive bond so the interaction at these interfaces is important from both an electrochemical and mechanical point of view. However due to the nature of this interface, it is difficult to understand the crevice geometry using traditional cross-sectioning and metallographic preparation techniques. On first inspections a similar crevice height was seen for roughened and polished samples; even though roughened samples demonstrated an increased resistance to localised crevice corrosion going against studies by Alkire and Lott, Scully, Shan and Wolfe [85, 176, 178, 179]. Thus a novel method using interferometry was developed to try and understand the effects of surface pre-treatment on the crevice corrosion mechanisms. Although ESEM images (Figure 6-2) suggested that the crevice height was similar for both surface roughnesses, interferometery measurements demonstrated that although the crevice heights may be similar across the 2-D section, the apparent free volume between the cement and metal was higher for samples with an increased surface roughness. An increase in the apparent volume was seen for LC CoCrMo with an increased surface roughness. It is thought that this increase in the apparent volume affects the local environment, mass transportation and diffusion kinetics of crevice corrosion [82, 93].

Figure 6-16 schematically demonstrates the crevice corrosion process for cemented CoCrMo. In the first stage the cathodic current equals the anodic current within the crevice, resulting in the reduction of oxygen to hydroxyl ions. During the second stage of crevice corrosion [82, 180], changes occur in the crevice solution as the metal cations from the alloy pass into the solution and hydrolyse (Equation 6-1). The metal ion concentration in the crevice increases until the solubility product of one or more of the metal hydroxides is exceeded. As the metal hydroxides precipitate from the crevice to the bulk solution due to an electrochemical imbalance, H^+ ions are

generated reducing the pH of the crevice solution. Cl^- ions will then enter the crevice to ensure electrochemical equilibrium, further reducing the pH by the formation of HCl. Breakdown of the passive film occurs when conditions within the crevice become sufficiently aggressive enough to cause permanent breakdown of the passive film. Oldfield [82] stated that 'The rate at which the crevice solution increases in acidity and chloride content is determined by the value of the passive current and volume of crevice solution, which is directly related to crevice height.'

Equation 6-1 - Primary hydrolysis reactions involved in the crevice corrosion of LC CoCrMo

$$Co^{2+} + H_2O \rightleftarrows Co(OH)^{2+} + H^+$$

$$Cr^{3+} + H_2O \rightleftarrows Cr(OH)^{3+} + H^+$$

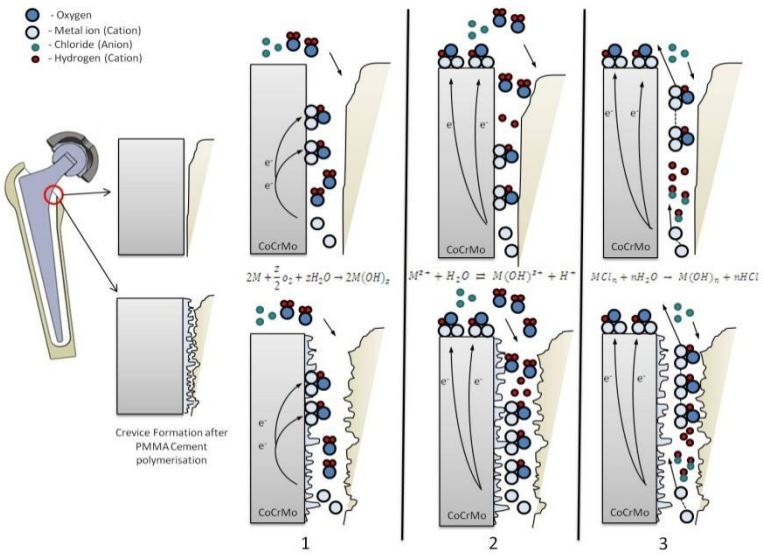

Figure 6-16 - Schematic representation of the initiation of crevice corrosion of cemented CoCrMo by each stage

Although the crevice height can be a key parameter when trying to understand the crevice corrosion mechanisms, it does not take into account the effects of surface roughness (i.e. volumes within asperities) and the volume present between two bodies caused when a crevice forming material 'wets' the surface of a metal. In this

case, it is proposed that the improved corrosion resistance of samples with an increased surface roughness results from the combination of the increase in apparent volume between the metal-cement interfaces, ultimately changing the mass transportation kinetics of the reactions, along with the presence of a SiO_2 film reported in Chapter 4.4.2. An increased apparent volume increases the total volume within the crevice that needs to be sufficiently concentrated with metal hydroxides to allow precipitation out of the crevice and into the bulk solution, thus inhibiting breakdown of the passive film whilst the SiO_2 film on the roughened samples with further decrease charge transfer due to the capacitive nature of the SiO_2 film.

6.4. Summary

In this chapter, the effects of mechanical pre-treatment on the interface and electrochemical characteristics under static conditions have been discussed. The results from this chapter can be summarised into the following;

- The THA procedure and polymerisation of the PMMA bone cement results in a stem-cement interface or crevice undesirable from an electrochemical point of view. The materials' resistance to localised corrosion was reduced when compared to crevice free samples.
- Mechanical surface pre-treatment can influence the formation and geometry of the crevice at the stem-cement interface.
- Aqueous bead blasting has been shown to increase the volume present at the stem-cement interface, whilst the polished surfaces demonstrated the lowest crevice volumes. Increased interdigitation of the bone cement was seen increasing the interfacial strength at the stem-cement interface.

- Surface pre-treatment has been shown to affect the initiation and propagation mechanisms of localised crevice corrosion.
- Accelerated electrochemical tests demonstrated that samples with a vaquasheened surface demonstrated an increased resistance to the initiation of localised corrosion compared to polished samples
- Long term immersion tests demonstrated that the propagation of localised corrosion was increased for polished femoral stems cemented with PMMA bone cement.
- The chemistry of the PMMA bone cement was also seen to influence the propagation rates of localised crevice corrosion as confirmed with light microscope and ICP-MS analysis.

CHAPTER 7 – EFFECTS OF PMMA BONE CEMENT CHEMISTRY ON THE CREVICE CORROSION MECHANISMS AND SOLUTION CHEMISTRY OF BIOMEDICAL ALLOYS

7.1. Introduction

So far in this study, the electrochemical data that has been presented has mainly focused on the effects of surface pre-treatment, crevice formation and crevice geometry. Currently in the UK, the use of PMMA bone cement is still the preferred option of fixation in patients over 65. However, with so many commercially available PMMA bone cement available in both the UK and internationally, a huge variability of PMMA bone cement chemistry exists.

The integration of antibiotic agents into PMMA bone cements for the treatment and prevention of infection has become common clinical practice since the 1970's, with gentamicin sulphate being extensively used as the primary antibiotic [44, 181]. Radiopaque agents are also included to aid visibility under X-ray conditions, with zirconium dioxide and barium sulphate being commonly used.

Studies to date have questioned the efficacy of the use of antibiotic-impregnated cements as the release mechanisms are poorly understood and difficult to control whilst maintaining the integrity of the implant [44]. Similarly, questions surrounding how antibiotics and radiopaque agents affect the corrosion and localised corrosion regimes of cemented implants need to be answered due to the increasing occurrence of corrosion at the stem-cement interface. To date, no studies have been conducted

looking at the influence of PMMA bone cement and their chemistry with respect to the localised corrosion mechanisms of biomedical alloys and the impact such variables have on the local environment.

This chapter aims to investigate the influence that PMMA bone cement plays in the degradation of cemented femoral stems. The influence of the PMMA bone cement chemistry will also be investigated under consistent, repeatable and systematic conditions. Cemented femoral stems and cylindrical corrosion samples were subjected to a variety of different analytical techniques. OCP, electrochemical polarisation, ICP-MS and SEM analysis were all utilised in order to quantify the effect that PMMA bone cement chemistry plays on the degradation mechanisms of biomedical alloys. During this study, five commonly used PMMA bone cements were tested of which the chemical composition can be found in the experimental materials chapter.

7.2. Crevice Corrosion of Cemented Femoral Stems under Static Long Term Conditions

Twelve polished low carbon CoCrMo Ultima™ TPS femoral stems (DePuy International, Leeds, UK) with an S_a=10nm were cemented using two commercially available antibiotic bone cements and two non-antibiotic bone cement using the same technique used by the surgeons at the Norfolk and Norwich centre. Each cemented stem was then immersed in 100mL of aerated 0.9% NaCl (pH7.4) at 37 ± 1 °C for 60 days. Approximately 6mL of distilled water was added each day to ensure the volume of solution in each test remain constant.

Stems were allowed to corrode at their free corrosion potential without the application of an external potential, a condition that will be established *in-vivo*. EIS

measurements were conducted intermittently in order to assess the effects of the materials' resistance to polarisation and any film formation that may have occurred. Light microscope analysis and scanning electron microscopy (SEM) was conducted after 60 days to determine the extent of initiation and propagation of localised corrosion at the stem – cement interface. At 60 days, electrolyte samples were extracted, placed in sterilised centrifuged tubes and analysed using inductively coupled plasma mass spectrometry (ICP-MS) according to the procedure outlined in Chapter 3.7.7.

7.2.1. Electrochemical Response

In order to capture the electrochemical response of twelve femoral stems immersed in NaCl for 60 days a Gill 12 potentiostat (ACM instruments, Cumbria, UK) was utilised. Each test consisted of a cemented femoral stem with an integrated 3 electrode electrochemical cell consisting of a LC CoCrMo WE, Ag/AgCl RE and a carbon rod CE. The test setup can be seen schematically in Figure 7-1.

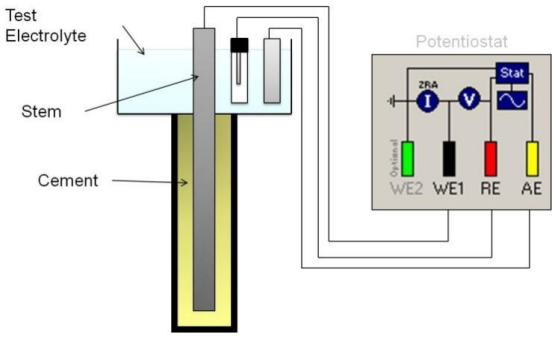

Figure 7-1 - Schematic of long-term static corrosion cell

7.2.1.1. OCP transients

Figure 7-2 demonstrates the average OCP response obtained when femoral stems were cemented with commercially available PMMA bone cements. OCP results allow a semi-quantitative estimation of a materials susceptibility to localised corrosion to be made, with a more negative OCP being associated with an increased

susceptibility to localised corrosion. An initial OCP of around -0.07 to -0.150V was observed when cemented femoral stems were initially immersed in 0.9% NaCl. An ennoblement in OCP with time was seen with positive potentials being observed after 1 day. The OCP was seen to further increase with time, reaching a steady state after 5 days. This gradual increase in OCP is associated with the formation and gradual hydration of a protective oxide/hydroxide film. Sudden negative fluctuations in OCP were observed throughout the duration of each test, a characteristic often associated with localised pitting corrosion.

It is interesting to note that differences in OCP were seen when femoral stems were combined with various PMMA bone cements. OCP results presented in Figure 7-2 suggest that both the antibiotic and radiopaque agent can influence the local environment that is found at the stem-cement interface resulting in a reduction in the OCP. The addition of $BaSO_4$ and antibiotics was seen to increase a femoral stems/ susceptibility to localised corrosion.

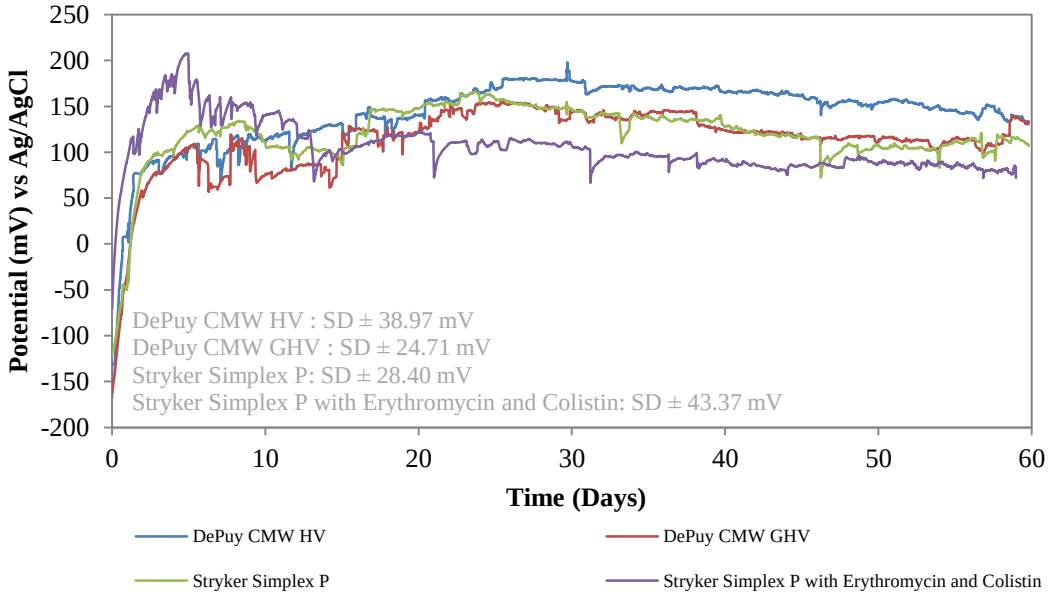

Figure 7-2 - Average OCP measurements for cemented femoral stems immersed in 0.9% NaCl over 60 days (n=3) average SD has been shown in the figure.

7.2.1.2. Electrochemical Impedance Spectroscopy (EIS) Response

Intermittent EIS measurements were conducted in order to gain a quantitative indication of a materials resistance to electrochemical polarisation; a direct evaluation of corrosion rate. EIS measurements also assisted in the evaluation of the electrical properties at the stem-cement interface helping to further understand the interactions taking place at the interface. Intermittent EIS measurements were taken throughout the duration of the immersion test in order to examine how the corrosion current varied over the 60-day test. EIS measurements were taken approximately every 24hrs and the resistance to charge transfer presented as I_{corr} and observed as a function of time. Figure 7-3 demonstrates the average I_{corr} vs. time. On average, femoral stems cemented with PMMA bone cement containing no antibiotics demonstrated lower I_{corr} values compared to the femoral stems cemented with antibiotic bone cement. The Stryker Simplex P with Erythromycin and Colistin demonstrated the highest I_{corr} measurements demonstrating an increased corrosion rate.

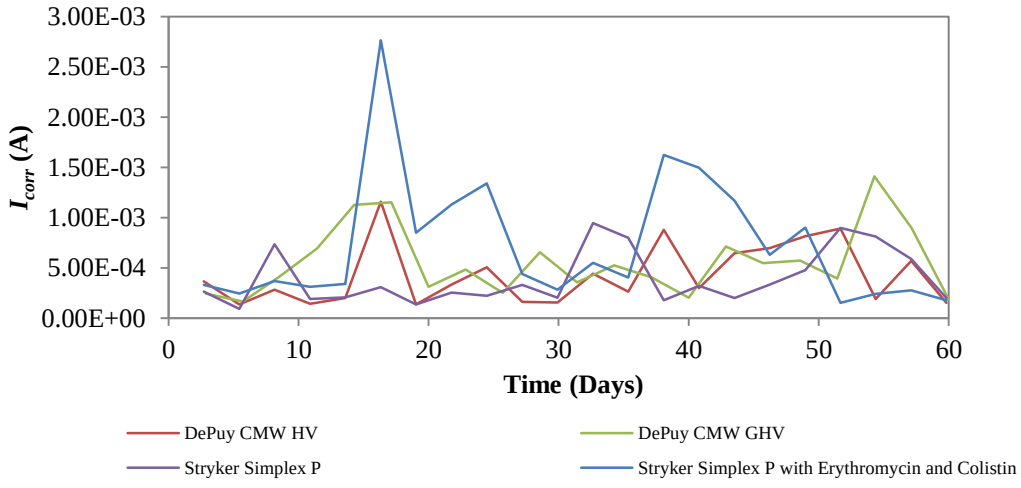

Figure 7-3 - Average intermittent I_{corr} values obtained from EIS measurements of cemented femoral stems immersed over 60 days (n=3).

Integration of the I_{corr} vs. Time curve and application of Faraday's law further complimented Figure 7-3, demonstrating differences in the total and cumulative mass loss rates. Figure 7-4 demonstrates the cumulative mass loss, as a function of time for each PMMA bone cement tested. It is interesting to note that each PMMA cement seems to exhibit similar mass loss rates for the first 13 days.

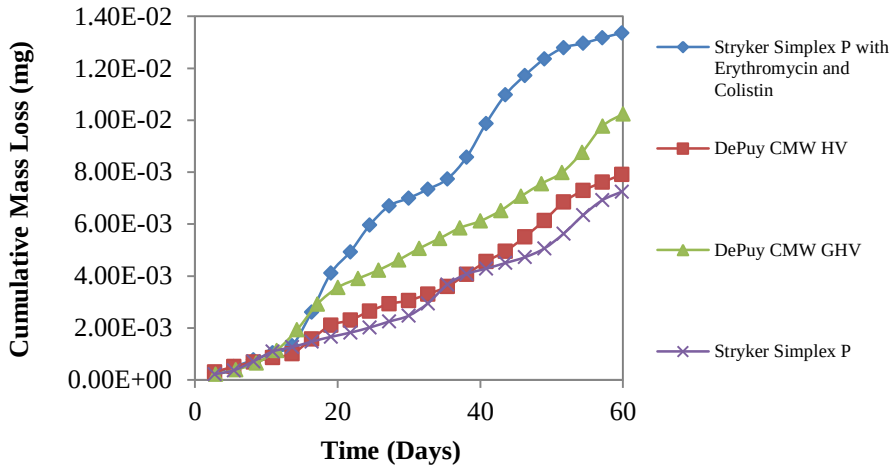

Figure 7-4 – Average cumulative mass loss calculated from I_{corr} measurements (n=3)

Linear trend lines were applied to the cumulative mass loss data in order to assess the average rate of mass loss over 60days immersion. Table 7-1 demonstrates the obtained mass loss rates with associated coefficient of fits. Again, the Stryker Simplex P cement with Erythromycin and Colistin was seen to exhibit the highest mass loss rate whilst the Stryker simplex P demonstrated the lowest.

Table 7-1 - Rate of mass loss with respect to time and associated coefficient of fit

Cement Type	Gradient $mgHr^{-1}$	R^2
DePuy CMW HV	1.36×10^{-4}	0.98
Stryker Simplex P	1.20×10^{-4}	0.97
DePuy CMW GHV	1.70×10^{-4}	0.99
Stryker Simplex P with Erythromycin and Colistin	2.61×10^{-4}	0.98

Figure 7-5 demonstrates the initial EIS spectra obtained when the femoral stems were initially immersed in 0.9% NaCl. Initially, each stem-cement demonstrated a high resistance to charge transfer, suggesting a very low corrosion rate. When the surface of the material was modelled using the equivalent circuit shown in Figure 7-7, differences in R_{ct} were seen between the four PMMA cements tested in this study. R_{ct} measurements (Table 7-2) further strengthen the evidence suggesting that $BaSO_4$ and antibiotics can increase a materials' susceptibility to localised corrosion.

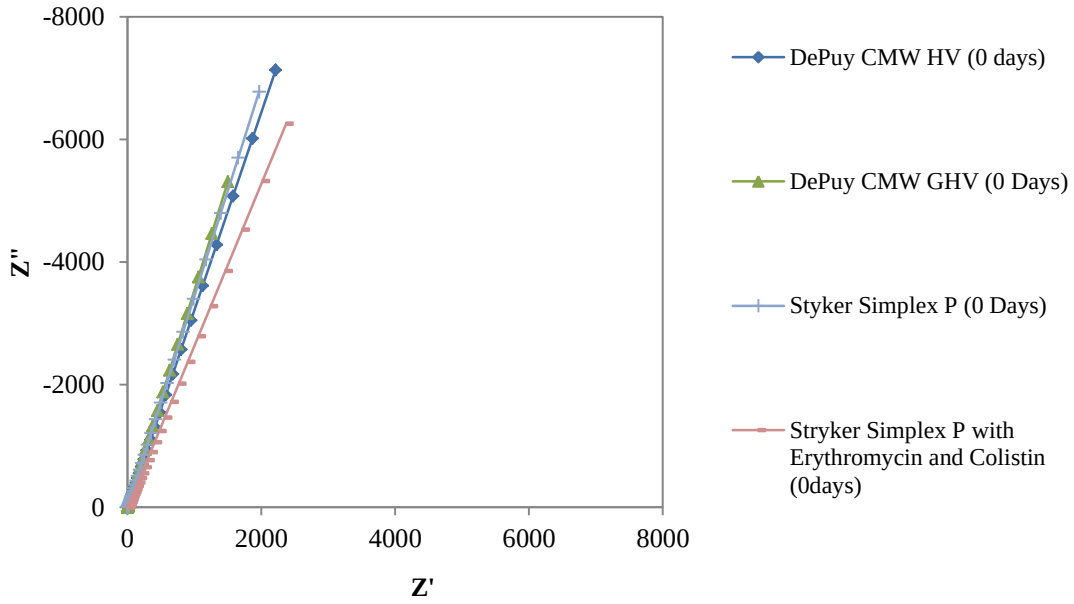

Figure 7-5 - EIS data at the point of immersion

Figure 7-6 demonstrates the EIS nyquist plots obtained for immersed femoral stems after 60days immersion. A decrease in R_{ct} was observed characterised by the curvature of the nyquist plots. A decrease in R_{ct} was observed when compared to the initial EIS data, indicating the initiation and propagation of localised crevice corrosion. Again, EIS measurements obtained at 60 days supported the hypothesis that the introduction of antibiotic and radiopaque agents into the PMMA bone cement can increase materials susceptibility to localised corrosion, displaying a similar trend observed in the above data. A decrease in C_{dl} was also observed after

60 days immersion. C_{dl} is commonly associated with the capability of the EDL to retain its charge at the surface of a material. A decrease in C_{dl} is often associated with decrease in oxide thickness and redistribution of charge at the surface. This decrease in C_{dl} and R_{ct} can be associated with a decrease in the area of material covered by oxide film.

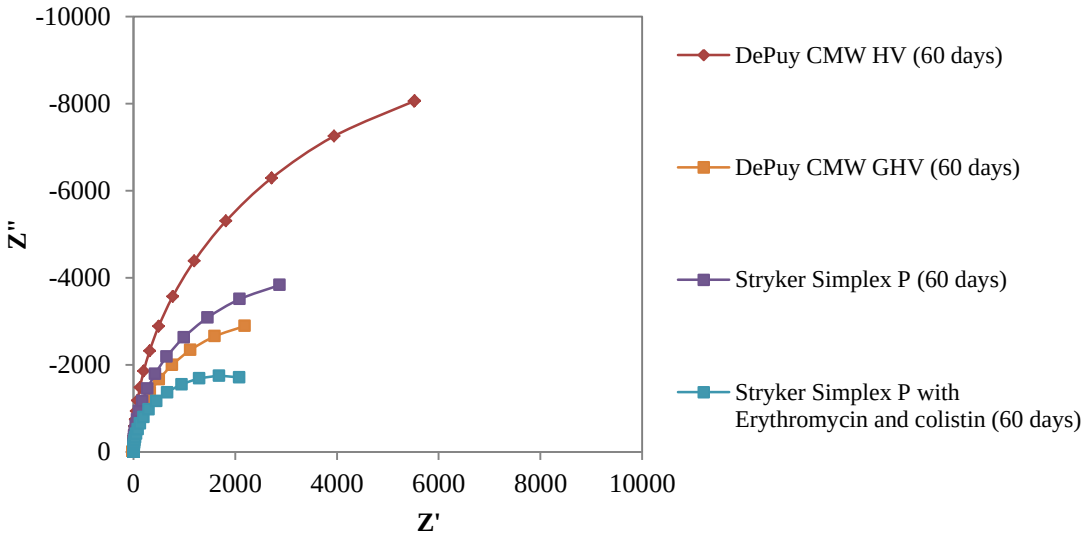

Figure 7-6 - EIS data at 60 days. A decrease in R_{ct} was seen demonstrating an increase in localised corrosion due to the initiation and propagation of crevice corrosion

In order to fully understand the electrical properties of the metal at the stem-cement interface the EIS data was modelled using the circuit presented in Figure 7-7. This consisted of a resistor in series to another resistor and a constant phase element (CPE) in a parallel arrangement. The two resistors used allowed the simulation of solution resistance (R_s) and the resistance to polarization (R_p). A CPE was used to model the capacitance of the EDL. The use of a CPE accounts for the non-idealities caused by the interaction between frequency and all of the physical and chemical processes that respond to that frequency change within the electrochemical cell and across the corroding interface. The application of this circuit demonstrates that a fairly simple electrical interaction exists at the stem-cement interface. It further

demonstrates that no films or deposits are formed on the surface as a result of the corrosion process as the system has been modelled using a single time constant model.

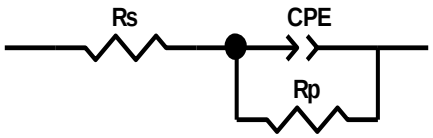

Figure 7-7 - Electrical Circuit used to model the metallic surface at the stem-cement interface.

Table 7-2 - R_s, C_{dl} and R_{ct} values obtained from EIS analysis at 0 and 60 days (n=3). The third replicate of DePuy CMW HV cement was lost due to electrode error.

	0 Days			60 Days		
	R_s (Ohms)	C_{dl} (F)	R_{ct} (Ohms)	R_s (Ohms)	C_{dl} (F)	R_{ct} (Ohms)
DePuy CMW HV	5.01	3.58E-05	1.42E+12	1.61	1.56E-04	6.10E+04
	2.97	4.52E-05	5.04E+11	1.02	2.07E-04	3.62E+04
	2.75	2.68E-04	7.67E+11	-	-	-
DePuy CMW GHV	3.28	1.19E-04	1.89E+11	0.96	1.48E-04	9.84E+03
	3.97	5.32E-05	4.75E+11	6.47	3.14E-05	3.96E+03
	4.29	2.53E-05	4.32E+12	3.70	1.14E-05	1.93E+04
Stryker Simplex P	4.19	8.98E-05	6.98E+11	72.79	7.12E-04	3.25E+03
	3.11	1.00E-04	4.30E+11	2.35	1.56E-04	4.37E+04
	4.40	6.49E-05	3.44E+10	13.56	1.49E-04	2.65E+03
Stryker Simplex P with Erythromycin and Colistin	5.04	4.81E-05	1.74E+11	3.07	2.04E-04	2.25E+04
	2.50	5.88E-05	1.21E+11	3.41	9.47E-04	2.71E+02
	4.93	3.66E-05	1.48E+12	2.54	2.39E-04	2.50E+03

7.2.2. Effects of localised corrosion on solution chemistry

Analysis of the solution chemistry using ICP-MS was further conducted in order to fully understand the localised corrosion regimes taking place at the stem-cement interface. ICP-MS analysis enabled a quantitative measurement of the metal ions released from the stem-cement interface due to localised corrosion. ICP-MS measurements further demonstrated that PMMA bone cement chemistry can influence the crevice corrosion rates at the stem-cement interface (Figure 7-8), with increases in Co 59 and Cr 52 levels being seen between antibiotic and antibiotic-free PMMA bone cement as well as cements containing different radiopaque agents. The addition of $BaSO_4$ was seen to increase the Co 59 concentrations when compared to the $BaSO_4$ and ZrO_2 containing cements. The Stryker Simplex P with Erythromycin and Colistin demonstrated the highest release of metal ions suggesting there may be a compounding effect between the two sulphate containing agents.

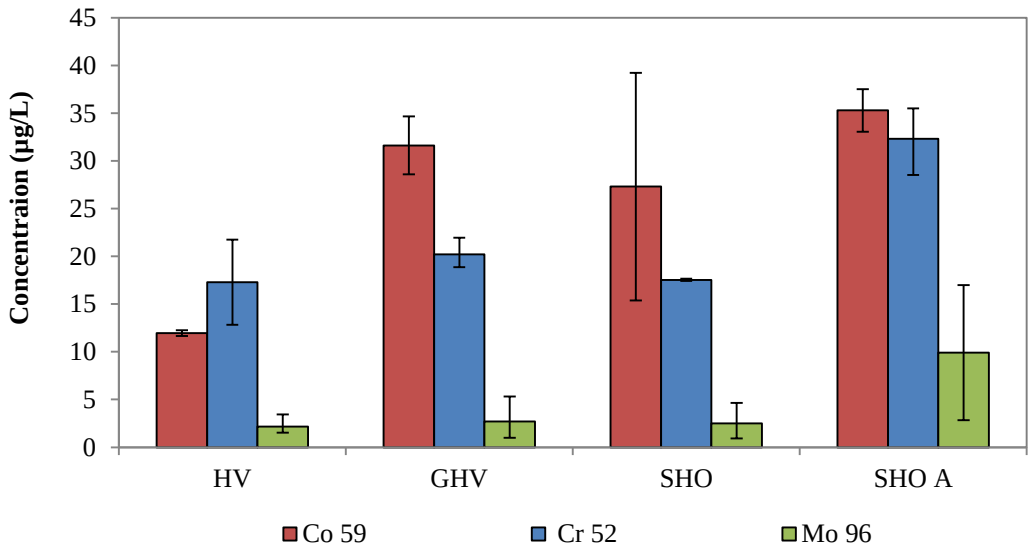

Figure 7-8 - Ion concentration found in the bulk solution after 60 days due to ionic transfer from the crevice (n=3±SD)

Figure 7-9 demonstrates the average ratios in which metal ions where released from the stem-cement interface. No differences within experimental error in release ratios were seen between any tests. Typically, a stoichiometric dissolution of the CoCrMo alloy was seen demonstrating a release ratio of 0.6Co:0.3Cr:0.1Mo. These results suggest that no selective dissolution of the alloy exists at the stem-cement interface.

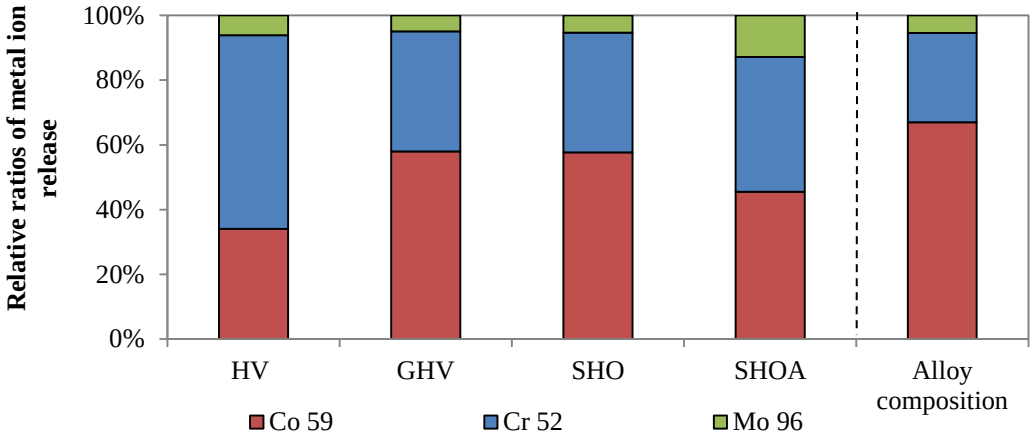

Figure 7-9 - Average stoichiometry in which ions released from the cemented femoral stems (n=3)

A comparison between Faradaic mass loss and measured mass loss was also made. Figure 7-10 demonstrates the mass loss calculated from electrochemical data and measured using ICP-MS. A good correlation between calculated and measured mass losses was seen further supporting the ICP-MS data.

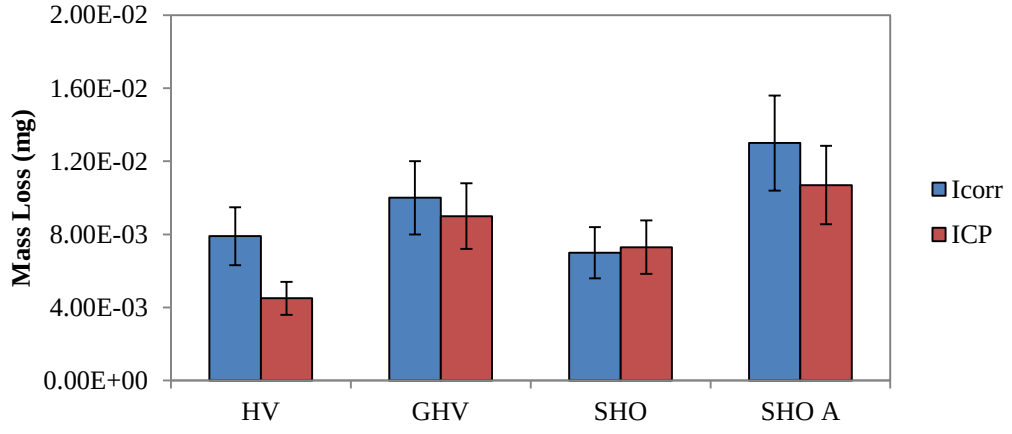

Figure 7-10 - Comparison of total mass loss measured using ICP-MS and calculated from I_{corr} measurements (n=3±SD)

7.2.3. Surface morphology of corroded cemented femoral stems

Figure 7-11 demonstrates the anterior and posterior surface profiles of the cemented portions of the femoral stems. The red dashed line represents the opening of the stem-cement interface. The area shown below the red dashed line is where the material was subjected to crevice corrosion. On a macroscopic level, localised corrosion was seen on the cemented portions of the femoral stems, typically characterised by localised areas of pitting. Increased amounts of localised corrosion on femoral stems cemented with PMMA bone cements containing antibiotic and $BaSO_4$ could be seen on a macroscopic level further supporting the electrochemical and surface chemistry results.

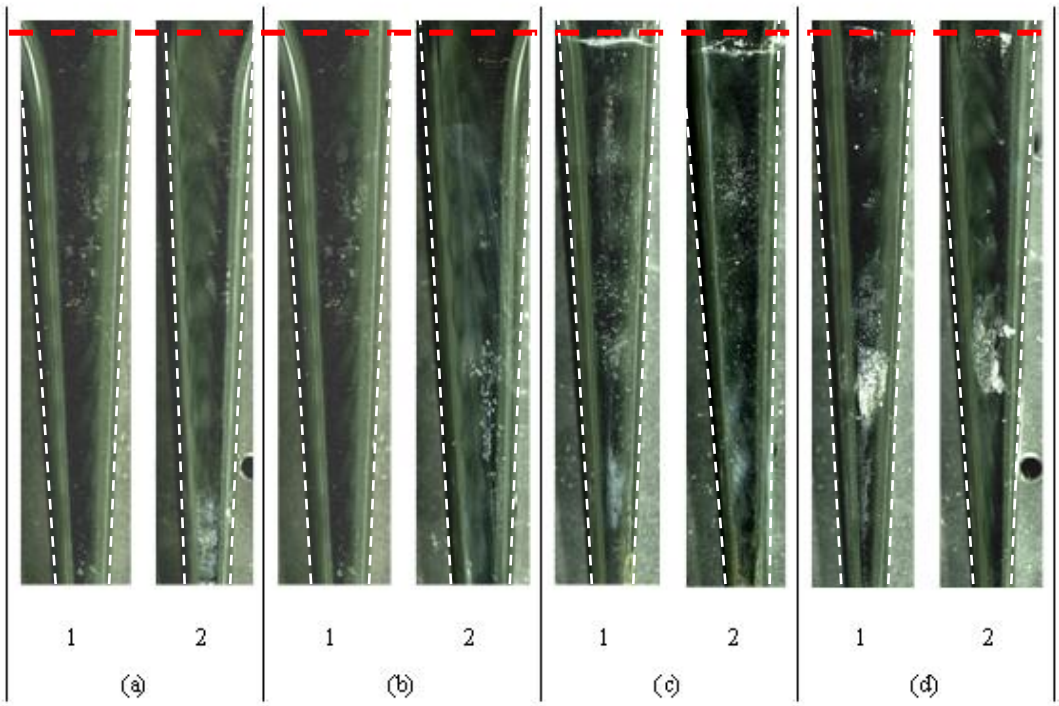

Figure 7-11 - (1) Posterior and (2) Anterior surface profiles of LC CoCrMo cemented femoral stems after 60 day immersion with (a) DePuy CMW HV, (b) DePuy CMW GHV, (c) Stryker Simplex P and (d) Stryker Simplex P with Erythromycin and Colistin PMMA bone cements. White dashed lines represent the boundary of the cemented femoral stem.

7.3. Accelerated crevice corrosion investigations

7.3.1. Electrochemical Results

Figure 7-12 demonstrates the free corrosion potential (E_{corr}) for 316L stainless steel samples when E_{corr} had stabilised to a rate of change less than 3 mV/min. It can be seen that samples combined with cements containing antibiotics had a more negative E_{corr} compared to samples combined with antibiotic-free cements. The more negative potential is considered to be associated with a materials tendency to corrode. These results would suggest that when a stainless steel specimen is combined with HV and MV bone cement, the tendency for that specimen to corrode is less, compared to samples combined with antibiotic cement. The results from the initial open circuit potential results were further strengthened by the breakdown potential (E_b) measurements.

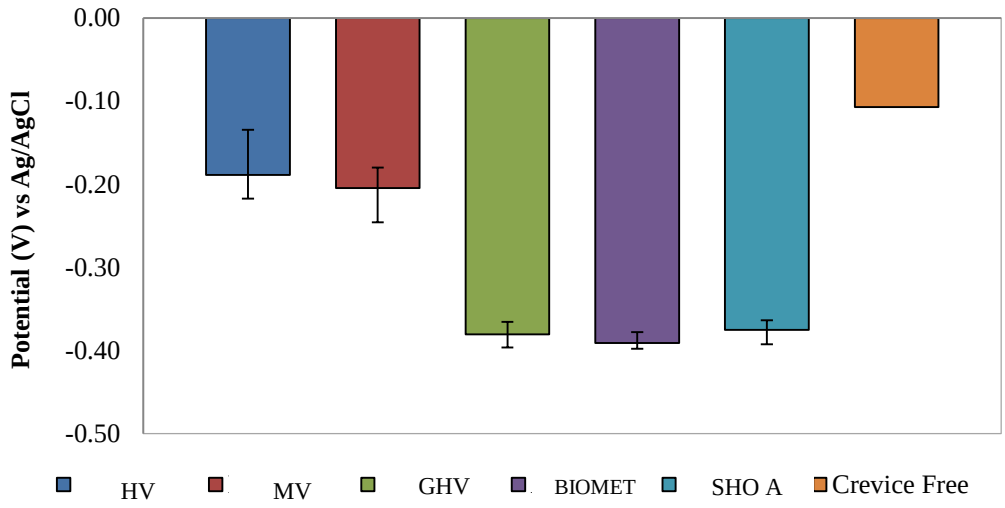

Figure 7-12 - E_{corr} when stabilised to a rate of change ≤ 3mV/sec for 316L stainless steel with commercially available bone cements (n=3±SD)

Figure 7-13 demonstrates the E_b measurements obtained from the potentiodynamic curves. It can be seen that the cements containing antibiotics demonstrated a lower breakdown potential, indicating that the antibiotic in the bone cement increases the susceptibility to localised corrosion for 316L. 316L stainless steel combined with HV bone cement had the highest resistance to localised corrosion, compared to SHO A, which demonstrated the lowest resistance to localised crevice corrosion.

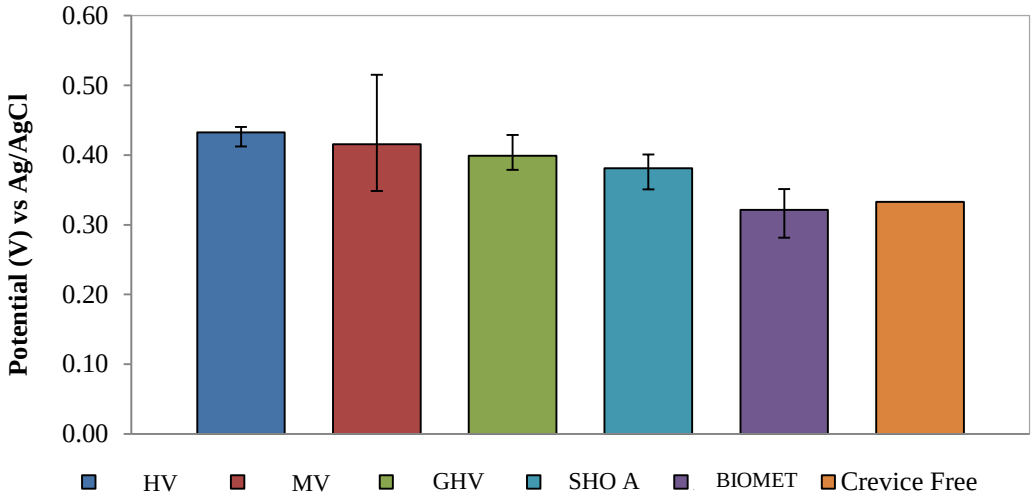

Figure 7-13 - E_b of 316L with commercially available bone cements at a current density of 10µA/cm^2 (n=3±SD)

A similar trend was also observed for the low carbon CoCrMo samples. Figure 7-14 demonstrates the initial open circuit potential measurements for CoCrMo samples when the rate of change in E_{corr} was ≤ 3mV/sec. It can be seen that the initial E_{corr} was more negative for the cements containing antibiotic with the exception of the GHV cement. Although E_{corr} measurements are of a semi-quantitative nature, this would suggest that the BIOMET and SHO A cements create an initial environment preferential to localised crevice corrosion.

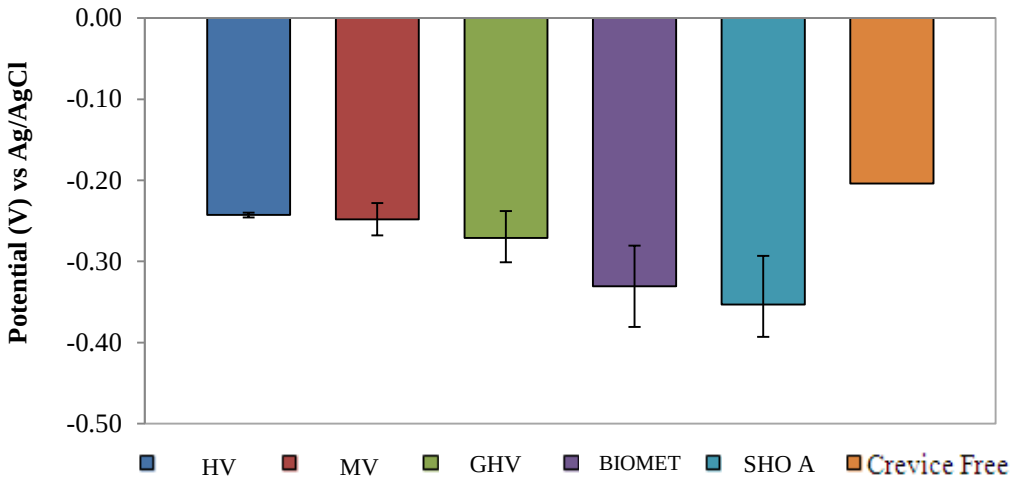

Figure 7-14 - E_{corr} when stabilised to a rate of change ≤ 3mV/sec for CoCrMo with commercially available bone cements (n=3±SD)

The results obtained from the polarisation curves again confirmed the E_{corr} measurements. A similar trend to the stainless steel samples was noted for the CoCrMo samples. A decrease in E_b was seen for samples combined with antibiotic cement, with samples combined with BIOMET cement displaying the worst susceptibility to localised crevice corrosion. Figure 7-15 demonstrates the breakdown potentials for CoCrMo specimens. Samples not fitted with a tapered collar demonstrated an increased breakdown potential, demonstrating that CoCrMo can be susceptible to localised crevice corrosion. Figure 7-16 demonstrates the repassivation potential values obtained for the CoCrMo specimens. The re-passivation potential represents the potential at which the passive film completely reforms during the reverse scan, deeming the surface of the material once again passive. It can be seen that samples combined with HV bone cement demonstrated an increased re-passivation potential, compared to the remaining samples. Figure 7-16 indicates that CoCrMo specimens combined with MV, GHV, BIOMET and SHO A had a similar repassivation potential.

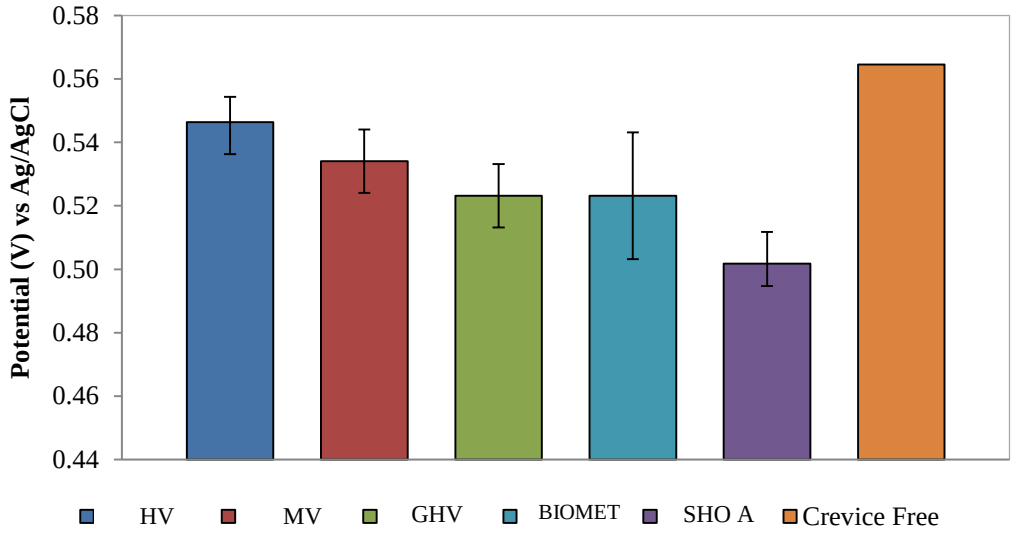

Figure 7-15 - E_b of low carbon CoCrMo with commercially available bone cements (n=3±SD)

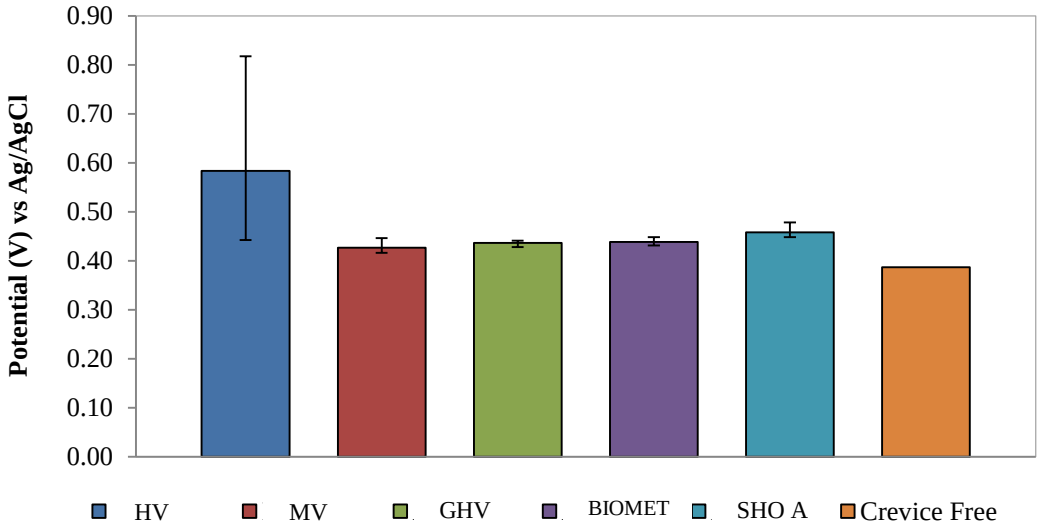

Figure 7-16 - E_r of low carbon CoCrMo with commercially-available bone cements (n=3±SD)

Crevice free samples were conducted as a control. In all cases a more noble E_{corr} and E_b values were seen demonstrating that the formation of a crevice can increase a material's susceptibility to localised crevice corrosion. It is interesting to note that the LC CoCrMo crevice-free specimen demonstrated the lowest repassivation potential. This suggests that the extent of corrosion was increased on crevice free samples. This is thought to be attributed to the type of corrosion taking place.

7.3.2. Surface Morphology after Accelerated Testing

Surface analysis of the samples was also carried out to quantify the type of corrosion on the surface of the materials. Initiation and propagation of localised corrosion was seen on the 316L samples, with a macroscopic difference being seen between the samples combined with the antibiotic cement. Figure 7-17a-b shows the optical images taken on 316L after polarisation. Scanning Electron Microscopy (SEM) images indicated a thick layer of corrosion product was present on the surface of 316L samples combined with HV, MV and GHV cements (Figure 7-18a). EDX analysis suggested that the layer of corrosion product was rich in Cr, O and Cl, with traces of Fe and Mn suggesting the formation of a chromium oxide corrosion product. Area 'A', on Figure 7-18b demonstrates the passive areas outside of the crevice; area 'B' demonstrates the active areas within the crevice. It is clear to see that a substantial amount of electrochemical damage has occurred as a result of localised crevice corrosion. Intergranular corrosion was also visible on all of the 316L specimens apart from specimens combined with the MV cement. In all cases SEM analysis indicated that localised crevice corrosion had occurred, with clear and visible areas of localised crevice corrosion being observed on each 316L stainless steel sample.

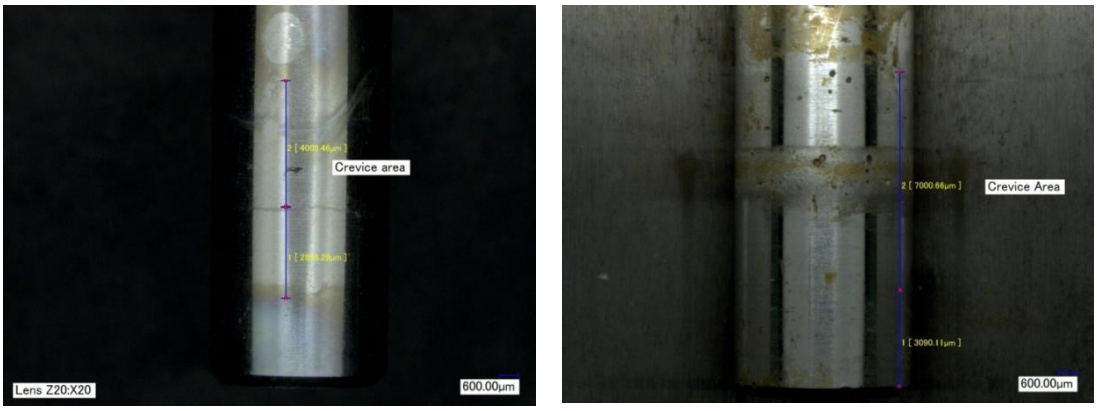

(a) **(b)**

Figure 7-17 - 316L Stainless steel with a) HV and b) SHO A PMMA bone cements

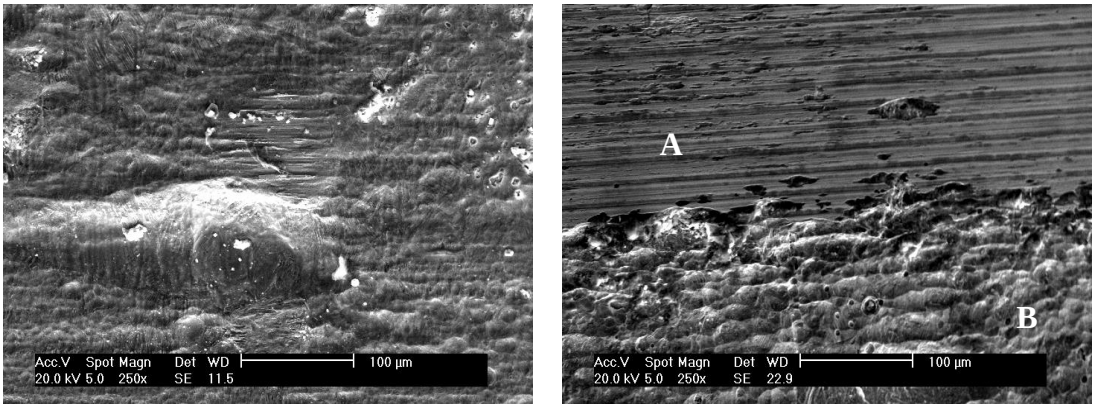

(a) **(b)**

Figure 7-18 - SE SEM images of a) corrosion product within the 316L and GHV bone cement crevice and b) crevice corrosion profile of the HV sample

SEM analysis was also conducted on the LC CoCrMo samples although the extent of localised corrosion was not as great due to the higher integrity of the alloy (Figure 7-19a-b). The enhanced localised corrosion resistance results from a more tenacious oxide film compared to 316L, primarily due to the higher Cr content. Small areas of localised corrosion were also noted. Noticeable changes in the surface topography and loss of the initial machining marks on the samples was observed thought to be due to breakdown of the passive film (Figure 7-19b). SEM analysis also complimented electrochemical findings.

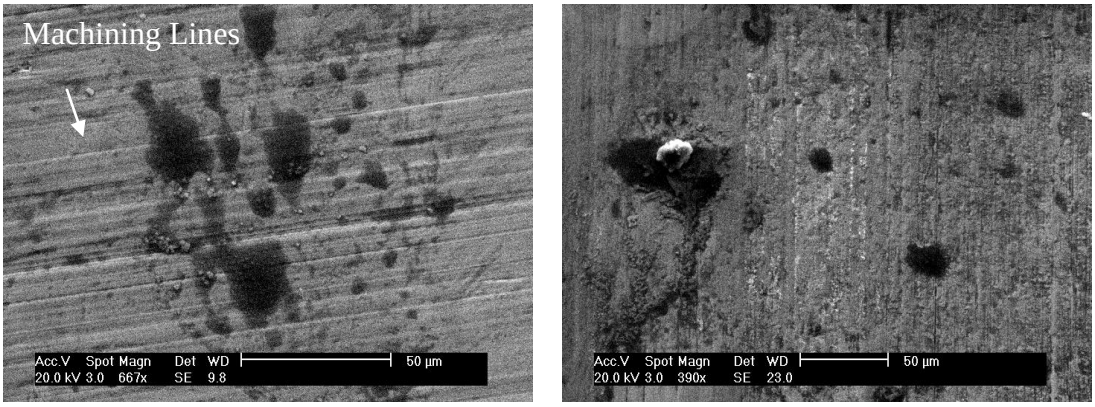

(a) **(b)**

Figure 7-19 - SE SEM image of corrosion product within the CoCrMo and GHV bone cement crevice. Note the clear presence of the machining marks and b) loss of the machining marks and breakdown of the passive film within the CoCrMo and SHO A bone cement crevice

7.3.3. Understanding the Influence of PMMA Bone Cement Chemistry

Cement variation tests were also conducted using the same test method to investigate the effects of different additives in PMMA base bone cement. Concentration and chemistry of the self-prepared cements can be found in the experimental method chapter. Figure 7-20 demonstrates the breakdown potentials that were obtained for the 316L alloy. Results indicate that the addition of antibiotic and radiopaque agents can affect the initiation mechanisms of 316L Stainless steel thus reducing the passivity of the alloy. A decrease from 0.32V to 0.28V was observed when 10g barium sulphate was added to the bone cement. It is worth noting that this is around double that found in commercially available bone cements. However, a decrease from 0.32V to 0.30V was observed when 4g of barium sulphate was added to the base cement.

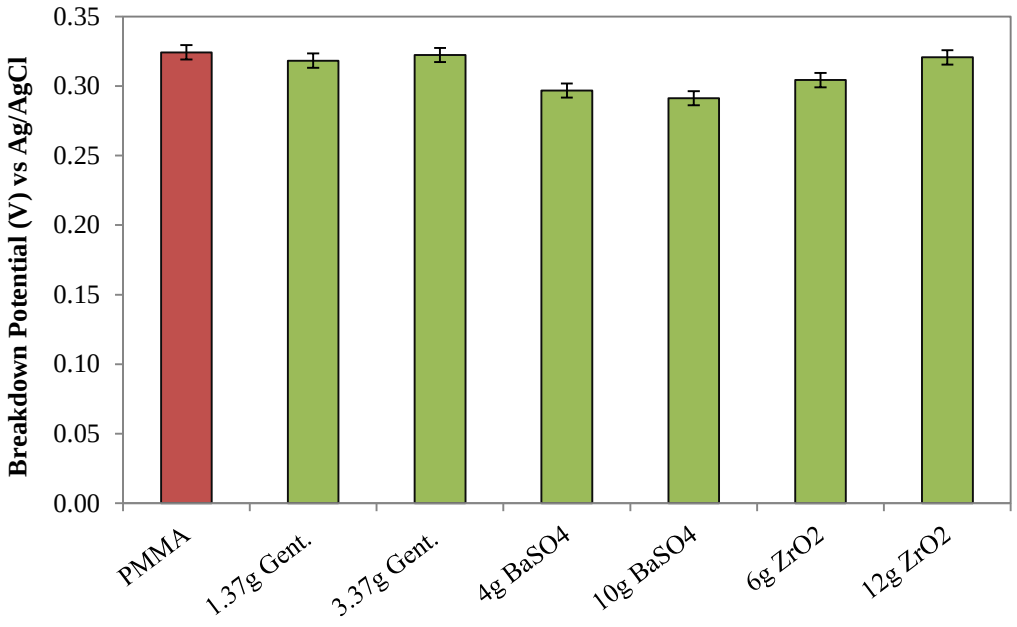

Figure 7-20 - E_b of 316L with different additions (n=3±SD)

Due to the increased passive nature of the LC CoCrMo compared to the 316L stainless steel, the addition of antibiotics and radiopaque agent had no effect with standard deviation on the E_b of the material. However, it was observed that propagation mechanisms of localised corrosion were affected with the addition of antibiotics and radiopaque agents. Propagation of localised corrosion was characterised by, and described as ΔE ($\Delta E = E_b - E_r$). Figure 7-21 demonstrates the ΔE values that were obtained from the CoCrMo samples. When compared with the base PMMA cement the addition of radiopaque agent and antibiotics was seen to influence the propagation mechanisms of localised corrosion.

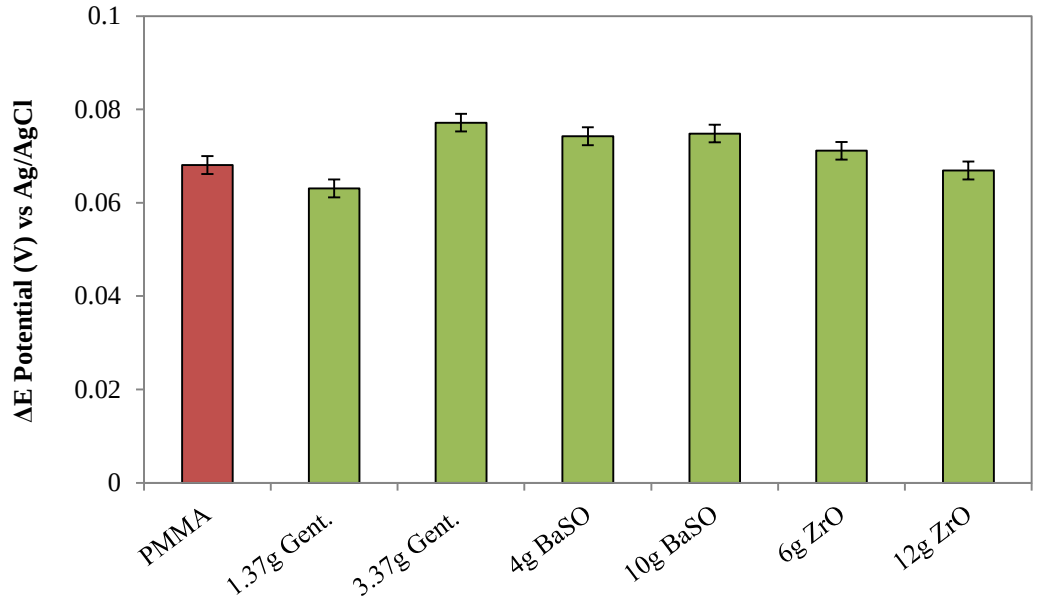

Figure 7-21 - ΔE values for CoCrMo Alloy (n=3±SD)

7.3.4. Influence of Time on Solution Chemistry

To complement the accelerated cement variation tests, seven-day immersion tests were also conducted in order to assess the actual effects of each individual additive on the propagation of localised crevice corrosion. Samples were allowed to freely corrode without the application of external voltage. After seven days immersion, 1mL of bulk electrolyte was extracted using a polymer tipped pipette and stabilised

in 9mL of 2%HNO_3. Inductively coupled plasma mass spectrometry (ICPMS) was utilised to determine concentrations of Co, Cr, Mo and Fe ions released during free corrosion conditions as a result of mass transfer from the crevice to the bulk electrolyte.

Figure 7-22 and Figure 7-23 demonstrate the Co, Cr, Mo and Fe ions released as a result of localised corrosion after seven days immersion. Ion release measurements for 316L stainless steel samples (Figure 7-22) demonstrated that the addition of antibiotic and radiopaque agent into PMMA bone cement can increase the dissolution rate of the alloy resulting in an increase in the total ions released from the metallic sample when compared to the base PMMA bone cement. Perhaps most interesting of all are the ratios in which alloy dissolution occurs.

On average a 9:1 ratio of Fe:Cr was observed for the 316L stainless steel samples combined with base PMMA bone cement collars. After 7 days Cr 52 quantities were seen to increase from 1.09µg/L to 5.06 and 5.58µg/L when 1.68g and 3.36g of gentamicin sulphate, respectively, were added to the base PMMA powder. An increase in Co 52 was also seen when both barium sulphate and zirconium dioxide was added to the base PMMA powder. For the PMMA bone cements containing barium sulphate, an increase in Cr 52 levels to 6.75 and 8.75µg/L for 4g and 10g barium sulphate, respectively were seen.

A similar trend was also seen for 316L stainless steel samples and PMMA bone cement collars containing zirconium dioxide. Increases in Cr 52 to 5.40 and 4.71µg/L were seen for cements containing 6g and 12g of zirconium dioxide again demonstrating that the addition of radiopaque agent can affect the localised crevice corrosion mechanisms of 316L stainless steel. On average, Fe:Cr ratios were seen to vary from approximately 9:1 when a plain PMMA bone cement collar was used to

7.2:2.8, 6:4 and 6.7:3.3 when the additions of gentamicin sulphate, barium sulphate and zirconium dioxide were made respectively. Although increases in Fe 58 were observed when 3.36g of gentamicin sulphate and 10g of barium sulphate, these increases were within standard deviation.

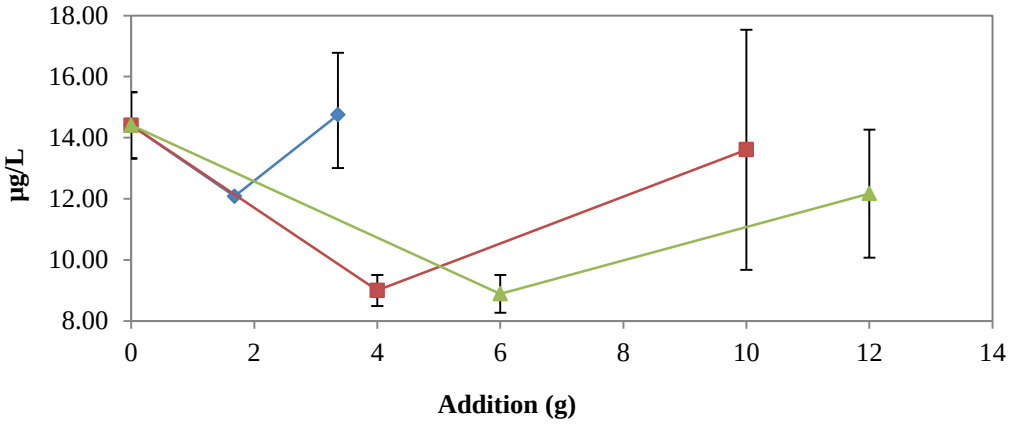

(a)

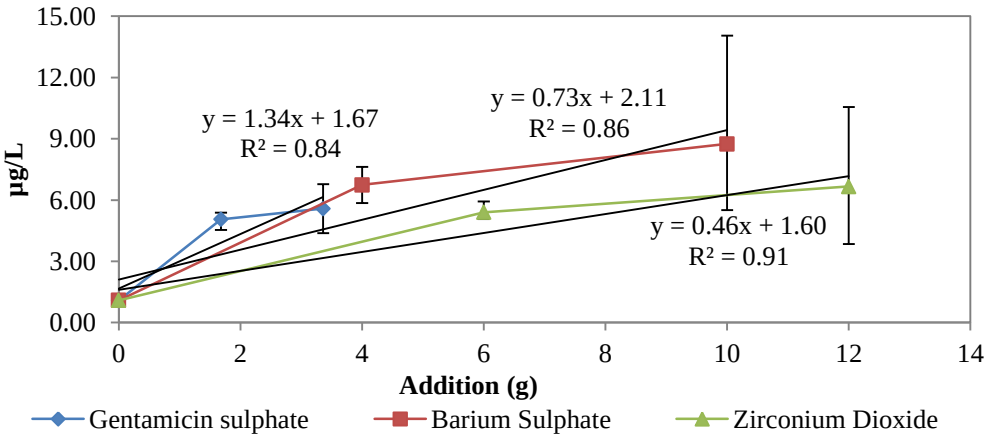

(b)

Figure 7-22 - Quantities of (a) Fe 58 and (b) Cr 52 after 7 day immersion at 37°C from 316L stainless steel (n=3±SD)

Figure 7-23 demonstrates the quantity of metal ions released from the LC CoCrMo with varying PMMA bone cement collars. On average, increased quantities of Cr 52 were seen when additions of gentamicin and barium sulphate were made in agreement with the results for stainless steel. Cr 52 was seen to increase from 3.49 to 4.4 and 5.38µg/L when 1.68 and 3.68g gentamicin sulphate were added to the base PMMA bone cement collars. A change in the stoichiometry in which dissolution had occurred was seen. For the plain PMMA bone cement collars a stoichiometric release of the alloy in the ratio of 6:3:1 (Co:Cr:Mo) was seen. This was seen to vary to approximately 5:4:1 when additions of gentamicin sulphate were made. A similar phenomenon was seen when additions of barium sulphate were made to the base PMMA bone cement. An increase in Cr 52 was seen from 5.01 and 5.44µg/L when compared to the base PMMA bone cement collars with the addition of 4 and 10g of barium sulphate to the base PMMA bone cement collars, respectively. Again, a change in the stoichiometry in which the alloy was observed to approximately 5.2:3.7:0.9 when additions of barium sulphate were made. No increase in Co 59 ions outside standard deviation was observed in all but one test. An increase in Co 59 was observed increasing from 7.04 to 8.22µg/L when an addition of 10g barium sulphate was made. It was interesting to note that there was no increase in Co 59, Cr 52 or Mo 96 outside standard deviation in tests with the addition of zirconium dioxide. The stoichiometry of ions released from the LC CoCrMo samples combined with PMMA cement collars containing zirconium dioxide collars was similar to the collars containing no additions.

When considering the change in ionic mass loss with respect to the difference of each addition made$\left(\frac{\Delta c}{\Delta g}\right)$, clear and differences with respect to standard deviation the how each additive affects the rate of dissolution. Because the level of mass added to

each cement was not consistent between additives, $\frac{\Delta c}{\Delta g}$ was used as a method to identify which additive had the dominant effect with respect to localised dissolution. Table 7-3 demonstrates how each addition affects the overall dissolution with respect to quantity added.

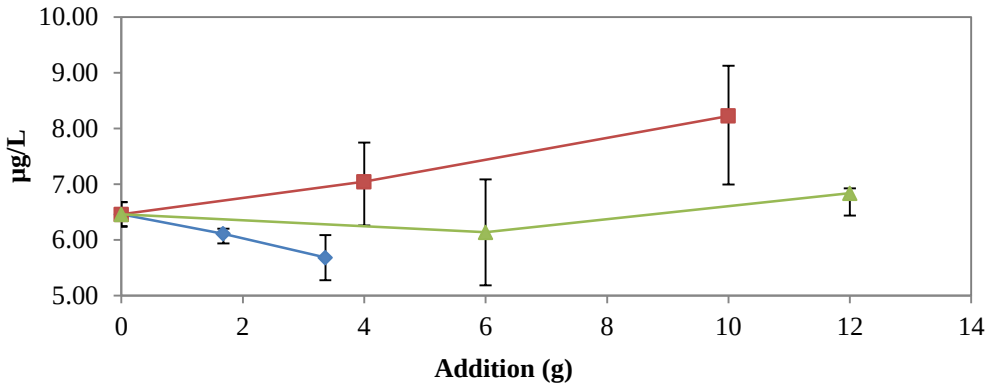

(a)

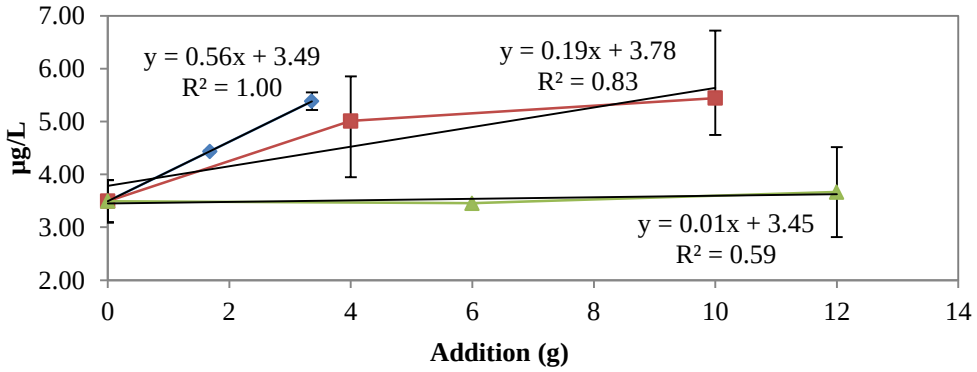

(b)

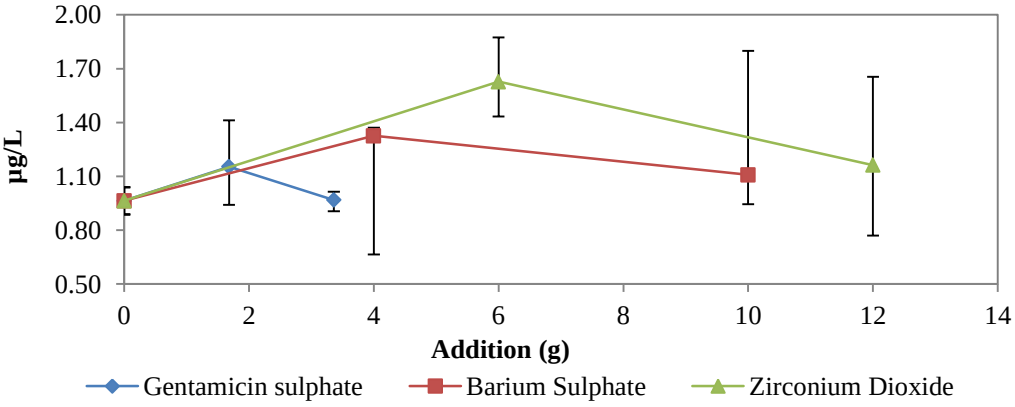

(c)

Figure 7-23 - Quantities of (a) Co 59 (b) Cr 53 and (c) Mo 96 after 7 day immersion at 37°C from LC CoCrMo alloy(n=3±SD)

Table 7-3 – Average change in concentration of Cr 52 released with respect to mass of additive present in the PMMA bone cement (n=3)

Material	Gentamicin Sulphate	R^2	Barium Sulphate	R^2	Zirconium dioxide	R^2
316L	1.34	0.84	0.73	0.86	0.46	0.91
LC CoCrMo	0.56	1.00	0.19	0.85	0.014	0.59

7.4. Effects of Crevice Acidification on Sulphate Elution from Antibiotic Containing PMMA Bone Cements

Initial studies were also conducted in order to investigate the role of crevice environment on the elution of sulphates from the PMMA bone cement. It is well acknowledged, and has been previously discussed in this thesis, the importance of crevice acidification in the initiation and propagation mechanisms of localised corrosion. From the initial cement variation test, it has been demonstrated that the presence of sulphate can have a influence on the initiation and propagation mechanisms of localised crevice corrosion. This simple study was therefore aimed at investigating the role of crevice solution acidification on the dissolution of sulphate from the cement into the bulk solution.

In order to do this 72hr immersion tests were conducted in which PMMA bone cement cylinders (surface area= 33.37cm^2) were immersed in 100mL of 0.9% NaCl at 37˚C in a pH of 7.4 and 2. Intermittent elution samples were taken at 1, 3, 5, 7, 9, 24, 48 and 72hrs and analysed with IC. BIOMET and GHV PMMA bone cements were utilised as they are both sulphate containing PMMA bone cements. HV (ZrO_2 only) was utilised as a control sample in which immersion tests were conducted for 27hrs.

Figure 7-24 demonstrates the cumulative sulphate release over 72hrs from PMMA bone cement as a function of pH. It can be seen that as pH decreases, the quantity of sulphate released from the PMMA bone cement surface increases with the BIOMET resulting in the highest elution of sulphate into the bulk environment at both a pH of 2.0 and 7.4. There were no measurable increases in sulphate from the HV PMMA bone cement.

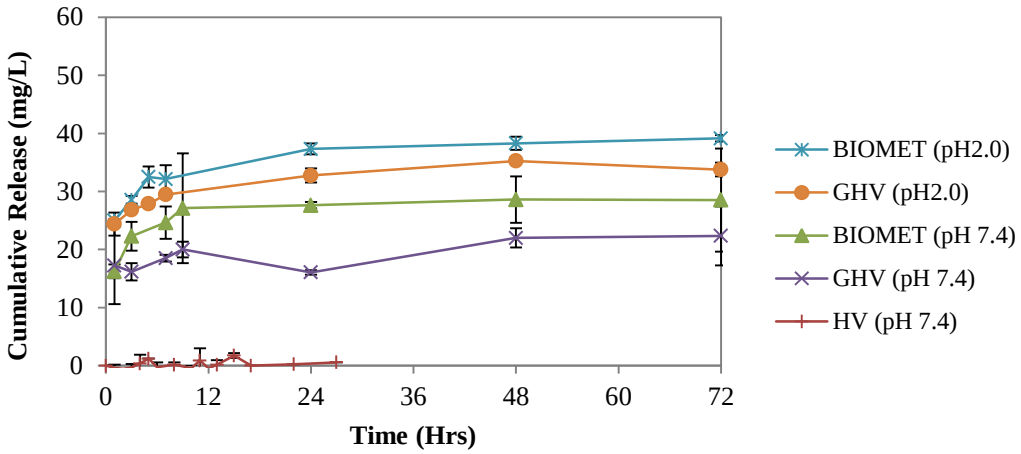

Figure 7-24 - Cumulative sulphate release over 72hrs from PMMA bone cement as a function of pH (n=3±SD)

Conversion of the cumulative release into release rate indicated a high initial release of sulphate followed by a rapid decay for each cement within 24hrs (Figure 7-25). This was the case for each cement at both pH levels. An increased release rate was seen for samples in solutions adjusted to a pH 2. An initial release rate of $25mgL^{-1}Hr^{-1}$ was observed for both cements in an acidic environment, compared to 17.26 and $16.2425mgL^{-1}Hr^{-1}$ for GHV and Biomet cements, respectively, in a neutral environment. In each case, the BIOMET PMMA bone cement was seen to have an increased sulphate release rate when compared to the GHV cement. This is due to the increased sulphate content of the PMMA bone cement, resulting in a higher concentration of sulphate at the surface of the PMMA samples in which elution into

the bulk environment can occur. With time, release rates were seen to tend to zero, with the maximum amount of eluted sulphate being seen at 192hrs which can be taken as an estimate of the total amount sulphate released. This has been summarised in Table 7-4.

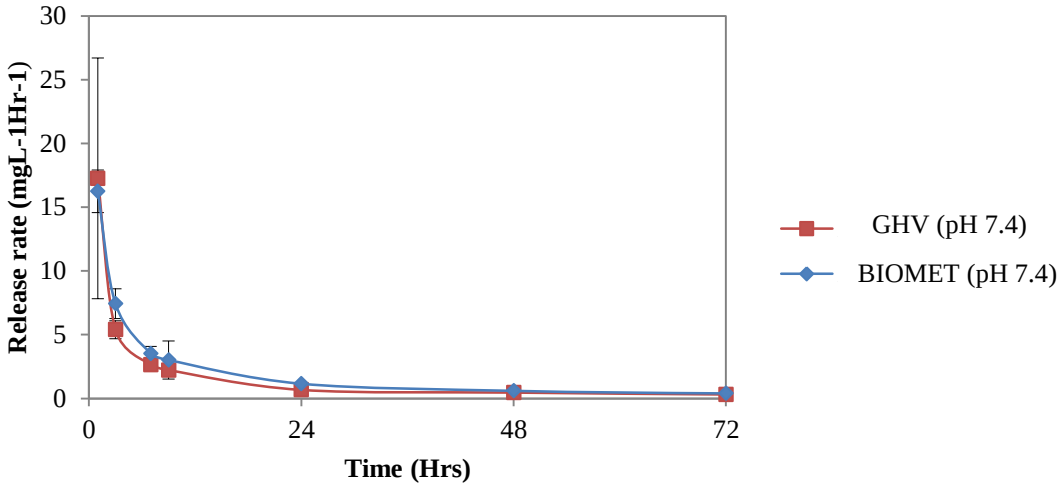

(a)

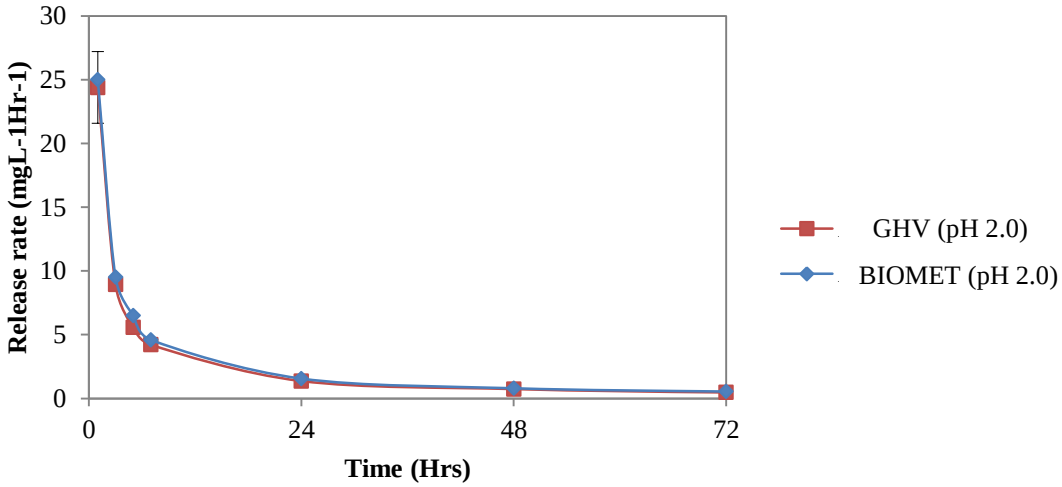

(b)

Figure 7-25 - Sulphate release rates from DePuy GHV and Biomet R+G at pH of a) 7.4 and c) 2.0 (n=3±SD)

Table 7-4 - The initial release rate and total release rate of sulphate in 0.9% NaCl at a pH of 7.4 and 2.0 (n=3±SD)

	Initial release rate ($mgL^{-1}Hr^{-1}$)	Total release after 192hrs (mg/L)	Initial release rate ($mgL^{-1}Hr^{-1}$)	Total release after 192hrs (mg/L)
Cement	pH 7.4		pH 2.0	
HV	0	0	-	-
GHV	17.26±9.43	15.37±1.56	24.39±0.22	48.18±0.12
GHV	16.24±1.76	23.15±3.22	25.00±0.37	44.12±9.20

7.5. Discussion

Electrochemical measurements have indicated that the composition of the bone cement can influence a metal's response to localised corrosion. For 316L stainless steel and CoCrMo it can be seen that when a metal is combined with sulphate containing cements, an increase in susceptibility to localised corrosion can occur. Findings in this chapter can be summarised into the following:

1. Electrochemical measurements indicated that for both materials, the presence of sulphate in the bone cement can increase a material's susceptibility to localised crevice corrosion.
2. It was found that the HV bone cement had an increased resistance to localised crevice corrosion whilst the BIOMET and SHO A bone cements were identified as the most susceptible to localised corrosion. This is thought to be attributed to a high gentamicin sulphate and a compounding effect existing between sulphate containing antibiotics and radiopaque agents resulting in an increased concentration of sulphate ions within the interface.

3. A higher repassivation potential for CoCrMo samples when combined with HV bone cement was noted, compared to samples combined with sulphate containing bone cements.
4. A decreasing pH was seen to increase the sulphate levels released from PMMA bone cement

The presence of sulphate ions is known to affect the corrosion characteristics of a material, being associated with shifting the breakdown potential in the cathodic direction and increasing current density indicating that the presence of sulphate ions will inhibit pit initiation. The presence of chloride ions has been associated with pit initiation. However, once a pit has been initiated, pit growth dominates due to the presence of sulphate ion [182, 183].

As well as producing a novel test method capable of assessing and ranking a material in terms of its resistance to crevice corrosion when combined with different PMMA bone cements, the effects of different additives and additive concentrations could be investigated whilst creating consistent and repeatable findings. The results presented in this study are from a simple design of experiments consisting of few variables, none the less the results obtained allow us to further the knowledge of how different constituents affect the localised corrosion mechanisms occurring at the stem-cement interface. The results in this study have shown that for LC CoCrMo, the addition of radiopaque agents and antibiotic were seen to have little effect on the initiation mechanisms of localised crevice corrosion. However, the amount of propagation was seen to vary with the addition of radiopaque agents. Conversely, for the 316L samples it was found that the addition of such additives affected the initiation mechanisms, with the addition of barium sulphate reducing passivity the most when compared to a plain PMMA base cement.

Ion release measurements after 7 day immersion further strengthened the argument that the addition of antibiotic and radiopaque agents can influence the localised crevice corrosion of biomedical alloys. For the 316L stainless steel samples, the addition of antibiotic and radiopaque agent was seen to increase the amount of Cr 52 released as a results of localised crevice corrosion, with barium sulphate again seen to have the predominant effect. A similar effect was also seen for the LC CoCrMo samples when combined with PMMA bone cement collars with varying chemistry. Ion measurements again complimented electrochemical measurements, demonstrating that the addition of antibiotic and radiopaque agent can affect the initiation and rate of propagation once localised crevice corrosion is initiated. One hypothesis is that the introduction of radiopaque and antibiotic agents into the PMMA bone cement may cause favourable conditions for the initiation and propagation of electrochemical corrosion due to the introduction of aggressive anions into the cement chemistry.

Antibiotics are commonly used in sulphate form to ensure their solubility *in-vivo* and have been shown to leach out of the bone cement over time from exposed surfaces and pores [44]. It is thought that this leaching out of antibiotics from the PMMA bone cement may result in an addition of sulphate ions within the crevice, creating conditions favourable of crevice corrosion. It is generally accepted that sulphate ions can inhibit metastable pitting and the initiation of active pits whilst increasing the rates of propagation once pitting has been initiated on stainless steels and other alloys [172, 184, 185]. However a study by Newman et al [183] demonstrated that the addition of sulphate had an unexpected effect of lowering the critical pitting temperature of austenitic stainless steels at sufficiently high enough concentrations. Due to the restricted geometry of the crevice and the temperature both *in-vivo* and *in-vitro*, it is expected that a high concentration of SO_4 will be

present due to the elution of antibiotics at the interface creating conditions preferential for the propagation of localised pitting. Barium sulphate is also extensively used as a radiopaque agent to enable the bone cement to be visible under radiographs and has been shown to influence dissolution rates. However it is unknown if the barium sulphate leaches out through similar mechanisms as the antibiotics or if disassociation of the Ba and SO_4^- occurs further influencing the chemistry of the crevice solution. This elution could serve to reduce the pH within the interface or simply increase the conductivity of the solution at the interface.

Although the release of prophylaxis from PMMA bone cements has been extensively researched, the effects of pH and overall sulphate release has, to the authors knowledge, never been investigated. This preliminary study has identified, that not only is sulphate released from the PMMA bone cement as expected, the quantity in which it is released is relatively high compared to the literature often using fluorescence polarisation immunoassay techniques [44]. Table 7-5 presents a comparison of total amounts of gentamicin released at eight days at a pH of 7.4 from related literature.

Table 7-5 - Comparison of gentamicin release levels at 8 days at pH7.4

Reference	Total antibiotic release at 192hrs (µg/mL = mg/L)
Moojen et al [186]	27.50
Frutos Cabanillas et al [187]	0.55
Hendriks et al [188]	6-8 (bulk solution) 4000 (in 6µL gap)
Neut et al [189]	1.8-2.8

It was also surprising to see that pH had a substantial effect on increasing the overall sulphate content. A three and two-fold increase in sulphate content was seen for the DePuy GHV and Biomet R+G when immersed in 0.9% NaCl at a pH 2.0. Such an observation has not been presented before and the reasons for this observation are not fully understood and thought to be out of the scope of this thesis. However it is thought that as the pH decreases, the solubility of the gentamicin sulphate increases, increasing the rates of sulphate release. Further studies are needed in order to quantify the influence of pH, as well as the interactions between gentamicin sulphate and $BaSO_4$, with respect to the overall levels of sulphate dissolution.

Although the cement elution studies are limited, the results produced are extremely interesting with respect to the role of sulphate within the stem-cement interface. Electrochemical tests have shown metal ion levels to increase and a materials resistance to localised corrosion to decrease with increasing levels of sulphate content of the PMMA cements. It has been hypothesised that this is due to a locally high level of sulphate found at the interface with cement elution studies further supporting this. It is anticipated that sulphate levels will become extremely concentrated having a significant influence on the dissolution.

Another interesting part of this study was the ratios of which Co 59, Cr 52 Mo 96 and Fe 58 were released from the bulk alloy. In this study a preferential release of Cr 52 was seen after 7days immersion. Lott *et al* [190] presented a study describing the dissolution of 304 stainless steel in artificial crevice conditions over 48hrs. Lott demonstrated that solution chemistry varied with respect to the different stages of crevice corrosion and hypothesised that Cr formed a non-equilibrium surface oxide by combining with dissolved oxygen. Initial increases in chromium were seen, whilst Fe was observed after breakdown of the passive film had begun. As a result

the pH of the crevice solution decreased as the Cr^{3+} were hydrolysed and precipitated out of the crevice.

In the case of 316L stainless steel and LC CoCrMo it is thought that when the alloy is first immersed, the alloy is free to actively corrode until a protective chromium hydroxide film is formed. Dissolution of the Cr rich passive films occurs resulting in the formation of chromium hydroxide and a decrease in pH within the crevice. It is thought that Cr^{3+} quantities will preferentially increase until complete localised dissolution of the chromium rich passive film has occurred, resulting in an increase of ions associated with the bulk alloy been released and a gradual change in crevice solution. This process is then thought to be accelerated by the presence of aggressive anions mentioned above that will further contribute to the dissolution rate of the alloys. It has been shown for cemented LC CoCrMo femoral stems subjected to long term static corrosion tests (>60 days) that a stoichiometric release of Co:Cr:Mo was seen, supporting the theory proposed by Lott [190].

It is important to fully understand how the chemistry of PMMA bone cement can impact upon the degradation of biomedical alloys. It has been shown in many studies that the introduction of micro-motion at the stem cement interface can accelerate the localised dissolution processes by mechanical removal of the passive film. It is thought that the combination of mechanically enhanced dissolution of a metallic surface, in the presence of high concentrations of aggressive oxidizing anions could potentially results in conditions aggressive enough to cause rapid and extensive dissolution of a cemented device. Careful consideration must therefore be taken when selecting PMMA bone cements containing sulphate based antibiotics and radiopaque agents.

7.6. Summary

In this chapter, the effects of PMMA bone cement chemistry on the localised crevice corrosion mechanisms of 316L stainless steel and LC CoCrMo has been evaluated using a variety of electrochemical, surface and solution analytical techniques. Findings in this section can be summarised into the following:

- Crevice corrosion has been shown to be a factor effecting the degradation at the stem-cement interface
- The long term corrosion responses of cemented femoral stems have been presented demonstrating different corrosion responses between commercially available bone cements.
- Bone cements containing barium sulphate and antibiotics demonstrated the highest susceptibility to localised corrosion. This was reflected in electrochemical and solution chemistry analysis.
- Accelerated crevice corrosion tests further supported the long term testing demonstrating that PMMA chemistry influences the passivity of biomedical alloys.
- Although cement variation tests demonstrated that addition of barium sulphate affected the initiation mechanisms of localised corrosion on 316L Stainless steel, no other difference outside standard deviation were seen between the two alloys with respect to the initiation of localised crevice corrosion.
- Addition of barium sulphate and antibiotics were seen to have an effects on the propagation mechanism with gentamicin seeming to have the more dominant effects.

- Long term corrosion tests demonstrated a stoichiometric release of metallic ions (according to concentration in the bulk alloy) demonstrating that dissolution of the oxide film and bulk substrate had occurred. Short term dissolution studies demonstrated a preferential release of Cr which can be attributed to the initial dissolution of the Cr rich oxide film.
- Increases in sulphate were seen in acidic conditions when compared to neutral environments. This is thought to significantly influence the propagation stages of localised crevice corrosion, initiated by the de-aeration and decrease in pH within the interface.

CHAPTER 8 – EFFECT OF GALVANIC COUPLING ON THE LOCALISED CREVICE-CORROSION OF CEMENTED FEMORAL STEMS UNDER LONG TERM STATIC CONDITIONS

8.1. Introduction

It is common to study how corrosion contributes to the degradation of biomedical alloys in isolation, by investigating the degradation mechanisms of a subsystem isolated from the entire system. However, in reality this is not the case. Complex electrochemical interactions are likely to exist at modular interfaces due to the implant being electrochemically coupled via their interfaces.

Previously no studies have considered how processes at the stem-cement interface may influence the degradation at the bearing or taper surfaces or vice-versa. The presence of mixed metal systems has been shown to lead to accelerated corrosion of the least noble alloy [191-195] however is not limited to mixed metal systems. In the Ultima TPS™ cohort a titanium acetabular shell was used in order to achieve stable fixation for the CoCrMo liner. This resulted in a surface area ratio of approximately 3:1 (Ti shell: CoCrMo femoral stem). Figure 8-1 presents a schematic representation of the Ultima TPS MoM THR and the associated degradation mechanisms. It is worth noting that although galvanic corrosion is commonly reported to occur in mixed metal systems, it is not limited to mixed metal arrangements.

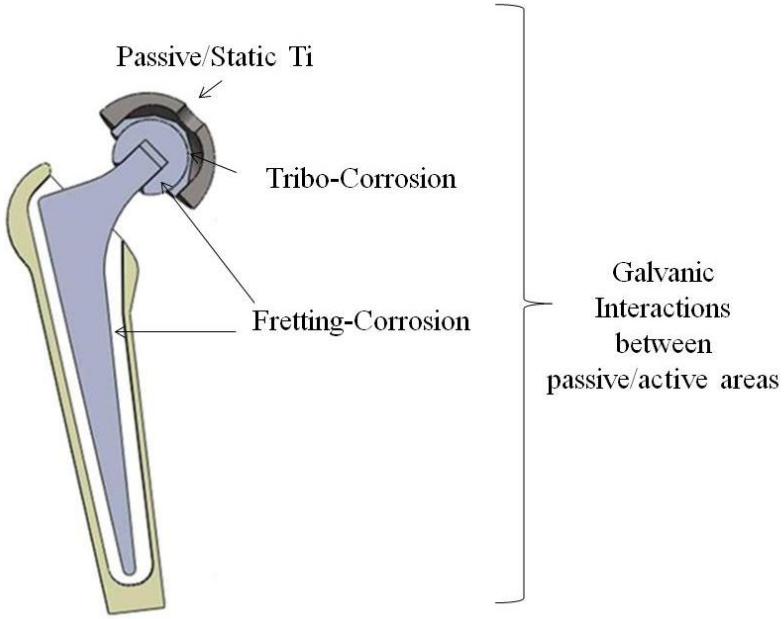

Figure 8-1 - Schematic diagram of the Ultima TPS™ MoM THR construct

The main aim of this chapter is to investigate how the presence of mixed metal systems and galvanic coupling can influence the localised corrosion rates and metal ion release from the stem-cement interface. MoM THRs typically consist of an all metal construct which can be same or mixed metal systems in which different electrochemical potentials will be established across the surfaces. Traditionally research into the degradation mechanisms occurring at the different interfaces has been limited to each interface in isolation.

This chapter aims to introduce and simulate the influences of other interfaces and mixed metal systems in order to study the impact on localised crevice corrosion. Cemented femoral stems were subjected to a variety of different analytical techniques. Electrochemical, ICP-MS and SEM analysis were all utilised in order to quantify the effect PMMA bone cement chemistry plays on the degradation mechanisms of biomedical alloys. During this study, four commonly used PMMA bone cements were tests of which the chemical composition can be found in the experimental materials chapter.

8.2. Test Arrangement

In order to facilitate galvanic corrosion measurements long term immersion tests, as mentioned in the materials and method chapter, were adopted. In addition to this a Ti ring, as described in Chapter 3.5.1.4, with the same surface area as the acetabular shell used in the Norwich cases (total surface area = 139.64cm^2) was manufactured and immersed with the cemented femoral stems. Each femoral stem and Ti ring was then electrochemically coupled via ZRA arrangement facilitated by a potentiostat (Figure 8-2). The net galvanic corrosion current and mixed open circuit potential were observed as a function of time in order to understand the presence of mixed metal systems plays on the localised corrosion rates at the stem-cement interface.

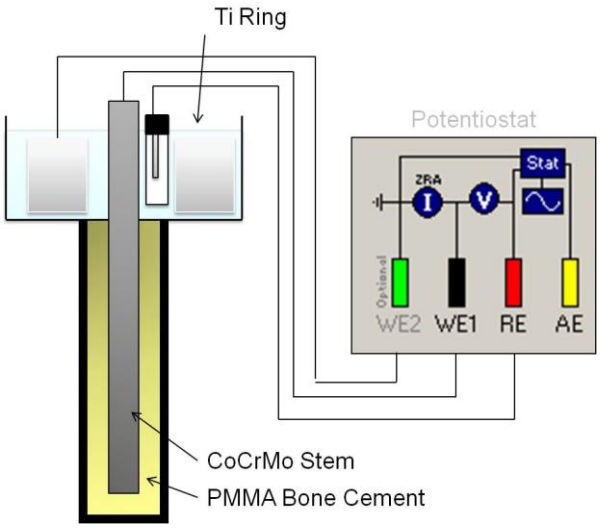

Figure 8-2 - Experimental setup to facilitate galvanic corrosion measurements

8.3. Galvanic Corrosion Theory

When two metals of alloys are joined such that electron transfer can occur between them in an electrolyte galvanic corrosion occurs. Coupling causes the corrosion potentials and corrosion currents to change from the values of that seen for the uncoupled materials. The magnitude of current shift depends on the potential and

area differences between anode and cathode and the relative rates of reactions. The relationship between measured current (I) and over-potential of a metal relative to the free corrosion potential (η) with corrosion current (I_{corr}) can be described by the Butler-Volmer equation.

Equation 8-1 – Butler-Volmer Equation

$$I = I_{corr}\left[exp\left(\frac{2.3\eta}{\beta_a}\right) - exp\left(-\frac{2.3\eta}{\beta_c}\right)\right]$$

β_a and β_c are the Tafel slopes for the anodic and cathodic reaction occurring on the metal. When the corroding metal is electrically coupled to another metal or passive/active areas, its free corrosion potential (E_{corr}) is shifted in the noble direction to the mixed corrosion potential (E_{mixed}) and its dissolution current will increase from I_{corr} to I_a (Equation 8-2). According to Equation 8-1 the cathodic term becomes insignificant at an over potential greater than 0.05V

Equation 8-2 - Anodic current resulting from galvanic coupling

$$I_a = I_{corr}\left[exp\left(\frac{2.3\ E_{mixed} - E_{corr}}{\beta_a}\right)\right]$$

The galvanic current (I_g), which can be measured by a ZRA arrangement, is the net current measurement and is the difference between the partial anodic and cathodic reaction occurring on the corroding metal at E_{mixed}. Due to the formation and reformation of an oxide film after depassivation, the rate of reduction of the oxygen on the surface of the anode and cathode are not equal. Therefore the following relationship and assumption (Equation 8-3) that is presented in many tribocorrosion studies does not hold and will result in an underestimation of the actual corrosion rates of the surfaces.

Equation 8-3 - Relationship between anodic current and galvanic current at high over potentials assuming no further reduction on the anode surface

$$I_a = I_g$$

Because further reduction on the surface to reform the metal oxide occurs, I_g is given as:

Equation 8-4 - Galvanic current expressed as the difference of anodic and cathodic reactions occurring on the metals' surface

$$I_g = I_a(E_{mixed}) - I_c(E_{mixed})$$

According to the galvanic series and current literature, as well as the electrochemical data already collected, the galvanic potential of Ti-CoCrMo couples will be similar to the corrosion potentials of the uncoupled materials putting the system in the mixed potential region (i.e. not in the Tafel region). This results in both anodic and cathodic reactions occurring on the anode with significant effect on the rate of anodic dissolution. For this case:

Equation 8-5 - Relationship between dissolution and galvanic currents

$$I_a = I_g + I_{corr}\exp\left(-\frac{2.3\ E_{mixed} - E_{corr}}{\beta_c}\right)$$

Equation 8-5 can also be presented to demonstrate the influence of area ratio effects. It can be seen that as the area of the cathode increases, the amount of current attributed due to galvanic coupling increases significantly.

Equation 8-6 - Influence of area ratio on the overall anodic, galvanic and self-corrosion currents

$$\frac{I_a}{A_a} = \left(I_g\frac{A_c}{A_a}\right) + \left(\frac{I_{corr}\exp\left(-\frac{2.3\ E_{mixed} - E_{corr}}{\beta_c}\right)}{A_a}\right)$$

In this chapter all currents are presented as absolute current values due to the localised nature of the corrosion. When considering mass losses from the anode due to corrosion, adjustment to all galvanic data has been made according to Equation 8-5.

8.4.Prediction with Mixed Potential Theory

Mixed potential theory was utilised in a preliminary attempt to see if any galvanic interactions occur at the interface prior to long term immersion tests. In order to do this, separate polarisation of the cemented femoral stem and Ti ring was conducted. For polished CoCrMo femoral stems a quick polarisation between scan ±0.05V vs. E_{corr} was conducted. A full cathodic scan was conducted on Ti ring -0.20V vs. E_{corr}. In this region the primary action occurring on the Ti surface will be oxygen reduction.

Mixed potential theory was used to evaluate the electrochemical reactions occurring within the interface, assuming that two partial oxidation and reduction reactions occur with no net accumulation of charge. Figure 8-3 demonstrates the oxidation reaction for polished femoral stems, as well as the oxygen reduction reaction occurring on the Ti. Metallic dissolution will occur at the point where the anodic and cathodic half-cell reactions are equal. It can be seen graphically that the only point in the system where the oxidation and reduction reactions are equal are at the point of intersect known as the mixed potential (E_{mixed}). At this point the rates of reactions are equal satisfying charge conservation. The current density at this point will represent the rate of oxidation and oxygen reduction of the system.

According to Figure 8-3, Ti effectively polarises the CoCrMo stem surface by 0.08V. Assuming that the anodic and cathodic reaction will precede on the CoCrMo and Ti surfaces respectively, corrosion will occur at the point at which the anodic cathodic reactions are equal. It can be seen in Figure 8-3 that the presence of Ti increased the corrosion current from approximately 9.5×10^{-7}A to 1.75×10^{-6}A.

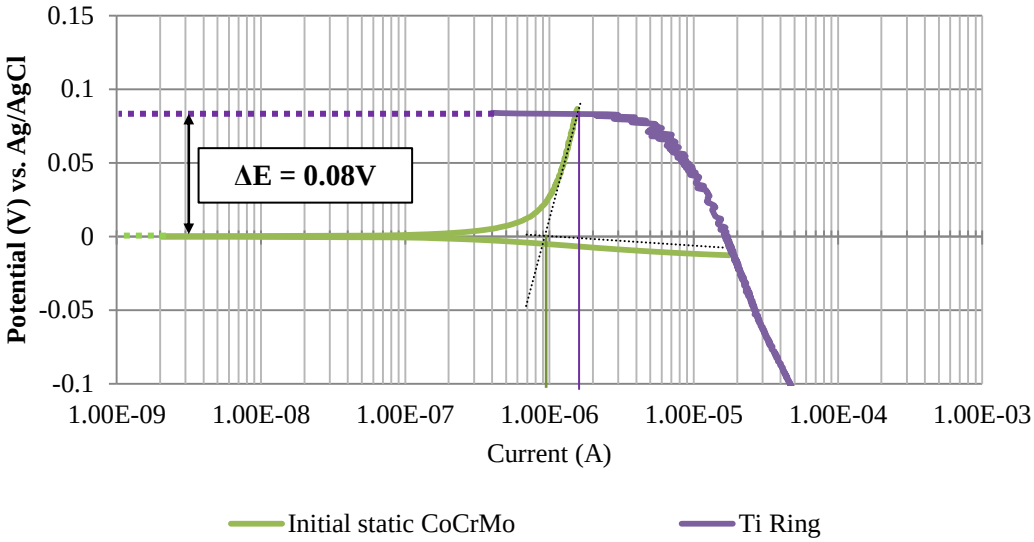

Figure 8-3 - Mixed theory potential prediction of mixed cell potential and galvanic corrosion current of cemented polished femoral stems coupled to Ti

8.5. Electrochemical Response

Figure 8-4 demonstrates the mixed corrosion potential of the LC CoCrMo and Ti when galvanically coupled through a ZRA arrangement. No notable differences outside standard deviation were seen in the mixed corrosion potentials between experimental variables. However when compared to the free corrosion potential measurements (Chapter 6) of uncoupled femoral stems, a 0.04-0.20V increase is seen due to the presence of the Ti. This is an important aspect that needs to be considered when evaluating galvanic corrosion systems as such shifts of corrosion potentials can alter the passive state of a material. Upon immersion, an increase in

E_{mixed} was seen, seeming to plateau after 500hrs (Figure 7-2). No differences outside standard deviation were seen between each repetition.

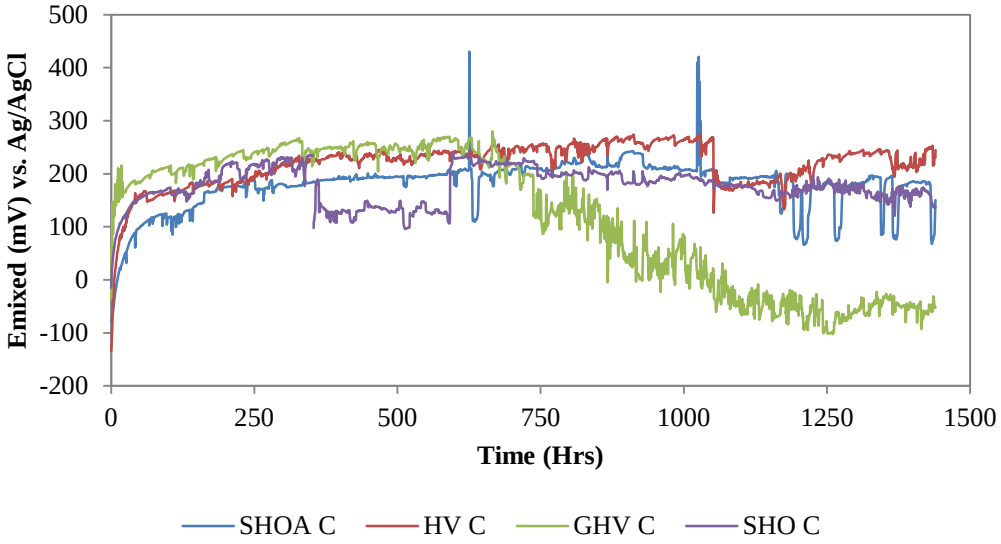

Figure 8-4 – Average mixed corrosion potential of LC CoCrMo femoral stems when galvanically coupled to Ti. 'C' galvanically coupled to Ti (n=3)

Galvanic current measurements were also taken in order to assess the magnitude and direction of current flow when Ti was present. It is important to consider that galvanic corrosion measurements only measure the excess electrons flowing to or from an electrode due to the presence of a mixed metal system and does not consider the number electrons flowing between the active and passive areas present on the femoral stem surface. Figure 8-5 demonstrates the galvanic current measurements over 60 day's immersion. Electrochemical measurements demonstrated a net anodic current flow from the femoral stem to the Ti ring demonstrating a flow of electrons, and release of metallic ions into the bulk solution from the CoCrMo femoral stem. Numerous current transients were also observed typically associated with localised corrosion. Due to the stochastic nature of localised corrosion, it was difficult to observe any differences outside of standard deviation between each experimental

set. The GHV C data presented negative current values (i.e. cathodic reactions taking place on the femoral stem) towards the end of the test.

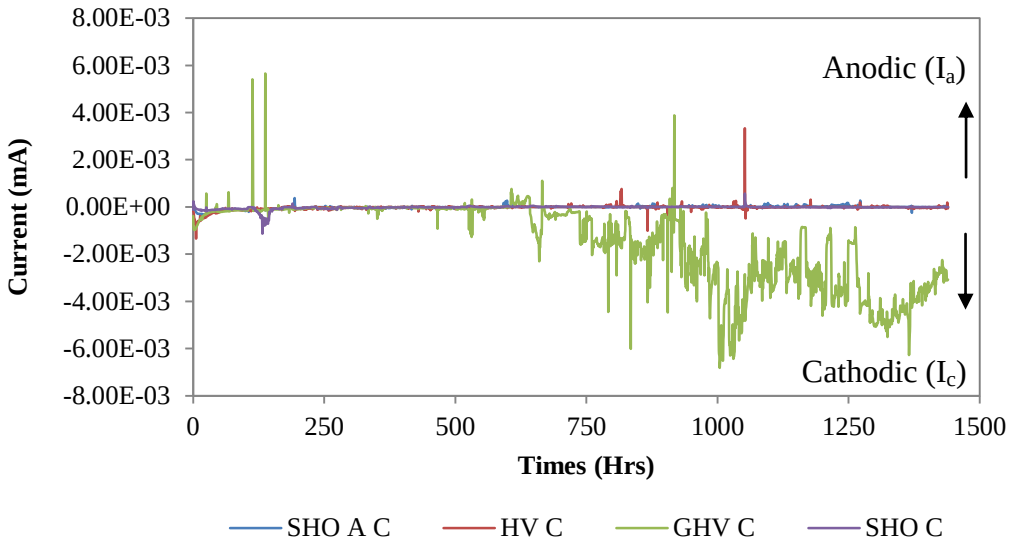

Figure 8-5 – Average galvanic corrosion measurements of cemented femoral stems (n=3)

In order to convert and evaluate the electrochemical data, integration of the current vs. time curve was conducted. An 'IF' command was utilised to sum the total anodic currents, in this case currents with positive convention, as these only associated with anodic dissolution and material loss. Cumulative mass loss with respect to time proved useful to distinguish any differences between each experimental variable. Integration and application of Faraday's law to the net anodic current demonstrated differences in the total mass loss due to corrosion (Figure 8-6). Femoral stems cemented the Stryker Simplex P (SHO C) PMMA bone cement where seen exhibit the lowest mass loss due to corrosion after 60 days immersion with a mass loss of 4.70±0.40µg been observed. In contrast the DePuy GHV PMMA (GHV C) cement was seen to result in the highest mass loss, 20.90±0.9µg.

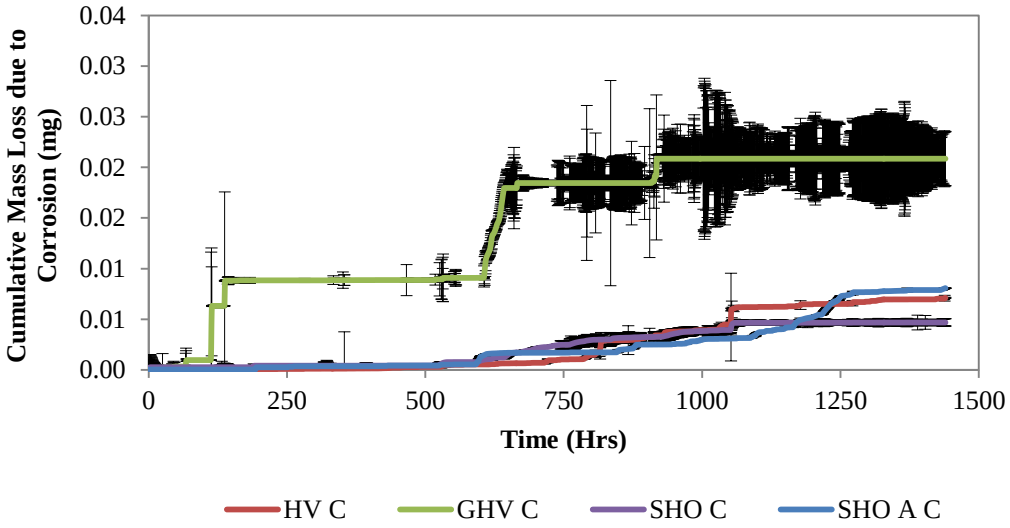

Figure 8-6 - Cumulative mass loss due to corrosion calculated from net anodic galvanic currents (n=3±SD)

Since the dissolution rates from galvanic current do not equal the true dissolution rate of the anode in a galvanic couple it is particularly important to correct and take this into consideration as highlighted earlier. It can be seen in Figure 8-3 that a small potential difference is established between the CoCrMo femoral stem and Ti very much in the mixed potential region where Equation 8-5 is satisfied. Therefore self-corrosion current of the anode will have a substantial influence on the overall rates and must be corrected for according to Equation 8-5. Figure 8-7 demonstrates the relative contributions of self-corrosion current (I_{corr}) and galvanic current (I_g) to the total mass loss from a cemented femoral stem. Due to the small polarising nature of the Ti, the addition of the self-corrosion rates, presented in Chapter 6, increases the overall mass loss due to corrosion. Compensation of reduction of species occurring of the surface of the anode at least doubled the rate of dissolution and contributed a sizable amount to the overall mass lost from the electrode.

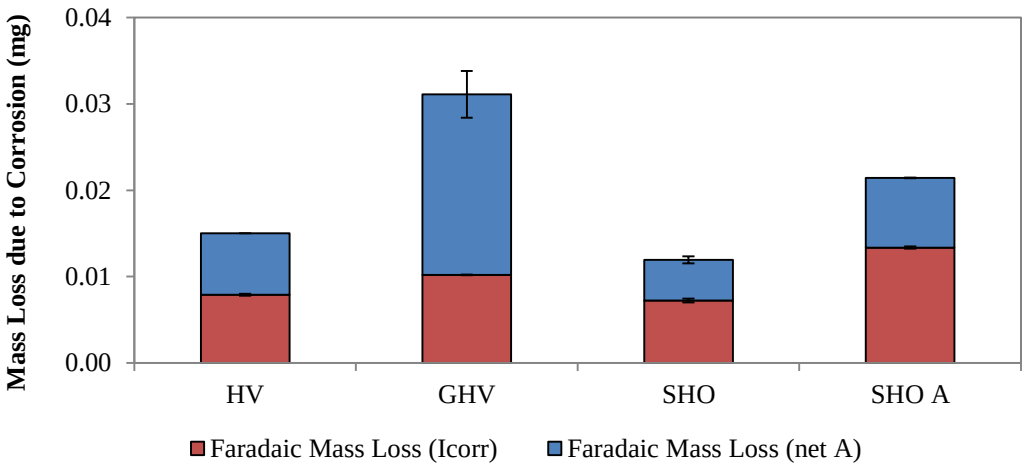

Figure 8-7 - Relative contributions of self-corrosion and galvanic current on the overall ionic mass loss from cemented femoral stems after 60 day's immersion (n=3±SD)

8.6. Solution Chemistry Analysis

ICP analysis was also conducted in order to validate electrochemical data. After 60 days immersion, each electrolyte was drained, stored and prepared according to the method outlined in Chapter 3. Figure 8-8 demonstrates the concentration of metal ions released into the bulk environment due to mass transportation from the stem-cement crevice. ICP-MS analysis demonstrated an increased amount of metal ions when compared to the uncoupled tests.

Increases in the Co 59 concentrations were seen for coupled femoral stems when compared to uncoupled tests. On average, 61.61 - 154.52µg/L of Co 59 was observed for coupled femoral stems. In comparison, Co 59 levels in the region of 11.96 – 35.28 µg/L were observed for uncoupled femoral stems. On average, Cr 52 concentrations of 21.45 - 56.57µg/L were observed for femoral stems coupled to Ti. In contrast, Cr 52 was seen in the region of 17-32µg/L for uncoupled femoral stems. ICP-MS further supported electrochemical data demonstrating that the addition of Ti can increase the rate of dissolution and metal ion production at the stem-cement interface.

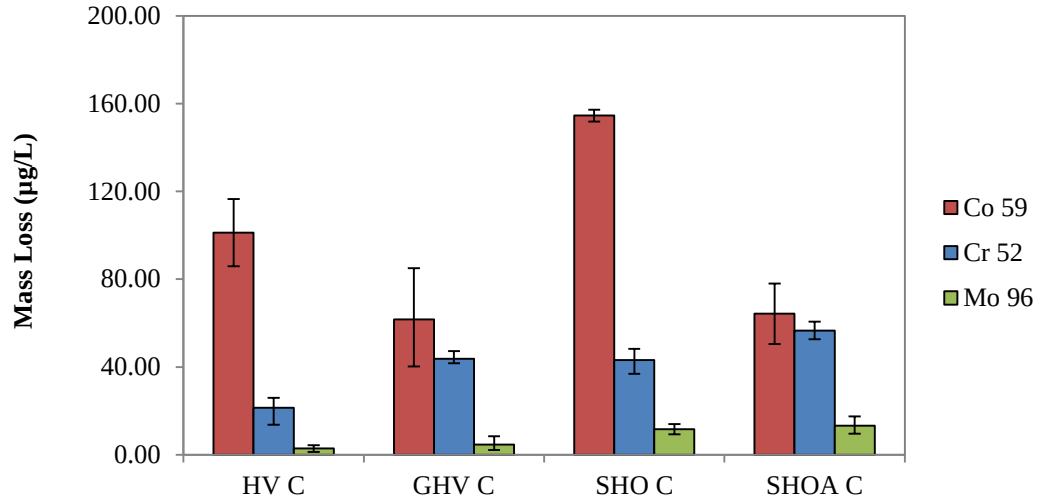

Figure 8-8 - Ion concentrations found in the bulk solution after 60 day's immersion for Ultima TPS femoral stems coupled to Ti (n=3±SD)

Ti levels were also examined to ensure reliability of the electrochemical and ICP-MS data. Ti 48 was seen in concentrations of 0.51±0.53, -1.11±1.17, -0.20±1.82 and 1.72±3.82µg/L for coupled femoral stems cemented with DePuy HV, DePuy GHV, Stryker Simplex P and Stryker Simplex P with Erythromycin and Colistin respectively demonstrating that no measurable levels of Ti were detected in solutions after 60 days immersion.

Figure 8-9 presents a comparison of the mass loss measurements obtained from electrochemical and ICP-MS techniques. A good correlation between electrochemical and ICP-MS data was seen for most samples apart from the samples cemented with the DePuy GHV cement. It is unknown if this error is due to dilution or errors with the electrochemistry as both techniques have fairly good repeatability. Although there seems to be some discrepancy with electrochemical results, a trend still exists demonstrating some differences between the PMMA cements containing sulphate based antibiotics.

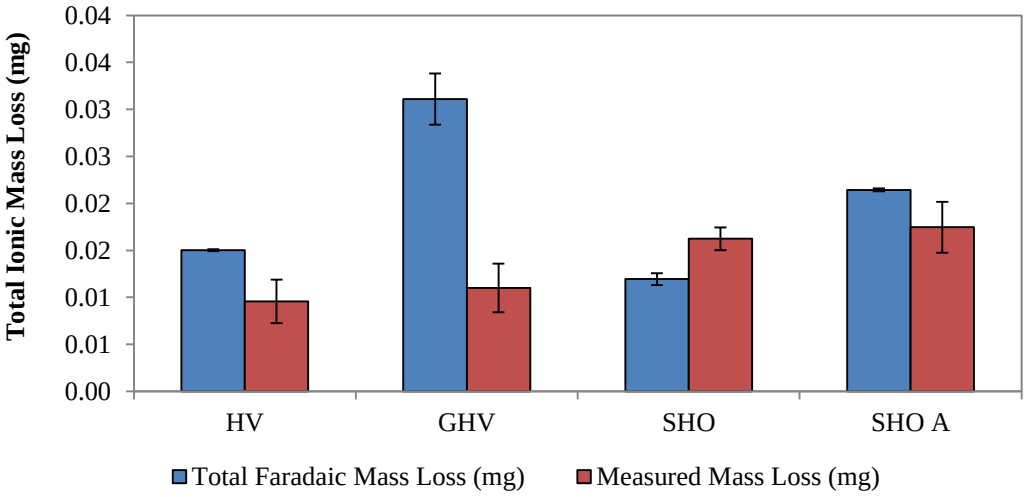

Figure 8-9 - Comparison of mass loss calculated from electrochemical (blue) and ICP-MS (red) techniques (n=3±SD)

8.7. Surface Morphology of Corroded Cemented Femoral stems

Upon removal of the femoral stems, localised corrosion at a macroscopic level could be seen (Figure 8-10). This was seen to occur throughout the surface of the cemented femoral stem. Again, surface analysis confirmed electrochemical findings with femoral stems cemented with sulphate containing PMMA bone cement demonstrating increased amounts of localised corrosion on the surface when compared to the surface profiles obtained in Chapter 6, Figure 6-11.

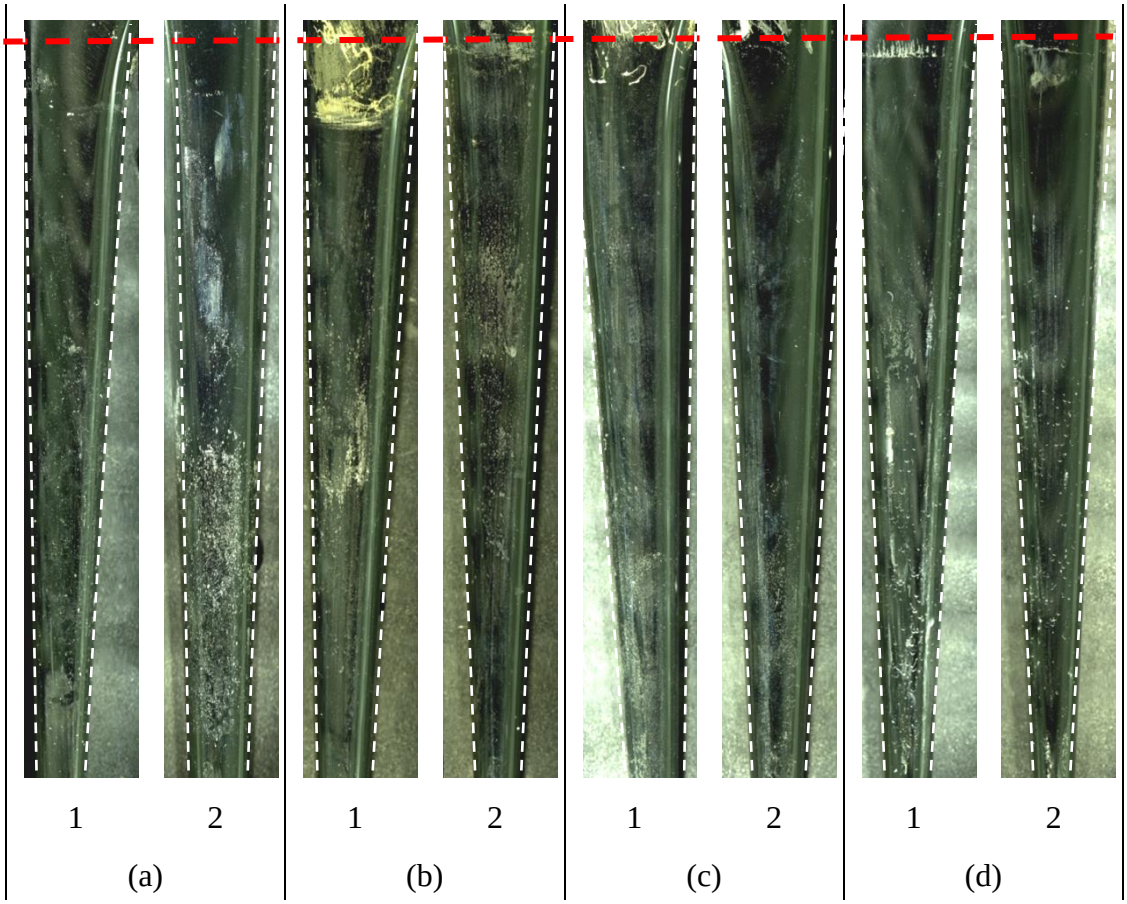

Figure 8-10 - Light microscope analysis of the cemented portions of Ultima TPS femoral stems cemented with a) DePuy CMW HV b) DePuy CMW GHV c) Stryker Simplex P and d) Stryker Simplex P with Erythromycin and Colistin. (1) Posterior and (2) anterior views

Figure 8-11 demonstrates the localised corrosion taking place within the interface. For the DePuy HV and GHV cements, a random distribution of localised pitting was seen. An interesting pattern of corrosion was seen on femoral stems cemented with the Stryker cements. On the femoral stems cemented with the Simplex P PMMA bone cement (Figure 8-11c) corrosion was seen to follow a pattern forming a 'branch like' appearance. For femoral stems cemented with the antibiotic Simplex bone cement (Figure 8-11d), corrosion was seen to take a crescent shape, appearing as a scalloping of the surface of the metallic surface. This is thought to result from the pores within the cement creating additional crevice within the interface.

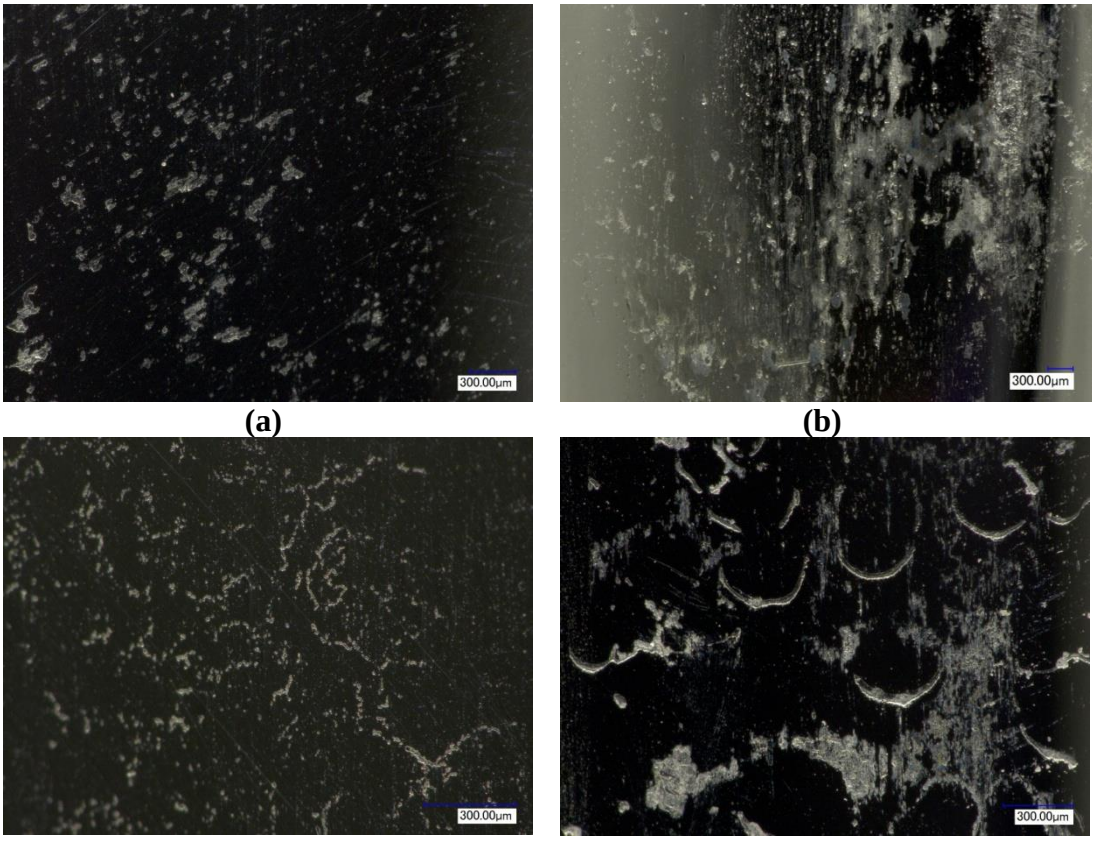

Figure 8-11 - Light microscope analysis of localised corrosion of Ultima TPS femoral stems cemented with a) DePuy CMW HV b) DePuy CMW GHV c) Stryker Simplex P and d) Stryker Simplex P with Erythromycin and Colistin

White light interferometery was also conducted in order to quantify the extent of localised corrosion. Figure 8-12 demonstrates the typical surface morphology at the stem-cement interface for two femoral stems cemented with (a-b) Stryker Simplex P and (c-d) Stryker Simplex P with Erythromycin and Colistin PMMA bone cements. Clear corrosion of the surface within the stem-cement interface can be seen with the depth of attack varying from 0.37 – 5.87µm on all femoral stems. Localised areas of pitting were also seen within the stem-cement interface (Figure 8-13) with depth of attack varying from 0.48 – 5.47µm.

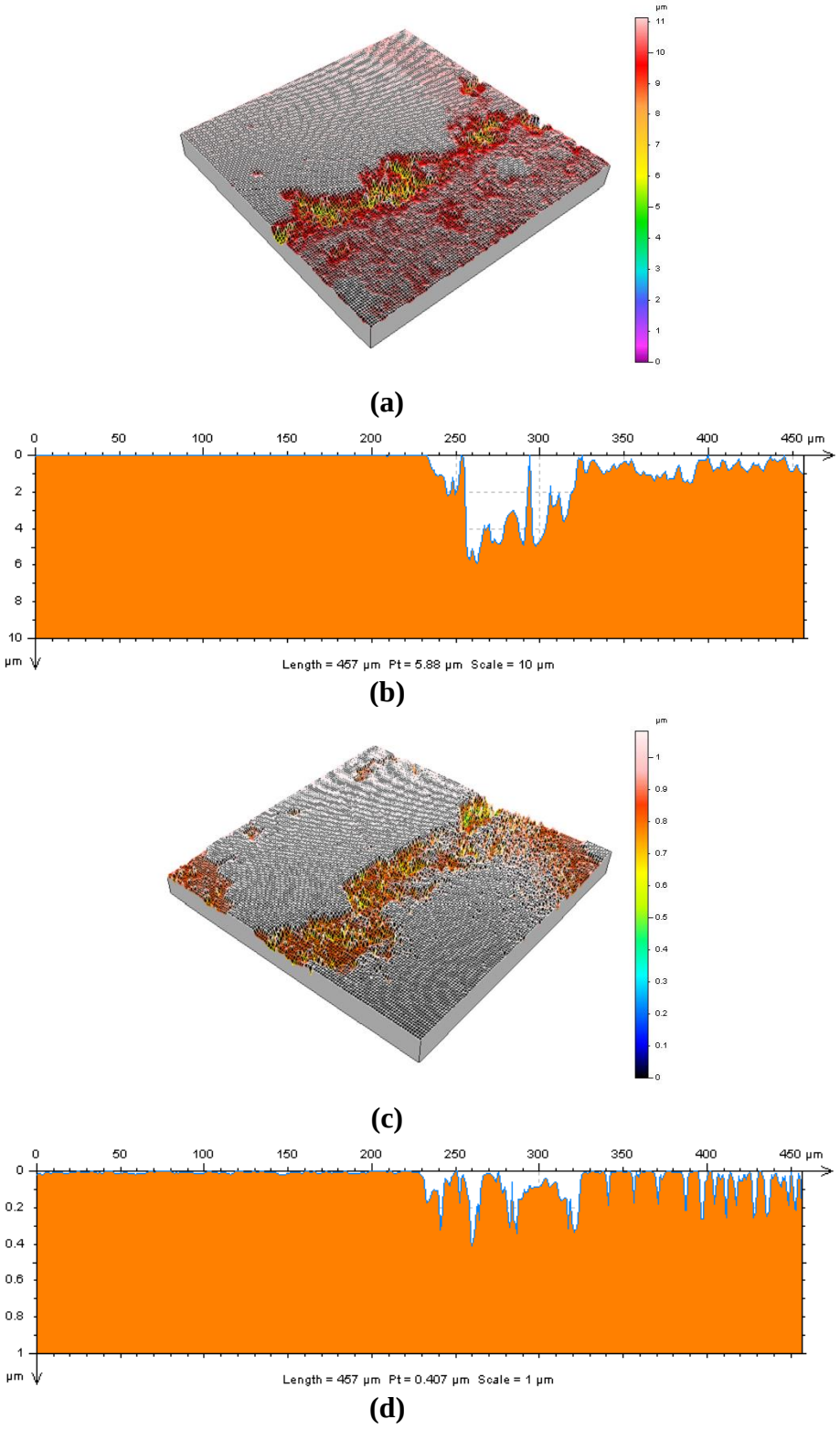

Figure 8-12 – Typical 3D and 2D interferometery surface morphology at the stem-cement interface for two femoral stems cemented with (a-b) Stryker Simplex P and (c-d) Stryker Simplex P with Erythromycin and Colistin PMMA bone cements

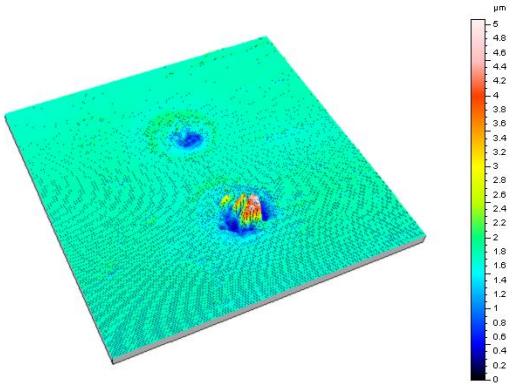

(a)

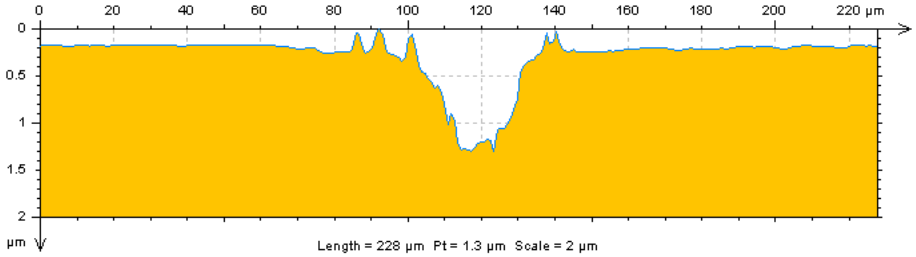

(b)

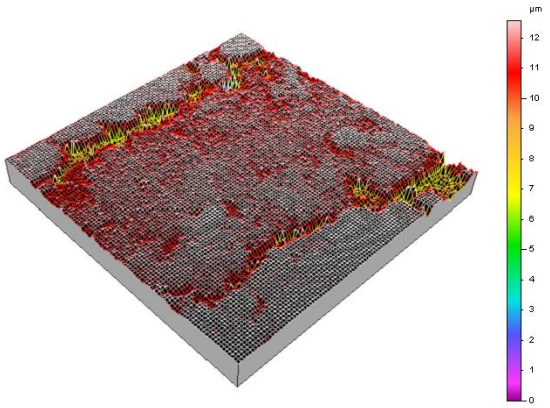

(c)

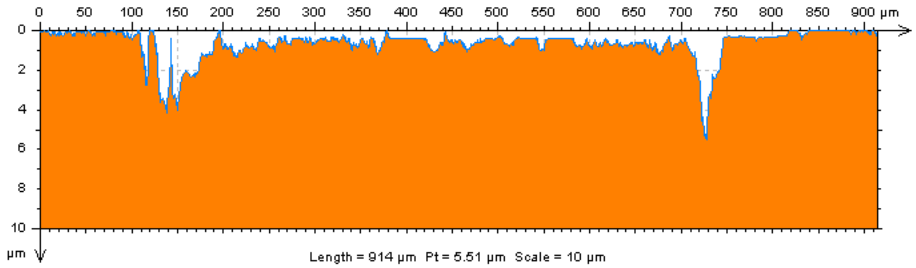

(d)

Figure 8-13 - Typical 3D and 2D interferometery surface morphology within interface for two femoral stems cemented with (a-b) Stryker Simplex P and (c-d) Stryker Simplex P with Erythromycin and Colistin PMMA bone cements

8.8. Discussion

In this chapter, the influence of galvanic coupling in mixed metal systems under static conditions has been investigated to understand and quantify the role of galvanic coupling and mixed metal systems in MoM THA. Electrochemical, surface morphology and solution chemistry techniques have all be used in order quantify the role of galvanic coupling on the dissolution rates of cemented femoral stems. Results demonstrate that the presence of Ti can drastically increase the overall rate of dissolution resulting in an increased release of metal ions into the bulk environment due to polarisation of the femoral stem surface. Comparison of uncoupled and coupled immersion tests demonstrate that the galvanic effects of Ti increase the ionic mass loss due to corrosion as shown in Figure 8-14.

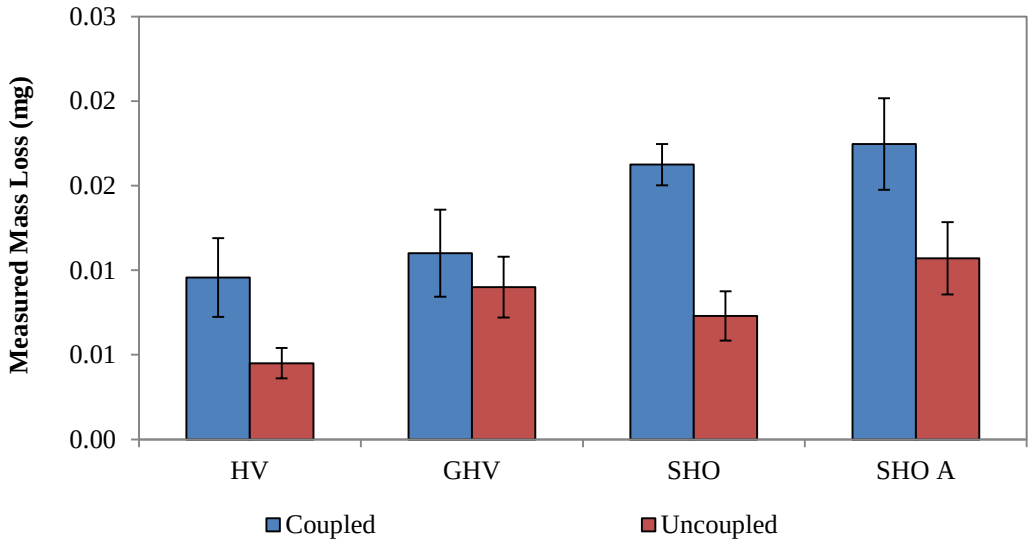

Figure 8-14 - Comparison of total ionic mass loss due to corrosion measured by ICP-MS (n=3±SD)

This chapter has also highlighted the importance of correcting for galvanic corrosion and additional dissolutions occurring on an electrode. Mansfeld [196] demonstrated the importance of correction of galvanic data to consider reduction rates owing to

repassivation of the anode surface. Mansfeld demonstrated that the ratio of galvanic current (I_g) to the dissolution current (I_a) can be expressed as the following:

Equation 8-7 - Ratio of galvanic to anodic current

$$\frac{I_g}{I_a} = 1 - exp\left(-\frac{2.3\beta_a + \beta_c}{\beta_a\beta_c}\ (E_{mixed} - E_{corr})\right)$$

It can be seen in Equation 8-7 that in the mixed potential range, discrepancies exist between the galvanic and anodic dissolution currents. Figure 8-15 demonstrates the ratio of anodic to cathodic current assuming Tafel constants of $\beta_a = \beta_c = 0.12$V/dec. Tafel constants of 0.12V/dec were chosen as they are a fairly good representation and common assumption of any corroding system when calculating intermittent measurements of corrosion currents [79]. This is due to the large number of samples required to complete Tafel analysis for each time point.

Comparison of the cell potentials for the uncoupled cemented femoral stems observed in Chapter 6 and the potentials observed in this chapter, on average an increase of 0.04V for the coupled system due to the polarising nature of the Ti. According to Equation 8-7 and Figure 8-15, the galvanic corrosion currents underestimate the total dissolution rate of the anode. It can be seen at potential differences of 0.04V, the galvanic corrosion current will contribute to approximately 77% to the overall dissolution rate due to the system lying within the mixed potential regions (<50mV above OCP). In contrast, evaluation of the relative proportions contributing to the overall dissolution rate presented in Figure 8-7 suggests that dissolution rates calculated from galvanic current data accounted for 38-68% of the overall dissolution rate. Discrepancy between these two values is thought to arise from the assumption of $\beta_a=\beta_c=0.12$V/dec. In order to satisfy the conditions observed in Figure 8-7 $\beta_a=\beta_c=0.18$V/dec have been utilised and are

demonstrated by the red-dashed line. In order to satisfy the criteria outlined in Equation 8-3, an over potential of 0.32V must be achieved assuming $\beta_a=\beta_c=0.12$V/dec which is not the case.

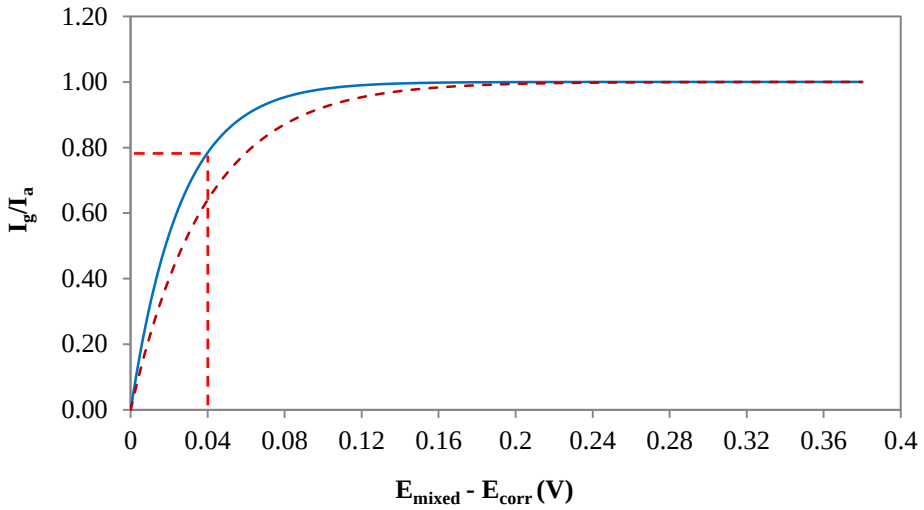

Figure 8-15 - Ratio of galvanic current to anodic dissolution current as a function of polarisation due to the presence of a mixed metal system

The subject of galvanic coupling has not received much attention with respect orthopaedic devices. Studies into the occurrence of galvanic corrosion on commonly used metallic biomaterials have been conducted but tend to be orientated towards dental applications and in the absence of tribological effects or in crevice free conditions.

Silva et al [197] presented a study investigating the galvanic couple between carbon and common metallic biomaterials in the presence of crevices. In their study they investigated the propensity for galvanic corrosion to occur in Ti, CoCrMo and 316L stainless steel alloys when coupled to carbon. The study demonstrated that Ti had the best crevice corrosion behaviour. Pitting and intergranular corrosion was seen to occur on both the 316L and CoCr alloy surfaces when sufficiently polarised. Each couple was evaluated using the mixed potential approach.

Serhan et al [198] is one of a few studies to look at the role of galvanic coupling between mixed metal systems when subjected to cyclic conditions. In this study, they investigated the tendency of galvanic corrosion to occur between Ti-Ti and Ti-316L contacts. From this study it was concluded that galvanic corrosion did not play a significant role in mixed metal system and that crevice corrosion and fretting were dominant over galvanic potential. However no electrochemical data was presented and SEM micrographs provide no evidence of micro-motion at the interfaces. They concluded that galvanic corrosion does not occur as 316L and Ti sit relatively closely on the reactivity table.

Reclaur et al [199] presented the galvanic current of the CoCr/REX734 stainless steel couples, evaluated by direct measurement and prediction using the mixed potential theory, was in the order of nano-amps. When electrically coupled, the CoCr becomes the anode while the REX734 is the cathode. They concluded that the crevice potential of both materials examined is much higher than the galvanic potential of the coupled systems. In consequence, there was no appreciable risk for a crevice corrosion caused or amplified by the galvanic coupling.

Although some studies into the tendency of galvanic corrosion to occur have been conducted, it is still unclear which couple provide adequate performance. In all of the literature reviewed it is universally agreed that 316L stainless steel is susceptible to localised corrosion, with its tendency to initiate and propagate increased when coupled to a more noble material. However questions still remain with respect to the suitability of CoCr, other stainless steel alloys and Ti alloys when used in mixed metal systems. This chapter further adds to the current understanding by demonstrating that galvanic corrosion occurs between creviced CoCrMo and Ti-6Al-4V.

8.9. Summary

In this chapter, the effects of galvanic coupling on the localised crevice corrosion mechanisms of cemented LC CoCrMo femoral stems coupled to Ti-6Al-4C has been evaluated using a variety of electrochemical, surface and solution analytical techniques. Findings in this section can be summarised into the following:

- Galvanic crevice corrosion occurs at the stem-cement interface when coupled to Ti.
- Net anodic currents seen from the femoral stem to Ti ring demonstrated corrosion and mass loss of the surface
- Reduction of oxygen on the surface of the femoral stem contributes to the overall anodic currents.
- Ionic mass losses calculated from electrochemical data were comparable with experimentally measured mass losses. These were seen to be in the region of 9.5×10^{-4} to 1.7×10^{-3}mg depending on the type of PMMA bone cement.
- A stoichiometric release of Co, Cr and Mo was seen similar to the uncoupled tests. No Ti was detected in the solution demonstrating no dissolution of the Ti ring
- Localised corrosion was seen on the cemented portions of the femoral stems with a maximum pit depth of approximately 5µm been observed.
- Examination of the galvanic corrosion theories indicate that galvanic corrosion accounts for 37.66-67.20% of the overall dissolution rate. However some discrepancies exist between the predicted portions and experimentally observed proportion. This is thought to be due to the assumption of Tafel constants.

CHAPTER 9 – THE EFFECT OF DYNAMIC LOADING ON THE DEGRADATION OF CEMENTED FEMORAL STEMS

9.1. Introduction

So far in this study, the effects of surface pre-treatment, crevice geometry and cement chemistry have been examined with respect to localised crevice corrosion under static conditions. However it has been well documented that the application of a gait cycle or dynamic loading can further increase the dissolution rates of cemented femoral stems. This chapter aims to investigate the influence that dynamic loading has on the dissolution of cemented femoral stems. In this chapter, the effects of dynamic loading, bone cement chemistry, surface pre-treatment and galvanic coupling were all investigated in an attempt to gain a full understanding into how each variable affects the overall degradation of cemented femoral stems.

9.2. General Electrochemical Response and Solution Chemistry Observations

Figure 9-1 demonstrates the average OCP response with experimental error for a cemented femoral stem. In each test the stem was loaded statically with 300N for 24hrs in order to let the OCP reach equilibrium and also represent the time for which a patient would not be typically load-bearing after surgery. Between point A-B, the stem is statically loaded and an ennoblement in the OCP is observed from -0.05V to -0.01V, suggesting the formation and stabilisation of the passive film. However, when the sinusoidal load was applied (B-C) a negative shift in OCP from -0.01V to -0.45V was recorded suggesting a de-passivation of the alloy had occurred resulting in an increase in corrosion rate and metal ion release [18-22]. After 1 million cycles

were complete the dynamic loading was stopped and held at peak load for a further 24 hours. An increase in OCP from -0.41V to -0.13V (C-D) was seen when the loading was removed demonstrating a re-passivation of the metallic surface and decrease in fretting-corrosion at the stem-cement interface. The OCP did not recover to the initial OCP at the start of the test suggesting that permanent damage of the metallic surface had occurred resulting in an accelerated rate of crevice-corrosion within the interface due to mechanically induced crevice corrosion.

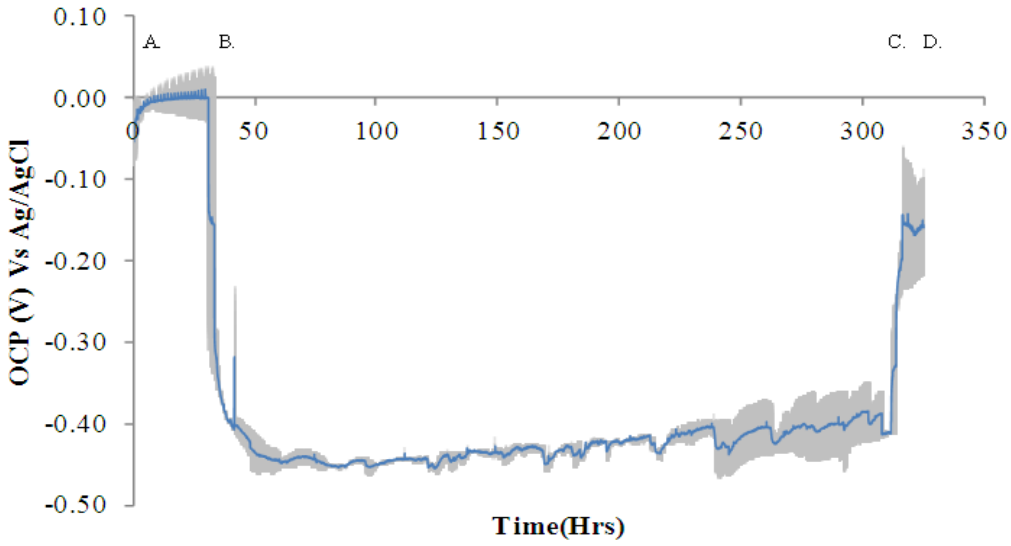

Figure 9-1 - General OCP response over 1million cycles (n=3±SD)

Intermittent LPR measurements were taken every 1hr in order to obtain a quantitative measurement of the self-corrosion rate of the cemented femoral stem. Figure 9-2 demonstrates the typical trend in I_{corr} values obtained for a cemented femoral stem when subjected to cyclic loading. Under static loading conditions, a typical corrosion current of 5.20×10^{-7}A was observed. This is similar to the corrosion currents observed by Ouerd *et al* [107] who observed the role environment has on the corrosion rates of CoCrMo alloys under static, unloaded conditions. This was seen to increase to 3.66×10^{-6}A when cyclic loading was applied to the femoral stem. A decrease in corrosion current was typically seen around 270,000 cycles (≈120hrs) with the corrosion current reaching an average of 2.34×10^{-6}A. In tribo-

corrosion systems a decrease in OCP and increase in corrosion current occurs when the protective passive layer is removed or fractured on a metallic surface changing the concentration and activity of species at the metallic surface by exposing an excess of electrons available for oxidisation. Oxidation and reduction of the reactive metallic substrate will result in the liberation of metallic ions into the aqueous environment as well as a reduction of oxygen to reform the oxide layer.

An immediate drop in corrosion current to around 1.30×10^{-6}A was seen when the test had completed 1 million cycles and the dynamic load was removed and held at 2.3kN. This demonstrated a decrease in wear-enhanced dissolution and a partial re-passivation of a protective passive film. Again I_{corr} did not recover to the initial starting corrosion current of the test suggesting that permanent damage of the metallic surface had occurred and a preferential environment established for mechanically induced crevice corrosion. It is important to note that the current measurements presented in this study are absolute current measurements calculated from the Stern-Geary coefficient assuming βa=βc=120mV.

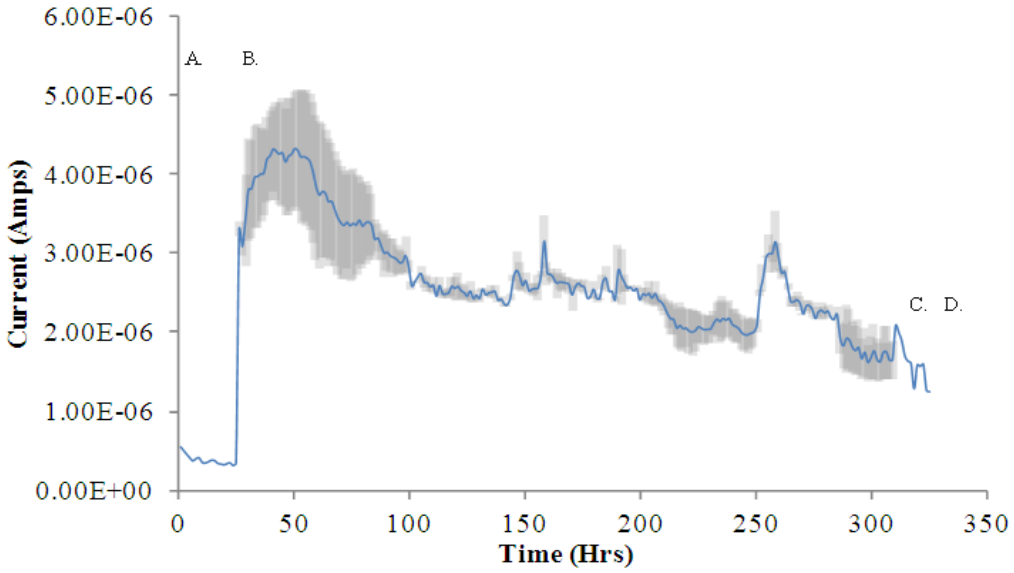

Figure 9-2 - General I_{corr} response over 1 million cycles (n=3±SD)

9.3. Influence of PMMA Bone Cement

In order to assess the influence of PMMA bone cement chemistry, tests were conducted for 500,000 cycles using three commercially-available PMMA bone cements (Table 3-2). OCP, LPR and ICP-MS analysis was conducted in order to quantify the role PMMA bone cement has on the fretting-corrosion rates at the stem-cement interface.

9.3.1. Electrochemical Results

OCP measurements were taken as semi-quantitative indications of a material's passivity (Figure 9-3). No differences outside standard deviation in OCP were observed between any of the tests. When the cemented femoral stems were immersed in 0.9% NaCl, an initial OCP of around -0.08V was observed. This was seen to slowly ennoble with time typically reaching values in the range of 0.08 – 0.10V suggesting the development of a protective oxide film [127, 200]. A decrease in OCP was seen under the application of cyclic load, decreasing to around -0.26 to -0.35V. This decrease in OCP suggests a mechanically induced de-passivation of the surface, increasing the corrosion rate of the metallic implant. After 500,000 cycles were complete the loading was removed. An ennoblement in OCP from around -0.35 to -0.04V was seen demonstrating partial re-passivation of the damaged surface and an apparent decrease in the corrosion rate of the cemented femoral stem.

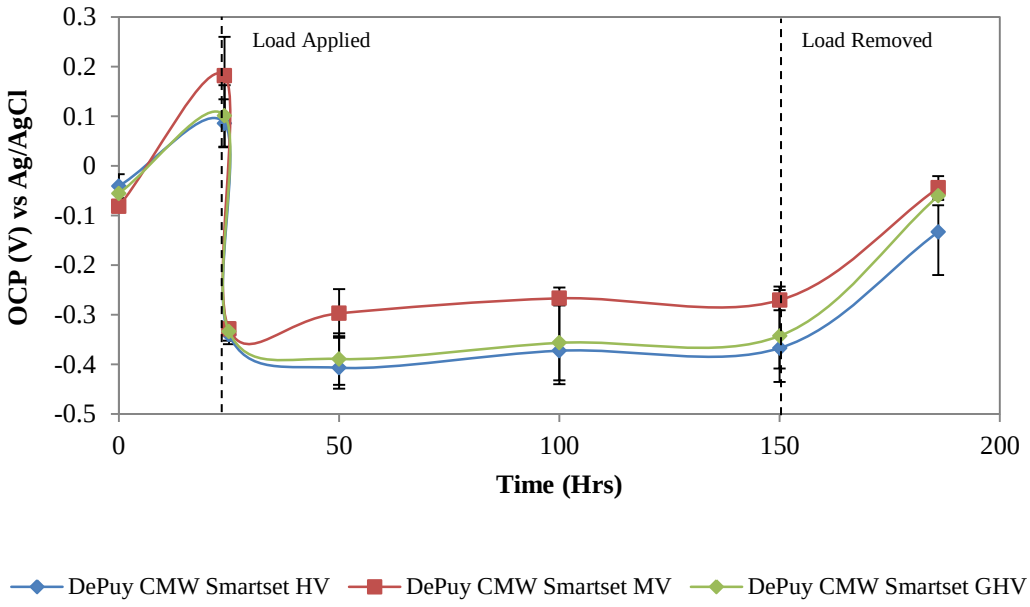

Figure 9-3 - Measured OCP data for cemented femoral stems with cemented with various PMMA bone cements (n=3±SD)

Figure 9-4 demonstrates the measured I_{corr} at various time intervals. Upon the application of cyclic loading, I_{corr} was seen to increase by an order of magnitude demonstrating depassivation of the metallic surface and an increase in the rate of oxidation taking place on the metallic surface. It is interesting to note that a difference in I_{corr} exists when different PMMA bone cements are used. PMMA bone cements containing sulphates demonstrated increases in I_{corr} under cyclic loading signifying an increased rate of corrosion at the stem-cement interface. The addition of $BaSO_4$ (SmartSet® MV) resulted in the highest measured fretting-corrosion current when compared to femoral stems cemented with SmartSet® HV and GHV bone cements. PMMA bone cements containing gentamicin sulphate also demonstrated an increase in I_{corr} under cyclic loading when compared to PMMA cements containing no gentamicin sulphate.

Furthermore the partial recovery of OCP upon the removal of cyclic loading, combined with the increased I_{corr} after cyclic loading had been removed, suggests the formation of an environment capable of sustaining an increased rate of localised crevice-corrosion, a characteristic commonly associated with fretting-corrosion of modular head-neck tapers of biomedical implants. PMMA bone cements containing gentamicin sulphate were seen to increase the measured corrosion current when cyclic loading was removed. Although the release mechanisms of gentamicin loaded antibiotic bone cements are fairly well understood under, the deformation and formation of micro-cracks and pores within the cement resulting from dynamic loading may further increase the sulphate concentrations within the interface, increasing the rate of electrochemical dissolution.

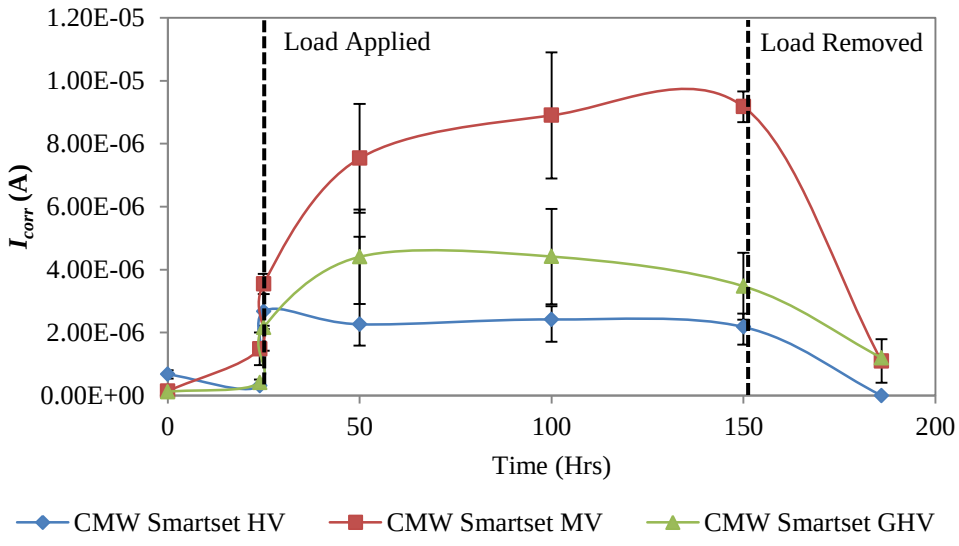

Figure 9-4 - Measured I_{corr} data for cemented femoral stems with cemented with various PMMA bone cements (n=3±SD)

9.3.2. Influence of Cement Chemistry on the Solution Chemistry

ICP-MS demonstrated increases in the Total Ionic Mass Loss (TIML) for cements containing sulphates (Table 9-1). The addition of gentamicin sulphate increased the TIML from 0.79 to 1.26mg when compared to the PMMA cement with the same base and radiopaque chemistry. The addition of $BaSO_4$ was seen to increase the TIML from 0.79 to 1.44 mg when compared to the SmartSet® HV bone cement. Again a preferential release of Co was seen in all tests accounting for 90% of all ions released (Figure 9-5).

Table 9-1 - Ionic mass loss measured and calculated using ICP-MS and Faradays law after 500,000 cycles (n=3±SD)

Test Name	Average total ionic mass loss measured using ICP (mg)
CMW SmartSet® HV	0.79±0.08
CMW SmartSet® GHV	1.26±0.22
CMW SmartSet® MV	1.44±0.11

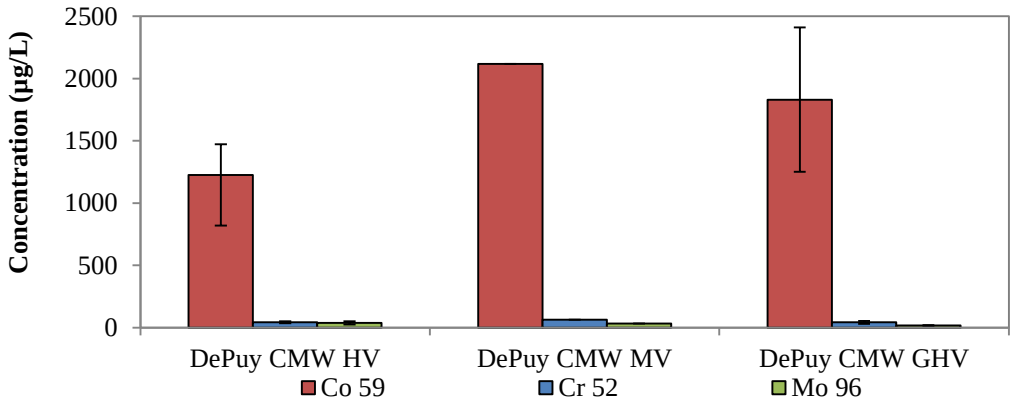

Figure 9-5 - Measured metallic ion levels for different commercially-available PMMA bone cements after 500,000 cycles of loading (n=3±SD)

9.4. Influence of Surface Pre-treatment

Many authors [201, 202] have shown that the cement mantle is just as important to the success of a femoral implant design as the stem itself. In order to optimise the design at this interface a number of different mechanical surface treatments are employed. Depending of the design philosophy of the femoral stem polishing or blasting may be desired. Where subsidence of the femoral component is not desired a mechanical blasting process known as vaquasheening, consisting of an aqueous bead blast, is employed in order to increase surface roughness to promote bone cement interdigitation. Studies have demonstrated that surfaces with an increased surface roughness exhibit a stronger mechanical interlocking with the bone cement due to the interdigitation of the bone cement within asperities of the surface [130, 203]. However in order to maintain the integrity of the interface, debonding of the interface must not occur. Such surface finishes have been linked with the production of polymethly methacrlyte (PMMA) particles due the abrasion of the surrounding cement [8]. In contrast polished femoral stems, designed to debond and subside within the PMMA bone cement, have over 20 years of clinical data supporting their design philosophy. Very different surface morphologies of retrieved femoral components have been seen depending on the surface pre-treatment applied to the prosthesis. In this section, the suffix 'TPS' refers to polished surfaces and 'TRS' to roughened surfaces.

9.4.1. Electrochemical Results

For femoral stems with an increased surface roughness electrochemical measurements demonstrated that the application of cyclic loading resulted in a gradual decrease of the OCP and increase in I_{corr}, demonstrating de-passivation of the usually passive CoCrMo and an increase in oxidation of the metallic surface.

Upon the removal of cyclic loading an increase in OCP and decrease in I_{corr} was seen demonstrating a partial repassivation and decrease in corrosion of the CoCrMo. Increased fretting-corrosion currents were observed for polished femoral stems (TPS) when compared to the vaquasheened femoral stems (TRS) (Figure 9-6). It is interesting to note that an immediate increase and decrease in current and potential respectively was not observed upon the application of cyclic loading, a characteristic observed for polished femoral stems. This is thought to be as result of the increased interdigitation of the bone cement with the surface of the femoral stem increasing the interfacial shear strength at the interface.

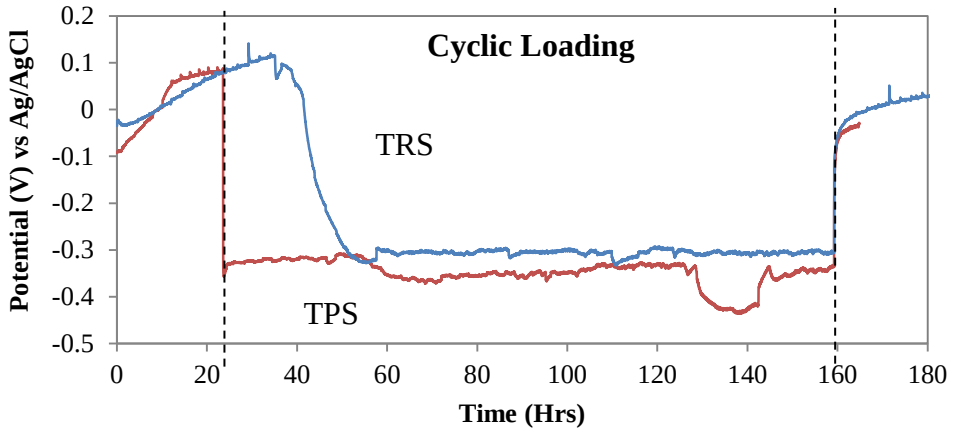

(a)

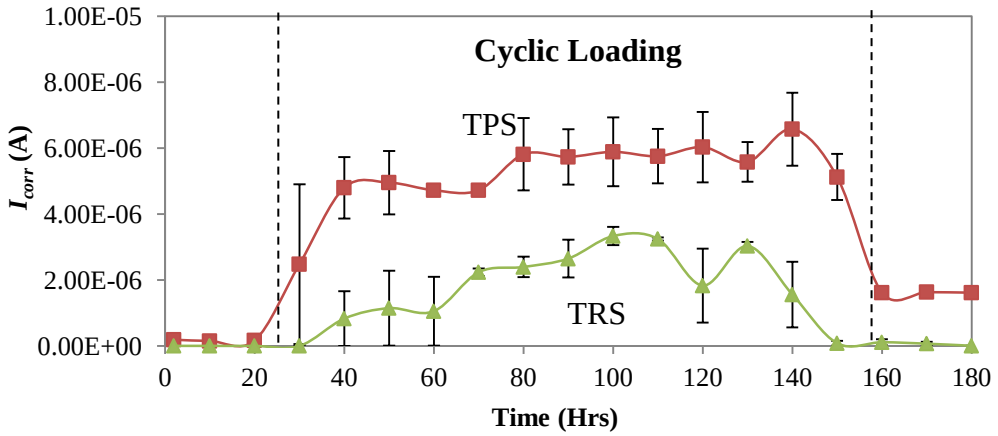

(b)

Figure 9-6 – a) OCP and b) I_{corr} response for femoral stems with varying surface finishes (n=3±SD)

Cumulative ionic mass loss due to pure-corrosion and wear-enhanced corrosion, determined by LPR, further supported this (Figure 9-7a). For polished surfaces, a linear cumulative ionic mass loss was seen for the duration of cyclic loading. Results for roughened femoral stems demonstrated upon the application of cyclic loading (t >24hs) the Faradaic mass loss was seen to remain constant up to 40hrs. After 40hrs, an increase in the cumulative ionic mass loss was seen until 140hrs where the rate of mass loss was seen to become constant with increasing cycles. Differentiation of the cumulative ionic mass loss curves during cyclic loading yield the rate in which metal ions are produced. This was seen to be $4.70 \times 10^{-3} \frac{mg}{Hr}$ and $1.5 \times 10^{-3} \frac{mg}{Hr}$ for polished and roughened stems respectively demonstrating an increased rate of wear induced oxidation for polished femoral stems. Electrochemical measurements were further supported by ICP-MS analysis of the bulk solution (Figure 9-7b).

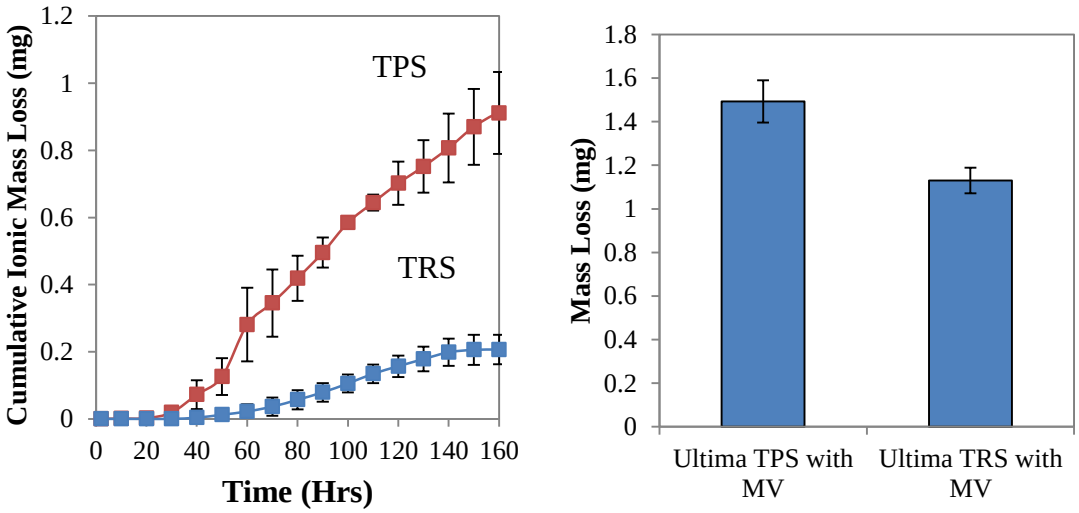

(a) *(b)*

Figure 9-7 - Ionic mass loss a) calculated from Faraday's law and b) experimentally measured using ICP-MS (n=3±SD)

9.5. Influence of Galvanic Coupling

It has been demonstrated in the previous chapter that coupling of the CoCrMo stem to titanium can drastically increase the rates of localised corrosion within the stem-cement interface due to the establishment of a galvanic cell. It has been demonstrated that both in this study and literature that upon the application of tribological conditions, a removal of the passive film will occur resulting in a decrease in corrosion potential. The measured corrosion potential reflects the galvanic coupling of two distinct surface states of the metal: (1) the passive metal (unworn area) and (2) the bare metal (worn area) exposed to the solution by abrasion of the passive film, effectively establishing a galvanic interaction across the surface of a material. For MoM THR, all interfaces are electrically connected via their interfaces resulting in a galvanic cell being established. Research into the degradation mechanisms of THRs are usually carried out by isolating the area of interest. However this section aims to introduce other interfaces/metals in order understand the role galvanic coupling plays on the corrosion of cemented MoM devices at dynamic interfaces.

9.5.1. Mixed Potential Theory Predictions

Mixed potential theory was used to evaluate the electrochemical reactions occurring within the interface, assuming that two partial oxidation and reduction reactions occur with no net accumulation of charge. Figure 9-8 demonstrates the oxidation reactions for polished and roughened femoral stems, as well as the assumed reduction reaction occurring on the Ti. Metallic dissolution will occur at the point where the anodic and cathodic half-cell reactions are equal. It can be seen graphically the only point in the system where the oxidation and reduction reactions are equal are at the point of intersect known as the mixed potential (E_{mixed}). At this

point the rates of reactions are equal satisfying charge conservation. The current density at this point will represent the rate of oxidation and oxygen reduction of the system.

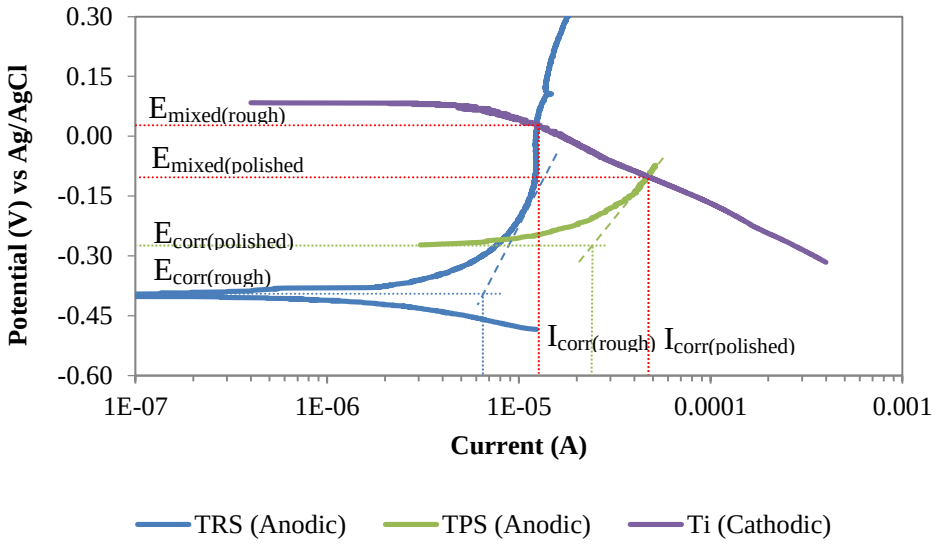

Figure 9-8 - Application of the mixed potential theory to demonstrate the role of galvanic coupling for femoral stems with different surface finishes under fretting conditions

An increase in I_{corr} from 1.5×10^{-5} to 3.5×10^{-5}A and 5.5×10^{-6} to 0.3×10^{-5}A for polished and roughened femoral stems, respectively, was seen when electrically connected to Ti. This is due to a large potential difference being established between active and passive areas on the metallic stem as well as the Ti. This analysis also suggests that under fretting conditions, the CoCrMo femoral stem will become the net anode whilst the Ti will act as the net cathode facilitating oxygen reduction.

An increase in the cell potential was also seen due to the presence and polarising nature of Ti relative to the active CoCrMo surface. This was seen to increase from -0.29 to -0.10V and 0.4 to 0.02V for the polished and roughened stems respectively. However it is interesting to note the magnitude of increase in cell potential when coupled to Ti. Although roughened surfaces have been seen to exhibit lower fretting

corrosion-currents compared to polished surfaces, it can be seen in Figure 9-8 that the presence of Ti sufficiently polarises the roughened CoCrMo stem into the passive region of the alloy limiting I_{corr}. This was not the case for the polished surfaces that demonstrated a linear increase in current with respect to applied potential.

9.5.2. *In-situ* Electrochemical Results

In order to investigate the influence of galvanic coupling under fretting crevice-corrosion conditions; a Ti ring with the same surface area of the acetabular shell was immersed with the femoral stem and subjected to cyclic loading. ZRA measurements were utilised to measure the mixed cell potential as well as the net galvanic currents. Figure 9-9 demonstrates the OCP response for uncoupled and coupled polished femoral stems. Increases in cell potential were seen when femoral stems were galvanically coupled due to the polarising nature of the Ti.

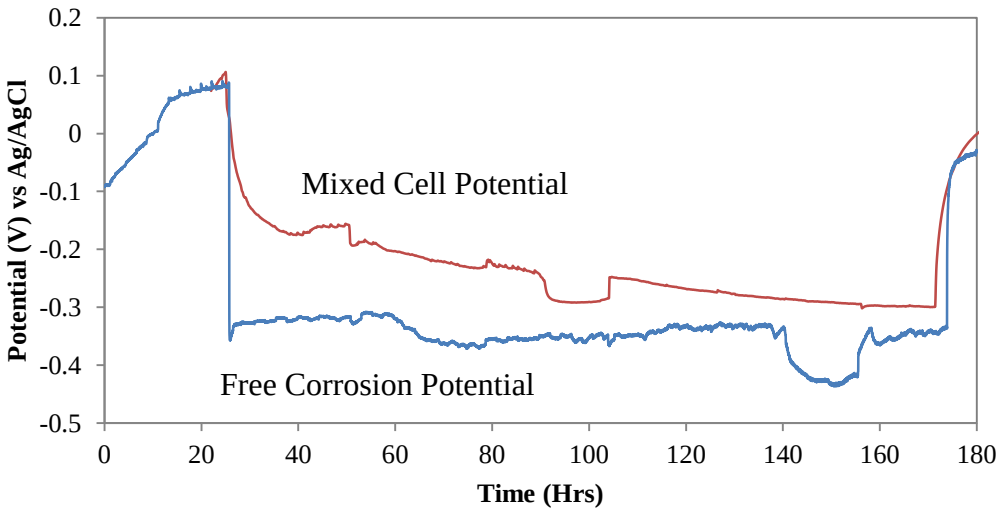

Figure 9-9 - Measured free corrosion and mixed potential for polished femoral stems when subjected to dynamic loading (n=1)

Figure 9-10 demonstrates the fretting-corrosion currents obtained from ZRA and LPR measurements for polished femoral stems. ZRA measurements demonstrated a net anodic current from the CoCrMo femoral stem to the Ti acetabular component complimenting the mixed potential results presented in Chapter 7.3. Upon the application of cyclic loading, an increase in current from 7.51×10^{-7}A to 1.75×10^{-5}A was seen demonstrating an increased rate of wear enhanced corrosion. The presence of a galvanic couple increases the rate of pure and wear induced corrosion within the interface. This demonstrates that the presence of other system components and interfaces can drastically increase the degradation rate of cemented components.

It is important to appreciate that net anodic current measurements do not take into consideration any reduction occurring within the stem-cement interface and in the current form are not comparable to I_{corr} as explained in Chapter 7. Fontana explained that the rate of oxidation follows the metal dissolution rate until the reversible potential for hydrogen, or in our case oxygen, is reached. Similarly the total rate of reduction will be the sum of both reductions reactions occurring within the system. The effect of this on the fretting-corrosion currents is demonstrated in Figure 9-10. Applying this factor, an increase in galvanic fretting corrosion current from 1.7×10^{-5} to 2.29×10^{-5}A was seen.

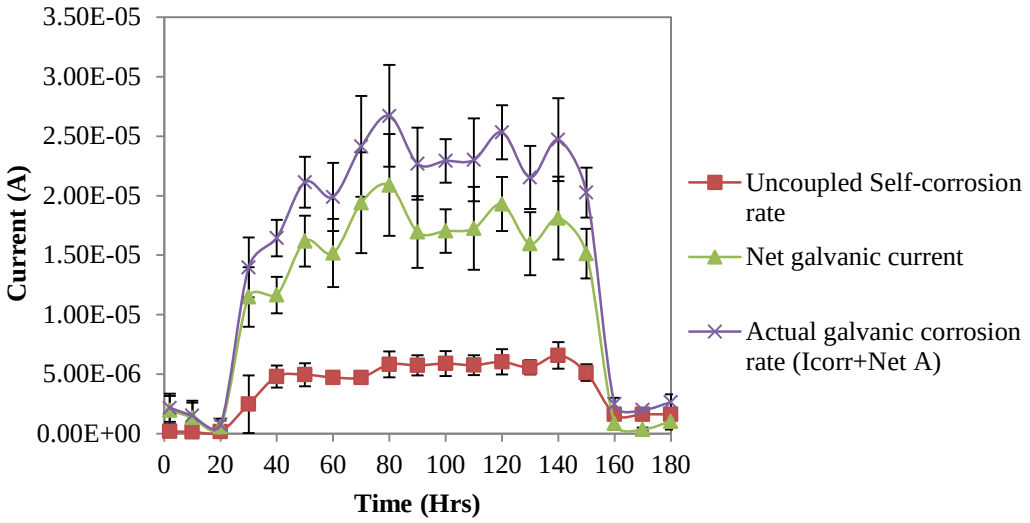

Figure 9-10 - Current response for uncoupled and coupled polished femoral stems when subjected to dynamic loading (n=3±SD)

Integration of the current versus time curve was also conducted in order to observe the cumulative ionic mass loss due to pure and wear enhanced corrosion (Figure 9-11). Galvanic coupling was seen to increase the ionic mass loss from 0.91 to 2.56mg. ICP-MS further supported these findings demonstrating a TIML of 2.74±0.19mg compared to 1.44±0.11mg for uncoupled polished femoral stems. An increase in the rate of ionic mass loss due to pure corrosion and wear enhanced corrosion as seen upon the application of cyclic loading from $4.70 \times 10^{-3} \frac{mg}{Hr}$ to $1.71 \times 10^{-2} \frac{mg}{Hr}$.

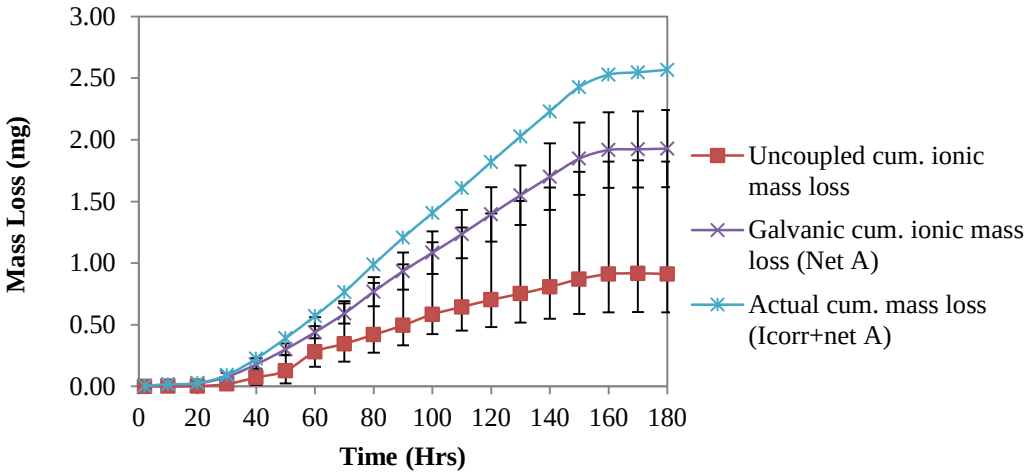

Figure 9-11- Cumulative ionic mass loss for uncoupled and coupled polished femoral stems when subjected to dynamic loading (n=3±SD)

A similar trend was seen on femoral stems with an increased surface roughness when subjected to cyclic loading (Figure 9-12). Again a net anodic current was measured greater than the self-corrosion rate of the alloy demonstrating the presence of Ti can influence the wear-enhanced corrosion reactions occurring within the interface of femoral stems with an increased surface roughness. Galvanic fretting-corrosion currents were seen to be an order of magnitude lower for femoral stems with an increased surface roughness.

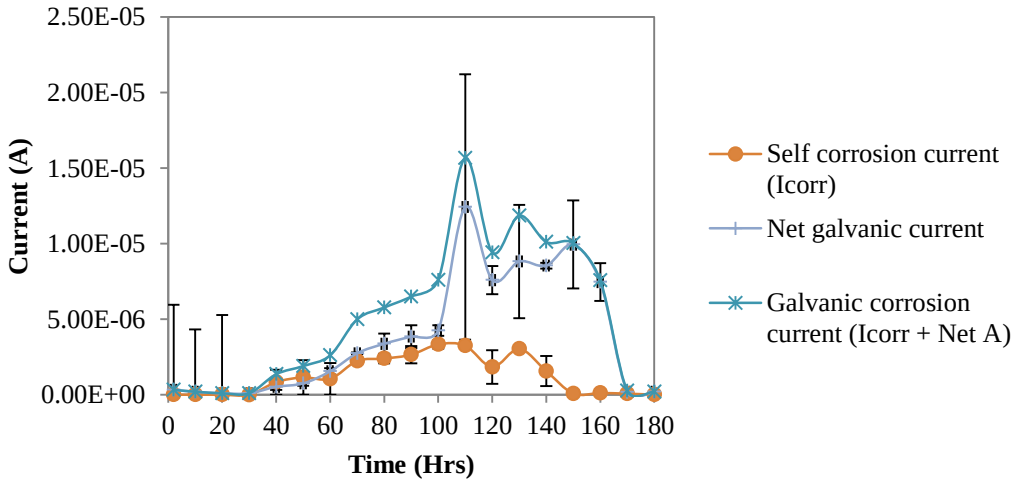

Figure 9-12 - Current response for uncoupled and coupled roughened femoral stems when subjected to dynamic loading

Integration of the current versus time curve for femoral stems with and increased surface roughness coupled to Ti (Figure 9-13) demonstrated a linear ionic mass loss rate up to 75hrs where $\frac{\partial m}{\partial t} = 1.8 \times 10^{-3} \frac{mg}{Hr}$ (Area 'A'). Following that a linear ionic mass loss was again seen at a higher rate of $8.60 \times 10^{-8} t$ under cyclic conditions (Area 'B'). A similar trend was seen for the uncoupled femoral stem with the rate of ionic mass loss increasing from $8.75 \times 10^{-4} \frac{mg}{Hr}$ to $2.35 \times 10^{-3} \frac{mg}{Hr}$. This suggests a change within both systems occurs resulting in an increased rate of metal ion production. This is thought to be due to a gradual debonding of the stem-cement interface increasing the overall depassivated area. Upon the removal of dynamic load the cumulative ionic mass loss for coupled femoral stems was seen to remain constant demonstrating cyclic loading increases the rate in which metal ions are liberated from the alloy. Again the presence of galvanic coupling increased the ionic mass loss due to pure corrosion and wear enhanced corrosion from 0.21 to 0.90mg. This was further supported by ICP-MS which demonstrated a TIML of 0.82mg.

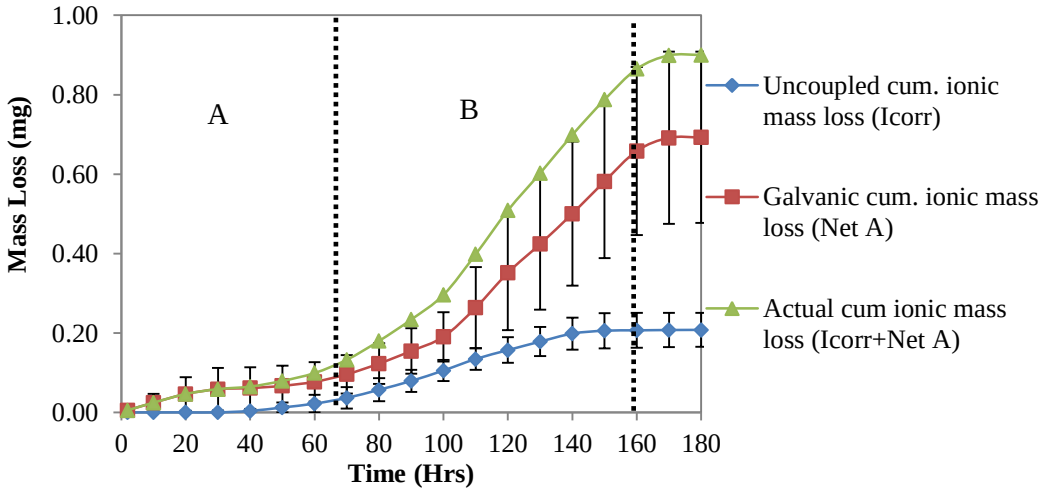

Figure 9-13 - Cumulative ionic mass loss for uncoupled and coupled roughened femoral stems when subjected to dynamic loading. Area 'A' and 'B' represent the changes in the rate of mass loss (n=3±SD)

9.6. Influence of Fretting-Corrosion on the External Environment

Intermittent ICP-MS measurements were also taken in an attempt to understand the evolution of metal ion release over time. For each data point, 1mL of test solution was drawn from the test using a sterile syringe and stabilised with 9mL of 2% HNO_3. Intermittent ion release measurements where conducted for the Ultima TRS and all galvanically coupled tests. Figure 9-14 demonstrates the ionic mass loss over 500,000 cycles calculated from Faradays law of electrolysis and measured using ICP-MS. For Ultima TRS femoral stems it can be seen from ICP-MS data that upon the application of cyclic loading an increase in ionic mass loss was seen. This was not replicated in the Faradaic mass loss measurements, demonstrating differences outside standard deviation between ionic mass losses measured by ICP-MS. This indicates that other mechanisms exist at the stem-cement interface of the Ultima TRS that result in metal ion release. This is thought to be caused by abrasion and dissolution of any metallic particles and PMMA particles which will further add to the overall ionic mass loss. Si was also seen to increase linearly ($R^2 = 0.48$) with the application of cyclic loading. After 500,000 cycles concentrations in the region of 800µg/L were observed.

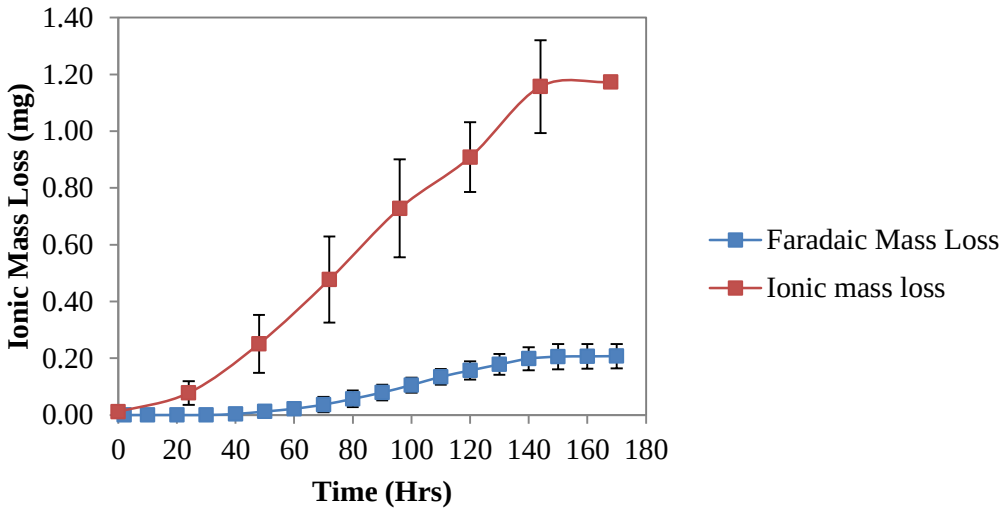

Figure 9-14 - Correlation of Faradaic and ICP-MS mass loss measurements for uncoupled Ultima TRS tests with DePuy MV PMMA bone cement (n=3±SD)

Figure 9-15 demonstrates the stoichiometry in which Co, Cr and Mo were released over 500,000 cycles of cyclic loading for the roughened femoral stems. Prior to cyclic loading, a preferential release of Cr was seen. Upon the application of cyclic loading at 24hrs, a ratio of approximately 0.8:0.15:0.5 for Co:Cr:Mo, respectively, was recorded. Co increased throughout the test accounting for 96.5% of all ions released at 500,000 cycles. It is clear from Figure 9-15 that upon the application of cyclic loading, a change in the system occurs resulting in a high and preferential release of cobalt into the bulk environment. This is particularly interesting as a study by Heisel et al [147] demonstrated a stoichiometric release of Co:Cr:Mo under sliding conditions for large diameter MoM resurfacing components. This further demonstrates that type of wear can drastically influence the type and quantity of metal ions released into the biological environment.

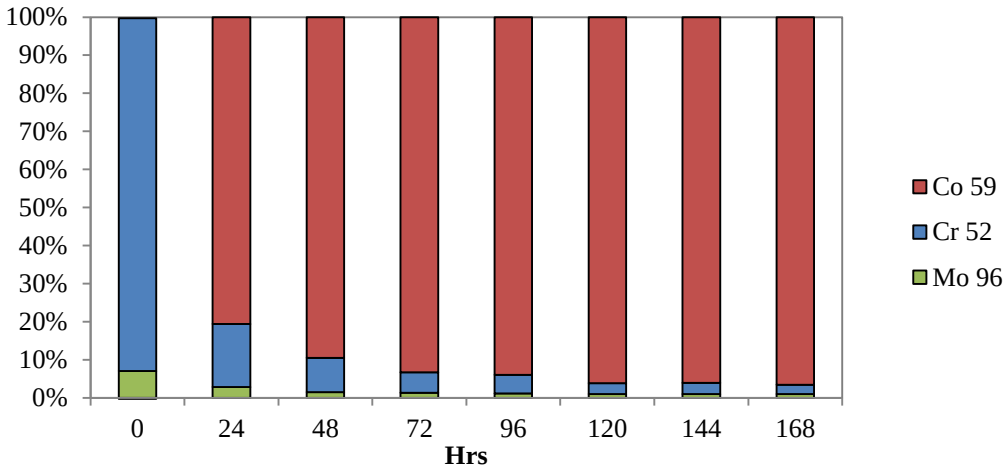

Figure 9-15 – Average Evolution of Co, Cr and Mo over 500,000 cycles for the Ultima TRS with DePuy MV bone cement (n=3)

Figure 9-16 demonstrates the correlation between Faradaic and ICP-MS ionic mass loss for polished femoral stems coupled to Ti. A good correlation between the two is clear suggesting the primary source of Co metal ion release from polished femoral stems is pure and wear induced corrosion. Again a similar trend and ratio of Co:Cr:Mo was released over the 500,000 cycles (Figure 9-17). A preferential release of cobalt was seen accounting for 98.42% of all metallic ions released after 500,000 cycles.

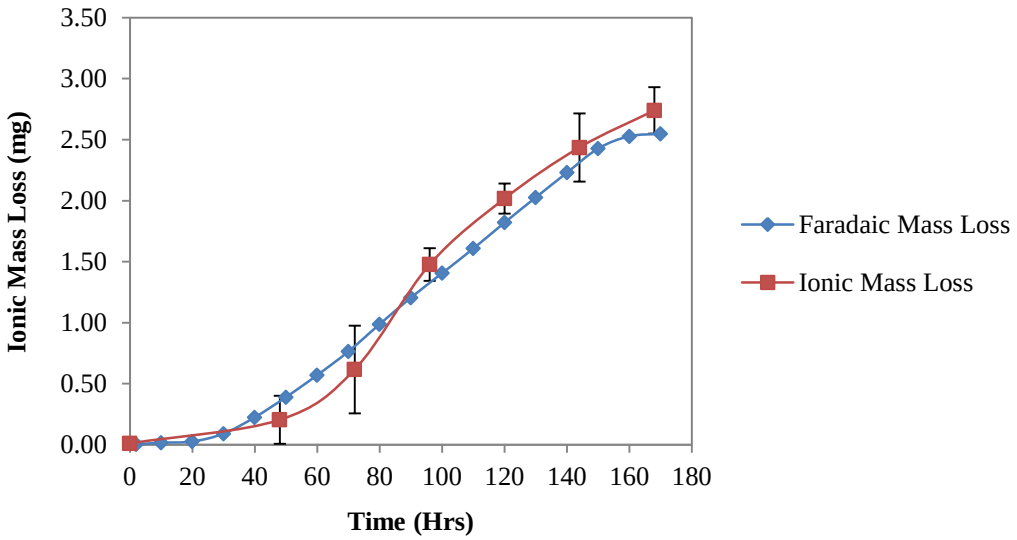

Figure 9-16 - Correlation of Faradaic and ICP-MS mass loss measurements for coupled Ultima TPS tests (n=3±SD)

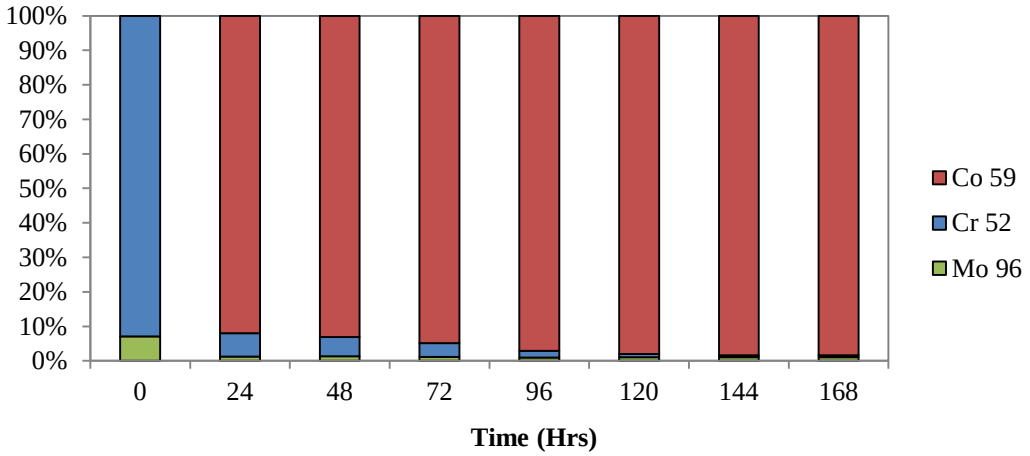

Figure 9-17 – Average evolution of Co, Cr and Mo over 500,000 cycles for coupled Ultima TPS with DePuy MV bone cement (n=3)

A similar trend in cumulative ionic mass loss was seen for femoral stems with an increased surface roughness when compared to that observed for polished femoral stems. A good correlation between the TIML, measured using ICP-MS, and Faradaic mass loss was observed. Figure 9-18 presents the relationship between electrochemical and measured mass losses. In this case, it can be seen that a close correlation exists between the two measurements although the TIML is less than the mass loss due to oxidation. This suggests that the majority of ions released into the bulk originate from oxidation of the surface. A decrease in the ionic mass loss when compared to the Faradaic mass loss may be associated with the retention of debris within the interface. However in this case it is thought that this is due to experimental variance.

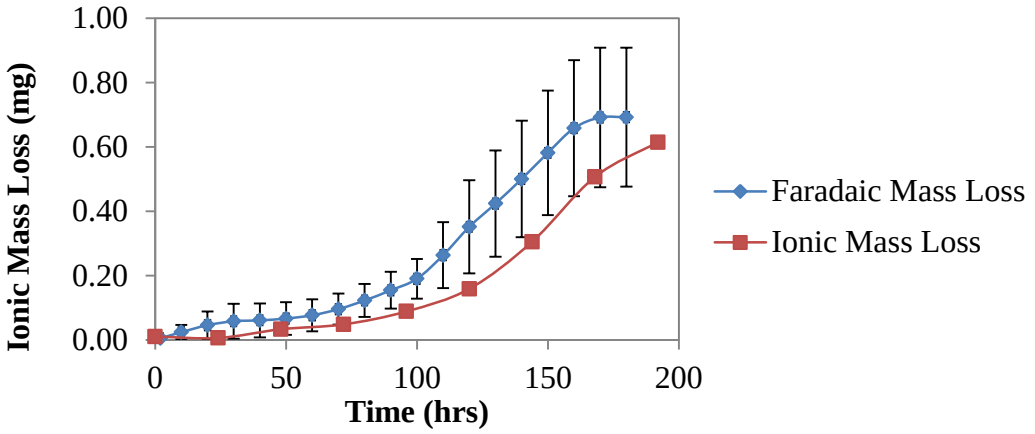

Figure 9-18 - Correlation of Faradaic and ICP-MS mass loss measurements for coupled Ultima TRS tests (n=3±SD)

The evolution of Co, Cr and Mo over 500,000 cycles was also seen to be affected by the presence of the Ti couple (Figure 9-19). Although a similar trend was seen over 500,000 cycles for the coupled Ultima TRS, the ratios in which Co, Cr and Mo were released were seen to vary. Upon the application of cyclic loading (t=24hrs) a ratio of 0.33:0.63:0.04 of Co:Cr:Mo was seen respectively. A preferential release of cobalt was seen for the remainder of the test, with cobalt, chromium and molybdenum accounting for 90, 7.5 and 2.5% respectively of all metal ions released. In all cases Ti was seen to be below the detection limit (<0.50µg/L). This again demonstrates that Ti was acting as the net cathode.

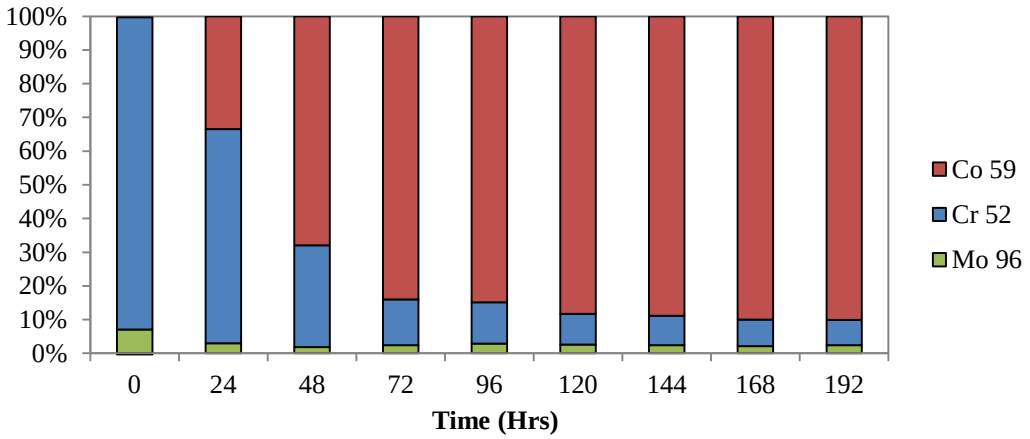

Figure 9-19 – Average evolution of Co, Cr and Mo over 500,000 cycles for coupled Ultima TRS with DePuy MV bone cement (n=3)

9.7. Influence of Gait on Current Transients

High resolution potentiostatic measurements, synchronised with the applied load, were conducted in order to identify the exact mechanism of de and re-passivation. An over-potential of +50mV relative to OCP was applied to the sample and the resultant current sampled at 25Hz in an attempt to get a high resolution snap shot of the de and re-passivation behaviour over one loading cycle. According to ISO 7206-4:2010, a simplified gait cycle based on the average weight of a European patient should be applied to the head of the femoral stem, typically consisting of a sinusoidal load between 200-2300N at 1Hz. The gait cycle has been extensively investigated since the 1960's demonstrating the pattern of variation of resultant force at the hip joint obtained by calculation from experimental measurements of body movement and ground-to-foot force observations. Figure 2-3 demonstrates the gait cycle that was presented by Paul et al [13]. It can be seen that the force experienced at the hip joint is 3.9 times body weight at periods of low velocity.

9.7.1. Simplified Gait Cycle

Figure 9-20 demonstrates the typical current and load transients for 3 cycles obtained during dynamic loading. An interesting repetitive cyclic current transient was seen, demonstrating a high current peak around minimum load and a second lower current peak just before maximum load typically occurring at 2.06±0.3kN. The two peak current transient was consistently seen throughout all tests conducted. Note the negative sign convention of the applied load due to sample being loaded in compression.

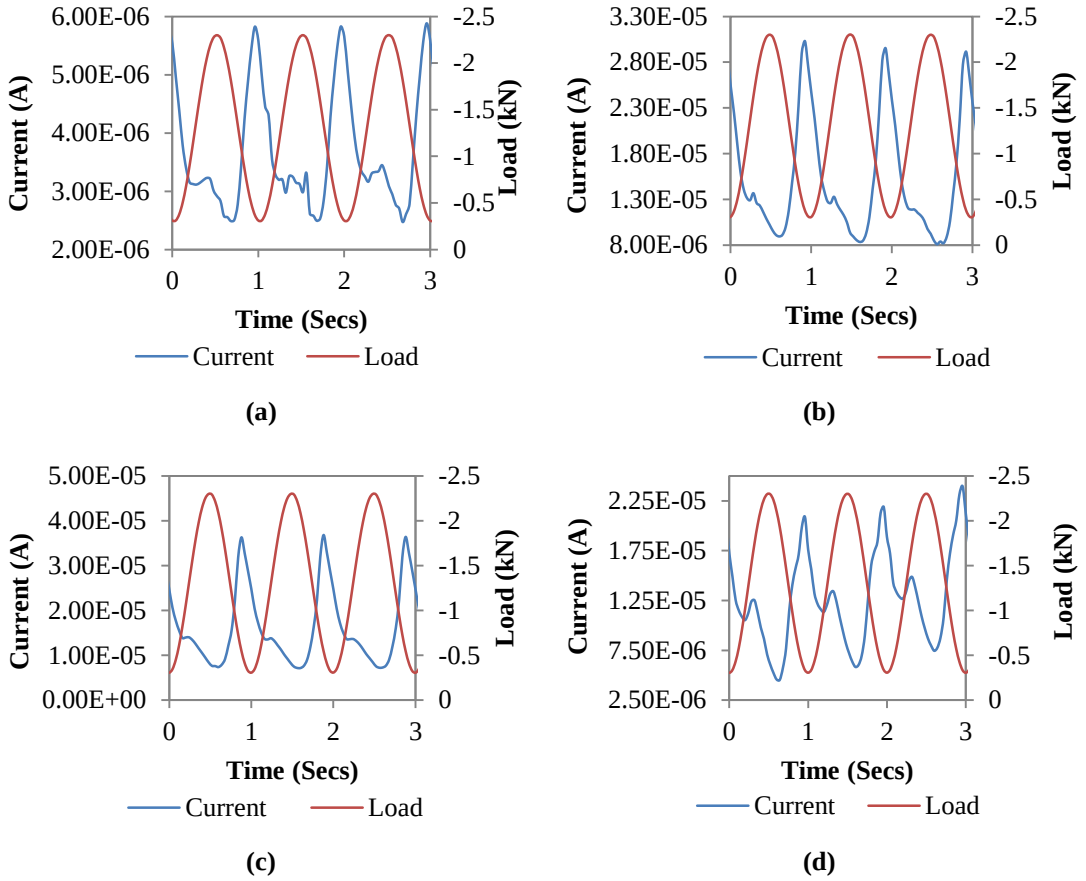

Figure 9-20 - Current and load transients vs. time at (a) 100,000 (b) 200,000 (c) 300,000 and (d) 400,000 loading cycles.

In order to understand how the current transients vary over 500,000 cycles a number of different parameters were observed. The time between peaks, denoted as ΔT, was observed to see if the parameters would change over the course of cyclic loading. The ratio between the max current height and min current (P_1/P_2) at T_1 and T_2, respectively, was also observed in an attempt to understand the evolution of current transients. Figure 9-21 demonstrates the determination of parameters associated with each current transient.

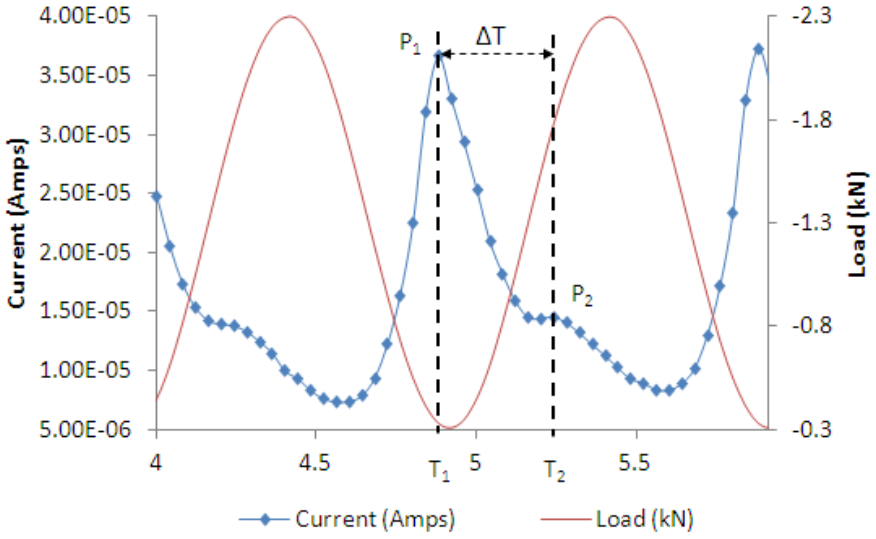

Figure 9-21 - Determination of parameters associated with the current transients

Figure 9-22 demonstrates the variation of parameters over 500,000 cycles of testing for polished femoral stems. The time period between the minimum and maximum current peak (T_2-T_1) was similar in all cases. P_1 was seen to occur just before minimum load was reached. P_2 was seen 0.39±0.09secs after the leading current transient at minimum load (P_1) at 2.06±0.2kN. On average, P_1/P_2 ranged from 1.4 to 2.1 depending on the number of cycles completed. This was not seen to vary between all experimental variables (n=9).

Figure 9-23 demonstrates the evolution of P1 and P2 over 500,000 cycles. It can be seen that P1 and P2 follow a similar trend throughout the test. The extent of corrosion was seen to increase or decrease the current baseline, shifting the transient in the positive of negative direction depending on the level of I_{corr} observed for the system.

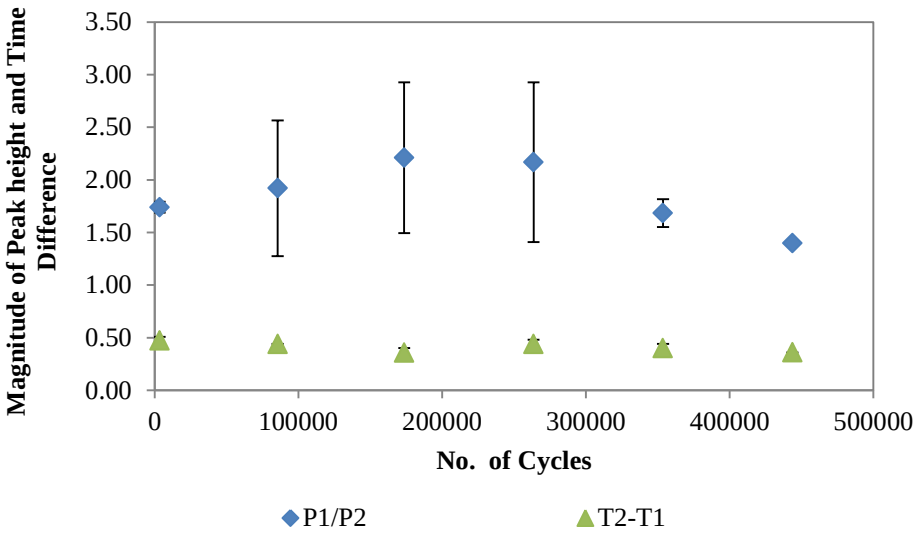

Figure 9-22 - Variation of parameters over 500,000 cycles of testing for polished femoral stems (n=9±SD)

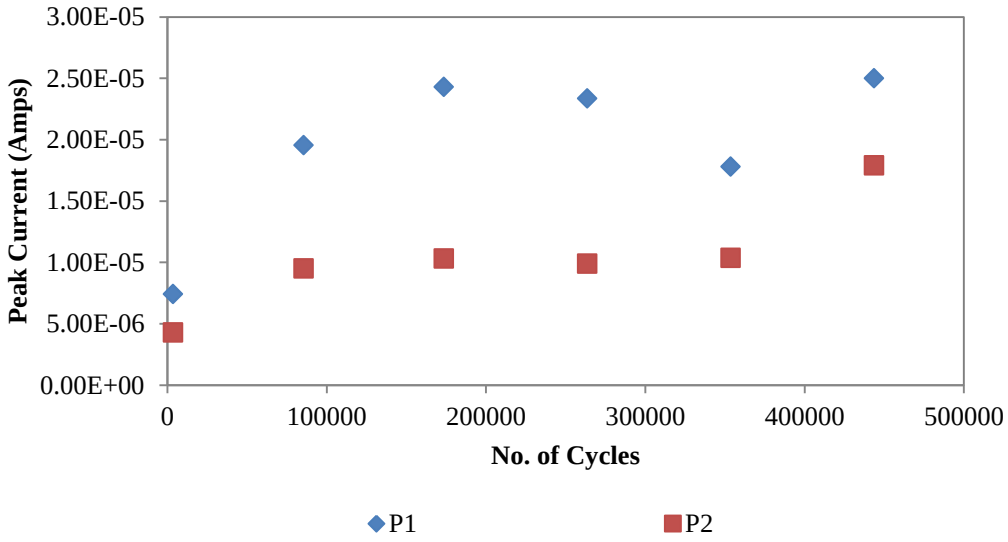

Figure 9-23 - Evolution of P1 and P2 over 500,000 cycles

9.7.2. Origins of Current Transients

Tests were also conducted using a variety of loads and velocities in order to establish how such factors influence the current transients. Figure 9-24 demonstrates how the peak current varies with increasing load and velocity. An increasing peak current was seen when maximum load was increased. This was seen to plateau after 2.3kN at velocities of 1 and 2Hz. This suggested that a threshold exists where the load applied does not affect the current released from the stem-cement interfaces. An increase in peak current was found with increasing velocity.

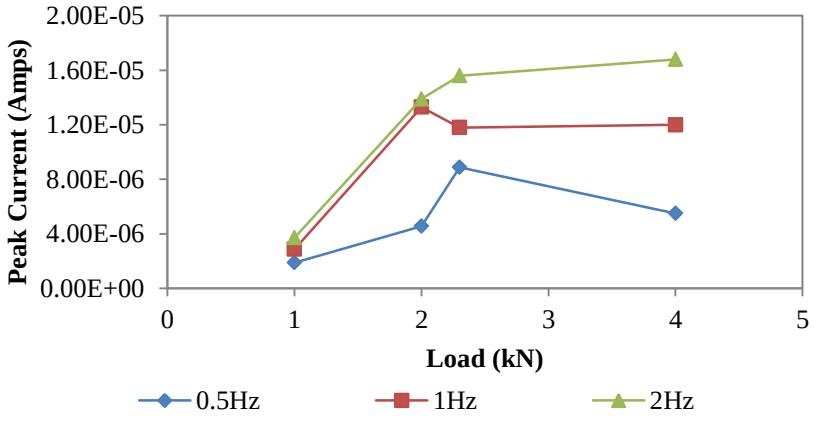

Figure 9-24 - Average effects of load and velocity on peak current (n=3)

In an attempt to isolate the characteristic peaks of the current transients a cemented femoral stem was taken and subjected to a modified loading cycle. Two loading profiles were selected. The first was a square loading pattern that applied, held and removed a sudden load with 10second dwell periods. The second was a sinusoidal loading pattern that applied, held and removed the load with a sinusoidal wave form ramp to the maximum and minimum load. Each loading pattern applied a load between 300 and 2300N; however was held at the maximum and minimum load for 10 seconds and then removed in an attempt to observe different current transients. Figure 9-25 demonstrates the current transients exhibited using the square wave loading pattern.

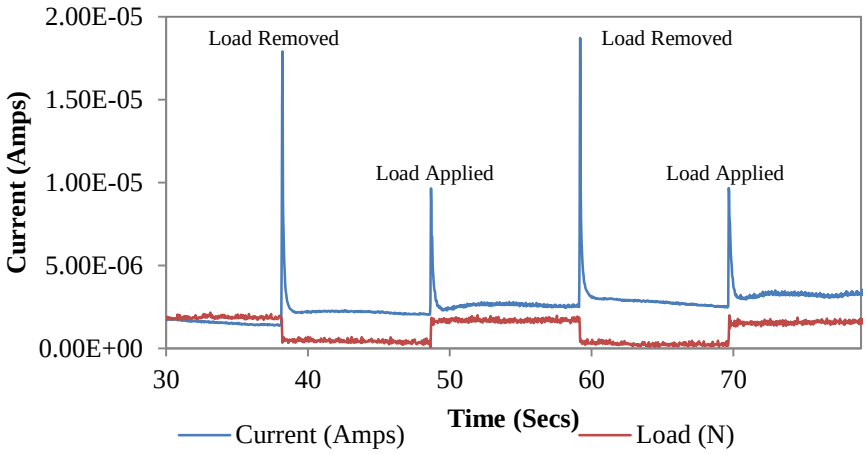

Figure 9-25 - Current transients exhibited using the square wave loading pattern

Two current transients per load cycle were seen when a square loading cycle was used. However a distinct difference between the two peaks was seen. When the maximum load (2300N) was applied a current transient was seen, peaking at ≈ 1.00×10^{-5}A followed by a decay to a base current of ≈ 2.22×10^{-6}A. A second current transient, in the region of 1.8×10^{-5}A, was seen when the load was removed from 2300N to 200N.

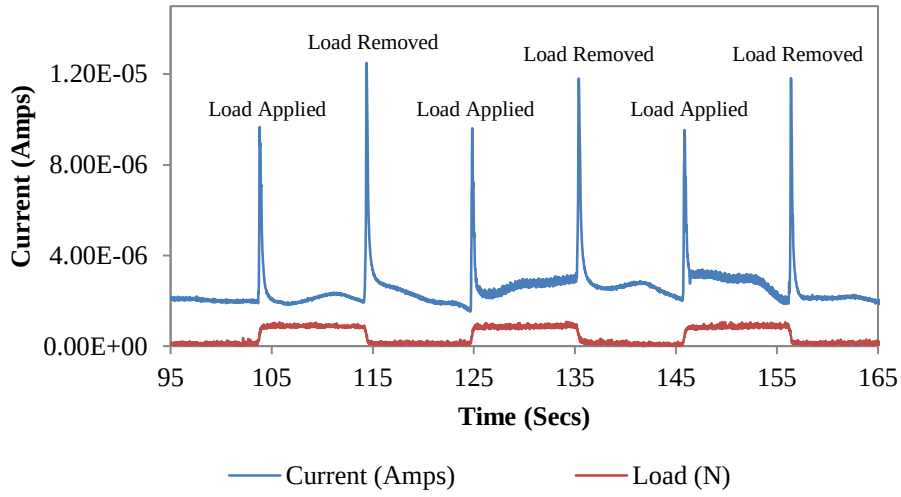

Figure 9-26 - Current transients exhibited using the sine wave loading pattern

9.7.3. Paul Gait Cycle

Figure 9-27 demonstrates the current transient response for a polished femoral stem when subjected to a Paul type gait cycle. An interesting current transient was seen, seeming to take the form of the loading cycle. As the load is applied an increase in current is observed (1). This was seen to decrease until the load was then increased again to maximum load (2). Upon the removal of load another current peak was seen (3). Application of an intermediate load (4) gave rise to a further current transient whilst maximum peak current was seen to occur upon the removal of load (5). Maximum peak current was seen to occur at 0.38kN. A similar observation was seen in Figure 9-20 suggesting that at a specific loading sufficient contact will occur to inhibit or accelerate de/repassivation.

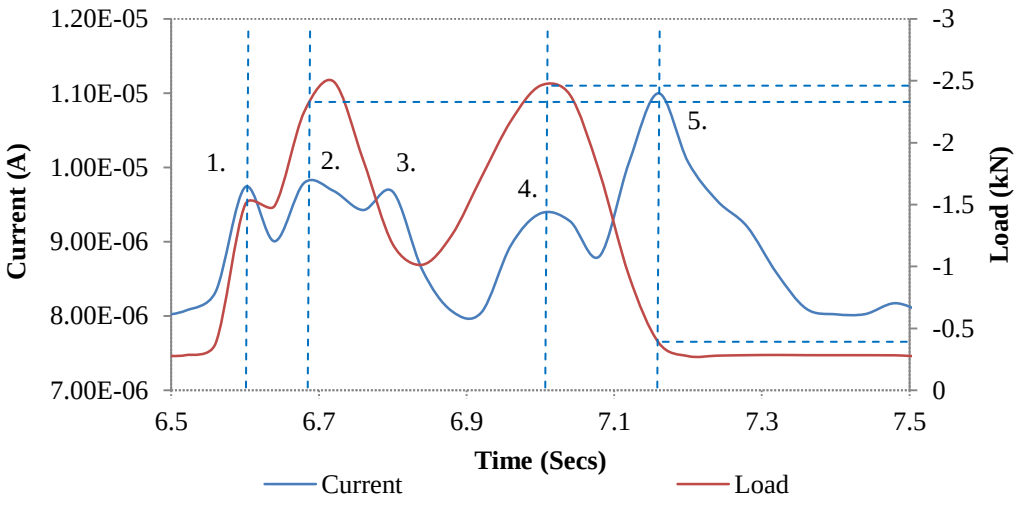

Figure 9-27 - Current and load response for a modified gait cycle

9.8. Influence of Micro-motion on the Surface Morphology, Chemistry and Formation of Fretting-Corrosion Product

Surface analysis was conducted in a systematic process in order to fully understand the effects of fretting-corrosion mechanisms on the surface morphology at the stem-cement interface. To further understand the surface morphology after testing, SEM/EDX, XPS, TEM and white light interferometry were conducted.

9.8.1. Macroscopic and Microscopic Analysis

Figure 9-29 demonstrates the typical surface morphology, on a macroscopic level, of a polished cemented femoral stem and counterpart bone cement after being subjected to cyclic testing. In order to assess the interfaces, each stem was carefully removed, the PMMA bone cement component sectioned using a hand saw and each femoral stem sectioned according to a simplified criteria outlined by Gruen et al [204] (Figure 9-28). Upon removal, extensive damage to the surfaces could be seen in Gruen zones 1-7 and 2-4 on the anterior and posterior planes. Damage was also seen on the medial and lateral surfaces in Gruen zones 1-7. However an increased amount of damage was seen on the medial and lateral edges in Gruen zones 1-2 and 7-6 in the lateral and medial edges respectively. A surface deposit, thought to be a metal oxide film was also seen on the surface of femoral stem and also the bone cement after cyclic testing.

Figure 9-28 - Location and orientation of Gruen zones used to map fretting corrosion

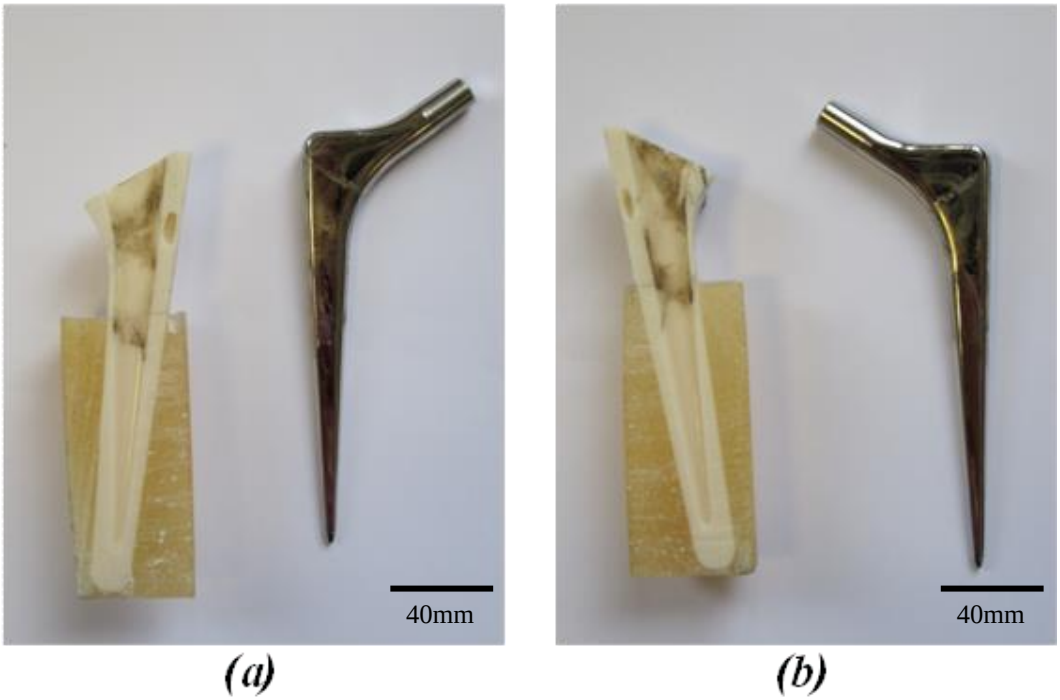

Figure 9-29 - Typical macroscopic surface morphology of polished femoral stems after cyclic testing

Damage could be seen on all surfaces of the femoral stem after cyclic loading; the mechanisms for this degradation varied in the proximal and distal regions. Under the light microscope it could be seen that gross slip had been occurring in Gruen zones 1 and 7 demonstrated by the evidence of plastic deformation and strong directionality at the surface. Although gross slip was observed on both the anterior and posterior surfaces, an increased amount of wear was seen on the posterior surfaces in Gruen zones 1 and 7. The medial and lateral edges were also seen to exhibit an increased amount of wear in the proximal regions of the cemented femoral stem. This is thought to be a result of torsion loading experienced by the stem due to its orientation. Figure 9-30a demonstrates a clear and distinct difference in the surface morphology within the stem-cement interface compared to external surfaces. A clear distinction in the areas subjected to mechanical wear could be seen. Figure 9-30b shows an SEM micrograph of the surface morphology obtained within the stem-cement interface. Extensive plastic deformation and distinct directionality of the surface were observed.

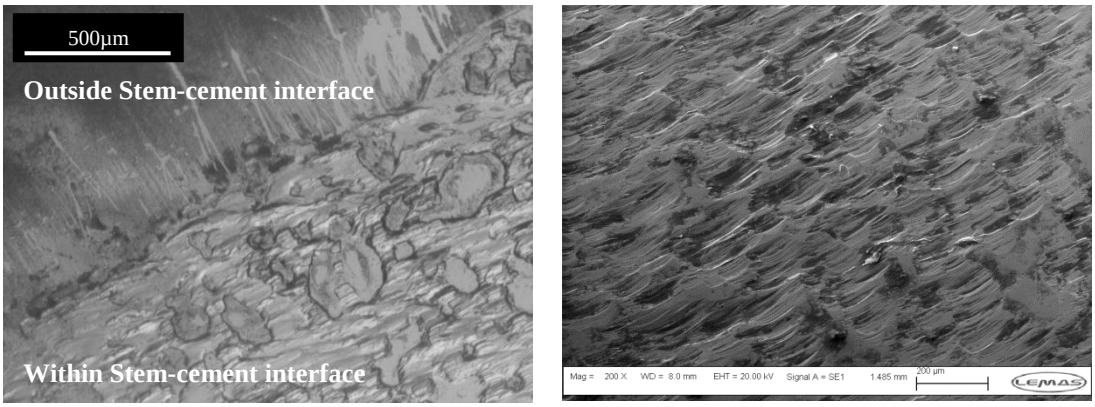

(a) ***(b)***

Figure 9-30 - (a) Optical and (b) SE SEM micrographs of the surface morphology in Gruen zones 1 and 7

The surface morphology was seen to vary distally, with the mechanism for degradation becoming more corrosive towards the distal portions of the stem. Figure 9-31 demonstrates the surface morphology observed in Gruen zones 2 and 6. Although there was some directionality of the surface as a result of micro motion present at the interfaces, a more corrosive attack was seen. This was typically seen in an inter-granular type attack accompanied by some directionality of the surface on areas that had not been affected by localised corrosion.

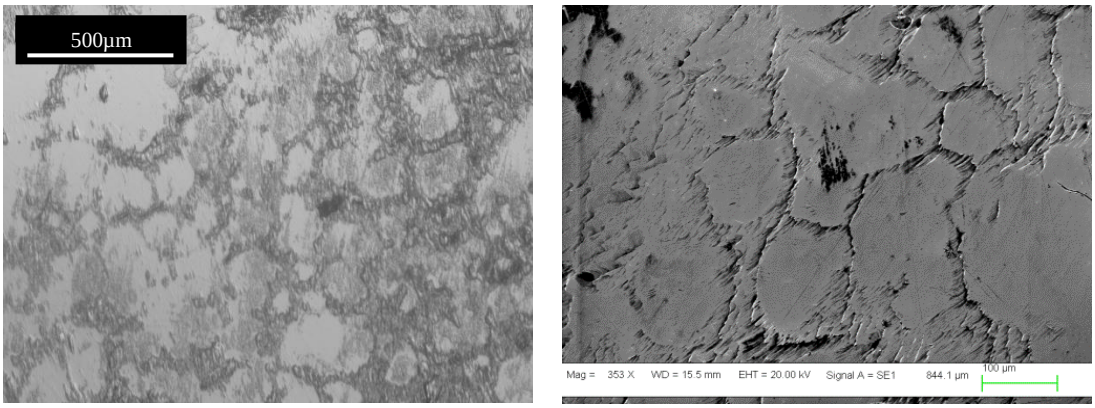

(a) ***(b)***

Figure 9-31 - (a) Optical and (b) SE SEM micrographs of the surface morphology in Gruen zones 2 and 6

Towards the distal portions of the stem, a more corrosive environment was seen where a seemingly inter-granular attack took place. Figure 9-32 demonstrates the surface morphology typically seen in Gruen zones 3-5. No directionality was seen on the distal surface, again suggesting a more corrosive attack rather than a 'mechanically induced' attack. This surface morphology was consistently seen on all simulated samples and varied with the number of loading cycles applied to the cemented femoral stem.

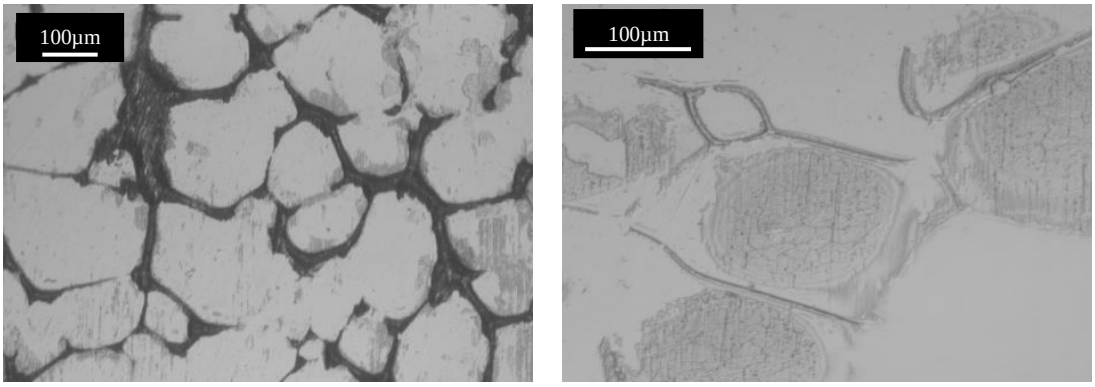

(a) ***(b)***

Figure 9-32 - Optical micrographs of the surface morphology in Gruen zones 3 and 5

Figure 9-33 demonstrates the surface morphology and location of fretting corrosion on femoral stems with an increased surface roughness. Some evidence of fretting-corrosion could be seen within Gruen Zone 7 and 1 on the posterior and anterior surfaces of the stem respectively. This was typically identified as 'polishing' of the femoral stem surface. No evidence of localised corrosion or fretting corrosion could be seen towards the distal regions of the roughened femoral stems. Gruen zones 2, 3, 5 and 6 were macroscopically clear and free of any signs of localised fretting-crevice corrosion. Howell et al [145] presented a comprehensive study on both retrieved polished and matte femoral stems, identifying that polished and matte femoral stems present two very different wear mechanisms. Although the wear mechanism was seen to differ, the location of wear, typically in the anterolateral and posteromedial aspects of the stem, was unaffected suggesting that the torsional loading is the prominent factor; an observation that has been seen in this study. A black surface deposit was also seen in regions of high levels of fretting corrosion on the PMMA cement, although not to the same extent as the polished femoral stem (Figure 9-29).

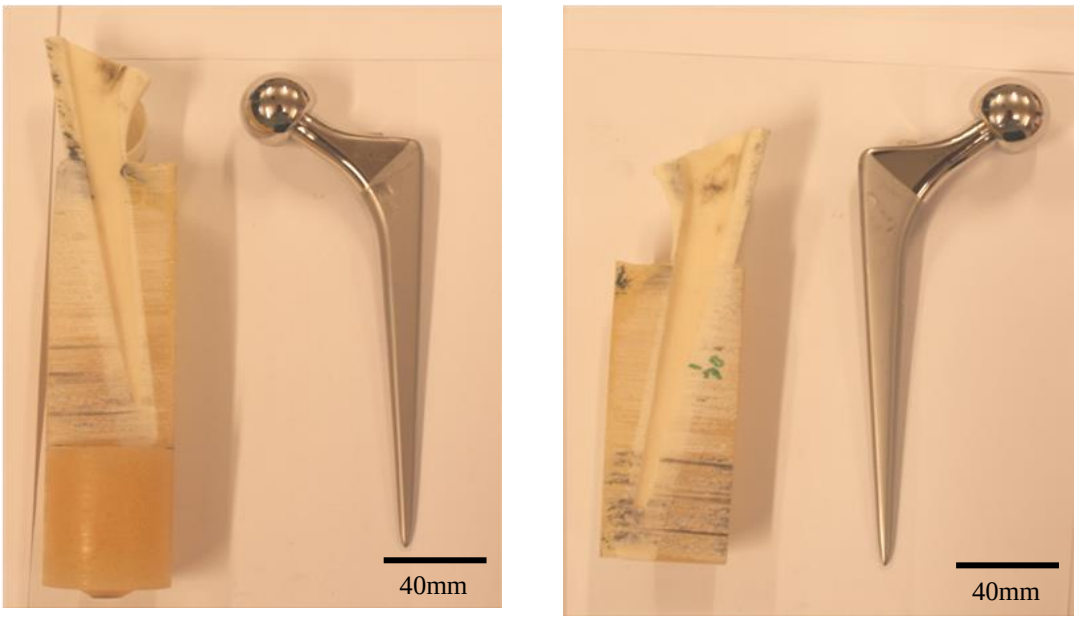

Figure 9-33 - Typical macroscopic surface morphology of roughened femoral stems after 500,000 cycles

Figure 9-34a demonstrates the typical surface morphology in Gruen zones 1 and 7. Fretting-corrosion, characterised by directionality and plastic deformation of the surface could be seen on the surface of the alloy with areas of unaffected material residing within the areas affected by wear. This suggests a partial slip fretting-wear mechanism in the proximal regions for the roughened samples in which some areas remained unaffected by wear whilst some areas exhibited signs of wear. It is thought that such a surface morphology results due to pores in the PMMA cement resulting in high and low areas of contact. No evidence of fretting-corrosion or localised corrosion could be seen towards the distal regions of the femoral stem (Figure 9-34b). Again, roughened femoral stems exhibit increased resistance to localised crevice-corrosion supporting the electrochemical data presented previously.

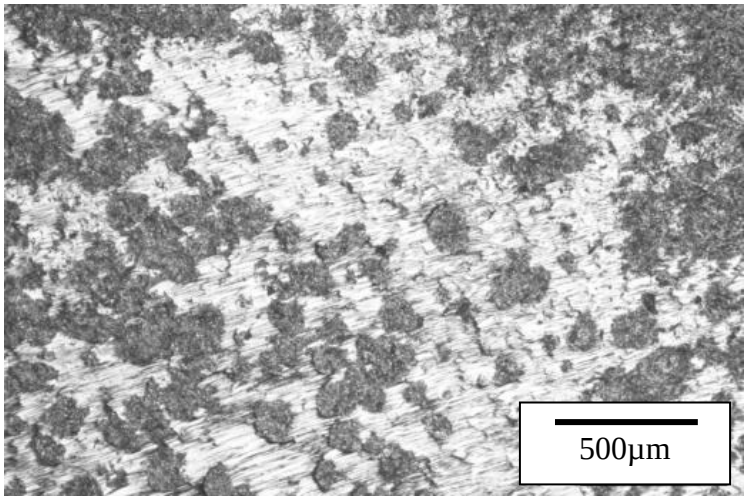

(a)

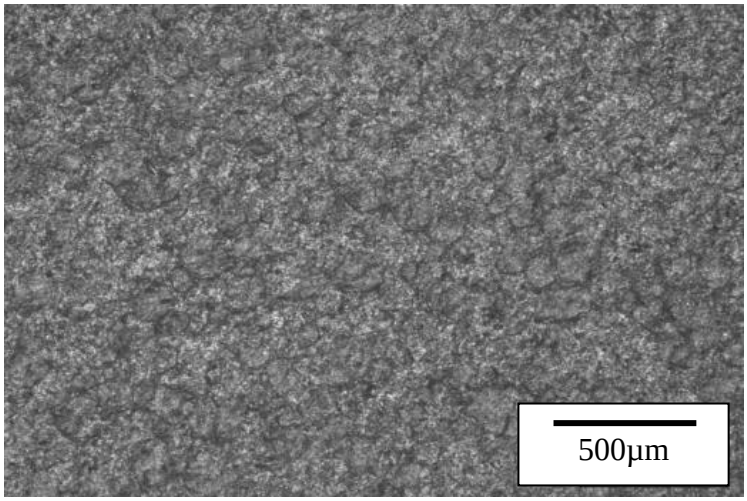

(b)

Figure 9-34 - Optical micrographs of roughened femoral stems in the a) proximal and b) distal regions

9.8.2. Interferometry Analysis

Interferometry was carried out on a select number of samples in order to quantify the extent of plastic deformation of the surface due to fretting-corrosion. Assessment of stem surface topography produced two types of data. Firstly, images of the surface were collected for each score of wear. Secondly, surface parameters were used to quantify the degree of wear exhibited on different areas of the stem. The parameters chosen to quantify wear are shown in Table 9-2, along with a simple explanation of each [145].

Table 9-2 – 3D Surface morphology parameters

Parameter	Abbreviation	Description
Average Surface Roughness	S_a	Mean height of surface topography
RMS deviation of the surface	S_q	A more 'stable' expression of surface roughness
Max. height to Min. Valley	S_z	Height between tallest peak and deepest valley
Direction of irregularities	S_{sk}	Indicates the direction of surface irregularities; zero for randomly rough surfaces, positive where peaks predominate, and negative where pits predominate

Figure 9-35 demonstrate the location and 3D interferometery images of polished femoral stems and counterpart PMMA bone cement after 500,000 cycles of cyclic loading. An increase in S_a was seen in the highly worn areas (SP1 and SP2) compared to distal regions of the femoral stem which were seen to be mainly affected by corrosion (SP3 and SP4) (Table 9-3). An increase is S_z was also seen between the areas suggesting an increased amount of plastic deformation at the proximal regions. A positive skew of the surface in SP1 indicated surface irregularities were in the positive direction suggesting 'ploughing' or deformation of the surface. It is interesting to note that the rest of the regions were seen to exhibit a negative skew. Even though directionally of the surface in SP2 could be seen, a negative S_{sk} suggests that the extent of slip at the interface is not as large compared to SP1. Interferometery observations are similar to those made by Brown and Blunt et al [132, 205] who demonstrated fretting wear initiates at pores within the interface due to relative motion. In SP3 and SP4 the negative S_{sk}, in the absence of any directionality, suggests the presence of pitting on the surface. This has been confirmed by optical and scanning electron microscopy. Pits were seen to range from 2-4µm in depth.

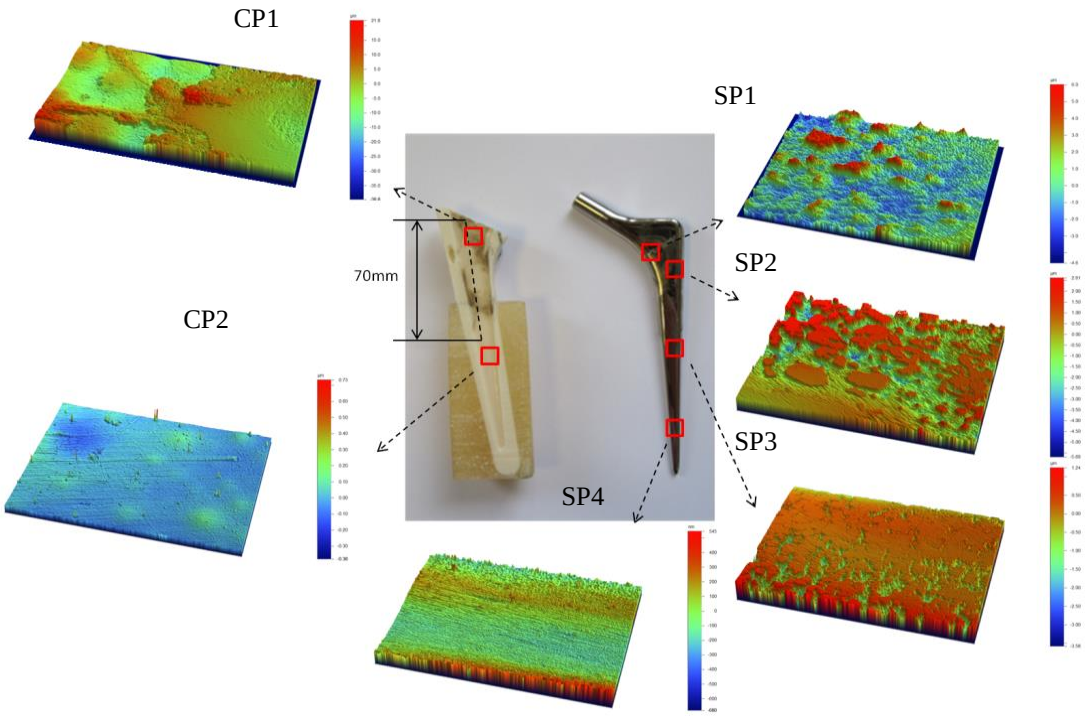

Figure 9-35 - Location and 3D interferometry analysis of polished femoral stems and counterpart PMMA bone cement after 500,000 cycles of cyclic loading

Table 9-3 - Obtained surface parameters for polished femoral stems

	Area				
Parameter	**SP1**	**SP2**	**SP3**	**SP4**	**Virgin Surface**
S_a (µm)	0.78	0.51	0.07	0.05	0.01±0.002
S_q (µm)	1.06	0.73	0.13	0.07	0.01±0.004
S_z (µm)	8.41	10.28	6.53	1.81	0.26±0.21
S_{sk}	0.92	-0.28	-2.30	-0.78	-0.30±0.23

Interferometry and contact 2D traces were also conducted on the PMMA bone cement (Figure 9-35 CP1 and CP2). An increase in surface roughness was seen in the proximal regions of the PMMA cement, approximately 50mm from the interface opening. Figure 9-36 demonstrates the 2D surface profiles of the PMMA bone cement. Increases in surface roughness (R_a) from 0.88 to 4.52µm were seen between bonded and debonded areas respectively due abrasion of the PMMA cement surface.

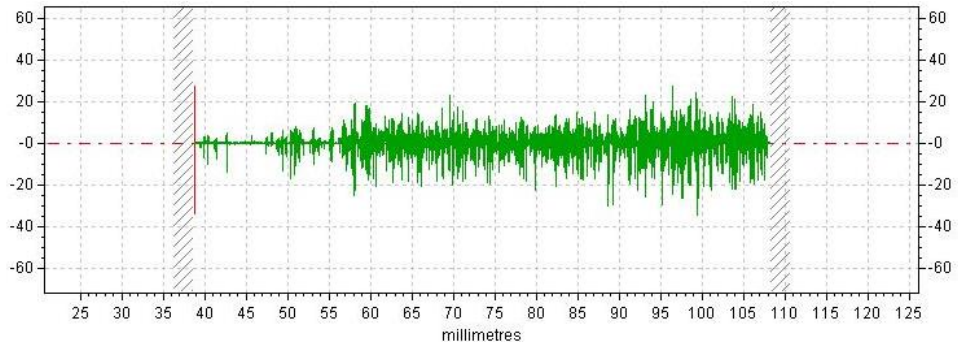

(a)

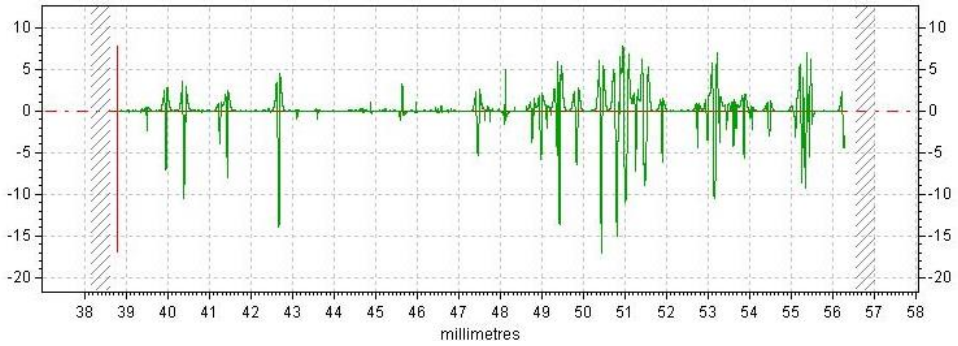

(b)

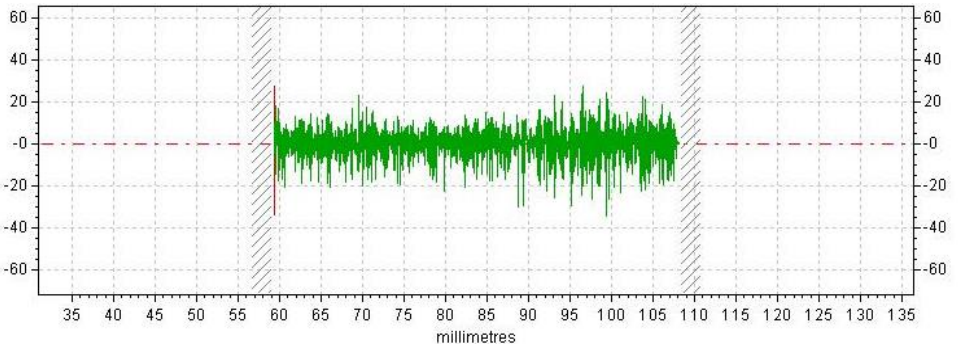

(c)

Figure 9-36 - 2D surface profiles of a) whole trace b) bonded and c) debonded regions on the PMMA bone cement

Figure 9-37 shows the 3D interferometry results for roughened femoral stems and the adjacent PMMA bone cement when subjected to cyclic loading. Table 9-4 demonstrates the different surfaces values obtained from the analysis. For the metallic femoral stem, S_a and S_q was not seen to differ between worn and unworn regions with analysis demonstrating the same amount of peaks and troughs around the mean plane of analysis. An increase in S_z was seen between the SR1 and SR2. For the SR1, S_z along with S_{sk} measurements demonstrate large surface irregularities in the positive direction suggesting ploughing and plastic deformation of the surface. For surfaces that had not been affected by wear or corrosion (SR2), S_z and S_{sk} measurements suggested the height between the maximum and minimum peak was lower, as well as the surface irregularities skewed in the negative direction when compared to SR 1. Interferometry analysis demonstrated that distal areas unaffected by wear and corrosion displayed similar surface values as virgin surfaces. This can be seen in the 2D line traces presented in Figure 9-38.

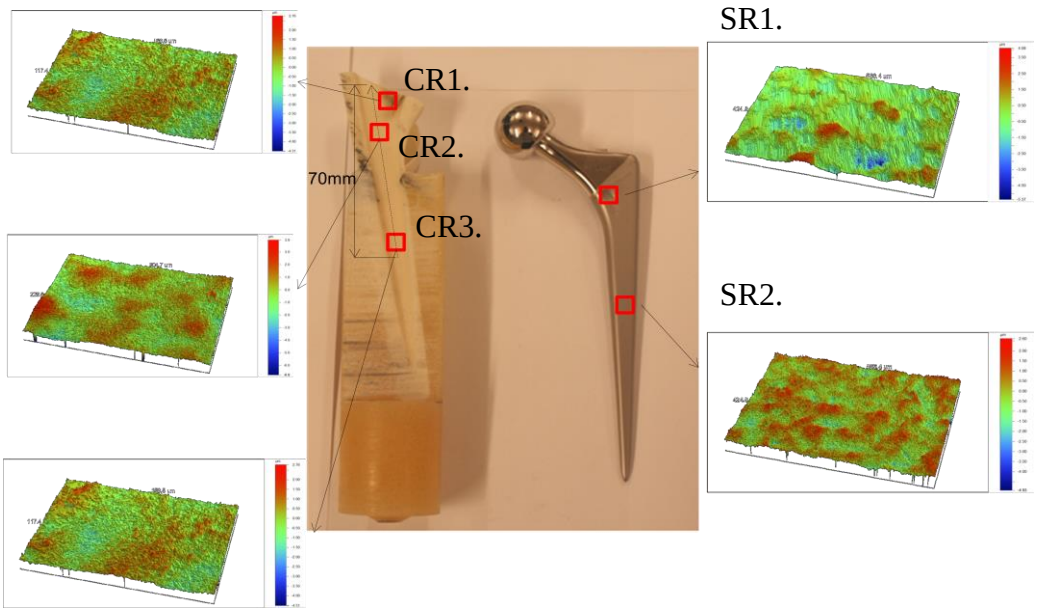

Figure 9-37 - Location and 3D interferometry analysis of roughened femoral stems after 500,000 cycles of cyclic loading

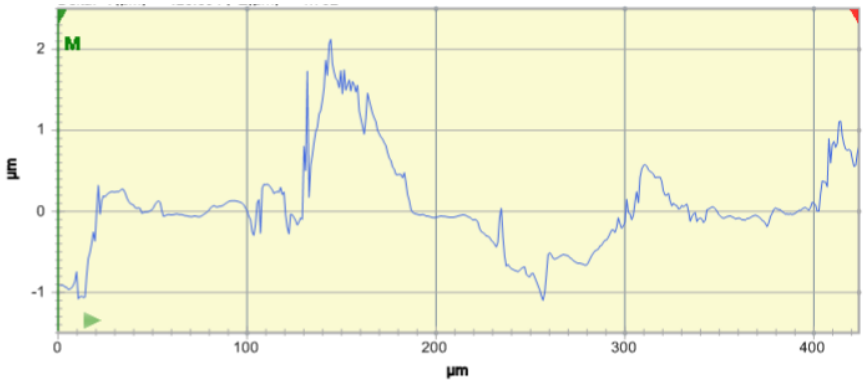

(a)

(b)

Figure 9-38 - 2D surface morphology of roughened femoral stems in a) SR1 and b) SR2 regions after 500,000 cycles

Table 9-4 - Measured surface parameters for roughened femoral stems

Parameter	SR1.	SR2.	Virgin Surface
S_a (µm)	0.54	0.54	0.51±0.01
S_q (µm)	0.74	0.69	0.67±0.01
S_z (µm)	9.38	7.45	7.88±0.71
S_{sk}	0.07	-0.59	-0.44±0.24

3D interferometry analysis was also conducted on the adjacent PMMA bone cement (Figure 9-37). Table 9-5 demonstrates the surface texture values obtained from the analysis. In the regions where high amounts of fretting-corrosion had occurred on the femoral stem (CR1), an increase in S_a, S_q and S_z was observed when compared to regions that had remained fully bonded to the femoral stem and not exhibited any signs of localised fretting-corrosion (CR3). S_{sk} was also seen to decrease suggesting more surface irregularities in the negative direction. Comparison between CR1 and CR2 demonstrated that although an increased amount of asperities were seen, the maximum height between asperities and direction of asperities was different. Figure 9-39 demonstrates 2D surface topography. From the 2D traces it can be seen that less asperities in the positive direction were found in CR 1 compared to CR2 and CR3. This suggest that a 'polishing' of the PMMA cement occurs in the regions of high fretting wear removing asperities in the positive direction. 2D length traces (Figure 9-40) of the PMMA bone cement demonstrated no changes in R_a down the length of the interface.

Table 9-5 - Obtained surface parameters for the counterpart PMMA bone cement after 500,000 cycles with a roughened femoral stem

Parameter	CR1	CR2	CR3
S_a (µm)	0.58	0.67	0.46
S_q (µm)	0.81	0.85	0.57
S_z (µm)	12.34	10.74	7.42
S_{sk}	-0.70	0.18	-0.17

(a)

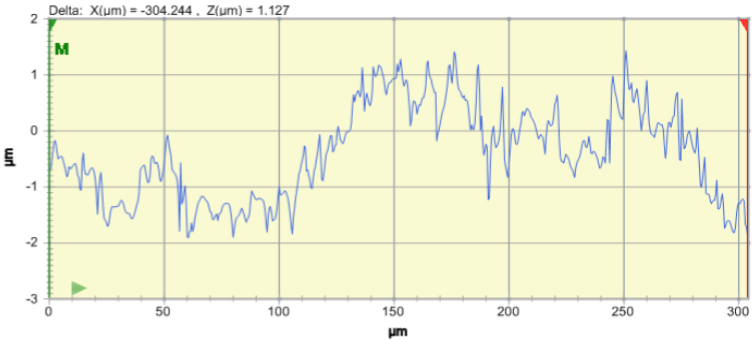

(b)

(c)

Figure 9-39 - 2D surface morphology of PMMA bone cement in a) Area 1 b) Area 2 and c) Area 3

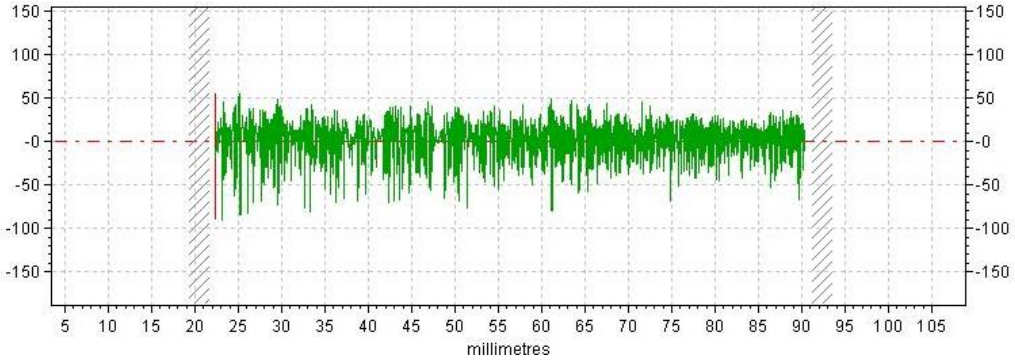

Figure 9-40 - 2D Trace of the counterpart PMMA bone cement with a roughened femoral stem

9.8.3. Influence of Cyclic Loading on Surface Tomography and Surface Chemistry

The surface tomography of femoral stems and the PMMA bone cement was observed under the TEM using a FIB preparation technique as shown in Figure 9-41. Sectioning of samples was conducted post testing in order to produce samples of an appropriate size to fit in the FIB-SEM. The FIB preparation procedure was then conducted according to the method outlined in Chapter 3.7.2.

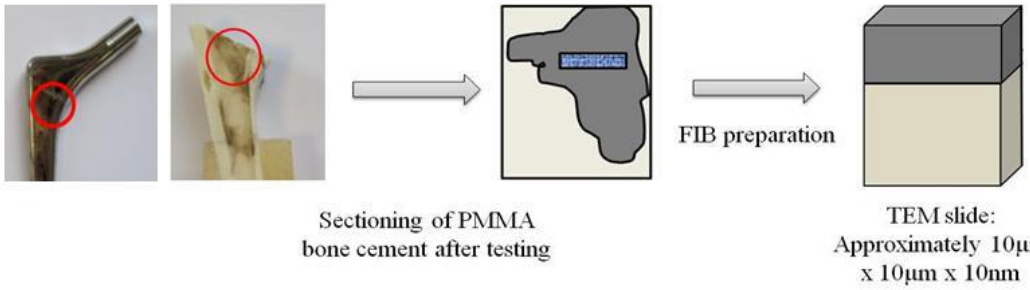

Figure 9-41 - Schematic diagram depicting the location of corrosion and site of FIB/TEM preparation

TEM imagery of the localised areas of debris typically seen on the cemented portions of the cemented femoral demonstrated a thick layer fretting-corrosion product (Figure 9-42a), seemingly sat on top of the LC CoCrMo femoral stem surface (Figure 9-42b). This layer was seen to vary from approx. 1.42 – 1.64µm.

Due to the nature of the TEM microscope it is possible to observe the way in which the transmitted electrons interact with the crystals present within the samples. Bragg diffraction is a consequence of interference between waves reflecting from different crystal planes. The pattern produced as a result of this diffraction gives information of the separations of crystallographic planes *d*, allowing the crystal structure to be deduced [64]. By measuring the radius of different rings of the diffraction image, estimation of the crystallite characteristic atomic spacing and crystal orientation of

the debris/deposit could be made. Analysis of the diffraction patterns demonstrated the fretting corrosion product had the characteristic d-spacing of Cr_2O_3 with crystals been orientated in the [110], [113], [116], [300], [220] and [226] planes. Crystallites of Cr_2O_3 (Figure 9-42c) were seen to exhibit a 'coffee bean' morphology, similar to the observations presented in Chapter 4.4. It was interesting to note that no re-orientation or formation of a nano-crystalline layer was seen in the subsurface LC CoCrMo femoral stem again complimenting the failure analysis.

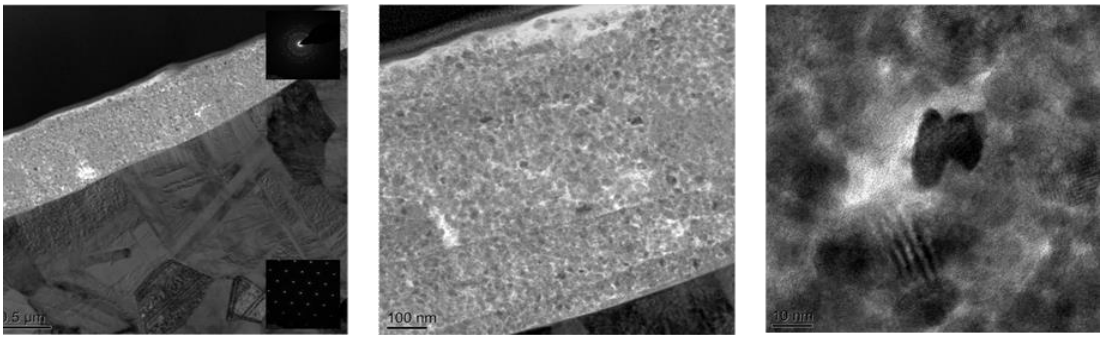

Figure 9-42 - TEM analysis of a) fretting-corrosion product and bulk materials with associated diffraction patterns b) debris and bulk material interface and c) debris within the interface on polished femoral stems 500,000 cycles.

(S)TEM/EDX (Figure 9-43) further complemented the analysis of diffraction patterns. A Cr and O rich deposit was seen on the surface of the LC CoCrMo femoral stem. A localised area of Co was seen towards the top regions of the analysed TEM slide. This is thought to result in the latter stages of the fatigue testing due to partial dissolution of any Co within the interface.

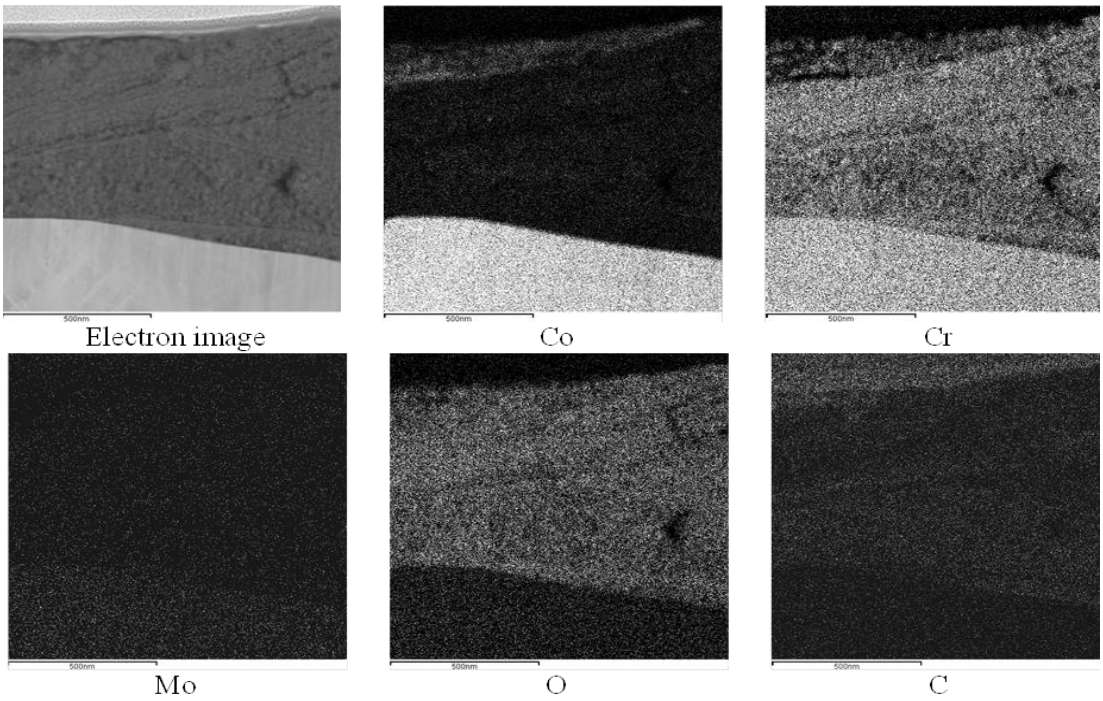

Figure 9-43 - EDX analysis of debris on the surface of the polished CoCrMo femoral stem

TEM imagery of the counterpart PMMA (Figure 9-44a) bone cement demonstrated a thick (≈1μm), dense and heterogeneous layer of crystalline metallic debris on the surface of the amorphous PMMA bone cement. Similarly, resolution of the SAED patterns presented a d-spacing characteristic of Cr_2O_3, suggesting the formation of crystalline Cr rich oxide debris on the surface of the PMMA bone cement. Closer examination of the debris-PMMA interface (Figure 9-44b) demonstrated that some degree of amalgamation of the debris within the PMMA bone cement occurred. This is presumably due to the continual removal of metallic debris from the metallic stem and compaction of debris due to the micro-motion present at the interface. Again crystallites of Cr_2O_3 (Figure 9-44c) with a 'coffee bean' morphology were seen similar to the debris seen on the metallic femoral stem.

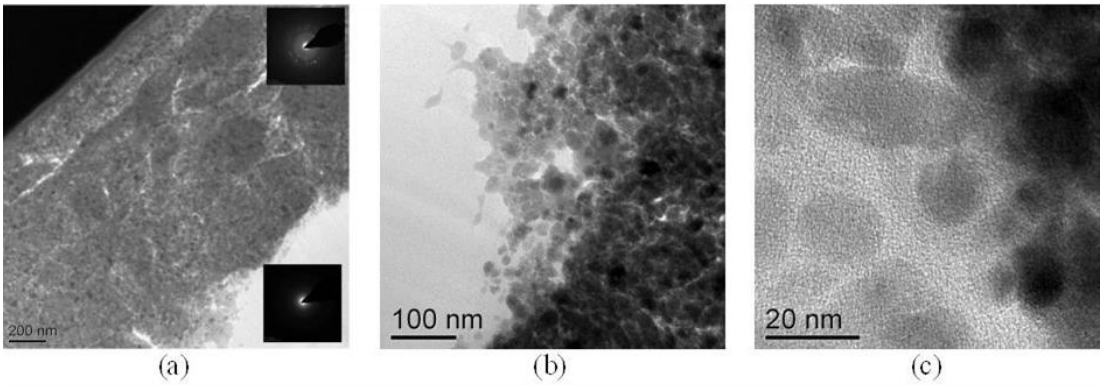

Figure 9-44 - TEM analysis of a) fretting-corrosion product and bulk materials with associated diffraction patterns b) debris and bulk material interface and c) debris within the interface on PMMA bone cement after 500,000 cycles

(S)TEM/EDX (Figure 9-45) further complemented the findings provided by the diffraction analysis. A Cr and O rich film was identified. Trace amounts of Co and Mo were also present in the debris found on the surface of the PMMA bone cement. Co and Mo were not seen in the same quantities typically observed in the bulk alloy due to the method of transfer from the femoral stem and assumed conditions within the interface.

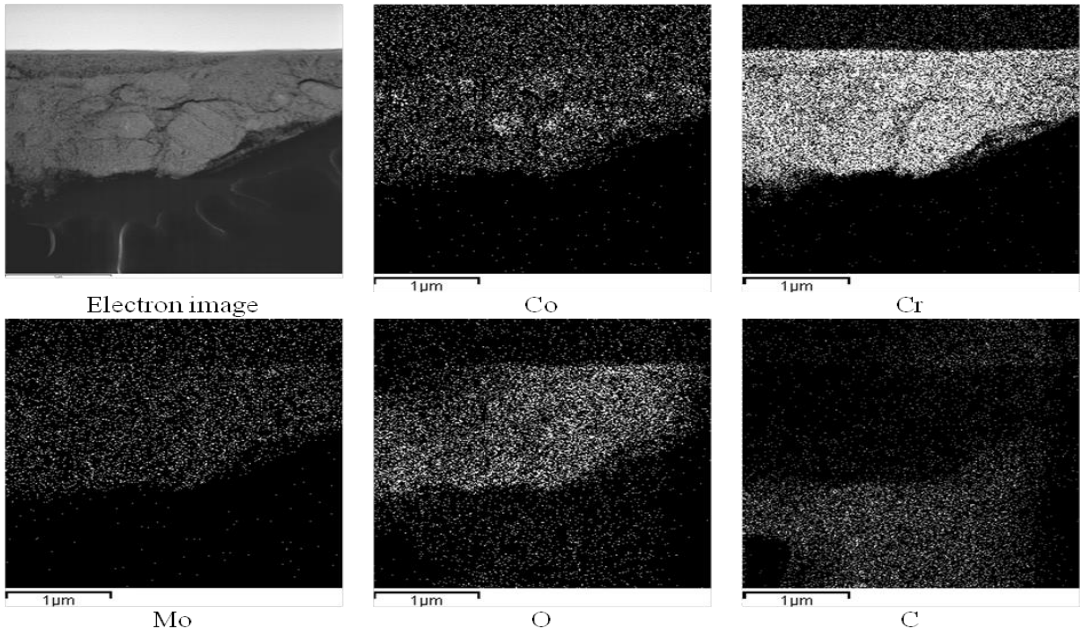

Figure 9-45 - EDX analysis of debris on the surface of the PMMA bone cement after 500,000 cycles of dynamic loading

XPS analysis was further conducted in order to determine the exact chemical speciation of elements present on the PMMA bone cement transfer film. Due to the spatial resolution of the XPS and location of the film, the technique was not deemed suitable for further analysis of the simulated femoral stems due to the relatively localised nature and location of the film. In order to obtain accurate data, an argon ion etch at 1µA/3mm^2 was applied to each of the surfaces in an attempt to eliminate any surface elemental contaminant. Charge compensation was also utilised due to the semi-conductive nature of the PMMA bone cement.

Figure 9-46 demonstrates the general XPS spectra of the black transfer film seen on the DePuy HV and MV PMMA bone cements after 500,000 cycles of fatigue testing. Initial scans suggested that a similar elemental composition existed between the two samples with the exception of Ba 3d and Zr 3d due to the radiopaque agent. Co 2p, Fe 2p, Cr 2p, O1s, N 1s, C 1s, Mo 3d, Cl 2p and H 1s where observed on both surfaces.

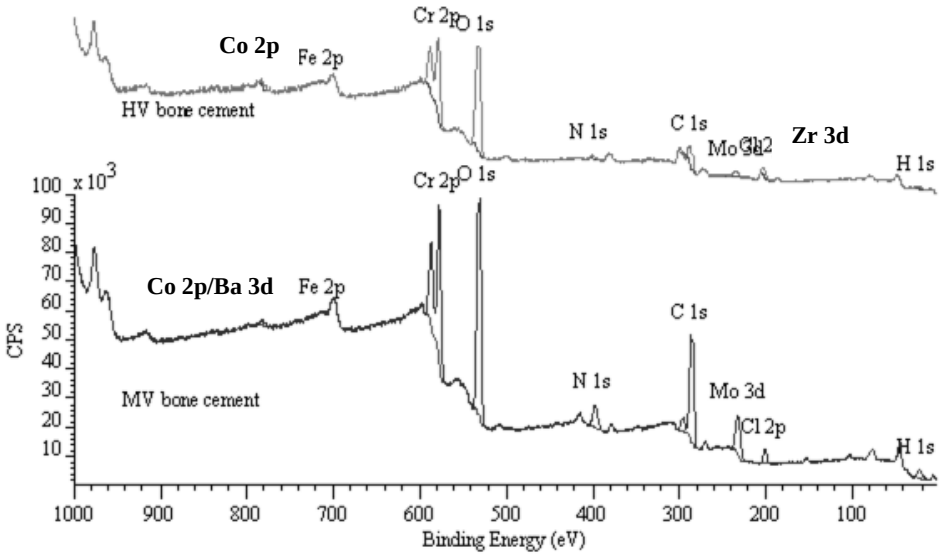

Figure 9-46 - General XPS survey scans for DePuy HV and MV PMMA bone cement

Figure 9-47 demonstrates the high resolution XPS spectra for Co 2p, Cr 2p, Mo 3d and O 1s. De-convolution of the Co 2p spectra indicated peaks occurring at 781.18 and 796.38eV and 788.00 and 803.31eV indicating the presence of $CoO+Co_2O_3/Co_2O_4$ and a $Co_{(III)}$ satellite, respectively, on the surfaces of the PMMA bone cement [112, 168]. Additional peaks were seen on the MV PMMA bone cement at 785.58 and 800.70eV suggesting the presence of $CoSO_4$ [206]. This is thought to arise from the interaction between the sulphate containing cement and metallic femoral stem.

Resolution of the Cr 2p spectra again demonstrated a comparable speciation of elements on the surfaces of the PMMA bone cement. Prominent peaks at 577.50 and 587.25eV were seen indicating the debris to be $Cr(OH)_3$ rich. Peaks were also resolved at 576.28 and 585.78eV suggesting the presence of Cr_2O_3 [109, 112, 168, 206]. Peaks were also resolved at 578.70 and 588.50eV and 581.28 and 591.08eV suggesting the presence of $Cr_{(VI)}$ and Na_2CrO_4 respectively [112]. $Cr_{(IV)}$ was only seen on the ZrO_2 bone cement however remains a controversial observation due to the toxic nature of speciation.

Further de-convolution of the Mo 3d spectra indicated the presence of metallic Mo, MoO_3 and MoO_2 with peaks being resolved at 228.50 and 231.11eV, 232.88 and 235.05eV and 229.77 and 232.88eV respectively [112, 168]. These are thought to be to be only trace quantities due to the level of CPS seen during the analysis.

Similar O 1s spectra where seen for each PMMA bone cement. Peaks could be resolved at 530.17, 531.45, 532.01 and 533.28eV indicating elemental O, OH^-, H_2O and chlorate/organic O, respectively, on the surfaces after fatigue testing .

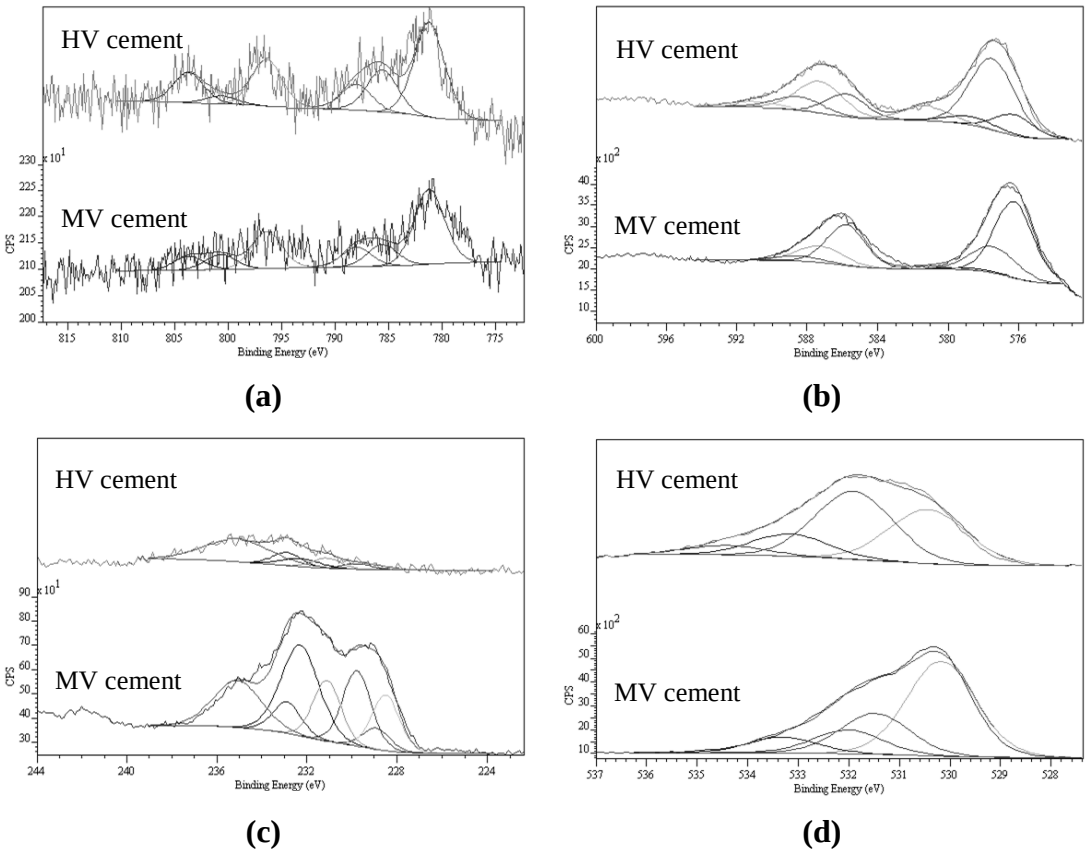

Figure 9-47 - Resolution of the a) Co 2p b) Cr 2p c) Mo 3d and O1s XPS spectra for fretting corrosion transfer film seen on DePuy HV and MV PMMA bone cement after 500,000 cycles of fatigue testing

9.9. Discussion

In this work, the electrochemical response and surface morphology of cemented CoCrMo femoral stems, subjected to fretting-corrosion conditions has been characterised using a variety of electrochemical and surface analysis techniques. Findings in this section can be summarised into the following:

1. The application of cyclic loading mechanically induces depassivation increasing the rate of dissolution.
2. Sulphate containing PMMA bone cements were seen to further increase the rates of wear-enhanced oxidation.

3. Surface roughness was seen to influence the fretting corrosion rates with an increased surface roughness reducing the fretting corrosion currents and total metallic ion release. This again affects the relative contributions of wear-induced corrosion and dissolution of particulate to the overall ionic mass loss.
4. Galvanic coupling was seen to increase the rates of pure and wear-enhanced oxidation. This was seen for both blasted and polished femoral stems.
5. The application of cyclic loading had a effect on the ratio in which metal ions where released. A preferential release of Co 59 was seen in fretting tests whilst a ratio of alloying elements similar to that found in the bulk alloy were seen in static dissolution studies.

This next section aims to discuss the findings and current hypothesis surrounding fretting corrosion of cemented femoral stems.

9.9.1. Influence of Micro-motion of the Dissolution of CoCrMo

The presence of fretting at the stem-cement interface has recently been studied by Zhang et al [205, 207, 208], who identified that significant wear can occur at the stem-cement interface resulting in accelerated deterioration of a cemented femoral stem. Geringer et al [209-211] further presented extensive studies demonstrating how corrosion and the local environment can influence the overall mass loss of Metal-PMMA bone cement contacts in fretting-corrosion environments. A variety of electrochemical techniques have been utilised in this chapter in order to understand how the wear at the stem-cement interface can influence the corrosion kinetics with respect to metal ion release from biomedical devices. Both the general tribo-corrosion response over 500,000 cycles and current transients per loading cycle have been characterised. In general, the results in

this study demonstrate that the application of cyclic loading results in a mechanically induced de-passivation of the metallic alloy leaving the exposed substrate free to corrode according to the reaction outlined in Equation 9-1.

Equation 9-1 - Anodic half reaction

$$M \rightarrow M^{n+} + ne^{-}$$

However, potentiostatic measurements indicate that the surface is in a constant state of de-passivation and re-passivation. Over each loading cycle the Cr rich passive film is fractured exposing the base alloy to the aqueous solution. Oxidation according to Equation 9-1 is thought to occur at the point of contact between the stem and cement. Repassivation of the depassivated areas will also occur resulting in the overall reaction presented in Equation 9-2 occurring within the interface. Both the ionic dissolution and repassivation reactions result in the liberation of free electrons which are subsequently detected as current transients [127, 212]. Each current transient is the algebraic sum of the dissolution and oxide growth from the depassivated region (Equation 9-2)

Equation 9-2 - Formation of the metallic oxide film

$$M + nH_2O \rightarrow MO_n + 2nH^{+} + 2ne^{-}$$

Figure 9-48a-e schematically demonstrates the depassivation and repassivation of the CoCrMo surface over one loading cycle. At the initial stages of loading the film, substrate, PMMA bone cement and points of contact are elastically deformed (a). As the load is increased, the fracture stress of the Cr oxide film is exceeded and rupture of the oxide film occurs, along with the plastic deformation of the metallic surface caused by the abrasion by Cr_2O_3 films formed generated during the initial stages of fretting and the potential generation of metallic

particulate debris due to mechanical wear (b). This results in the CoCrMo substrate being exposed to the solution resulting in an anodic current flow, participating in Equation 9-2. At the point where maximum load has been applied, the stem-cement interfaces are held together with the PMMA bone cement protecting most of the depassivated areas in the oxide film from the electrolyte resulting in no current flow (c). It is thought that the transfer of metallic debris occurs when the CoCrMo and PMMA bone cement surfaces are in contact resulting in compressed Cr_2O_3 debris. As the load is removed the surfaces gradually become separated until the contact area is sufficiently reduced to expose the ruptured oxide film and substrate to the electrolyte (d). This results in a net anodic current flow resulting in the dissolution and partial repassivation of the oxide film occurs according to Equation 9-2. Partial repassivation occurred due to the oxidation and reduction of the Cr^{3+} and H_2O resulting in a protective Cr_2O_3/Cr_2OH film reducing oxidation to a minimum (e).

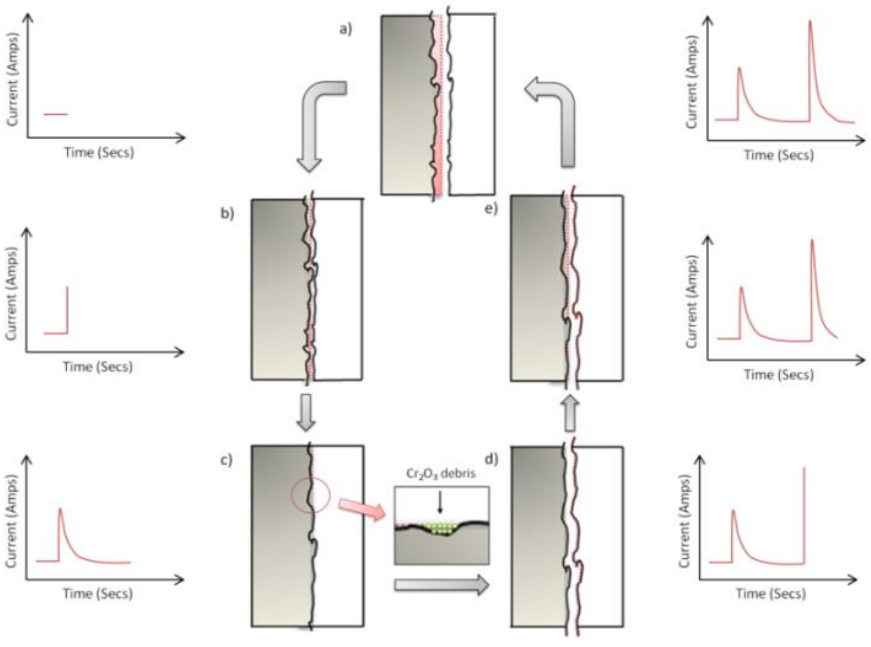

Figure 9-48 - Schematic representation of current transients observed at the stem-cement interface as a function of loading/contact.

A study by Goldberg [212] demonstrated that the total current (i_t) observed at a surface is the sum of the currents (Equation 9-3) due to film growth (i_f) and ionic dissolution (I_d) ($i_t=i_f+i_d$). Where δ= oxide thickness, ρ= oxide film density, θ= area fraction covered by oxide, η = over potential for dissolution reaction and β= Tafel slope for dissolution. Goldberg also identified, through a series of scratch tests, that as the load increased, deeper scratches would occur resulting in a larger initial scratch area (A_o). As A_o increases, both terms in Equation 9-3 increase resulting in an increase in current.

Equation 9-3 - Current transient owing to anodic dissolution and repassivation of the surface

$$i_t = \frac{\delta \rho F A_o}{M_w}\frac{d\theta}{dt} + j_{crit}A_0(1-\theta)exp^{\frac{\eta_f}{\beta_a}}$$

The plastic and elastic deformation of the surfaces could also result in the formation of 3rd body debris which will further contribute to the overall anodic current flow and metallic ion release due to an abrasion and further localised mechanical depassivation mechanism. This is an important consideration as particulates produced at the stem-cement interface have been associated with osteolysis and other inflammatory responses [213-215].

Studies investigating the repassivation kinetics of CoCrMo and other alloys have demonstrated that the magnitude of current decreases when multiple scratches or indentations are made. This phenomenon has been consistently seen by Goldberg, Sun and Fushimi [212, 216, 217] suggesting that the reformed oxide layer may display different properties to the originally formed oxide film. Sun et al [217] further proposed that localised deformation may also change the crystalline orientation of the alloy, promoting a strain induced transformation

from FCC → HCP, affecting both tribological and corrosion characteristics of the material. A similar observation has been seen in this study with a decrease in I_{corr} and potentiostatic current measurements with increasing number of loading cycles. However further studies are required in order to understand how the electro-mechanical properties of passive film vary with load and gait cycle.

9.9.2. Interactions between Wear and Corrosion

Because tribocorrosion describes both the mechanical removal of material as well as the chemical degradation of a material, it is important to appreciate and to identify the contribution of corrosion and wear to material/ionic loss. Uhlig first recognised the role wear and corrosion play on the degradation in fretting contacts as cited by Mischler [127]. It was demonstrated material deterioration results from mechanical wear and wear-accelerated corrosion as shown in Equation 9-4 where V_{mech} represents the volume of material removed by mechanical wear, V_{chem} is the material loss due to wear accelerated corrosion.

Equation 9-4 - Uhlig's mechanistic model for the interactions between wear and corrosion as cited by Mischler [127]

$$V_{tot} = V_{mech} + V_{chem}$$

Due to the nature of the system, it is difficult to quantify the total mass loss from the metallic stem gravimetrically due to the formation and accumulation of corrosion product within the cement mantle. Removal of the femoral stem from the PMMA cement will further influence any gravimetric results providing in-accurate and unrepresentative measurements. Therefore it is not possible to relate the relative contribution of wear and corrosion to the overall mass loss of the system. However through a combination of techniques the relative contributions of oxidation and ionic

material derived from dissolution of debris to the total ionic mass loss can be semi-quantitatively estimated.

The ionic mass loss due to pure oxidation and wear induced corrosion of the metallic surface can be calculated by application of Faraday's Law (Equation 9-5). Where Q is the total electric charge passed through a substance ($Q = \int_0^t I\delta t$, where t is the total time constant, I is the corrosion current obtained through LPR), F = 96,485 C mol^{-1}, M is the molar mass of the substance (58.93g assuming stoichiometric dissolution of the alloy) and n is the valence number of ions in the substance (in this case 2 was assuming oxidation according to $Co \rightarrow Co^{2+} + 2e^{-}$).

Equation 9-5 - Faraday's law of electrolysis

$$m = \left(\frac{Q}{F}\right) \times \left(\frac{M}{n}\right)$$

Corrosion currents measured with the LPR technique do not take into consideration any ionic/metallic debris liberated from the metallic surface due to mechanical wear; only wear enhanced corrosion and pure oxidation as shown in Figure 9-49. Any additional metal ions that are produced due to the production and dissolution of debris will therefore be measured by ICP-MS, a measure of the total ionic mass loss (TIML).

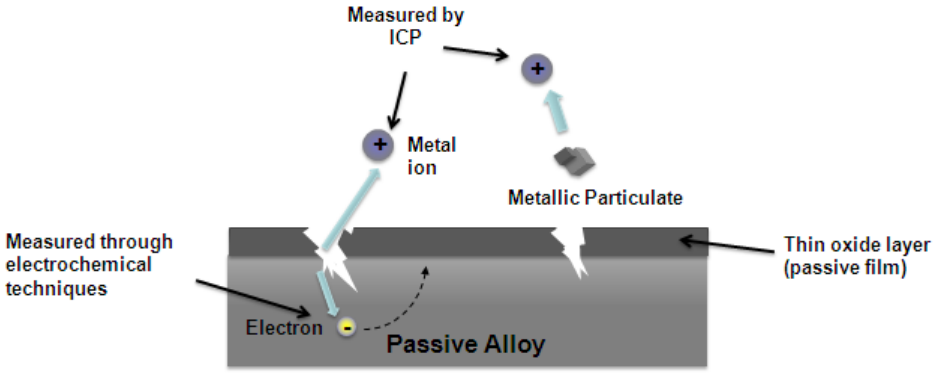

Figure 9-49 - Schematical representation of metal ion and particle release in tribo-corrosion systems

Table 9-6 demonstrates the total ionic mass loss along with the relative contributions of corrosion and further dissolution of any particulate liberated during the fatigue testing. Pure corrosion and wear-enhanced corrosion was seen to account for 65-80% of all metallic ions released into the bulk environment indicating a corrosive wear mechanism at the stem-cement interface. It is interesting to note that for the DePuy MV PMMA cement, oxidation accounted for 65% of all metal ions released into the bulk environment. This is in contrast to the other cements that indicated corrosion accounted for 80% of all metal ions produced (Figure 9-50). This suggests that the presence of barium sulphate not only increases the pure and wear enhanced corrosion, but also increases the ionic mass loss due to an increased production of metallic debris which can further corrode and contribute to the total ionic mass loss.

Table 9-6 - Comparison of metal ions released due to corrosion and dissolution of wear debris (n=3±SD)

Test Name	Average total ionic mass loss measured using ICP (mg)	Average ion release due to corrosion calculated from Faradays law (mg)	Average ion release due to wear/particles (mg)
CMW SmartSet® HV	0.79±0.08	0.65±0.03	0.14
CMW SmartSet® GHV	1.26±0.22	1.03±0.11	0.23
CMW SmartSet® MV	1.44±0.11	0.94±0.30	0.80

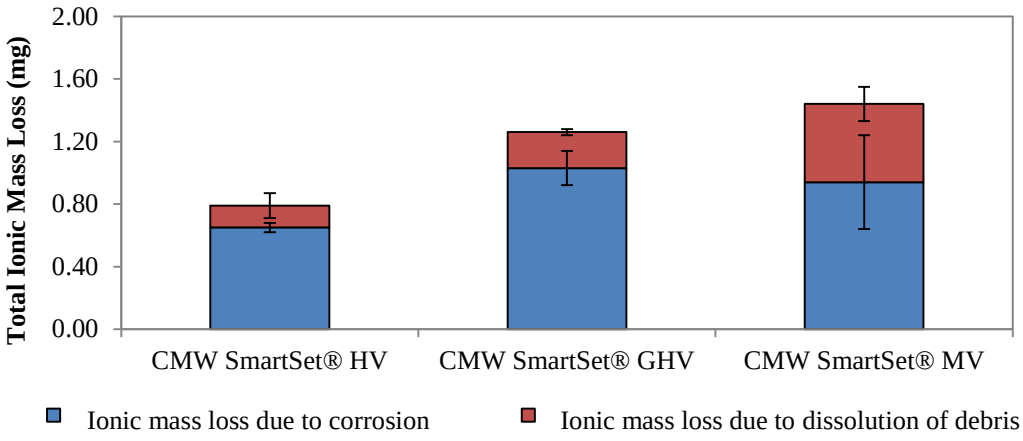

Figure 9-50 - Relative proportions of wear and corrosion over 500,000 cycles for different PMMA bone cements (n=3±SD)

Surface roughness was seen to further influence the relative contributions of corrosion and dissolution of debris to the TIML. For roughened femoral stems (Figure 9-51), pure corrosion and wear-enhanced corrosion accounted for 25% of all metal ions released, whilst further dissolution of metallic debris accounted for the remaining 75%. This can be explained by abrasion of the femoral stem and PMMA cement surfaces in debonded regions resulting in the formation of metallic debris which will further corrode contributing to the TIML.

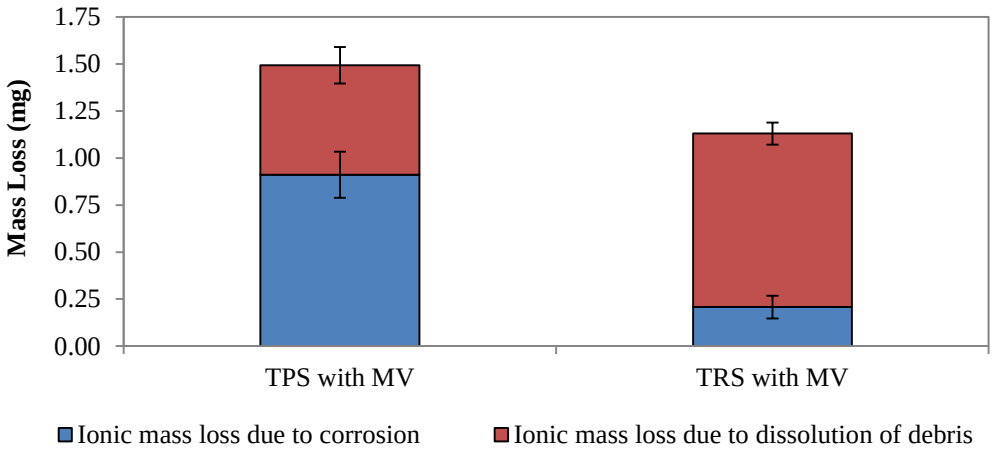

Figure 9-51 - Relative proportions of wear and corrosion for femoral stems with different surface roughness values (n=3±SD)

Galvanic coupling was seen to have a substantial influence on the relative contributions of ion release. The presence of the Ti couple was seen to increase the proportion of metallic ions released due to corrosion in both cases. It has been demonstrated that the presence of Ti has a polarising effect on the CoCrMo femoral stem, substantially increasing the rate of pure and wear-enhanced oxidation within the stem-cement interface.

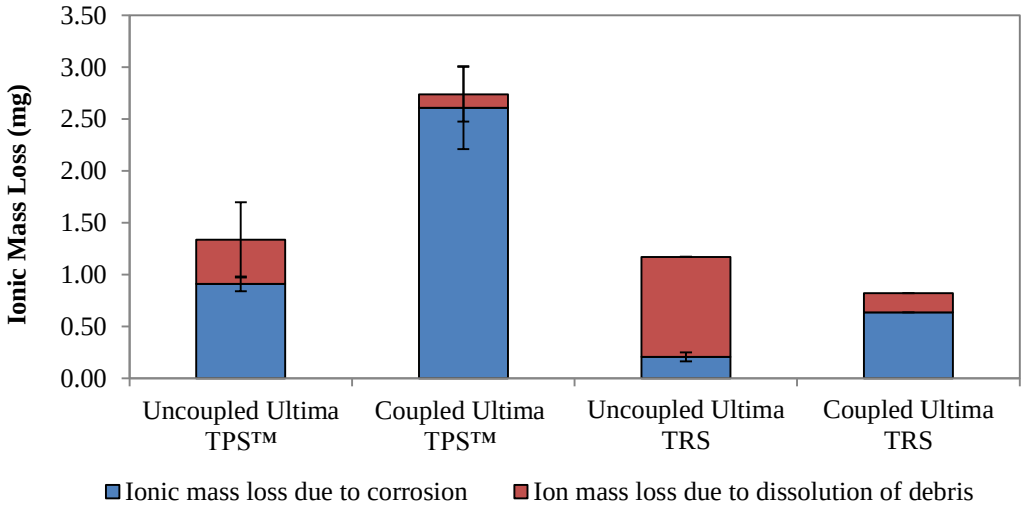

Figure 9-52 - Influence of galvanic coupling on the relative contributions of ion release from wear and corrosion (n=3±SD)

9.9.3. Influence of PMMA bone cement, Surface Pre-treatment and Galvanic Coupling

It has previously been shown that sulphate containing cements can increase a materials susceptibility to localised corrosion as well as passive dissolution rates. This was also seen under fatigue conditions. Sulphates have been described to increase corrosion rates of metallic surfaces by increasing the rates at which hydrogen is reduced at the metallic surface. In this system there is also the possibility of an increase in the local conductivity of the electrolyte at the interface due to the elution of sulphate from the PMMA bone cement, further affecting the

rates of corrosion. As a result, excess metallic valance electrons at the metallic surface will be liberated at an increased rate resulting in more metallic ions being liberated from the metallic matrix. The combination of mechanical depassivation of an alloy and the presence of aggressive anions within the electrolyte will result in conditions capable of promoting high amounts of mechanically induced dissolution. Furthermore, the occurrence of 'micro-pores' and 'micro-cracking' of the PMMA bone cement at the stem-cement interface, as a result of cyclic loading, is thought to further increase the surface area of the PMMA bone cement increasing the concentration of sulphate found within the stem-cement interface. From the results presented in this chapter it is thought that the presence of sulphate within the interface not only influences the re-passivation kinetics of the CoCrMo alloy, but will also increase the rate of dissolution during the mechanically-induced depassivation of the surface. This is due to the high concentration of electrochemically negative anions within the interface available to discharge and remove electrons from the metallic interface.

Furthermore it is important to consider the abrasive nature of the radio-pacifiers added to the PMMA bone cements to ensure there visibility under X-ray conditions. Commercially available PMMA bone cements commonly use ZrO_2 and $BaSO_4$, two compounds known for their abrasive characteristics due to high fracture toughness. Some authors have hypothesized that the presence of such compounds may plough the surface of the material further increasing the fretting-corrosion damage found at these interfaces. In a recent study by Zhang et al [208], the influence of bone cement type on the fretting wear of polished femoral stems was observed using scanning electron and 3-D interferometery techniques (Figure 9-53). Zhang [208] concluded that no significant difference could be seen between femoral stem wear and type of

PMMA bone cement used. Although this study has demonstrated a difference between commercially available PMMA bone cement in terms of oxidation and metallic debris production, it is thought that the chemistry of the PMMA bone cement mainly contributes to the chemical dissolution of the alloy but also the mechanical wear which may require more sensitive methods of measurements to quantify.

Figure 9-53 - Fretting wear reproduced on the femoral stem with the use of (a) Simplex P bone cement; (b) Palacos R bone cement; (c) CMW3 bone cement [208]

Surface pre-treatment was also seen to influence the extent of fretting-corrosion and overall mass losses. It has been shown throughout the study that roughened surfaces resulted in a superior corrosion resistance both under static and dynamic conditions. It is hypothesised that under fretting conditions, the combination of a SiO_2 film formed on the metallic surface due to the blasting as well as the increased interfacial strength due to interdigitation of the PMMA bone cement on the metallic surface resulting in different fretting wear regimes at the interface. Zhang et al [218] investigate the role surface roughness plays in the debonding of metallic and PMMA bone cements.

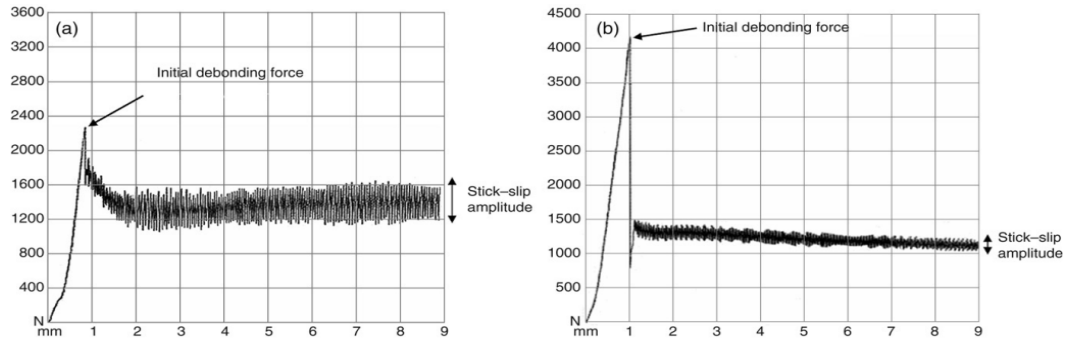

Figure 9-54 - Force required to initiate debonding at a metallic-PMMA bone cement interface for a) polished and b) vaquasheened surfaces [218]

Zhang [218] demonstrated that the type of surface processing can influence the load required to initiate debonding between the PMMA cement and metallic surface. Zhang demonstrated polished surfaces were seen to debond at 2.3kN, the same maximum load used in this study. For polished femoral stems, debonding and depassivation at the interface occurs immediately due to the lack of interdigitation between the PMMA bone cement with the metallic surface. This results in gross slip between the interface resulting in an increased rate of plastic deformation of the surface and an increased rate of oxidation within the interface as observed in the experimental data.

For vaquasheened surfaces, Zhang demonstrated a load of 4.0kN is required to initiate debonding. It is thought partial debonding will occur between at the stem-cement interface for surfaces with an increased surface roughness, whilst areas not affected by wear will have increased corrosion resistance due to the presence of the SiO_2 film. Blunt et al [132] demonstrated that the micro-pores in the bone cement act as initiation sites for fretting wear. Partial debonding of the surfaces will result in fretting-corrosion of the areas in contact with the PMMA bone cement (i.e. at the edge of pores) whilst material within pores will remain unaffected by wear and corrosion resulting in a partial slip type fretting mechanisms and an 'island' type surface morphology commonly seen on femoral stem surfaces.

It is proposed, for both the polished and roughened femoral stems, in regions of metallic and PMMA contact, typically at the edges of micro-pores within the cement, an increased amount of fretting wear will occur due to the micro-motion at the interface. At this point, depassivation and plastic deformation of the metallic substrate will occur, along with the additional abrasion of the PMMA bone cement and CoCrMo surface resulting in the liberation of metallic ions and debris into the interface and bulk environment. This process is thought to occur until one body is sufficiently worn to result in full contact and slip between the two interfaces. This phenomenon is thought to remain localised for roughened femoral stems due to the level and nature of slip between the interfaces. However for polished femoral stems slip along with initiation and propagation of fretting wear will occur almost instantaneously. This also supports the hypothesis outlined in Chapter 4. From the evidence presented in this chapter it is thought an abrasive wear mechanism exists at the stem-cement interface. This is due to the formation and transfer of a Cr_2O_3 particulate film. Subsequently a hardness differential between the femoral stem (5-10GPa) and Cr_2O_3 film (14-30GPa) will be established, resulting in abrasion of the

femoral stem and depassivation of the surface. From these findings, surface roughness is thought to contribute to the type and levels of slip found at the interface as well as the magnitude of load necessary to overcome the initial shear force needed to initiate sliding. The process has been shown schematically in Figure 9-55.

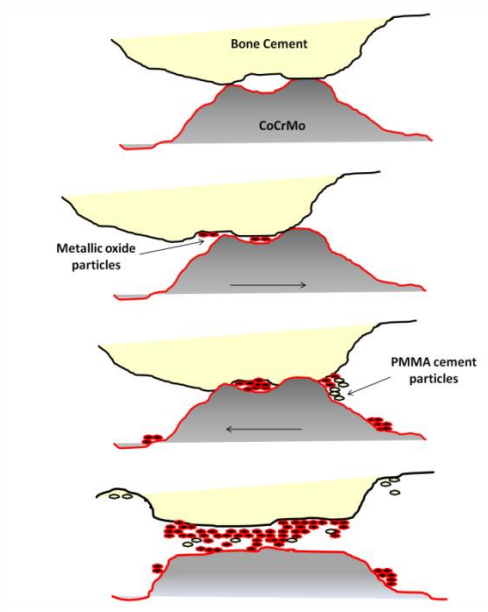

Figure 9-55 - Schematic representation of PMMA-metallic contact resulting in PMMA and fretting corrosion product.

Galvanic coupling was also seen to have an influence on the fretting corrosion rates. The presence of Ti was seen to increase the wear enhanced oxidation of the metal surface by an order of magnitude. This is due to the large potential difference been established across the system due to depassivation of the usually passive surfaces. Depassivation of CoCrMo has been shown in this study, and by other authors [108, 200], to result in a decrease in OCP to around -0.350 to -450V. In contrast Ti will remain passive at an OCP of typically 0.100V, resulting in a potential difference of 0.5V being established across the system. This difference in potential between the LC CoCrMo and Ti has a polarising effect in the anodic direction for the LC CoCrMo.

Application of the mixed potential theory demonstrated the electrochemical reactions occurring at the stem-cement interface were different for polished and roughened femoral stems when coupled to Ti. For polished femoral stems, a linear increase in current was seen with respect to increasing potential, characteristic of Tafel polarisation behaviour [79]. For roughened femoral stems a different polarisation characteristic was seen. Roughened femoral stems were seen to exhibit an active to passive behaviour along with a low passive current. Although the presence of Ti appeared to increase the mixed potential, and subsequently the over-potential exerted on the CoCrMo stem, it is though the rate of oxidation is limited by the rate in which metal ions can travel through the protective SiO_2 layer. The capacitive nature of the film therefore limits the rate in which oxidation of the metallic surface can occur lowering the fretting corrosion currents.

The subject of galvanic corrosion in the biomedical industry has been recently discussed highlighting the potential importance of mixed metal systems and the current lack of knowledge and understanding in the area. The implications of mixed metal systems under tribological conditions have not revived much consideration with respect to orthopaedic devices. Currently there are no scientific investigations that cover the issue of galvanic corrosion in mixed metal fretting conditions, however have been hypothesised by some authors [136-140]. He et al [192] presented a study looking at the galvanic corrosion behaviour of Co–Cr–Mo and Ti–6Al–4V alloys under corrosive fretting conditions. He stated that CoCrMo and Ti–6Al–4V are not susceptible to galvanic corrosion, but when subjected to fretting, the fretted surfaces will become more vulnerable to galvanic corrosion. He also noticed the effect of surface area with acceleration of anodic dissolution of the fretted area been dominated by a “large cathode effect”. However this paper was withdrawn

from the journal. This study has demonstrated that the presence of a Ti couple can increase both the static and fretting corrosion currents, almost doubling the metal ion release by increasing the rate of wear enhanced oxidation within the interface due to polarisation and acceleration of the anodic half-cell reactions.

9.9.4. Influence of Fretting Corrosion on the External Environment and the formation of fretting products

The role fretting-corrosion plays in the generation and magnitude of metallic ions produced at the stem-cement interface has also been considered. Solution analysis using ICP-MS has identified that a preferential release of Co is seen to account for 94% of all metallic ion release. This supports the data recently published by Hart et al [35] who analysed periprosthetic tissue from two cohorts of patients. Hart found that for patients with the Ultima TPS™ femoral stem (the same femoral stem used in this study); a preferential release of cobalt was seen in the retrieved tissue compared to patients who received hip resurfacing replacements. Hart et al hypothesised that this finding was due to the type of degradation mechanisms taking place at the interface driven by the locally high potentials caused by inflamed tissues.

An *in-vitro* study by Heisel et al [147] demonstrated that metallic ions liberated from the articulation surfaces were released in a ratio according to the concentrations in the alloy. This further suggests that wear mechanism drastically influences the quantity and type of metallic ions released. The findings by Hesketh et al [200], who observed the tribo-corrosion behaviour of 36mm MoM bearings, further strengthens this argument presenting much lower corrosion currents than the stem-cement interface despite the same electrochemical test parameters being used. Although the overall mass loss is expected to be far

higher from the bearing surfaces due to the mechanical removal of material, the ionic mass loss from stem-cement interface is expected to be higher than that of the bearing surface due to the more corrosive degradation mechanism.

TEM and XPS techniques have been used to identify and quantify the surface morphology and chemistry of the 'metallic staining' typically seen on the PMMA bone cement and cemented portions of simulated THR. Thick layers, primarily consisting of Cr_2O_3 were observed. No segregation of alloying species was seen when the microstructure of the alloy was observed under SEM/EDX conditions. High levels of Co can be best explained by the thermodynamic stability of the species within the interface. Thermodynamics can be used to evaluate the theoretical activity of a given metal or alloy in a known corrosion environment. However it is important to understand that the environment that actually affects the metal corresponds to a micro-environment, i.e. the local environment at the surface of the metal [11].The ability for any chemical reaction to occur, including the reaction of a metal within its environment is measured by the Gibbs free-energy change (ΔG) (Equation 9-6). Where *n* is number of valence electrons involved in the reaction, *F* is Faraday's constant and E_{cell} is the electrochemical cell potential ($E_{cell} = E_{cathodic} - E_{anodic}$). Where $E_{cathodic} = O_2 + 4H^+ + 4e^- \rightarrow 2H_2O = 1.23V$) and $E_{anodic} = Co \rightarrow Co^{2+} + 2e^- = -0.28V$ *or* $Cr \rightarrow Cr^{3+} + 3e^- = -0.74V$ are the standard electrode potentials for the anodic and cathodic reactions respectively.

Equation 9-6 - Gibbs free energy change

$$\Delta G = -nFE_{cell}$$

The driving force for the reaction to occur increases as the ΔG becomes more

negative. Although the Gibbs free energy change is a good indication of the material's susceptibility to corrosion, it cannot be used to measure the corrosion rate of a material. It is thought that Cr is favoured as the species to undergo reaction due to the lower ΔG (-590.29kJ/mol) resulting in the formation of Cr_2O_3 corrosion products within the interface. The formation of Cr_2O_3 layers and the selective dissolution of Co are characteristics commonly found in engineering fretting systems and clinical scenarios [7, 8, 36].

A study by Gilbert et al [37] identified the formation of metallic 'inter-layer' and the selective dissolution of Co within modular head-neck connections, typically characterised by 'etching' of the CoCrMo alloy. Gilbert proposed that such surface morphologies result from mechanically assisted crevice corrosion and cold welding between two metallic interfaces. Although this study has demonstrated a preferential release of Co into the bulk solution, no selective dissolution of Co was seen from the metallic substrate.

Due to the location of the black layer (predominantly seen on the bone cement surface) and no evidence of selective leaching of Co from the alloy, it is thought that the mechanism producing metal-oxide layers and Co rich external environments are different to that proposed for the head-neck taper. Thick oxide films occurring within the stem-cement interface are thought to be a result of fretting-corrosion liberating Co, Cr and Mo ions along with fractured oxide and metallic particulate into the interface. Cyclic loading will result in the compression of any metallic oxide and debris onto the counterpart cement. It is thought that the compression of debris within the interfaces, along with further oxidation/redox of any metallic debris, results in the formation and precipitation of thick Cr_2O_3 within the interface. Cobalt, presumed to be in the Co^{2+}, liberated

through oxidation of the alloy, is thought to remain soluble within the interface whilst also been preferentially dissolved from the compressed debris. This is due to the local environment within the interface and thermodynamic stability of the species.

Consultation of the Pourbaix diagrams (assuming an activity coefficient of unity for Hydrogen reduction) for Co and Cr demonstrates that at the potentials experienced at the interface, and expected pH levels Co will remain in the Co^{2+} state whilst chromium will further reduce with oxygen to form Cr_2O_3 (Figure 9-56). The dissolved Co^{2+} ions will then leave the interface due to an electrical potential being established between internal and external areas of the interface. This is thought to also be the case for stainless steels femoral stems with Fe^{2+} being the ion predominantly released from the interface into the bulk environment.

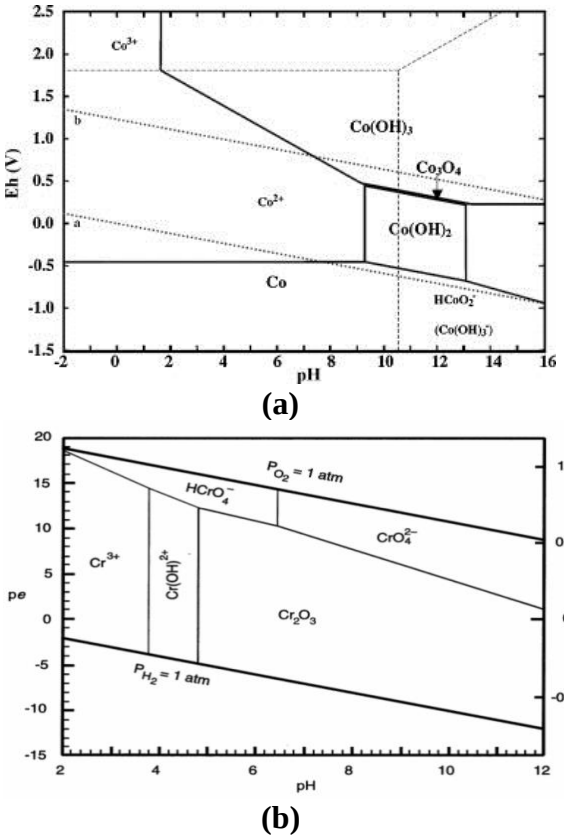

Figure 9-56 - Pourbaix diagrams for a) Co and b) Cr in salt solution

CHAPTER 10 – OVERALL DISCUSSION, CONCLUSIONS AND FUTURE WORK

10.1. Overall Discussion

This thesis presents a systematic investigation into the degradation mechanisms occurring within the stem-cement interfaces which was initiated by the need to understand a particular failure in the Norwich series, as well as other complaints, of Ulitma hips. The influence of surface pre-treatment, PMMA bone cement chemistry and galvanic coupling on the crevice corrosion and fretting corrosion mechanisms have been investigated and discussed in detail. A full cohort analysis of clinical retrievals was conducted in order to validate test methods and findings. This chapter will conclude experimental and clinical findings, highlight any limitations and propose future work to be conducted.

This study has demonstrated that cyclic loading, surface roughness, galvanic coupling and PMMA bone cement can influence the rates and mechanisms for metallic ion release from the stem-cement interface. Experimental findings seem to complement clinical data, with high levels of ARMD resulting from fretting-corrosion of the cemented portions of polished CoCr femoral stems being seen when used in conjunction with a MoM device and antibiotic PMMA bone cement. Shetty et al [150] presented the findings of the Ultima TPS femoral stem when used in conjunction with a MoP articulation. No hips required revision within 5 years due to ARMD. When used in conjunction with a MoP articulation the Ulitma TPS was seen to have a similar performance as the Exeter femoral stem which has at least 20 years of clinical prevalence [151].

Distinct similarities have been seen between the retrieved and simulated parts. Fretting-corrosion was seen to be the predominant factor in the accelerated degradation of the Ultima TPS femoral stem. From experimental results, system variables such as galvanic coupling and surface roughness were the predominant factors influencing the rate of dissolution within the interface. The addition of sulphate within the cement was also seen to increase the rate of both pure and wear enhanced oxidation within the interface however not thought to be as significant as the variables mentioned previously. Tribochemical reactions were also seen to be important factor when considering the stoichiometry in which metal ions are liberated from the interface with Cr_2O_3 tribo films being formed as a result of cyclic loading. Analysis of the clinical cohort demonstrated fretting-corrosion to occur in similar locations on the femoral stems. Along with this, fretting-corrosion product was seen to be comparable between experimental and retrieved components.

In the past the stem-cement interface has been neglected as a primary source of metal ion release. Results from this study have demonstrated that the ion release mechanisms at this interface are not trivial. Studies into the quantity, relative ratios and the exact source of metal ion release from the interfaces of actual biomedical components are rare and limited to MoM articulations. Hesketh et al [66, 200] demonstrated corrosion currents in the region of 2.5×10^{-6}A for 36mm MoM bearings. These were also seen to decrease to 1.0×10^{-6}A after 500,000 cycles due to the formation of a tribofilm. Ionic concentrations in the regions of 1330-2000µg/L were observed after 1 million cycles with a 0.6:0.3:0.1 release of Co, Cr and Mo respectively and corrosion accounting for 45% of all metal ions released. Al-Hajjar et al [219] presented ionic mass loss measurements for 28 and 36mm MoM bearings under standard and adverse loading conditions. For 28mm MoM bearings a volumetric wear rate of 0.99 and 4.62mm^3/million cycles was observed at a 45º

inclination angle under standard gait and micro-separation conditions respectively. This correlated to a 500 and 2500µg/L release of Co and 100 and 800 µg/L of Cr. Heisel et al [147] demonstrated for the large diameter MoM resurfacings (ASR, DePuy) a stoichiometric release of metal ions was seen after 500,000 cycles with concentrations of approximately 6,000µg/L of Co, 3,000µg/L of Cr and 500µg/L. The latter of these devices has been implicated in high revision rates due ARMD, primarily thought to be due to poor device design and surgical orientation.

In contrast to the articulation surfaces, fretting corrosion currents originating from the stem-cement interface were in the region of the 3.5×10^{-6} to 2.5×10^{-5}A demonstrating corrosion to be higher at this interface compared to the articulation surfaces. A total ionic mass loss of 2,000µg/L was observed after 500,000 cycles in which Co accounted for 95-98% of all metal ions released for uncoupled femoral stems. The presence of Ti dramatically increased the total ionic mass loss to 4566µg/L where corrosion accounted for 60-90% of all metal ions released. This is almost double the concentrations presented by Hesketh and Al-Hajjar et al [66, 200, 219]. Tribo-chemical reactions were seen to be a predominant factor influencing the ratios in which metallic ions were released. To date there have been no reported *in-vitro* studies of direct measurements of ionic mass loss from the stem-cement interface into the bulk environment. Results in this thesis are further supported by Hart et al [165], who demonstrated a preferential release of Co into the biological environment from the stem-cement interface. These observations also question the use of *in-vivo* metal ion measurements as a surrogate marker of wear in MoM total hip replacements.

Furthermore results in this study also raise the issues relating to the suitability of current simulation techniques. Although this study has shown that the presence of

different interfaces and mixed metal systems can have a dramatic and detrimental effect on the rate in which metal ions are produced, it is still unknown what the overall effect of the MoM system will be with respect to wear and corrosion at the different interfaces.

10.2. Conclusions

The questions raised in the aims and objectives have been addressed and in addition the following conclusions have been made. Due to the number of findings and complex nature these have been split into two sections; Static corrosion, Fretting-corrosion and retrieval analysis conclusions.

10.2.1. Static Corrosion Conclusions

- Anodic polarisation of polished and vaquasheened femoral stems free from any crevice demonstrated polished surfaces to be the most susceptible to localised corrosion. This is in contradiction with modern corrosion theory.
- Crevice corrosion was seen to occur within the stem-cement interface in the absence of an applied potential. This was seen for both long term and 7 day immersion tests. The presence of the stem – cement interface was seen to increase the materials susceptibility to corrosion. Localised corrosion could be seen on a macroscopic level in all cases.
- Accelerated and long term immersion tests demonstrated vaquasheened surfaces to have superior corrosion characteristics when compared to polished and wrought surfaces. Surface processing was seen to cause a localised re-orientation of the femoral stem surfaces due to a shear induced transformation. In addition to this, a 20nm SiO_2film was formed on the vaquasheened surface thought to increase the materials resistance to

corrosion by acting as a protective film, increasing the materials resistance to charge transfer.

- PMMA bone cement was seen to increase the rates of dissolution. Under static conditions, commercially available PMMA bone cements containing antibiotics were seen to decrease pitting potential for both 316L and CoCr alloys.

- Cement variation tests further identified that the addition of sulphate was seen to decrease the pitting potential for 316L stainless steels. For CoCr alloys the presence of sulphate in the PMMA cement increased the extent of oxidation due to high local concentrations of sulphate at the metal-cement interface. This was seen in commercially available and self-prepared PMMA bone cements. Sulphate in the form of antibiotics was seen to have the most effect due to the active leaching out mechanism.

- In 7 day immersion tests a preferential release of Cr was seen from 316L and CoCr alloys due to dissolution of the passive film. This is in contrast to the 60 day immersion tests which demonstrate a stoichiometric release of alloying elements. This is due to complete dissolution of the passive film and sustained dissolution of the CoCrMo substrate.

- The presence of a galvanic couple was seen to increase the rate of dissolution within interface. This was characterised with ZRA, surface morphology and ICP-MS techniques. Under static conditions, the presence of a galvanic couple increased metal ion release by 48% (on average) when compared to uncoupled long term immersion tests.

10.2.2. Fretting-Corrosion Conclusions

- The application of cyclic loading was further seen to increase the rate of oxidation within the interface. This is due to fretting being established at the interface resulting in depassivation of the femoral stem surface. This increased corrosion currents by an order of magnitude or greater.
- Linear ionic mass losses due to pure and wear enhanced corrosion were observed. This was also the case for ions released due to pure and corrosion induced wear.
- Vaquasheened surfaces demonstrated a decrease in wear induced corrosion. Surface analysis suggests that this is due to the differing mechanism of slip as well as increased corrosion resistance due to surface processing. Polished surfaces demonstrated higher corrosion currents and ionic mass losses.
- Surface roughness also influenced the relative proportions of metal ion release. Polished femoral stems demonstrated a more corrosive environment with pure and wear enhanced oxidation accounting for 65-86% of all metal ions released depending on the PMMA bone cement used. Roughened femoral stems exhibited an abrasive fretting wear, with corrosion accounting for 20% of all metal ions released.
- An abrasive wear mechanism exists at the stem-cement interface for both blasted and polished surfaces. This is due to a hardness differential between the femoral stem (5-10GPa) and Cr_2O_3 film (14-30GPa), resulting in abrasion of the femoral stem and depassivation of the surface.
- Surface roughness is thought to contribute to the type and levels of slip found at the interface as well as the magnitude of load necessary to overcome the initial shear force needed to initiate sliding.

- PMMA bone cement was seen to further influence the rate of wear enhanced dissolution. The presence of sulphate was seen to increase pure and wear enhanced dissolution. For PMMA cements containing ZrO_2 and Antibiotics, wear enhanced and pure oxidation was seen to account for 81-86% of all metal ions produced. PMMA bone cements containing $BaSO_4$ not only increased the rate of pure and wear induced oxidation, the overall ionic mass loss was higher with corrosion accounting for 65% of all metal ions released into the bulk environment.

- Galvanic coupling increased the rates of pure and wear enhanced corrosion for polished and roughened surfaces. For polished femoral stems, the presence of Ti increased metal ion release by 105% with corrosion accounting for 95% of all metal ions released into the bulk environment when cemented with $BaSO_4$ containing PMMA bone cements. For vaquasheened surfaces, metal ion release due to pure and wear enhanced corrosion increased three fold. However the total ionic mass loss was seen to be lower. This is due to the large potential difference being established between the active CoCr and passive Ti surfaces.

- Hi-Res electrochemical analysis demonstrated characteristic corrosion currents depending on the loading profile selected. These were seen to be a function of the loading cycle with max peak current occurring at minimum load. These also demonstrated the surface to be in a constant state of de-passivation and partial repassivation.

- In all cases a preferential and high release of Co was observed. This is due to the thermodynamic stability of alloying elements and the formation of Cr_2O_3 films within the interface.

10.2.3. Retrieval Analysis Conclusions

- Retrieval analysis demonstrated similar surface morphologies and locations of wear similar to those observed on the simulated parts. Gross slip and plastic deformation was seen in the proximal regions whilst a more corrosive phenomenon was seen towards the distal regions.
- The formation of black 'tribo-reaction' films was seen. These were seen to be predominantly Cr_2O_3 with the presence of organic material derived from HSA. This was confirmed with TEM and XPS analysis and is in good agreement with experimental findings, along with the findings presented by Hart et al [146].
- Statistical analysis demonstrated three significant correlations. A 10 degree lipped liner had significantly more impingement ($P<0.001$). Females had significantly more corrosion ($P<0.025$). Heads with +5 offset had significantly more 'Moderate' corrosion than the 0 offsets ($P< 0.199$). A weak correlation between the corrosion score and the size of the acetabular component was seen ($P<0.138$).
- There was no significant correlation with time *in-vivo* and corrosion score ($P<0.251$). No significant correlations where seen for size of femoral stem and corrosion score ($P<0.272$). No correlation between the cement type ($P<0.471$) or brand ($P<0.661$) versus Corrosion score was seen indicating that cement type or chemistry does not have an influence on the extent of fretting-corrosion.

10.3. Limitations of this Study and Future Work

Although this study has highlighted some important and novel findings with respect to the metal ion release from cemented devices, there are still a number of limitations that need to be addressed.

- **Use of physiologically realistic and modified electrolytes** –Further fretting-corrosion simulations in protein containing fluids is required, along with the application of extensive surface analysis, in order to quantify the role proteins play on the fretting-crevice corrosion mechanisms presented in this study. The presence of proteins within the stem-cement interface may decrease the corrosion induced by fretting due to the adsorption and formation of protective protein films onto the metallic surface, whilst in the areas of pure corrosion the presence of protein may increase the rate of dissolution.

  The use of saline solutions at different pH levels also needs to be conducted in order to validate the hypothesis leading to film formation and the metal ion release into the bulk environment. It has been hypothesised that because of the pH experienced *in-vivo* and cell potentials within the interface, there is a tendency for a solid Cr and O rich corrosion product to form whilst the Co is free to migrate away from the interface. According to the Pourbaix diagrams decreasing the pH to around 2-3 will result in Cr and Co remaining in a soluble ionic form and hence should leave the interface in the relative ratios in which they are produced.

- **Use of a standardised Paul gait profile –** This study has demonstrated that the gait profile can influence passivation kinetics and ionic mass loss due to corrosion of cemented femoral stems. However these tests were conducted

out of interest, over very small time scales and were not the focus of the study. Long term fretting corrosion tests utilising a standard Paul gait cycle should be conducted in order to replicate a physiological representative loading typically experienced *in-vivo*.

- **Stop/Start application of load –** It has been seen in previous chapters that upon the application of cyclic loading an increase in corrosion current is typically seen. When the load is removed a decrease in current is seen typically not recovering to its original value indicating an elevated level of crevice corrosion. Corrosion is typically thought of as a time dependent response, with an increase in mass loss typically being seen with increasing time**.** In the tests conducted in this study, a continuous dynamic load is applied to the sample accurately simulating/accelerating 0.5million cycles of mechanical wear. In reality, the walking is typically broken up by periods of dwell. At this point wear enhanced corrosion will cease. Due to the intimate nature of the interface localised crevice corrosion will be established and further contribute to the overall ionic mass loss and has not been considered in this study. Stop start test accurately representing the desired distance/number of cycles with periods of dwell representative of that typically experienced in daily life need to be conducted in order to quantify the actual contributions of wear and corrosion to ion release as well as to understand the implication with respect to total ionic mass losses.

- **Influence of stem design and material type –** This study has mainly been focused on the corrosion and production of ionic material from cemented tapered polished CoCrMo femoral devices. It is important to conduct similar

experiments on devices of different materials and stem design philosophy to see how it influences the fretting-corrosion rates and metal ion release.

- **Influence of other corroding/articulating interfaces and surface area effects –** To date studies have mainly focussed on studying biomedical parts in isolation. This study has demonstrated that the presence of mixed metals can significantly influence the corrosion rates at other influences. It can be assumed to that other tribo-corrosion reactions occurring at other interfaces (e.g. articulation or modular taper) may also influence the relative rates of dissolution and local potentials at a particular interface. For example a large amount of wear and corrosion may result in the taper and femoral stem becoming the net cathode significantly lowering the rate of dissolution. It is therefore important that future studies take this into consideration and a new generation of electrochemical and simulation techniques developed to account for this.

  Galvanic coupling of mixed metals has also been seen to have an influence on corrosion reactions both under static and fretting conditions. However it is important to understand that this can occur between same metal systems. Further testing needs to be conducted from a medical, as well as a theoretical, tribocorrosion point of view to understand the influence of different metal combinations, Anodic: cathodic surface area ratios and the evolution of local anodic and cathodic potentials.

10.4. Closing Statement

From the evidence presented in this thesis it is concluded that the use of polished CoCrMo femoral stems in conjunction with sulphate containing PMMA bone cement and a MoM articulation can lead to accelerated degradation at the stem-cement interface. This has been demonstrated in both clinical failure and experimental analysis. The understanding and knowledge developed in this thesis has been applied to current industrial product lines and processes. Appendix B presents a 'Field Safety Notice' that was distributed worldwide by DePuy International. This project has also influenced and created new design rules and procedures relating to the subject of tribo-corrosion in both the design and pre-clinical testing stages of THR development.

REFERENCES

[1] L.A.Reynolds, E.M.Tansey Early development of total hip replacement. Vol. 29, 1 ed. London, UK: Wellcome Trust Centre , 2006.

[2] National Joint Registry. National Joint Registry for England and Wales: 9th Annual Report 2012. Http://www.njrcentre.org.uk/njrcentre/default.aspx . Date Last Accessed (5-2-2013)

[3] World Health Organisation. Musculoskeletal conditions affect millions. Http://www.who.int/mediacentre/news/releases/2003/pr81/en/ . Date Last Accessed (5-2-2013)

[4] S.Donell, C.Darrah, J.Nolan, J.Wimhurst, A.Toms, T.Barker, C.Case, J.Tucker, Early failure of the Ultima metal – on – metal total hip replacement in the presence of normal plain radiographs. Journal of Bone and Joint Surgery [Br] 2010;92:1501-8.

[5] B.Bolland DC, D.Langton, J.Millington, N.Arden, J.Latham, High Failure rates with a large-diameter hybrid metal-on-metal total hip replacement. Journal of Bone and Joint Surgery [Br] 2011;93:608-15.

[6] B.Meier As Use of Metal-on-Metal Implants Grows, Studies Raise Concerns. In. New York Times, 2010.

[7] J.Ungoed-Thomas and G.Duffill. Tumor fear over metal hip replacements. Http://times.cluster.newsint.co.uk/tol/life_and_style/health/article7100905.ece . Date Last Accessed (20-5-2011)

[8] H.Willert, L.Broback, G.Buchhorn, P.Jemsen, G.Koster, I.Lang, P.Ochsner, R.Schenk, Crevice corrosion of cemented titanium alloy stems in total hip replacements. Clin Orthop Relat Res 1996;333:333-51.

[9] S.Thomas, D.Shukla, P.Latham, Corrosion of cemented titanium femoral stems. Journal of Bone and Joint Surgery [Br] 2004;86:974-8.

[10] D.Dowson, V.Wright (1981), Introduction to the Biomechanics of Joints and Joint Replacements (Vol. 1, 1 ed). United Kingdom: Wiley-Blackwell.

[11] H.Gray (2011), Gray's Anatomy, USA: Running Press.

[12] J.Paul, The biomechanics of the Hip-joint and its clinical relevance. Proceedings of the royal society of medicine, Section of Orthopeadics 1966;59.

[13] G.Bergmann, G.Deuretzbacher, M.Heller, F.Graichen, A.Rohlmann, J.Strauss, N.Duda. Hip Contact Forces and Gait Patterns From Routine Activities. J biomech; 2001; 34: 859-871.

[14] Y.Yan Corrosion and Tribo-corrosion behaviour of metallic orthopaedic implant material. PhD Thesis: University of Leeds 2006.

[15] World Health Organisation. Musculoskeletal conditions affect millions. Http://www.who.int/mediacentre/news/releases/2003/pr81/en/ . Date Last Accessed (20-5-2011)

[16] Australian Institue of Health and Welfare. Chronic Diseases. Http://www.aihw.gov.au/chronic-diseases/ . Date Last Accessed (20-5-2011)

[17] T.Fagerson (1998), The Hip Handbook, United Kingdom:Butterworth Heinmann.

[18] K.Lundon (2000), Orthopaedic rehabilitation science, United Kingdon: Butterworth and Hienmann

[19] M.Mont, D.Hungerford, Non-traumatic avascular necrosis of the femoral head. Journal of Bone and Joint Surgery [Br] 1995;77:459-74.

[20] M.Roba, M.Naka, E.Gautier, N.Spencer, R.Crockett, The adsorption and lubrication behaviour of synovial fluid proteins and glycoprotiens in the bearing surface materials of hip replacements. Biomaterials 2008;30:2072-8.

[21] X.He, D.Carter, Atomic structure and chemistry of human serum albumin. Nature 1992;358.

[22] M.Heuberger, M.Widmer, E.Zoberley, R.Glockshuber, N.Spencer, Protein mediated boundary lubrication in Arthroplasty. Biomaterials 2005:1165-73.

[23] Y Liao, R Pourzal, MA Wimmer, JJ Jacobs, A Fischer, LD Marks, Graphitic tribological layers in metal-on-metal hip replacements. Science 2011;334:1687-90.

[24] MA Wimmer, C Sprecher, R Hauert, G Täger, A Fischer, Tribochemical reaction on metal-on-metal hip joint bearings: A comparison between in-vitro and in-vivo results. Wear 2003;255:1007-14.

[25] Y Yan, A Neville, D Dowson, Biotribocorrosion of CoCrMo orthopaedic implant materials: assessing the formation and effect of the biofilm. Tribology International 2007;40:1492-9.

[26] J Wolff, The Law of Bone Remodeling: Berlin Heidelberg New York: Springer, 1986.

[27] J.Bojescul, J.Xenos, J.Callaghan, C.Savory, Results of porous coated anatomic total hip Arthroplasty without cement at fifteen years. The Journal of Bone and Joint Surgery [Br] 1988;70:337-46.

[28] Plus Orthopeadics. Anatomical Hip Stem Prothesis - Product information. Http://www.plusorthopedics.com/portal/itxpim_produkte/dateien/1148_1553-e_sbg_-_nt_-_ed._06-06.pdf . Date Last Accessed (1-8-2013)

[29] J.Fowler, G.Gie, A.Lee, R.Ling Experience with the Exeter total hip replacement scince 1970. Orthopaedic clinics of North America 2011;19:477-89.

[30] National Joint Registry. National Joint Registry for England and Wales: 9th Annual Report 2012. Http://www.njrcentre.org.uk/njrcentre/default.aspx . Date Last Accessed (5-2-2013)

[31] G.Gie, R.Ling, Loosening and the Mirgation of the Exeter THR. The Journal of Bone and Joint Surgery [Br] 1994;76.

[32] I.Learmonth, Conservative hip implants. Current Orthopaedics 2005;19:225-62.

[33] Y.Kim, Cementless total hip arthroplasty with a close proximal fit and short tapered distal stem (third-generation) prosthesis. Journal of Athroplasty 2002;17:841-50.

[34] National Joint Registry for England and Wales. National Joint Registry 7th Annual Reports. Http://www.njrcentre.org.uk/njrcentre/default.aspx Date Last Accessed (17-8-2010)

[35] A.Bellare, M.Turell, A.Gomoll, T.Thornhi, Fatigue fracture of poly(methyl methacrylate) bone cement containing radiopacifier nanoparticles. Journal of Athroplasty 2011:1.

[36] J.Webb, R.Spencer, The role of polymethylmethacrylate bone cement in modern orthopaedic surgery. The Journal of Bone and Joint Surgery [Br] 2007;89.

[37] O.Furnes, B.Espehaug, S.Lie, Prospective studies of hip and knee prostheses. The Norwegian Arthroplasty Register 1987-2004. American Academy of Orthopaedic Surgeons 2004;23.

[38] S.Hook, E.Moulder, P.Yates, The Exeter universal stem: a minimum ten year review from an independent centre. The Journal of Bone and Joint Surgery [Br] 2006;88:1584-90.

[39] G.Lewis, Properties of acrylic bone cement: state of the art review. Journal of Biomedical Materials Research 1997;38:155-82.

[40] E.Lautenschlager, G.Marshall, K.Marks, J.Schwartz, C.Nelson, Mechanical strength of acrylic bone cements impregnated with antibiotics. Journal of Biomedical Materials Research 1976;10:837-45.

[41] H.van de Belt, D.Neut, D.Uges, W.Schenk, J.van Horn, H.van der Mei, H.Busscher, Surface roughness, porosity and wettability of gentamicin-loaded bone cements and their antibiotic release. Biomaterials (73) 2000;21:1981-7.

[42] National Joint Registry. National Joint Registry for England and Wales: 9th Annual Report 2012. Http://www.njrcentre.org.uk/njrcentre/default.aspx . Date Last Accessed (5-2-2013)

[43] H.Malchau, P.Herberts, T.Eisler The Swedish total hip replacement register. The Journal of Bone and Joint Surgery 2002;84.

[44] H.van de Belt, D.Neut, D.Uges, W.Schenk, J.van Horn, H.van der Mei, H.Busscher Surface roughness, porosity and wettability of gentamicin-loaded bone cements and their antibiotic release. Biomaterials 2000;21:1981-7.

[45] R.Barrack, R.Mulroy, W.Harris Improved cementing techniques and femoral component loosening in young patients with hip Arthroplasty. The Journal of Bone and Joint Surgery 1992;74:385-9.

[46] B.Wroblewski, Results of improved cement distribution. 20th Annual Hip Course 1990.

[47] L.Sanzer, A.Carlsson, G.Josefsson, Revision operations on infected total hip athroplasty. Two to nine year follow up study. Clinical Related Orthopeadic Research 1988;229:165.

[48] J. Parvizi, Efficacy of antibiotic-impregnated cement in total hip replacement. Acta Orthopeadica 2008;79:335-41.

[49] J.Callaghan, A.Rosenberg, H.Rubash (2008), The Adult hip (Vol. 2, 2ed.). Philadephia, USA: Lippincott Williams & Wilkins

[50] J.Mcauley, D.Moore, W.Culpepper, C.Engh, Total hip Arthroplasty with porous coated prthosthesis fixed without cememet in patients who are sixty-five of age or older. The Journal of Bone and Joint Surgery [Br] 1998;80:1648-55.

[51] MHRA. Expert Advisory Group on 'Biological effects of metal wear debris generated from hip implants: genotoxicity': Scientific background. Http://www.mhra.gov.uk/Safetyinformation/Generalsafetyinformationandadvice/Product-specificinformationandadvice/Product-specificinformationandadvice%E2%80%93M%E2%80%93T/Orthopaedicimplants/expertadvisorygrouponbiologicaleffectsofmetalweardebrisgeneratedfromhipimplantsgenotoxicity/Scientificbackground/index.htm . Date Last Accessed (20-5-2011)

[52] A.Santavirta, M.Bohler, W.Harris, Alternative materials to improve total hip replacement tribology. Acta Orthop Scand 2003;74:380-8.

[53] H.Weber, T.Fiechter Polyäthylen-Verschleiss und Spätlockerung der Totalprothese des Hüftgelenkes. Neue Perspektiven für die Metall/Metall Paarung für Pfanne und Kugel. Orthopäde 1989;18:370-6.

[54] F.Chan, Engineering issues and wear performance of metal on metal hip implants. Clinical Related Orthopeadic Research 1996;333:66-107.

[55] P.Walker, M.Erkman, Metal – on – metal lubrication in artificial human joints. Wear 1972;21:377-92.

[56] P. Campbell, Biologic and Tribologic considerations of alternative bearing surfaces. Clinical Orthopeadics 2004;418:98-111.

[57] Y.Park, Y.Moon, S.Lim, J.Yang, G.Ahn, Y.Choi, Early Osteolysis following second generation metal on metal hip replacement. The Journal of Bone and Joint Surgery [Br] 2005;87:1515-21.

[58] R.Clayton, I.Beggs, D.Salter, H.Grant, J.Patton, D.Porter, Inflammatory pseudotumor associated with femoral nerve palsy following metal on metal resurfacing of the hip. The Journal of Bone and Joint Surgery [Br] 2008;90:1988-93.

[59] E.Riska, Ceramic endoprosthesis in total hip arthroplasty. Clinical Orthopeadics 1993;297:87-94.

[60] L.Zichner, H.Willert, Comparison of alumina– polyethylene and metal–polyethylene in clinical trials. Clinical Orthopeadics 1992;282:86-94.

[61] R.Rajagopal (2011), Physical metallurgy & Advanced materials. United Kingdom: Butterworth-Heinemann.

[62] P.Sury, M.Semlitsch, Corrosion behaviour of cast and forged cobalt based alloys for double-alloy joint endoprothesis. Journal of Biomedical Materials Research 1978;12:723-41.

[63] W.Betteridge Introduction. In: Cobalt and its alloys, 2011:11-2.

[64] Alan Cottrell An Introduction to Metallurgy, 2 ed: The Institute of Materials, 1995.Cambridge.

[65] R.Varano, J.Bobyn, J.Medley, S.Yue, The effect of microstructure on the wear of cobalt-based alloys used in metal-on-metal hip implants. Proc imeche Pat H: J Engineering in Medicine 2005;220:145-59.

[66] J. Hesketh, X. Hu, Y. Yan, D. Dowson, A. Neville, Biotribocorrosion: Some electrochemical observations from an instrumented Hip Joint Simulator. Tribology International 2013; 59:332-338.

[67] R.Pourzal, R.Theissmann, M.Morlock, A.Fischer, Micro-structural alterations within different areas of articulating surfaces of a metal-on-metal hip resurfacing system. Wear 2009;267:689-94.

[68] JE.Lemons, Properties of Biomaterials. Journal of Athroplasty 1986;1:144.

[69] Davis J Metals, Handbook, 2nd Revised edition ed. United States: ASM International, 1998.

[70] Ellis D.Verink Corrosion Testing Made Easy. Vol. 3: NACE International, 1994.

[71] E.Giordano, N.Alnso-Falleiros, I.Ferreira, O.Balancin, Electrochemical behavior of two austenitic stainless steel biomaterials. R ESC Minas, Ouro Preto 2010;63:159-66.

[72] E.Giordano, N.Alnso-Falleiros, I.Ferreira, O.Balancin Electrochemical behavior of two austenitic stainless steel biomaterials. R ESC Minas, Ouro Preto 2010;63:159-66.

[73] R.Jaimes, M.Alfonso, S.Rogero, S.Agostinho, C.Barbosa, New Material for Orthopeadic implants: Electrochemical study of nickel free P558 stainless steel in minimum essential medium. Materials Letters 2010;64:1476-9.

[74] H.Willert, L.Broback, G.Buchhorn, P.Jemsen, G.Koster, I.Lang, P.Ochsner, R.Schenk, Crevice corrosion of cemented titanium alloy stems in total hip replacements. Clin Orthop Relat Res 1996;333:333-51.

[75] N.Thompson, R.Buchanan, JE Lemons, In vitro corrosion of Ti-6A1-4V and type 316L stainless steel when galvanically coupled with carbon. J Biomed Mater Res 1979;13.

[76] JP Schoen, JE Lemons, Biomaterials Science, degregation of materials in the biological environment. Academic Press 2011:263-5.

[77] M.Kamachi, T.Sridhar, R.Baldev, Corrosion of Bio implant. Sadhana 2003;28:601-37.

[78] R W Revie, Thermodynamics:corrosion tendancy and electrode potentials. In: Corrosion and corrosion control, 1 ed. New York: John Wiley and Sons, 2000:22-66.

[79] M.Fontanna, N.Greene, Corrosion Engineering. New York: Mc Graw Hill, 1978.

[80] E. Stansbury, R. Buchanan, Fundamentals of Electrochemical Corrosion, 1 ed. Ohio: ASM International, 2000.

[81] J.Oldfeild, W.Suttton, New Technique for Predicting the Perfromance of Stainless Steels in Sea Water and other Chloride-containing Enviroments. British Corrosion Journal 1979;15.

[82] J.Oldfeild, W.Suttton, Crevice Corrosion of Stainless Steel I – A Mathematical Model. Corrosion journal 1978;13:13-22.

[83] RC. Alkire, SE. Lott, Initiation of crevice corrosion on grade 304 stainless steel. In: Extended Abstracts, Spring Meeting - Electrochemical Society, 85-1 ed. Toronto, Ont, Can: Electrochemical Soc, 1985:17.

[84] DW. Siitari, RC. Alkire, Initiation of crevice corrosion. Journal of the Electrochemical Society 1982;129:481-7.

[85] R. Alkire, T. Tomasson, Critical geometry for initiation of crevice corrosion of aluminum. In: Extended Abstracts, Spring Meeting - Electrochemical Society 1984, 84-1 ed. Cincinnati, OH, Engl: Electrochemical Soc Inc, 1984:3.

[86] HW. Pickering, On the roles of corrosion products in local cell processes. Corrosion 1986;42:125.

[87] L. Stockert, H. Boehni, Metastable Pitting Processes and Crevice Corrosion on Stainless Steels. Advances in Localized Corrosion 1987: 467-473.

[88] JW. Oldfield, TS. Lee, RM. Kain, Avoiding crevice corrosion of stainless steels. In: Stainless Steels '84. Goteborg, Swed: Inst of Metals (Book n 320), 1985:205-16.

[89] NJ. Laycock, J. Stewart, RC. Newman, The initiation of crevice corrosion in stainless steels. Corrosion Science 1997;39:1791-809.

[90] BK.Nash, RG.Kelly, Characterization of the crevice solution chemistry of 304 stainless steel. Corrosion Science 1993;35:817-825.

[91] N. Sridhar and D. S. Dunn (1994) Effect of Applied Potential on Changes in Solution Chemistry Inside Crevices on Type 304L Stainless Steel and Alloy 825. Corrosion: November 1994, Vol. 50, No. 11, pp. 857-872.

[92] G.Kennell, R.Evitts, K.Heppner, Critical crevice solution and IR drop crevice corrosion model. Corrosion Science 2008;1:1-10.

[93] S.White, G.Weir, N.Laycock, Calculating chemical concentrations during the initiation of crevice corrosion. Corrosion Science 2000;42:605-29.

[94] J. Kruger, K. Rhyne, Current understanding of pitting and crevice corrosion and its application to test methods determining the corrosion susceptibility of nuclear waste metallic containers. Nuclear and chemical waste management 1982;3:205-27.

[95] T.Lee, R.Kain, Factors influencing the crevice corrosion behaviour of stainless steels in seawater. National Association of Corrosion Engineers 1983;83:1-12.

[96] G.Frankel, Pitting corrosion of metals: A review of the critical factors. Journal of Electrochemical Society 1998;145:2186-98.

[97] J.Galvele, Tafel's law in pitting corrosion and crevice corrosion suseptibility. Corrosion Science 2005;47:3053-67.

[98] H.Pickering, R.Frankenthal, On the Mechanism of Localized corrosion of Iron and Stainless Steel II . Morphological Studies. J. Electrochem. Soc. 1972;119:1304-1310.

[99] R.Wolfe, H.Pickering, B.Shaw, Microprobe Study of ph During the Induction Period Preceding Crevice Corrosion. Journal of Electrochemical Society 2006;135:25-32.

[100] X. Shan, J.Payer, Comparison of Ceramic and Polymer Crevice Formers on the Crevice Corrosion Behavior of Ni-Cr-Mo Alloy C-22. National Association of Corrosion Engineers 2007.

[101] Z.Szlarska-Smialowska, Pitting corrosion of metals. National Association of Corrosion Engineers 1986.

[102] J.Horvath, H.Uhlig, Critical Potentials for Pitting Corrosion of Ni, Cr-Ni, Cr-Fe, and Related Stainless Steels. J. Electrochem. Soc. 1968;115: 791-795.

[103] H.Ogawa, H.Omata, I.Itoh, H.Okada (1978) Auger Electron Spectroscopic and Electrochemical Analysis of the Effect of Alloying Elements on the Passivation Behavior of Stainless Steels. Corrosion: February 1978, Vol. 34, No. 2, pp. 52-60.

[104] AJ. Betts, RC. Newman, The effect of alloyed molybdenum on the activation of anodic dissolution by reduced sulphur compounds. Corrosion Science 1993;34(9):1551-1555.

[105] G.Clark, D.Williams, The effects of proteins on metallic corrosion. Journal of Biomedical Materials Research 1982;16:125-34.

[106] A.Munoz, S.Mischler, Interactive effects of Albumin and phosphate ions on the corrosion of CoCrMo implant alloy. Journal of the electrochemical Society 2007;154:562-70.

[107] A.Ouerd, C.Alemany-Dumony, B.Normand, S.Szunerits, Reactivity of cocrmo alloy in physiological medium: Electrochemical characterization of the metal/protein interface. Electrochemica Acta 2008;53:4461-9.

[108] Y. Yan, A. Neville, D. Dowson, Tribo-corrosion properties of cobalt-based medical implant alloys in simulated biological environments. Wear 2007;263:1105-11.

[109] A.Hodgson, S.Kurz, S.Virtanen, V.Fervel, C.Olsson, S.Mischler, Passive and transpassive behaviour of cocrmo in simulated biological solutions. Electrochemica Acta 2004;49:2167-78.

[110] B.Borex, I.Olefjord, Preferential dissolution of iron during the polarization of stainless steels in acids. The Institute of Metals 1985;84:134.

[111] G.Frankel. Advances in Localised Corrosion. Proceedings of the second International Conference on Localized Corrosion, June 1-5, 1987, Orlando, Florida

[112] I. Milosíev, M. Remskar, production of nanosized metal wear debris formed by tribochemical reaction as confirmed by high-resolution TEM and XPS analyses. Journal of Biomedecical Materials Research: Part A 2009;91A:1100-10.

[113] T.Hryniewicz, K.Rokosz, R.Rokicki, Electrochemical and XPS studies of AISI 316L stainless steel after electropolishing in a magnetic field. Corrosion Science 2008;50:2676-81.

[114] A.Kocija, I.Milosev, B.Pihlar, Colbalt-based alloys for orthopeadic applications studied by electrochemical and XPS analysis. Journal of Materials Science: Materials in Medicine 2004;15:643-50.

[115] T.Hoar, The production and breakdown of the passivity of metals, Corrosion Science 1967;7:341-355.

[116] N.Sato, K. Kudo, T. Noda, The anodic oxide film on iron in netrual solutions. Journal of Electrochemical Society 1971;16:1683.

[117] HH. Uhlig,. Adsorbed and reaction-product films on metals. J. Electrochem. Soc. 1950:97:215.

[118] JA Richardson, GC. Wood, The interpretation of impedance changes on oxide-coated aluminum produced by immersion in inhibitive and corrosive aqueous media. J. Electrochem. Soc. 1973;120:193-202

[119] J.Galvele set 1989;21:221.

[120] JW Oldfield, Crevice corrosion of stainless steels - the importance of crevice geometry and alloy composition. Metaux corrosion-industries 1981;56:134-47.

[121] D.Silverman, Tutorial on cyclic potentiodynamic polarization technique. Corrosion 98 1998.

[122] N. Rothwell, Tullmin The corrosion monitoring handbook: Coxmoor publishing, 2008.

[123] J.Williams, Engineering Tribology, 2 ed: Cambridge University Press, 1994.

[124] R.B.Waterhouse, Fretting Corrosion: International series of monographs on materials science and technology, Pergamon press, 1972.

[125] D.Sun (2009), Abrasion-corrosion of cast CoCrMo in simulated hip joint enviroments. PhD thesis. University of Southampton.

[126] I.Feng, Barrans S, An experimental study of fretting. Proceedings of the Institution of Mechanical Engineers 1956;170:1055-64.

[127] S.Mischler, Triboelectrochemical techniques and interpertation methods in tribocorrosion: A comparative evaluation. Tribology International 2008;41:573-83.

[128] SW Watson, FJ Friedersdorf, BW Madsen, SD Cramer, Methods of measuring wear-corrosion synergism. Wear 1995;181-183, Part 2:476-84.

[129] H.Zhang, L.Brown, L.Blunt, X.Jiang, S.Barrans, Understanding initiation and propagation of fretting wear on the femoral stem in total hip replacement. Wear 2009;266:566-9.

[130] H.Zhang, L.Brown, L.Blunt, S.Barrans, Influence of femoral stem surface finish on the apparent static shear strength at the stem-cement interface. Journal of mechanical behaviour of biomedical materials 2008;1:96-104.

[131] HY. Zhang, LA. Blunt, XQ. Jiang, LT. Fleming, SM. Barrans, The influence of bone cement type on production of fretting wear on the femoral stem surface: A preliminary study. Clinical Biomechanics 2012;27:666-72.

[132] L.Blunt, H.Zhang, S.Barrans, X.Jiang, L.Brown, What results in fretting wear on polished femoral stems. Tribology International 2009;42:1605-14.

[133] J.Pellier, J.Geringer, B.Forest, Fretting-corrosion between 316L SS and PMMA: Influence of ionic strength, protein and electrochemical conditions on material wear. Application to orthopeadic implants. Wear 2011;271:1563-71.

[134] J. Geringer, DD. Macdonald, Modeling fretting-corrosion wear of 316L SS against poly(methyl methacrylate) with the Point Defect Model: Fundamental theory, assessment, and outlook. Electrochimica Acta 2012;79:17-30.

[135] J.Geringer, F.Atmani, B.Forest, Friction-corrosion of AISI 316L/bone cement and AISI 316L/PMMA contacts: ionic strength effect in tribological behaviour. Wear 2009;267:763-9.

[136] J Jacobs, J.Gilbert, R.Urban, Current concepts review – Corrosion of metal orthopaedic implants. The Journal of Bone and Joint Surgery [Am] 1998;80:268-82.

[137] Channel 4 Dispatches- The Truth About Going Under the Knife. In: 60mins, 2011.

[138] D.Langton, R.Sidaginmale, J.Lord, A.Nargol, T.Joyce, Taper junction failure in large-diameter metal-on-metal bearings. Bone Joint Res 2012;1:56-63.

[139] J.Gilbert, C.Engh, Mechanical -electrochemical interactions occurring during in virto fretting corrosion tests of modular connection. Total hip revision surgery 1995:41-50.

[140] J.L.Gilbert, C.A.Buckley, J.J.Jacobs, corrosion of modular hip prosthesis components in mixed and similar metal combinations. The effect of crevice, stress, motion, and alloy coupling. Journal of Biomedical Materials Reseach 1993;27:1533-44.

[141] R.Urban, J Jacobs, J.Gavrilovie, M.Tomlison, J.Black, T.Turner, J.Galante, Dissemination of metal alloy particles in the liver and spleen of patients with total hip or knee replacement prosthesis. Trans fifth world biomater Cong 2011;1:660.

[142] JJ. Jacobs, AK. Skipor, LM. Patterson, NJ. Hallab, WG. Paprosky, J. Black, JO. Galante, Metal release in patients who have had a primary total hip arthroplasty. A prospective, controlled, longitudinal study. Journal of Bone and Joint Surgery [Am] 1998;80:1447-58.

[143] S.Cook, K.Thomas, A.Harding, C.Collins, R.Haddad, M.Milicic The proformance of 250 internal fixation devices: a follow up study. Biomaterials 1987;8:177-84.

[144] JP.Collier, V.Surprenant, R.Jensen, M.Mayor, H.Surprenant, Corrosion between the components of modular femoral hip prostheses. Journal of bone and joint surgery [Br] 1992;74-B:511-7.

[145] JR. Howell, L. Blunt, C. Doyle, RM. Hooper, AJ. Lee, RS. Ling, Surface Wear Mechanisms of Femoral Components of Cemented Total Hip Arthroplasties. The Journal of Arthroplasty 2004;19.

[146] AJ. Hart, PD. Quinn, F. Lali, B. Sampson, JA. Skinner, JJ. Powell, J. Nolan, K. Tucker, S. Donell, A. Flanagan, JF. Mosselmans, Cobalt from metal-on-metal hip replacements may be the clinically relevant active agent responsible for periprosthetic tissue reactions. Acta Biomaterialia 2012;10: 3865-73.

[147] C.Heisel, N.Striech, M.Krachler, E.Jaubowitz, P.Kretzer, Characterization of the Running-in Period in Total Hip resurfacingarthroplasty: An and in Vitro Metal Ion Analysis.The Journal of Bone and Joint Surgury [Am] 2008;90:125-33.

[148] B.Purbach, P.Kay, M.Wroblewski, P.Siney, P.Flemming, Triple tapered cemented polished stem in total hip arthroplasty. a review of 1008 cases using the c-stem with a minimum of 5 years clinical and radiological follow-up. The Journal of Bone and Joint Surgury [Br] 2009;91-B.

[149] J.Burston, J.Barnett, R.Amirfeyz, P.Yates, G.Bannister, Clinical and radiological results of the collarless polished tapered stem at 15 years follow-up The Journal of Bone and Joint Surgury [Br] 2012;94:889-94.

[150] N. Shetty, AJ. Hamer, I. Stockley, R. Eastell, JM. Wilkinson, Clinical and radiological outcome of total hip replacement five years after pamidronate therapy. The Journal of Bone and Joint Surgury [Br] 2005;88-B:1309-15.

[151] N. Shetty, AJ. Hamer, RM. Kerry, I. Stockley, JM. Wilkinson, Exeter versus ultima-tps femoral stem: a randomised early outcomes study. The Journal of Bone and Joint Surgury [Br] 2006;88-B:248.

[152] G. Afrolarnmi, Disposistion of metal ions in patients after release from orthopeadic athroplasties. In: Department of Pharmaceutical Science, Univeristy of Strathclyde, 2008.

[153] R.Michel, M.Nolte, M.Reich, F.Loer, Systemic effects of implanted protheseses made of cobalt-chromium alloys. Acta Orthop Trauma Surg 1991;110:61-74.

[154] H.Dobbs, M.Minski, Metal ion release after total hip replacement. Biomaterials 1980;1:193-8.

[155] C.Hammond, The Basics of Crystallography and Diffraction, 3 ed. Oxford, UK: Oxford univeristy Press, 2009.

[156] Fairley N, Casa Software Ltd, Casa Software Ltd casaxps Manual 2.3.15: Introduction to XPS and AES: Casa Software, Limited, 2009.

[157] A.Salinas-Rodriguez, The Role of the FCC-HCP Phase Transformation During the Plastic Deformation of Co-Cr-Mo-C Alloys for Biomedical Applications. American Society for Testing and Materials 1999:108-21.

[158] H.Willert, L.Broback, G.Buchhorn, P.Jemsen, G.Koster, I.Lang, P.Ochsner, R.Schenk, Crevice corrosion of cemented titanium alloy stems in total hip replacements. Clin Orthop Relat Res 1996;333:333-51.

[159] P.Yates, B.Burston, E.Whitley, G.Bannister, Collarless polished tapered stem. The Journal of Bone and Joint Surgury [Br] 2007;90-B:16-22.

[160] G.Gie, R.Ling, Loosening and the Mirgation of the Exeter THR. The Journal of Bone and Joint Surgury [Br] 1994;76.

[161] J.Fowler, G.Gie, A.Lee, R.Ling Experience with the Exeter total hip replacement scince 1970. Orthopaedic clinics of North America 2011;19:477-89.

[162] M.Jasty, W.Maloney, C.Bragdon, D.O'Conner, T.Haire, W.Harris, The initiation of failure in cemented femoral components of hip arthroplasties. The Journal of Bone and Joint Surgury [Br] 1991;73-B:551-8.

[163] JR Howell, LA Blunt, C. Doyle, RM. Hooper, AJC. Lee, RSM. Ling, Surface Wear Mechanisms of Femoral Components of Cemented Total Hip Arthroplasties: The Influence of Wear Mechanism on Clinical Outcome. Journal of Arthroplasty 2004;19.

[164] J.Walczak, F.Shahgaldi, F.Heatley, corrosion of 316L stainless steel hip implants: morphology and elemental composistions of corrosion products. Biomaterials 1998;19:229-37.

[165] AJ. Hart, PD. Quinn, F. Lali, B. Sampson, JA. Skinner, JJ. Powell, J. Nolan, K. Tucker, S. Donell, A. Flanagan, JF. Mosselmans, Cobalt from metal-on-metal hip replacements may be the clinically relevant active agent responsible for periprosthetic tissue reactions. Acta Biomaterialia 2012;10: 3865-73.

[166] Y.Yan, A.Neville, D.Dowson, Biotribocorrosion-an appraisal of the time dependence of wear and corrosion interactions: II. Surface analysis . J Phys D: Appl Phys 2006;39:3206.

[167] H.Lin, J.Bumgardner, Changes in the surface oxide composition of Co–Cr–Mo implant alloy by macrophage cells and their released reactive chemical species. Biomaterials 2004;25:1233-8.

[168] I.Milosev, H.Strehblow, The composition of the surface passive film formed on cocrmo alloy in simulated physiological solution. Electrochemica Acta 2003;48:2767-74.

[169] MJH. Pourbaix. Atlas of electrochemical equilibria in aqueous solutions / translated from the French by James A. Franklin . Oxford: Pergamon Press, 1966.

[170] C.Tedmon, D.Vermilyea, J.Rosolowski, Intergranular Corrosion of Austenitic Stainless Steel. Journal of Electrochemical Society 1971;118:192-202.

[171] T.Brand, Materials and Metallurgy. In: Derek Mcminn, ed. Modern Hip Resrufaceing: Springer, 2009:43-63.

[172] Y. Zuo, H. Wang, J. Zhao,J. Xiong, The effects of some anions on metastable pitting of 316L stainless steel. Corrosion Science 2002;44:13-24.

[173] M.Browne, P.Gregson, Effect of mechanical Surface pretreatment on metal ion release. Biomaterials 2000;21:385-92.

[174] SN Simison, SR. de Sanchez, DJ. Schiffrin. Crevice corrosion test cell: a new design. Corrosion 1989;45:967-70.

[175] A.Alavai, R.Cottis, The determination of ph, Potential and Chloride Concentration in Corroding Crevices on 304 Stainless Steel and 7475 Aluminium Alloy. Corrosion Science 1987;27:443-51.

[176] X. Shan, J.Payer, Comparison of Ceramic and Polymer Crevice Formers on the Crevice Corrosion Behavior of Ni-Cr-Mo Alloy C-22. National Association of Corrosion Engineers 2007.

[177] AT.Kuhn, Corrosion of Co-Cr alloys in aqueous enviroments. Biomaterials 1981;2:68-77.

[178] F.Bocher, F.Presuel-Moreno, N.Budiansky, J.Scully, Couple Multielectrode investigation of crevice corrosion of ASI 316 Stainless steel. Journal of Electrochemical Society 2007;10:16-20.

[179] R.Wolfe, K.Weil, B.Shaw, H.Pickering, Measurement of ph gradients in the crevice corrosion of iron using a palladium hydride microelectrode. Journal of Electrochemical Society 2005;152:82-8.

[180] M.Fontanna, N.Greene, Corrosion Forms in Corrosion Engineering, 1 ed. New York: Mc Graw Hill, 1967.

[181] E.Lautenschlager, G.Marshall, K.Marks, J.Schwartz, C.Nelson, Mechanical strength of acrylic bone cements impregnated with antibiotics. Journal of Biomedical Materials Research 1976;10:837-45.

[182] J.Flis, K.Kowalczyk, Effect of sulfate anionson tunnel etching of aluminium. Journal of Applied Electrochemisrty 1995;25:501-507.

[183] MH. Moayed, RC. Newman, Deterioration in critical pitting temperature of 904L stainless steel by addition of sulfate ions. Corrosion Science 2006;48:3513-30.

[184] G.Gece, Drugs: A review of promising novel corrosion inhibitors. Corrosion Science 2011;53:3873-98.

[185] PC.Pistorius, GT.Burstein, Growth of corrosion pits on stainless steel in chloride solutions containing dilute sulphate. Corrosion Science 1992;33:1885-987.

[186] D.Moojen, B.Hentenaar, H.Vogely, A.Verbout, R.Castelein, W D, In vitro release of antibiotics from commercial PMMA beads and articulating hip spacers. The Journal of Arthoplasty 2008;23:1152-6.

[187] P. Frutos Cabanillas, E. Düez Pea, JM. Barrales-Rienda, G. Frutos, Validation and in vitro characterization of antibiotic-loaded bone cement release. International Journal of Pharmaceutics 2000;209:15-26.

[188] J.Hendriks, D.Neut, J.van Horn, H.van der Mei, H.Busscher, The Release of Gentamicin from Acrylic Bone Cements in a Simulated Prosthesis-Related Interfacial Gap. Biomed Mater Res Part B: Appl Biomater 2002;65:1-5.

[189] D.Neut, H.van der Belt, J.van Horn, H.van der Mei, H.Busscher, The effect of mixing on gentamicin release from polymethylmethacrylate bone cements. Acta Orthop Scand 2003;6:676.

[190] SE. Lott, RC. Alkire, The variation of solution composition during the initiation of crevice corrosion on stainless steel. Corrosion Science 1988;28:479-84.

[191] K.Oh, K.Kim, Electrochemical properties of suprastructures galvanically coupled to titanium implants. Journal of Biomedical Materials Research 2003;70:318-31.

[192] D. He, T. Zhang, Y. Wu, Fretting and galvanic corrosion behaviors and mechanisms of Co-Cr-Mo and Ti-6Al-4V alloys. Wear 2002;249:883-91.

[193] N.Taher, A.Jabab, Galvanic Corrosion behavior of implant suprastructure dental alloys. Dental Materials 2003;19:54-9.

[194] F. Mansfeld, Galvanic corrosion of Al alloys. Werkstoffe und Korrosion 1974;25.

[195] F. Mansfeld, E. Parry, Galvanic corrosion of bare and coated a1 alloys coupled to stainless steel 304 or ti-6a1-4v. Corrosion Science 1973;13:605-21.

[196] F. Mansfeld, The relationship between galvanic current and dissolution rates. Corrosion 1973;29:403-5.

[197] RA. Silva, M. Barbosa, GM. Jenkins, I. Sutherland. Electrochemistry of galvanic couples between carbon and common metallic biomaterials in the presence of crevice. Corrosion 1990;11:336-40.

[198] H. Serhan, M. Slivka, T. Albert, S. Kwak, Is galvanic corrosion between titanium alloy and stainless steel spinal implants a clinical concern? The Spinal Journal 2004;4:379-87.

[199] L.Reclaru, R.Lerf, P.Eschler, A.Blatter, J.Meyer, Pitting, crevice and galvanic corrosion of REX stainless-steel/cocr orthopeadic implant materials. Biomaterials 2002;23:3479-85.

[200] J. Hesketh Q. Meng, D. Dowson, A.Neville, Biotribocorrosion of metal-on-metal hip replacements:How surface degradation can influence metal ion formation.Tribology International 2013 http://dx.doi.org/10.1016/j.triboint.2013.02.025i. Date Last Accessed (1-8-2013)

[201] M.Jasty, W.Maloney, C.Bragdon, D.O'Conner, T.Haire, W.Harris, The initiation of failure in cemented femoral components of hip arthroplasties. The Journal of Bone and Joint Surgery [Br] 1991;73-B:551-8.

[202] P.Yates, B.Burston, E.Whitley, G.Bannister, Collarless polished tapered stem. The Journal of Bone and Joint Surgery [Br] 2007;90-B:16-22.

[203] A.Lennon, B.mccormack, P.Predergast, The relationship between cement fatigue damage and implant surface finish in proximal femoral prostheses. Medical Engineering & Physics 2003;25:833-41.

[204] T.Gruen, G.mcneice, H.Amustuz, Modes of Failure if Cemented Stem-type Femoral Components: A radiographic Analysis of Loosening. Clin Orthop Relat Res 1979;141:17-27.

[205] L. Brown, H. Zhang, L. Blunt, S. Barrans, Reproduction of fretting wear at the stem-cement interface in total hip replacement. Proceedings of the Institution of Mechanical Engineers Part H, Journal of engineering in medicine 2007;221.

[206] J.Moulder, W.Stickle, P.Sobol, K.Bomben, Handbook of X-ray Photoelectron Spectroscopy, 1 ed: Perkin-Elmer corporation, 1992.

[207] HY. Zhang, L. Brown, S. Barrans, L. Blunt, XQ. Jiang, Investigation of relative micromotion at the stem-cement interface in total hip replacement. Proceedings of the Institution of Mechanical Engineers Part H, Journal of engineering in medicine 2009;223:Nov.

[208] HY. Zhang, LA. Blunt, XQ. Jiang, LT. Fleming, SM. Barrans, The influence of bone cement type on production of fretting wear on the femoral stem surface: A preliminary study. Clinical Biomechanics 2012;27:666-72.

[209] J. Geringer, DD. Macdonald, Modeling fretting-corrosion wear of 316L SS against poly(methyl methacrylate) with the Point Defect Model: Fundamental theory, assessment, and outlook. Electrochimica Acta 2012;79:17-30.

[210] J.Geringer, F.Atmani, B.Forest, Friction-corrosion of AISI 316L/bone cement and AISI 316L/PMMA contacts: ionic strength effect in tribological behaviour. Wear 2009;267:763-9.

[211] J.Pellier, J.Geringer, B.Forest, Fretting-corrosion between 316L SS and PMMA: Influence of ionic strength, protein and electrochemical conditions on material wear. Application to orthopeadic implants. Wear 2011;271:1563-71.

[212] J.Goldberg, J.Gilbert, Electrochemical responce of CoCrMo to high-speed fracture of its metal oxide using an electrochemical scratch test method. J Biomed Res 1997;37:421-31.

[213] A.Lennon, B.McCormack, P.Predergast, The relationship between cement fatigue damage and implant surface finish in proximal femoral prostheses. Medical Engineering & Physics 2003;25:833-41.

[214] M.Archibeck, J Jacobs, K.Roebuck, T.Glant, The basic science of periprosthetic Osteolysis. The Journal of Bone and Joint Surgery [Am] 2000;82:1478.

[215] Y.Park, Y.Moon, S.Lim, J.Yang, G.Ahn, Y.Choi, Early Osteolysis following second generation metal on metal hip replacement. The Journal of Bone and Joint Surgery [Br] 2005;87:1515-21.

[216] K.Fushimi, K.Takase, K.Azumi, M.Seo, Current transients of passive iron observed during micro-indentation in ph 8.4 borate buffer solution. Electrichemica Acta 2006;51:1255-63.

[217] D.Sun, J.Wharton, R.Wood, Micro- and Nano-scal Tribo-Corrosion of Cast cocrmo. Tribol Lett 2011;41:525-33.

[218] H.Zhang, L.Brown, L.Blunt, S.Barrans, Influence of Femora; stem surface finish on the apparent static shear strength at the stem-cement interface. Journal of mechanical behaviour of biomedical materials 2008;1:96-104.

[219] M. Al-Hajjar, J. Fisher, S. Williams, JL. Tipper, LM. Jennings, Effect of femoral head size on the wear of metal on metal bearings in total hip replacements under adverse edge-loading conditions. J Biomed Mater Res Part B 2013;101:213-22.

APPENDIX A: Bone cement chemistries

This section included the details relating to the exact chemistry of commercially available PMMA bone cements utilised in this study.

Cement Brand	Cement Type	Packet Size (grams)	Antibiotic Agent/ Content (%w/w)	Radiopaque Agent/Content (%w/w)
DePuy CMW	MV	40	-	Barium Sulphate (10.00)
DePuy CMW	HV	40	-	Zirconium Dioxide (15.00)
DePuy CMW	GHV	40	Gentamicin Sulphate (4.22)	Zirconium Dioxide (14.37)
Biomet	Refobacin Bone cement R	20.4	Gentamicin Sulphate (1.96)	Zirconium Dioxide (15.10)
Styker	Antibiotic Simplex	41	Erythromycin (1.21) & Colistin sulphomethate sodium (3,000,000 iu)	Barium Sulphate (9.75)

NB: Colistin sulphomethate sodium contains the pentasodium salt of the penta(methanesulfonic acid) for fighting gram-negative bacilli. Erythromycin is in glucoheptonate form
Gentamacin Sulphate is used for gram negative and gram positive bacilli. Is used in the sulphate form to ensure solubility.

APPENDIX B: Commercial documentation and evidence of application and impact of findings arising from this thesis

The following includes evidence relating to the impact of the project in the orthopaedic market. This section includes a Field Safety Notice (FSN) which was distributed in multiple regions as well as the affected products.

DePuy
a Johnson & Johnson company

Field Safety Notice (FSN)

Product Name: DePuy G2, FJORD, TPS, EUROMETRIC, LUSTER and FREEMAN Cemented Femoral Hip Stems

FSCA-identifier: DINT17473

Type of Action: Field Safety Notice

Date: XXXXX

Attention: Trust Chief Executives, the Clinical Director-Orthopaedic Department, the Orthopaedic Theatre Manager, the Safety Liaison Officer, General Managers – Private Sector Hospitals

Type of device: Total Hip Replacement Implant – Cemented, Polished[1], Cobalt Chromium Alloy (CoCr) Femoral Hip Stems in Combination with Metal-on-Metal (MoM) Articulations[2] of an all metal type

Model names: DePuy G2, FJORD, TPS, EUROMETRIC, LUSTER and FREEMAN Cemented Femoral Hip Stems

Model number: Reference Appendix A

Batch / lot number of affected devices: All lots

Important Announcement:

A MHRA Medical Device Alert, MDA/2007/054, was issued on the 14th June 2007, as a consequence of DePuy issuing a Field Safety Notice in February 2007, to communicate that one UK study centre had reported 43 revisions (from a cohort of 637 hips) of the polished CoCr DePuy ULTIMA TPS total hip replacement femoral stems. These revisions were associated with extensive peri-prosthetic soft tissue necrosis. In all cases the femoral hip stem was implanted in combination with a metal-on-metal acetabular cup (ULTIMA Metal-on-Metal) of an all metal type. When these stems were explanted, extensive corrosion was observed on the polished surface within the area of the cement mantle (i.e. the area of the stem in contact with the bone cement).

Since the above alert was circulated, DePuy has continued to carry out post market surveillance activities and research into this issue.

These activities have led DePuy to conclude that, when used in combination with a metal-on-metal (MoM) articulation[2] of an all metal type, DePuy's cemented, polished[1], CoCr femoral hip stems could potentially exhibit corrosion of the polished surfaces which are within the cement mantle. This corrosion may in turn lead to an increased incidence of peri-prosthetic soft tissue necrosis. Therefore, DePuy is issuing a Field Safety Notice to advise against the implantation of the following configuration: **DePuy's cemented, polished[1], CoCr alloy femoral hip stems combined with any metal-on-metal (MoM) articulation[2] of an all metal type. DePuy will also update its labeling for relevant and current products with an appropriate warning.**

This Field Safety Notice applies only to the DePuy G2, FJORD, TPS, EUROMETRIC, LUSTER and FREEMAN cemented, polished[1], CoCr stems (product codes as listed within Appendix A) when combined with a metal-on-metal (MoM) articulation[2] of an all metal type.

Please note that DePuy's post market surveillance data sources have not identified any adverse events related to corrosion of the G2, FJORD, EUROMETRIC, LUSTER or FREEMAN hip stems.

However, based on DePuy's research, the risk versus benefit related to this combination is no longer considered to be acceptable to DePuy. Accordingly, DePuy has decided to amend the Instructions for Use (IFU) product labeling for the G2 hip stems. The new IFU will include a warning against implantation of these specific hip stems combined with a metal-on-metal articulation[2] of an all metal type. The IFU product labeling for the following products will not be updated as these products are now obsolete: FJORD, TPS, EUROMETRIC, LUSTER and FREEMAN

Patient Care:
Patients should be followed according to local guidance/standard of care for patients receiving metal on metal articulations. Please refer to your local orthopaedic association for detailed information related to the treatment of patients with metal on metal articulations.

NOTE: The above products remain safe and effective when used in any other approved bearing combination.

Transmission of this Field Safety Notice:
This notice has been sent to you as our records indicate that your organisation has purchased the G2, FJORD, TPS, EUROMETRIC, LUSTER or FREEMAN hip stems.

This notice needs to be passed on to all those who need to be aware within your organisation or to any organisation where these products may have been transferred.

Contact:
Paul Arnott
DePuy International Ltd.
St Anthony's Road
Leeds LS11 8DT
England

This FSN has been notified to the appropriate Regulatory Agency.

Date: ***XXXXX***

Paul Arnott
Vigilance Manager

Notes:

1. Within the cement contact area
2. Including head and acetabular cup and where the cup is of an all metal construction (monobloc or modular)

Appendix A

Product codes (to be confirmed):

Brand	Code	Description
TPS	85-2781	Ultima TPS Femoral Stem Size 0
Released June 1997	85-2782	Ultima TPS Femoral Stem Size 1
Obsolete 2009	85-2783	Ultima TPS Femoral Stem Size 1M
	85-2784	Ultima TPS Femoral Stem Size 2
	85-2785	Ultima TPS Femoral Stem Size 2M
	85-2786	Ultima TPS Femoral Stem Size 3
	85-2787	Ultima TPS Femoral Stem Size 3M
	85-2920	Ultima TPS Femoral Stem Size 4
	85-2921	Ultima TPS Femoral Stem Size 4M
	85-2922	Ultima TPS Femoral Stem Size 5
	85-2923	Ultima TPS Femoral Stem Size 5M
TPS	85-9894	Ultima TPS Femoral Stem Size 1
Released Nov 1996	85-9895	Ultima TPS Femoral Stem Size 2
Obsolete 2009	85-9896	Ultima TPS Femoral Stem Size 3
	85-9897	Ultima TPS Femoral Stem Size 4
	85-9898	Ultima TPS Femoral Stem Size 5
	85-9899	Ultima TPS Femoral Stem Size 1M
	85-9900	Ultima TPS Femoral Stem Size 2M
	85-9901	Ultima TPS Femoral Stem Size 3M
	85-9902	Ultima TPS Femoral Stem Size 4M
	85-9903	Ultima TPS Femoral Stem Size 5M
Brand	**Code**	**Description**
LUSTER	152180001	LUSTER Hip Size 1
Released July 1996	152180002	LUSTER Hip Size 2
Obsolete 2005	152180003	LUSTER Hip Size 3
	152180004	LUSTER Hip Size 4
	152180005	LUSTER Hip Size 5
	152180006	LUSTER Hip Size 1 High Offset
	152180007	LUSTER Hip Size 2 High Offset
	152180008	LUSTER Hip Size 3 High Offset
	152180009	LUSTER Hip Size 4 High Offset
	152180010	LUSTER Hip Size 5 High Offset

Brand	Code	Description
EUROMETRIC	L712110	EUROMETRIC Cemented Stem Size 1 Right
Released 2003	L712120	EUROMETRIC Cemented Stem Size 2 Right
Obsolete Sept 2011	L712130	EUROMETRIC Cemented Stem Size 3 Right
	L712135	EUROMETRIC Cemented Stem Size 3.5 Right
	L712140	EUROMETRIC Cemented Stem Size 4 Right
	L712145	EUROMETRIC Cemented Stem Size 4.5 Right
	L712150	EUROMETRIC Cemented Stem Size 5 Right
	L712155	EUROMETRIC Cemented Stem Size 5.5 Right
	L712160	EUROMETRIC Cemented Stem Size 6 Right
	L712170	EUROMETRIC Cemented Stem Size 7 Right
	L712210	EUROMETRIC Cemented Stem Size 1 Left
	L712220	EUROMETRIC Cemented Stem Size 2 Left
	L712230	EUROMETRIC Cemented Stem Size 3 Left
	L712235	EUROMETRIC Cemented Stem Size 3.5 Left
	L712240	EUROMETRIC Cemented Stem Size 4 Left
	L712245	EUROMETRIC Cemented Stem Size 4.5 Left
	L712250	EUROMETRIC Cemented Stem Size 5 Left
	L712255	EUROMETRIC Cemented Stem Size 5.5 Left
	L712260	EUROMETRIC Cemented Stem Size 6 Left
	L712270	EUROMETRIC Cemented Stem Size 7 Left

Brand	Code	Description
G2 CEMENTED ARTICULEZE	900000141	G2 Cemented Stem 1 Articuleze Taper
Released May 2000	900000143	G2 Cemented Stem 3 Articuleze Taper
Current	900000145	G2 Cemented Stem 5 Articuleze Taper
	900000147	G2 Cemented Stem 7 Articuleze Taper
	900000149	G2 Cemented Stem 9 Articuleze Taper
	900000151	G2 Cemented Stem 11 Articuleze Taper
	900000161	G2 Cemented Stem 1L Articuleze Taper
	900000163	G2 Cemented Stem 3L Articuleze Taper
	900000165	G2 Cemented Stem 5L Articuleze Taper
	900000167	G2 Cemented Stem 7L Articuleze Taper
	900000169	G2 Cemented Stem 9L Articuleze Taper
	900000171	G2 Cemented Stem 11L Articuleze Taper
G2 CEMENTED 11/13	85-8400	G2 Polished Femoral Component Size 1 11/13
Released Sep 1998	85-8401	G2 Polished Femoral Component Size 3 11/13
Current	85-8402	G2 Polished Femoral Component Size 5 11/13
	85-8403	G2 Polished Femoral Component Size 7 11/13
	85-8404	G2 Polished Femoral Component Size 9 11/13
	85-8405	G2 Polished Femoral Component Size 11 11/13
	85-8407	G2 Polished Femoral Component Size 1M 11/13
	85-8408	G2 Polished Femoral Component Size 3M 11/13
	85-8409	G2 Polished Femoral Component Size 5M 11/13
	85-8410	G2 Polished Femoral Component Size 7M 11/13
	85-8411	G2 Polished Femoral Component Size 9M 11/13
	85-8412	G2 Polished Femoral Component Size 11M 11/13
G2 CEMENTED RSA 11/13	85-7475	G2 Polished Stem RSA Study Size 1 11/13
Released June 2000	85-7476	G2 Polished Stem RSA Study Size 3 11/13
Current	85-7477	G2 Polished Stem RSA Study Size 5 11/13
	85-7478	G2 Polished Stem RSA Study Size 7 11/13
	85-7479	G2 Polished Stem RSA Study Size 9 11/13
	85-7480	G2 Polished Stem RSA Study Size 11 11/13
	85-7481	G2 Polished Stem RSA Study Size 1M 11/13
	85-7482	G2 Polished Stem RSA Study Size 3M 11/13
	85-7483	G2 Polished Stem RSA Study Size 5M 11/13
	85-7484	G2 Polished Stem RSA Study Size 7M 11/13
	85-7485	G2 Polished Stem RSA Study Size 9M 11/13
	85-7486	G2 Polished Stem RSA Study Size 11M 11/13

Brand	Code	Description
FJORD	L96909	FJORD Cemented Standard Femoral Stem 12/14 Size 9
Released 1997	L96910	FJORD Cemented Standard Femoral Stem 12/14 Size 10
Obsolete May 2011	L96911	FJORD Cemented Standard Femoral Stem 12/14 Size 11
	L96912	FJORD Cemented Standard Femoral Stem 12/14 Size 12
	L96913	FJORD Cemented Standard Femoral Stem 12/14 Size 13
	L96914	FJORD Cemented Standard Femoral Stem 12/14 Size 14
	L96915	FJORD Cemented Standard Femoral Stem 12/14 Size 15
	L96916	FJORD Cemented Standard Femoral Stem 12/14 Size 16
	L96918	FJORD Cemented Standard Femoral Stem 12/14 Size 18
	L96932	FJORD Cemented Long Femoral Stem 12/14 Size 12
	L96934	FJORD Cemented Long Femoral Stem 12/14 Size 14
	L96936	FJORD Cemented Long Femoral Stem 12/14 Size 16
	L96938	FJORD Cemented Long Femoral Stem 12/14 Size 18

Brand	Code	Description
FREEMAN Finsbury	133-111	Freeman Cemented Hip Stem 12mm Short Neck
Launched 2004	133-112	Freeman Cemented Hip Stem 12mm Medium Neck
Obsolete July 2011	133-121	Freeman Cemented Hip Stem 14mm Short Neck
	133-122	Freeman Cemented Hip Stem 14mm Medium Neck
	133-131	Freeman Cemented Hip Stem 16mm Short Neck
	133-132	Freeman Cemented Hip Stem 16mm Medium Neck
	133-142	Freeman Cemented Hip Stem 18mm Medium Neck
	133-421	Freeman Cemented Revision Stem 14mm Short Neck
	133-422	Freeman Cemented Revision Stem 14mm Medium Neck
	133-431	Freeman Cemented Revision Stem 16mm Short Neck
	133-432	Freeman Cemented Revision Stem 16mm Medium Neck

APPENDIX C: Full list of current and intended publications, conference proceedings and conference publications

The following is a compilation of all the publications and presentations of the author arising from the subject of this thesis. Copies of the papers are not included. A full reference has been made to publications that are currently available.

CURRENT AND INTENDED PUBLICATIONS

Michael Bryant, Xinming Hu, Richard Farrar, Robert Freeman, Ken Brummitt, Anne Neville, **Crevice corrosion of biomedical alloys: A novel method of assessing the effects of bone cement and its chemistry**, Journal of Biomedical Materials Research Part B: Applied Biomaterials, 101B, 5, 2013, Pages 792-803. http://dx.doi.org/10.1002/jbm.b.32883

M. Bryant, R. Farrar, K. Brummitt, R. Freeman, A. Neville, **Fretting corrosion of fully cemented polished collarless tapered stems: The influence of PMMA bone cement**, Wear, Volume 301, Issues 1–2, April–May 2013, Pages 290-299, ISSN 0043-1648, http://dx.doi.org/10.1016/j.wear.2012.12.042.

Michael Bryant, Richard Farrar, Robert Freeman, Ken Brummitt, Anne Neville, **Fretting corrosion characteristics of polished collarless tapered stems in a simulated biological environment**, Tribology International, Available online 11 April 2013, ISSN 0301-679X, http://dx.doi.org/10.1016/j.triboint.2013.01.024.

Michael Bryant, Michael Ward, Richard Farrar, Robert Freeman, Ken Brummitt, John Nolan, Anne Neville, **Failure analysis of cemented metal-on-metal total hip**

replacements from a single centre cohort, Wear, Volume 301, Issues 1–2, April–May 2013, Pages 226-233, ISSN 0043-1648, http://dx.doi.org/10.1016/j.wear.2012.12.013.

Characterisation of the Surface Topography, Tomography and Chemistry of Fretting Corrosion Product Found on Retrieved Polished Femoral Stems - J Biomed Mater Res Part B: Appl Biomater

Influence of Galvanic Coupling on the Fretting Corrosion of Cemented Femoral Stems – Acta Biomaterilia

Influence of Surface Roughness on the Fretting Corrosion of Cemented Femoral Stems – Tribology International/ImechE

Crevice Corrosion of LC CoCrMo Cemented Femoral Stems – TBC

PRESENTATIONS/CONFERENCE PROCEEDINGS

NACE CORROSION (2011) - Crevice corrosion of cemented metal-on-metal total hip replacements: The effect of antibiotic bone cement.

KTP Residential (2011) - Crevice Corrosion of Cemented Metal on Metal Total Hip Replacement: The Effects of Antibiotic Bone Cement.

Depuy Warsaw visit (2011) - DePuy Ultima TPS corrosion project.

Depuy CMW visit (2011) - Depuy Ultima TPS corrosion project.

ImechE Engineers and Surgeons: Joined at the Hip III (2011) - Crevice Corrosion of Cemented Metal-on-Metal Total Hip Replacements.

NACE CORROSION (2012) - Crevice Corrosion of Biomedical Alloys: A Novel Method of Assessing the Effects of Bone Cement and its Chemistry.

Leeds-Lyon Tribology Conference (2012) - Fretting Corrosion Characteristics of Fully Cemented Polished Tapered Femoral stems in a Simulated Biological Environment.

Corrosion Science Symposium (2012) - Effects of Surface Pre-treatment on the Surface Chemistry, Metallurgy and Crevice Corrosion Mechanisms of Low Carbon CoCrMo Alloys Used in Cemented Total Hip Arthroplasty.

5th Advanced Hip Resurfacing Course (2012) - Future Designs and Materials: Corrosion of Orthopaedic Devices.

British Hip Society (2013) - Fretting-corrosion of taper polished femoral stems: comparison of clinical and experimental findings.

NACE CORROSION (2013) - Fretting corrosion of cemented CoCrMo femoral stems: Electrochemical response and characterisation of ionic debris.

Wear of Materials (2013) - Failure Analysis of Cemented Metal-on-Metal Total Hip Replacements from a Single Centre Cohort.

Wear of Materials (2013) - Fretting corrosion of cemented CoCrMo femoral stems: the influence of PMMA bone cement.